

MAGNETISM AND THE KONDO EFFECT IN CERIUM HEAVY-FERMION
COMPOUNDS CERIUM-ALUMINUM-3 AND CERIUM-LEAD-3

By

RICHARD PIETRI

A DISSERTATION PRESENTED TO THE GRADUATE SCHOOL OF THE
UNIVERSITY OF FLORIDA IN PARTIAL FULFILLMENT OF THE
REQUIREMENTS FOR THE DEGREE OF DOCTOR OF PHILOSOPHY

UNIVERSITY OF FLORIDA

2001

ACKNOWLEDGMENTS

I would like to dedicate this work to my parents Gilberto Pietri and Palmira Santiago, who made it possible for me to complete my education. There is no way to measure the amount of support and advice I have received from these two wonderful human beings. I give thanks to an all-powerful, everlasting God for my parents, and for the opportunity to pursue my goals and dreams. I also thank my relatives for all their support during my years at UF.

The most influential person in this project was my research advisor, Dr. Bohdan Andraka. He was the source behind many of the ideas on this dissertation. He was also a great mentor in the lab, from whom I learned countless experimental “tricks.” He has my deepest appreciation. The second most influential person was Prof. Greg Stewart, an endless source of information. I thank him very much for letting me work in his lab. His written work inspired me throughout my graduate career. I would also like to thank my other committee members, Prof. Mark Meisel, Prof. Pradeep Kumar, and Prof. Cammy Abernathy for their patience in reading this work, for many discussions, and for their advice regarding this dissertation. My appreciation also goes to people whom I worked with in the lab over many years. I thank Dr. Jungsoo Kim and Dr. Steve Thomas for their training and technical advice, and Josh Alwood and Dr. Hiroyuki Tsujii for help in the lab and with some of the experiments. Greg Labbe and the people at the Cryogenics Lab were also very helpful, especially while using the magnet dewar. Other people in this field I would like to acknowledge are Prof. Kevin Ingersent, for many discussions about my research and for an excellent collaboration; Prof. Peter Hirschfeld for introducing me to the theory of heavy-fermions and to the Kondo

effect; and Dr. Ray Osborn and Dr. Eugene Goremychkin, whose work motivated part of this study, for very enlightening discussions over the last year and during the 2000 APS March Meeting. I am indebted to Dr. Youli Kanev and my good friend Dr. Mike Jones for developing the L^AT_EX UF thesis template, which greatly simplified all of the formatting work, and to my fellow graduate students, especially Rich Haas, Dr. Tony Rubiera, and Brian Baker for interesting physics discussions and advice. My thanks go also to Susan Rizzo and Darlene Latimer for all the grad-school related paperwork and for taking care of my registration over the years.

Finally, my life would have been unbearable without the company and emotional support of many people here in Gainesville, FL. They helped me stay motivated and cope with the ups and downs of Physics Graduate School. I would like to thank my dearest friends James Bailey, Ferdinand Rosa, Dr. Carlos (“Caco”) Ortiz, Iván Guzmán, Clinton Kaiser, Dr. Fernando Gómez, Soraya Benítez, Cristine Plaza, Diana Serrano, Jorge Carranza, Franco Ortiz, Lyvia Rodríguez, Anthony Wells, Diana Hambrick, and Charles and Sarah Reagor. I apologize to the countless others who are not on this list, including the people at the Southwest Recreation Center, the Worldwide Church of God, Latin nights at the Soul House, Saoca, La Sala, Rhythm, and all the “tailgators” over the years.

TABLE OF CONTENTS

	<u>page</u>
ACKNOWLEDGMENTS	ii
ABSTRACT	vii
CHAPTERS	
1 INTRODUCTION	1
2 THEORETICAL BACKGROUND	6
2.1 Landau Fermi-Liquid Theory	6
2.1.1 Theoretical Basis for a Fermi-liquid	7
2.1.2 Thermodynamic and Transport Properties	10
2.2 Localized Magnetic Moments in Metals	11
2.2.1 Electronic States of Magnetic Ions	12
2.2.2 Anderson Model	14
2.3 Single-ion Kondo Model	18
2.4 Anisotropic Kondo Model	20
2.5 Kondo Lattice	27
2.6 Non-Fermi-Liquid Effects	30
3 PROPERTIES OF CeAl ₃ AND CePb ₃	34
3.1 Properties of CeAl ₃	34
3.1.1 Crystal Structure	34
3.1.2 Specific Heat	36
3.1.3 Magnetic Susceptibility	37
3.1.4 Transport Measurements	40
3.1.5 Nuclear Magnetic Resonance	42
3.1.6 Muon Spin Rotation	45
3.1.7 Neutron Scattering	48
3.1.8 Chemical Substitution Studies	48
3.2 Properties of CePb ₃	51
3.2.1 Crystal Structure	51
3.2.2 Specific Heat	51
3.2.3 Sound Velocity Measurements	54
3.2.4 Transport Measurements	58
3.2.5 Magnetic Susceptibility	60
3.2.6 Neutron Scattering	63
3.2.7 Chemical Substitution Studies	65

4	MOTIVATION	68
4.1	Importance of CeAl ₃ and CePb ₃	68
4.2	Objectives	70
4.2.1	Magnetism and Heavy-Fermion Behavior in Ce Kondo Lattices	70
4.2.2	Ground State of CeAl ₃	71
5	EXPERIMENTAL METHODS	73
5.1	Sample Preparation	73
5.1.1	Synthesis	73
5.1.2	Annealing	77
5.2	Diffraction of X-Rays	78
5.3	Magnetic Measurements	79
5.4	Specific Heat Measurements	80
5.4.1	Equipment	82
5.4.2	Thermal Relaxation Method	86
5.5	Experimental Probes	89
5.5.1	Experiments on CeAl ₃	90
5.5.2	Experiments on CePb ₃	91
6	STRUCTURAL AND THERMODYNAMIC PROPERTIES OF CeAl ₃ ALLOYS	93
6.1	Lattice Parameter Study of CeAl ₃ Alloys	93
6.1.1	Lanthanum Doping: Ce _{1-x} La _x Al ₃	96
6.1.2	Yttrium Doping: Ce _{1-x} Y _x Al ₃	100
6.1.3	Mixed Doping: Ce _{0.8} (La _{1-x} Y _x) _{0.2} Al ₃	108
6.1.4	Summary	113
6.2	Thermodynamic Measurements of Ce _{1-x} La _x Al ₃ Alloys	116
6.2.1	Magnetic Susceptibility	116
6.2.2	Specific Heat	118
6.2.3	Discussion	127
6.3	Thermodynamic Measurements on Ce _{1-x} Y _x Al ₃ Alloys	134
6.3.1	Magnetic Susceptibility	134
6.3.2	Specific Heat	137
6.3.3	Discussion	139
6.4	Thermodynamic Measurements on Ce _{0.8} (La _{1-x} Y _x) _{0.2} Al ₃ Alloys	141
6.4.1	Magnetic Susceptibility	141
6.4.2	Specific Heat	144
6.4.3	Discussion	147
6.5	Heat Capacity of Ce _{0.8} La _{0.2} Al ₃ and Ce _{0.3} La _{0.7} Al ₃ in Magnetic Fields	153
6.5.1	Results	154
6.5.2	Discussion	157

7	MAGNETIC FIELD STUDY OF CePb ₃ ALLOYS	165
7.1	Specific Heat of CePb ₃ in Magnetic Fields	165
7.2	Single-Ion Kondo Behavior of Ce _{0.6} La _{0.4} Pb ₃ in Magnetic Fields	175
7.2.1	Results	175
7.2.2	Discussion	179
8	CONCLUSION	184
8.1	Summary	184
8.1.1	Ideas for Future Work	187
	REFERENCES	189
	BIOGRAPHICAL SKETCH	198

Abstract of Dissertation Presented to the Graduate School
of the University of Florida in Partial Fulfillment of the
Requirements for the Degree of Doctor of Philosophy

MAGNETISM AND THE KONDO EFFECT IN CERIUM HEAVY-FERMION
COMPOUNDS CERIUM-ALUMINUM-3 AND CERIUM-LEAD-3

By

Richard Pietri

August 2001

Chairman: Bohdan Andraka

Major Department: Physics

Measurements of the lattice parameters, magnetic susceptibility, and specific heat between 0.4 and 10 K in magnetic fields up to 14 T have been conducted on $\text{Ce}_{1-x}\text{M}_x\text{Al}_3$ alloys, with M = La ($0 \leq x \leq 1$) and Y ($0 \leq x \leq 0.2$). The specific heat of CePb_3 and $\text{Ce}_{0.6}\text{La}_{0.4}\text{Pb}_3$ was also measured up to 14 T. The above experiments were performed to study the anomalies in the specific heat of CeAl_3 and CePb_3 , and to better understand the interplay between magnetism and Kondo behavior in the ground state of Ce heavy-fermion systems.

Data for x-ray diffraction of $\text{Ce}_{1-x}\text{M}_x\text{Al}_3$ confirmed an anisotropic lattice volume expansion for M = La (decreasing c/a ratio) and a contraction for M = Y. The low-temperature magnetic susceptibility and specific heat of $\text{Ce}_{1-x}\text{La}_x\text{Al}_3$ are consistent with Doniach's Kondo necklace model. The electronic coefficient γ decreases with Y concentration, and has a nonmonotonic dependence for M = La with a minimum at $x = 0.2$. The temperature position of the anomaly T_m has a maximum around $x = 0.3$ for La doping. The lack of a suppression

of T_m for Y $x < 0.2$ suggests a dependence of this maximum on the absolute-value change in c/a . Magnetic field measurements on La-doped CeAl_3 alloys revealed that the field dependence of T_m is inconsistent with the anisotropic Kondo model, with T_m for $\text{Ce}_{0.8}\text{La}_{0.2}\text{Al}_3$ decreasing only by 0.4 K at 14 T. Experiments on $\text{Ce}_{0.8}(\text{La}_{1-x}\text{Y}_x)_{0.2}\text{Al}_3$ revealed that $C/T \propto \chi \propto T^{-1+\lambda}$ for $x = 0.4$, with λ comparable to that of heavy-fermion alloys with scaling similar to that associated with a quantum Griffiths phase.

Specific heat measurements up to 14 T on polycrystalline CePb_3 indicated a shift in T_N to lower values, disappearing for $H > 6$ T. The ratio A/γ^2 is field-dependent below 6 T. Studies on $\text{Ce}_{0.6}\text{La}_{0.4}\text{Pb}_3$ revealed that the electronic specific heat ΔC of this alloy can be described by the single-ion Kondo model in magnetic fields, with $T_K \simeq 2.3$ K. A previously undetected anomaly in C/T was found below 2 K, shifting toward higher temperatures with increasing field. This maximum appears to be a feature of the Kondo model in magnetic fields.

CHAPTER 1

INTRODUCTION

Over the last century, our current understanding of the metallic state developed as a result of substantial experimental and theoretical work based on the discovery of the electron by J. J. Thomson in 1897 and the advent of modern quantum physics. The behavior of solids has long been described in terms of the dynamics of its constituents, electrons and nuclei; with the former being responsible for electrical conduction and dominating the thermodynamic properties at very low temperatures. This single-electron picture of the solid state has been remarkably successful in describing the properties of many body systems that, as a whole, are much more than a simple array of atoms. The current picture of a lattice of ions embedded in a gas of electrons obeying Fermi-Dirac statistics is justified by the theoretical framework set by Landau on his Fermi-liquid theory, for which he won the Nobel Prize in 1962. Based on the principle of adiabatic continuity, the theory states that the metallic state at low temperatures can be described quantum-mechanically in terms of a fluid of weakly-interacting particles (Fermi-liquid, see Chapter 2). The properties of this quantum fluid are similar in form to those of a gas of noninteracting electrons. Landau's Fermi-liquid theory has been successfully applied to a variety of systems, including liquid ^3He and normal metals like Au and Ag. It is one of the foundations of modern condensed matter physics, rivaled in its scope only by the standard model of particle physics.

Since the development of Fermi-liquid theory, the synthesis of new materials displaying unusual properties presented challenges to this well-established description of condensed matter systems. A large number of these materials exhibit strong

electron correlations in their normal (paramagnetic) state, stretching the limits of applicability of Fermi-liquid theory. In some materials, the effect of these interactions is reflected in the deviations of their thermodynamic and transport properties from the predictions of this theory. This group includes the normal state of high-temperature superconductors and non-Fermi-liquid systems [1, 2, 3]. In others, their normal-state properties remarkably agree with Fermi-liquid theory, despite the presence of strong interactions between electrons and even the coexistence with a magnetic phase. It is in this group that we find most heavy-fermion compounds.

Heavy-fermion systems are alloys where one of their constituents is a member of the lanthanide (Ce, Yb) or actinide (U, Np) family. They are so called because the effective mass of the particles dominating the thermodynamics, which have half-integer spin (fermions), is hundreds of times that of a free electron (heavy). Extensive reviews on these systems have been written over the last two decades [4, 5, 6, 7, 8]. In these systems, the interactions between localized f electrons and the conduction band reduce the f magnetic moment and give rise to a Fermi-liquid-like state at low temperatures. The large effective mass m^* is a consequence of the large density of states at the Fermi energy $N(0)$.

The most widely used experimental parameter to determine both the density of states and the effective mass of these particles is the Sommerfeld coefficient of the specific heat γ . In Fermi-liquid theory, γ is proportional to both m^* and $N(0)$. The specific heat of metals in their normal state at low temperatures is approximated by the following formula [9, 10]:

$$C = \gamma T + \beta T^3, \quad (1.1)$$

where γ is the electronic contribution and β is the Debye contribution from lattice vibrations. Values of γ for heavy-fermion compounds typically range from several hundred to several thousand mJ/K² mol, compared to less than one for normal metals like Cu and Au. The presence of additional contributions to the specific

heat makes the determination of γ more difficult, and γ is usually represented as the extrapolated value of C/T at zero temperature.

The heavy-fermion character is also reflected in other properties, like magnetic susceptibility and electrical resistivity. The magnetic susceptibility at high temperatures follows the Curie-Weiss form [9, 10],

$$\chi = \frac{C}{T + \Theta_{\text{cw}}}, \quad (1.2)$$

where C is the Curie constant and Θ_{cw} is the Curie-Weiss temperature. At lower temperatures, the susceptibility reaches a constant value (~ 10 to 100 memu/mol), proportional to the density of states $N(0)$ according to Fermi-liquid theory. The electrical resistivity of metals at very low temperatures is given by

$$\rho = \rho_0 + AT^2. \quad (1.3)$$

Here, ρ_0 is the temperature-independent term due to scattering off impurities and defects, and A is the Fermi-liquid term. Values for A in heavy fermions are in the order of tens of $\mu\Omega\text{cm}/\text{K}^2$, much larger than those corresponding to normal metals.

An intriguing fact of heavy-fermion systems is that the observed Fermi-liquid properties are not exclusive to the normal state of these materials. The variety of ground states for these compounds [5, 6] ranges from nonmagnetic, as in UPt_4Au [11], to antiferromagnetic (UCu_5 , U_2Zn_{17} , CeAl_2) to superconducting (UBe_{13} , CeCu_2Si_2), to both magnetic and superconducting (UPt_3 , URu_2Si_2 , UPd_2Al_3 , UNi_2Al_3). The presence of magnetism and/or superconductivity in these compounds indicates that the heavy Fermi-liquid ground state coexists with a different phase.

This unconventional ground state, when tuned as a function of pressure, magnetic field, and/or chemical disorder, can completely move away from Fermi-liquid behavior. These non-Fermi-liquid (NFL) alloys have been widely studied

during the last decade [3, 12]. Their thermodynamic and transport properties are characterized by power laws in temperature. Theoretical models for the description of these effects are currently under development. Examples of these systems [3, 12] include $\text{UCu}_{5-x}\text{Pd}_x$, $\text{CeCu}_{6-x}\text{Au}_x$, $\text{U}_{1-x}\text{Y}_x\text{Pd}_3$, Ce_7Ni_3 (pressure-induced NFL), and CeNi_2Ge_2 [13], $\text{U}_2\text{Pt}_2\text{In}$, and $\text{U}_2\text{Co}_2\text{Sn}$ [14] (NFL compounds).

Among the many unresolved issues in heavy-fermion materials is the coexistence of magnetic and Fermi-liquid degrees of freedom giving rise to the ground state. In addition, a recent interpretation of the ground state in terms of an anisotropic interaction between f electrons and the conduction band has been proposed for these systems [15]. Both topics are confronted in this dissertation by studying structural and thermodynamic properties of two well-studied canonical heavy-fermion compounds: CeAl_3 and CePb_3 . Cerium-based compounds were chosen because of their simpler electronic configuration. There is only one $4f$ spin per Ce ionic site, as opposed to two or three $5f$ spins per U ionic site. The ground state properties of the above compounds are not well understood, despite more than 20 years of study. The experiments presented here will help clarify these issues in order to motivate further discussion of these topics on both theoretical and experimental grounds.

The outline of the dissertation is as follows: The necessary theoretical background behind heavy-fermion physics is presented in Chapter 2. The chapter begins with an overview of Landau's Fermi-liquid theory, followed by a discussion of the energies involved in the determination of the ionic ground state and magnetic moments in metals. The Kondo effect, the mechanism responsible for the Fermi-liquid state at low temperatures in heavy fermions, is then presented along with its anisotropic version. The concept of a Kondo lattice is also introduced, and the consequences of extending the Kondo model to a concentrated system are discussed. Chapter 3 gives an experimental review of the essential physical

properties of both CeAl_3 and CePb_3 . It is then followed by a discussion of the motivation behind this study (Chapter 4). Chapter 5 gives a general description of the experimental apparatus and methods used in this dissertation. The results of structural and thermodynamic measurements on CeAl_3 and CePb_3 alloys are then explained in Chapters 6 and 7, respectively. Finally, Chapter 8 summarizes the main findings of the dissertation and elaborates on its contributions to the field. The dissertation ends by pointing out unresolved issues and elaborating on ideas for future studies.

CHAPTER 2

THEORETICAL BACKGROUND

This chapter discusses the current theoretical models describing the characteristics and behavior of heavy-fermion systems, such as Fermi-liquid theory, ionic configurations in solids, and the Kondo effect.

2.1 Landau Fermi-Liquid Theory

Landau's theory of interacting fermions at low temperatures [16] stands as one of the most remarkable achievements of theoretical condensed matter physics. It has often been compared to the standard model of elementary particle physics, as far as its scope and prediction of physical properties is concerned. The basis of its success is the adaptation of the Fermi gas model of noninteracting electrons to a system of interacting fermions at low densities and energies. This mapping allows for a single-particle description of thermodynamic and transport properties of Fermi systems like liquid ^3He and normal metals like copper, silver, and gold. Although Landau's Fermi-liquid theory has been successfully applied in a large number of condensed-matter systems, its validity relies on a series of assumptions that apply mostly to weak interactions and isotropic scattering between fermions. Heavy-fermion systems, often described as having a Fermi-liquid ground state, exhibit strong many-particle correlations that lead to magnetic order in many cases. The relation between magnetism and Fermi-liquid behavior in heavy fermions is at present not fully understood. Nevertheless, the theory has been successful in predicting the properties of these compounds. In this section, the differences

between Fermi-gas and Fermi-liquid models are outlined, followed by a description of thermodynamic and transport properties of the Fermi liquid.

2.1.1 Theoretical Basis for a Fermi-liquid

For a system of noninteracting particles obeying Fermi-Dirac statistics, with mass m , momentum \mathbf{p} and spin σ , the probability of finding a particle with energy ε is given by the Fermi distribution function $n(\varepsilon)$ [17],

$$n(\varepsilon) = \frac{1}{1 + e^{(\varepsilon - \mu)/k_B T}}, \quad (2.1)$$

where k_B is Boltzmann's constant and $\mu = \varepsilon_F$, the Fermi energy. The spins are assumed to be quantized along the z -axis.

In the absence of an external field, the energy of a particle becomes $\varepsilon = \varepsilon_{\mathbf{p}} = p^2/2m$, and the ground state distribution $n_{\mathbf{p}\sigma}^0$ is given by

$$n_{\mathbf{p}\sigma}^0 = \begin{cases} 1 & p \leq p_F \\ 0 & p > p_F \end{cases}, \quad (2.2)$$

where p_F is the Fermi momentum. The ground state energy of the system E_0 is equal to

$$E_0 = \sum_{\mathbf{p}\sigma} n_{\mathbf{p}\sigma}^0 \varepsilon_{\mathbf{p}}. \quad (2.3)$$

The total energy is the sum of the ground state energy and the excitation energies of the system. The number of excitations is given by the difference between the ground-state and excited-states distribution functions:

$$\delta n_{\mathbf{p}\sigma} = n_{\mathbf{p}\sigma} - n_{\mathbf{p}\sigma}^0, \quad (2.4)$$

where $\delta n_{\mathbf{p}\sigma} > 0$ corresponds to a particle excitation and $\delta n_{\mathbf{p}\sigma} < 0$ to a hole excitation. Since the excitation energies depend on the number of excitations, the total energy of the system can be expressed as

$$E = E_0 + \sum_{\mathbf{p}\sigma} \varepsilon_p \delta n_{\mathbf{p}\sigma}. \quad (2.5)$$

Despite the strong electrostatic forces between electrons in a solid, the Fermi gas model for noninteracting electrons is capable of describing their behavior in metals. At metallic electron densities, the kinetic and Coulomb energy terms are comparable in magnitude to each other. The justification for the predictions of this model come from their close resemblance to those of the interacting case. Through adiabatic continuity [16], it is possible to label the states of an interacting Fermi system in terms of the states of a Fermi gas. When the interaction potential is treated as a perturbation, and is turned on slowly enough to prevent a change in the eigenstates of the Hamiltonian, there is a one-to-one correspondence between the initial and final states. The excitation energies of the final state are different from those of the Fermi gas because of the additional interaction term in the Hamiltonian. The final state has also the same entropy and can be described by the same distribution function as the noninteracting Fermi gas. The system resulting from the adiabatic perturbation is called a Fermi liquid. The excited states of a Fermi liquid are no longer associated with independent electrons, but to negatively charged, spin-1/2 fermions called quasiparticles, with an effective mass m^* different from that of a free electron. These quasiparticles have a sufficiently long lifetime τ between collisions at low temperatures. The condition for the applicability of Fermi-liquid theory is that the uncertainty in the energy of a particle, of order $\hbar/\tau \propto (k_B T)^2$, is much smaller than the width of the excitation spectrum of the Fermi distribution function, of order $k_B T$ [18]:

$$\hbar/\tau \ll k_B T. \quad (2.6)$$

This condition applies to a system with excitation energies much smaller than $k_B T$.

Due to the mutual interaction between quasiparticles, the total energy of the system is no longer represented by the sum of ground state and individual excitation energies. As a consequence, each quasiparticle is under the influence of a self-consistent field from other quasiparticles. This self-consistent field affects

both potential and kinetic energy terms of each individual quasiparticle. The energy E then becomes a functional $E\{n_{\mathbf{p}\sigma}\}$ of the distribution function. The excitation (quasiparticle) energy, which itself is a functional of the distribution function, ($\varepsilon = \varepsilon\{n_{\mathbf{p}\sigma}\}$), has an additional term corresponding to the interaction energy between two quasiparticles $f_{\mathbf{p}\sigma, \mathbf{p}'\sigma'}$, each with momentum and spin $\mathbf{p}\sigma$ and $\mathbf{p}'\sigma'$, respectively. This energy term is also a functional $f\{n_{\mathbf{p}\sigma}\}$ of the distribution function, so that the quasiparticle energy becomes an expansion in terms of the number of excitations $\delta n_{\mathbf{p}\sigma}$ [19]:

$$\varepsilon_{\mathbf{p}\sigma} = \varepsilon_{\mathbf{p}\sigma}^0 + \sum_{\mathbf{p}'\sigma'} f_{\mathbf{p}\sigma, \mathbf{p}'\sigma'} \delta n_{\mathbf{p}'\sigma'} + \dots, \quad (2.7)$$

where $\varepsilon_{\mathbf{p}\sigma}^0$ is the ground-state quasiparticle energy. As a result, the total energy of the system is also an expansion in $\delta n_{\mathbf{p}\sigma}$:

$$E = E_0 + \sum_{\mathbf{p}\sigma} \varepsilon_{\mathbf{p}\sigma}^0 \delta n_{\mathbf{p}\sigma} + \frac{1}{2} \sum_{\mathbf{p}\sigma, \mathbf{p}'\sigma'} f_{\mathbf{p}\sigma, \mathbf{p}'\sigma'} \delta n_{\mathbf{p}\sigma} \delta n_{\mathbf{p}'\sigma'} + \dots. \quad (2.8)$$

When considering an ensemble of quasiparticles with spins quantized along different axes, the distribution function $n_{\mathbf{p}\sigma}$ should be treated as a 2×2 matrix in spin space, that is, as a linear combination of the Pauli matrices. In the absence of higher-order scattering processes, like spin-orbit coupling, the interaction energy can be expressed as the sum of symmetric and antisymmetric (spin-dependent) terms

$$f_{\mathbf{p}\mathbf{p}'} = f_{\mathbf{p}\mathbf{p}'}^s + f_{\mathbf{p}\mathbf{p}'}^a \boldsymbol{\tau} \cdot \boldsymbol{\tau}', \quad (2.9)$$

where $f_{\mathbf{p}\mathbf{p}'}^s$ and $f_{\mathbf{p}\mathbf{p}'}^a$ are the symmetric and antisymmetric terms, respectively, and $\boldsymbol{\tau}, \boldsymbol{\tau}'$ are Pauli matrices. Both $f_{\mathbf{p}\mathbf{p}'}^s$ and $f_{\mathbf{p}\mathbf{p}'}^a$ are dependent on the angle between \mathbf{p} and \mathbf{p}' , and can be expressed as an expansion in Legendre polynomials, with coefficients f_l^s and f_l^a , in the case of isotropic scattering (spherical Fermi surface). In some metals, the presence of crystal-field and spin-orbit coupling effects significantly distorts the Fermi surface, changing the angular dependence of

$f_{\mathbf{p}\mathbf{p}'}^s$ and $f_{\mathbf{p}\mathbf{p}'}^a$. The Landau parameters F_l^s and F_l^a are defined with respect to the coefficients f_l^s and f_l^a corresponding to isotropic scattering:

$$\begin{aligned} F_l^s &\equiv N(0) f_l^s, \\ F_l^a &\equiv N(0) f_l^a, \end{aligned} \tag{2.10}$$

where $N(0)$ is the density of states at the Fermi energy.

2.1.2 Thermodynamic and Transport Properties

Since the total energy of the system of quasiparticles is an expansion in terms of the variation in the distribution function $\delta n_{\mathbf{p}\sigma}$, it follows that the thermodynamic properties are expansions in powers of the temperature. The first term of the expansion corresponds to the result for the noninteracting Fermi gas. Subsequent terms are finite temperature corrections due to coupling with spin fluctuations within the interacting fermion fluid.

The specific heat of a Fermi liquid is given by:

$$C = \gamma T + a T^3 \ln T + \dots, \tag{2.11}$$

where the Sommerfeld coefficient γ is

$$\gamma = \frac{2\pi^2 k_B^2}{3} N(0) = \frac{k_B^2 m^* p_F}{3\hbar^3}. \tag{2.12}$$

The first term is linear in temperature, and proportional to the effective quasiparticle mass m^* . The effective mass is related to the free-electron mass m by

$$\frac{m^*}{m} = 1 + \frac{1}{3} F_1^s, \tag{2.13}$$

where F_1^s is one of the Fermi-liquid parameters. The second term in the specific heat is a smaller correction and originates from quasiparticle coupling to spin fluctuations.

The magnetic susceptibility is independent of the temperature to first order:

$$\chi = 2\mu_{\text{eff}}^2 N(0) + \dots = \frac{\hbar^2}{4} \frac{\gamma^2 N(0)}{1 + F_0^a} + \dots, \tag{2.14}$$

where μ_{eff} corresponds to the quasiparticle effective magnetic moment, γ is the linear coefficient of the specific heat, and F_0^a is a Fermi-liquid parameter. The second term in the expansion is of order $T^2 \ln T$.

The electrical resistivity due to quasiparticle scattering is inversely proportional to the time between collisions τ , and proportional to the square of the temperature [20]:

$$\rho = AT^2 = \frac{\pi^2 e^2 m(76.06)}{16N(0)h^3} \left(\frac{T}{T_F^*} \right)^2, \quad (2.15)$$

where e is the electronic charge, m is the mass of a free electron, h is Planck's constant, and T_F^* is the effective Fermi temperature of the Fermi liquid.

2.2 Localized Magnetic Moments in Metals

Electrons in metals are not entirely free particles. They are constantly under the influence of a periodic potential due to a charged lattice. In addition, the distances between electrons are close enough for the Pauli exclusion principle to play an important role in the formation of energy levels. In general, electrons with energies in the vicinity of the Fermi energy tend to be delocalized and form part of the conduction band. To a first approximation, the equation of motion of nearly-free electrons is given in the Hartree-Fock form. Orbital states within a single ion are formed by electrons with energies below ε_F , and are more localized. Their wave functions retain some ionic character. For the most part, the thermodynamics of a metallic system in its normal state can be described by taking into account the individual contributions of quasiparticles (Fermi-liquid theory) and localized free spins. However, in many systems, the lattice of localized electrons near or below the Fermi level strongly interacts with conduction electrons. The resulting potential can have a major effect on the thermodynamics not accounted for by nearly-free electron models. In order to understand the behavior of $4f$ magnetic

moments in metals, it is important to have a knowledge of the interactions that give rise to their formation.

2.2.1 Electronic States of Magnetic Ions

The localized states of electrons in metals are similar to those of free magnetic ions [21]. For each energy level n , there are $(2s+1)(2l+1)$ degenerate states, where n , l , and s are the principal, orbital, and spin quantum numbers, respectively. The degeneracy is partially lifted by the electron-electron Coulomb interaction, of order 10 eV. These energy levels, called multiplets, are filled up according to Hund's rules and the Pauli exclusion principle. Once all $2(2l+1)$ levels are fully occupied, the sum total of spin and orbital angular momenta equals zero, so that a filled shell has no magnetic moment.

In an incompletely filled shell, one of two relevant interactions responsible for lifting any additional degeneracies is spin-orbit coupling. The spin of each orbiting electron couples with an effective magnetic field due to its motion about the nucleus. The effective field is proportional to the orbital angular momentum of the electron. The total spin-orbit interaction is then given by

$$\mathcal{H}_{\text{so}} = \lambda(\mathbf{L} \cdot \mathbf{S}) = \pm g\mu_{\text{B}}^2 Z_{\text{eff}} \left\langle \frac{1}{r^3} \right\rangle \frac{1}{2S} (\mathbf{L} \cdot \mathbf{S}), \quad (2.16)$$

where g is the electron g -value, μ_{B} is the Bohr magneton, Z_{eff} is the effective atomic number, and \mathbf{L} and \mathbf{S} are the total orbital and spin angular momenta, respectively. The coefficient λ is positive when the shell is less than half-filled, and negative for more than half-filled. The coupling between \mathbf{L} and \mathbf{S} has an effect on the eigenstates of the ionic Hamiltonian. Both operators are no longer constants of the motion, and the states are now labeled by the total angular momentum $\mathbf{J} = \mathbf{L} + \mathbf{S}$. As a consequence, the degenerate states of each multiplet split into $2S+1$ levels for $L > S$ or $2L+1$ levels for $L < S$, each carrying a $2J+1$ degeneracy.

The second interaction responsible for the splitting of degenerate energy levels of a multiplet is due to the surrounding ions. Crystal-field effects represent the influence of Coulomb interactions from neighboring charges on localized states. The crystal-field contribution is given by the net Coulomb energy due to point charges located at the different crystallographic sites, and by the direct Coulomb interaction between the outermost localized orbitals of surrounding ions. To a first approximation,

$$\mathcal{H}_{\text{CEF}} = -e \sum_i V_{\text{CEF}}(\mathbf{r}_i) = -e \sum_{ij} \frac{Ze_j}{|\mathbf{r}_i - \mathbf{R}_j|}, \quad (2.17)$$

where \mathbf{R}_j and Ze_j are the position vector and charge of the j th ion, respectively, and \mathbf{r}_i and e indicate the position and charge of the electrons. The potential V_{CEF} can be expressed in polar coordinates and expanded in terms of the spherical harmonics $Y_l^m(\theta, \phi)$. The result is an expansion in powers of $\langle r \rangle$ and of the angular momentum operators \mathbf{L}^2 and \mathbf{L}_z (or $\mathbf{J}^2, \mathbf{J}_z$). The crystal-field interaction partially lifts the degeneracy of the ionic states. The number of states is determined by the symmetry of the crystal structure, and typically increases for structures of low point-group symmetry.

In solids with magnetic ions, the relative strength of spin-orbit and crystal-field energies depends on the localized character of the wave function corresponding to the incompletely-filled shell. The spin-orbit interaction increases as the distance from the nucleus decreases ($\mathcal{H}_{\text{SO}} \propto \langle 1/r^3 \rangle$). The crystal-field contribution \mathcal{H}_{CEF} , on the other hand, increases with the radial extent of the wave function. For electrons in incomplete d orbitals, $\mathcal{H}_{\text{CEF}} > \mathcal{H}_{\text{SO}}$ due to their direct interaction with orbitals from neighboring ions. In contrast, electrons in incomplete f orbitals are very localized and reside close to the nucleus. Therefore, the spin-orbit interaction is very large (≥ 0.1 eV), and the crystal-field contribution \mathcal{H}_{CEF} comparatively smaller (≥ 0.01 eV). As a consequence, the lowest-lying multiplet is first split by the spin-

orbit interaction, and each of these levels is split further by the crystal field. The ground state of the system is the crystal-field ground state. For example, in Ce^{3+} , there is only one $4f$ electron ($S = \frac{1}{2}$), and the lowest-lying multiplet corresponds to $L = 3$. \mathcal{H}_{so} splits the multiplet into two 6-fold degenerate levels: $|J = \frac{5}{2}\rangle$ and $|J = \frac{7}{2}\rangle$. The lowest-energy level ($J = \frac{5}{2}$) is then split by \mathcal{H}_{CEF} into a doublet and a quartet for cubic crystal symmetry and into three doublets in the case of hexagonal symmetry. For a crystal-field doublet ground state, the effective total angular momentum of Ce^{3+} is $J = \frac{1}{2}$.

2.2.2 Anderson Model

The fundamental problem in magnetic alloys (including heavy-fermion systems) is the coexistence and interaction of the electron liquid with localized atomic orbital states. From this point of view, the conduction band is formed primarily of electrons in the outermost s and p shells, and the localized states consist of d or f orbitals in iron-group and rare-earth ions, respectively. The following discussion will focus on localized f states. Electrons in a partially-filled f shell have a finite probability of mixing and are free to interact with the conduction band if their energy is close to the Fermi level. The interaction with the conduction electrons regulates the average occupancy and magnetic moment of the f level. This problem was described by Anderson [22] in the following Hamiltonian for a single impurity embedded in a free-electron environment:

$$\mathcal{H}_{\text{And}} = \mathcal{H}_0 + \mathcal{H}_{0f} + \mathcal{H}_{ff} + \mathcal{H}_{cf}, \quad (2.18)$$

The first term is the unperturbed free-electron Hamiltonian:

$$\mathcal{H}_0 = \sum_{\mathbf{k}\sigma} \varepsilon_{\mathbf{k}} n_{\mathbf{k}\sigma}. \quad (2.19)$$

Here, $\varepsilon_{\mathbf{k}} n_{\mathbf{k}\sigma}$ is the energy of a free-electron state with wave number \mathbf{k} and spin σ , and $n_{\mathbf{k}\sigma}$ is the number operator

$$n_{\mathbf{k}\sigma} = a_{\mathbf{k}\sigma}^\dagger a_{\mathbf{k}\sigma}, \quad (2.20)$$

with $a_{\mathbf{k}\sigma}^\dagger$ and $a_{\mathbf{k}\sigma}$ the creation and annihilation operators, respectively, for a free electron state with labels \mathbf{k} and σ . The second term is the unperturbed energy of the localized f level:

$$\mathcal{H}_{0f} = \sum_{\sigma} E_f n_{f\sigma}, \quad (2.21)$$

where E_f corresponds to the energy of the f level and

$$n_{f\sigma} = a_{f\sigma}^\dagger a_{f\sigma}. \quad (2.22)$$

The third term represents the on-site Coulomb repulsion between two f electrons of opposite spin:

$$\mathcal{H}_{ff} = U n_{f\uparrow} n_{f\downarrow}, \quad (2.23)$$

with U the Coulomb integral between the two f states, and $n_{f\uparrow}$ and $n_{f\downarrow}$ the number operators for f states with up and down spin, respectively. The last term denotes the mixing between conduction electrons and the f orbital:

$$\mathcal{H}_{cf} = \sum_{\mathbf{k}\sigma} V_{\mathbf{k}f} (a_{\mathbf{k}\sigma}^\dagger a_{f\sigma} + a_{f\sigma}^\dagger a_{\mathbf{k}\sigma}). \quad (2.24)$$

Here $V_{\mathbf{k}f}$ is the hybridization matrix element between localized and conduction electronic states.

The effect of the Anderson Hamiltonian on the localized f states depends on the relative magnitudes of the Coulomb and mixing terms. The Coulomb repulsion U determines the separation of the up and down spin f levels with respect to each other. The hybridization term $V_{\mathbf{k}f}$ is responsible for a broadening of the f levels, which determines the overlap between the lowest f state and the Fermi energy. These levels are represented by a Lorentzian of width 2Γ , where

$$\Gamma = \pi |V_{\mathbf{k}f}|^2 N(0), \quad (2.25)$$

and $N(0)$ is the density of states at the Fermi energy. Figure 2.1 illustrates the density of states of up and down-spin free-electrons and localized levels for different relative strengths of Coulomb repulsion and mixing width. For $U \gg |V_{\mathbf{k}f}|$, the localized up and down-spin levels (d or f) have a small width 2Γ and are well separated by U . The down-spin level resides far above the Fermi energy and is therefore unoccupied, favoring the formation of a strong local magnetic moment. If the energy of the up-spin state is close to the Fermi energy in the limit $U \rightarrow \infty$, the localized moment couples strongly with the conduction band (Kondo effect). This scenario corresponds to integer valence, and is conducive to the formation of the heavy-fermion state when the impurity concentration is of the order of Avogadro's number N_A and the magnetic ions achieve the periodicity of the crystal lattice. For $U \approx |V_{\mathbf{k}f}|$, both localized levels are significantly broad and might overlap with the Fermi energy due to a reduction in U . An overlap with the conduction band results in partial occupancy of both up and down-spin levels, leading to mixed valence and the formation of a weak local magnetic moment. In the limit $|V_{\mathbf{k}f}| \gg U \approx 0$, both levels have the same energy and occupancy and the impurity loses its magnetic moment.

By studying the limit in which $\Gamma \ll E_f$, Schrieffer and Wolff [24] were able to perform a canonical transformation on the Anderson Hamiltonian that eliminates the hybridization term $V_{\mathbf{k}f}$. Instead, the transformed Hamiltonian is expressed in terms of \mathcal{H}_0 , \mathcal{H}_{0f} , \mathcal{H}_{ff} , and an exchange interaction between f -ion and conduction electron spins

$$\mathcal{H}_{ex} = - \sum_{\mathbf{kk}'} J_{\mathbf{kk}'} \mathbf{S}_k \cdot \mathbf{S}_f, \quad (2.26)$$

where \mathbf{S}_k and \mathbf{S}_f are the spin polarization of the conduction electrons and the spin of the impurity, respectively, and $J_{\mathbf{kk}'}$ the exchange coupling constant. Close to the Fermi level, $\mathbf{k}, \mathbf{k}' \simeq \mathbf{k}_F$, and $J_{\mathbf{kk}'}$ becomes

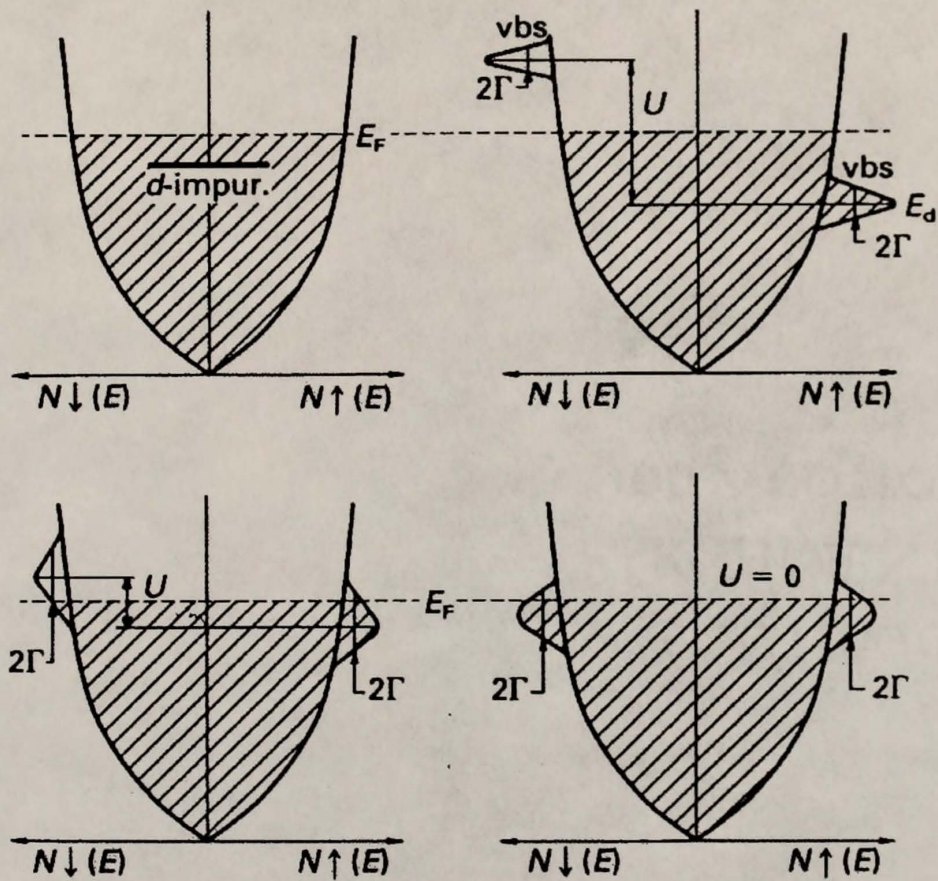


Figure 2.1: Spin-up and spin-down electronic density of states distributions for a localized d orbital embedded in a sea of conduction electrons. Upper left: $U = |V_{kf}| = 0$; upper right: $U \gg |V_{kf}|$; lower left: $U \approx |V_{kf}|$; lower right: $U \ll |V_{kf}|$; ($U = 0$) (from Mydosh, 1993) [23].

$$J_{\mathbf{k}_F \mathbf{k}_F} \equiv J = 2|V_{\mathbf{k}_F f}|^2 \frac{U}{E_f(E_f + U)} < 0, \quad (2.27)$$

where J is the Kondo coupling constant. In this manner, the Anderson Hamiltonian effectively transforms into the Kondo Hamiltonian in the limit $\Gamma \ll E_f$ (or $N(0)J \ll 1$).

2.3 Single-ion Kondo Model

The Kondo problem is that of a single localized magnetic impurity in a metallic host. This scenario corresponds to the above-mentioned $U \rightarrow \infty$ limit of the single-impurity Anderson model, with E_f close to the Fermi level. The following discussion refers to the case of a spin- $\frac{1}{2}$ impurity in a sea of conduction electrons, as in the crystal-field ground state of Ce^{3+} . As the temperature decreases, the localized f orbital hybridizes with the conduction band, spin-flip scattering increases, and a scattering resonance appears near the Fermi level, known as the Kondo or Abrikosov-Suhl resonance. The Hamiltonian describing these processes is the Kondo (or s - d) Hamiltonian, of the form

$$\mathcal{H}_{\text{Kondo}} = -J \sum_i \delta(\mathbf{r}_i)(\mathbf{s}_i \cdot \mathbf{S}), \quad (2.28)$$

where J is the effective coupling constant between f and conduction electrons (as in Eq. 2.27), \mathbf{S} is the localized spin, and \mathbf{s}_i and \mathbf{r}_i represent the i th conduction-electron spin and position vector, respectively. In the case where both E_f and $U + E_f$ are symmetric with respect to the Fermi energy ($U/2 = |\varepsilon_F - E_f|$),

$$J \propto \frac{|V_{\mathbf{k}_F f}|^2}{|\varepsilon_F - E_f|}, \quad (2.29)$$

where ε_F is the Fermi energy. A perturbation treatment of $\mathcal{H}_{\text{Kondo}}$ beyond the Born approximation leads to an expansion of the thermodynamic and transport properties in powers of $JN(0) \ln(k_B T/D)$. Here, $N(0)$ is the density of states at the

Fermi energy and D is the bandwidth of scattering states. The electrical resistivity was calculated by Kondo [25] using third-order perturbation theory:

$$\rho = \rho_B \left(1 + 2JN(0) \ln \frac{k_B T}{D} \right). \quad (2.30)$$

The constant term

$$\rho_B = \frac{3}{2} \frac{m\pi}{ne^2\hbar} \frac{J^2}{4\varepsilon_F} S(S+1), \quad (2.31)$$

obtained from the Born approximation, is a residual resistivity term due to the presence of the magnetic impurity. The third-order term diverges at low temperatures. The specific heat and magnetic susceptibility due to the impurity are given by

$$C = (-JN(0))^4 \pi^2 S(S+1) k_B \left(1 + 4JN(0) \ln \frac{k_B T}{D} + \dots \right) \quad (2.32)$$

and

$$\chi = \frac{g^2 \mu_B^2 S(S+1)}{3k_B T} \left[1 + JN(0) \left(1 - JN(0) \ln \frac{k_B T}{D} \right)^{-1} \right], \quad (2.33)$$

respectively. The perturbation treatment for $J < 0$ breaks down at a temperature

$$k_B T_K = D \exp \left(\frac{-1}{JN(0)} \right). \quad (2.34)$$

The temperature T_K is called the Kondo temperature.

At low temperatures ($T \ll T_K$), the impurity spin strongly couples with the conduction electron spin polarization, forming a many-body singlet that completely suppresses the localized magnetic moment at $T = 0$. In this range, the thermodynamic and transport properties can be described by Fermi-liquid theory due to the absence of an impurity spin. The zero-temperature susceptibility of the impurity is inversely proportional to the Kondo temperature [26],

$$\chi_0 = \left(\frac{1}{2} g \mu_B \right)^2 \frac{1.29}{\pi k_B T_K}, \quad (2.35)$$

and the linear coefficient of the specific heat γ is given by

$$\gamma = 1.29 \frac{\pi k_B}{6T_K}. \quad (2.36)$$

The ratio of the magnetic susceptibility to the electronic specific heat coefficient γ , called the Wilson ratio, is given by

$$\frac{\chi_0}{\gamma} = \frac{3}{2} \left(\frac{g\mu_B}{\pi k_B} \right)^2. \quad (2.37)$$

This value is twice that corresponding to the noninteracting electron gas.

The exact solution to the Kondo Hamiltonian and its thermodynamic properties in terms of $T < T_K$ and $T > T_K$ and a range of magnetic fields were obtained using the Bethe ansatz [26, 27, 28, 29]. The above equations follow the exact solution obtained with this method. Numerical solutions for the specific heat and the magnetic susceptibility of a spin- $\frac{1}{2}$ impurity in different magnetic fields are illustrated in Figs. 2.2 and 2.3. The zero-field specific heat reaches a maximum at a temperature just below T_K . Both the magnitude and the temperature position of the maximum increase with field, reaching a shape corresponding to the Schottky anomaly of a free uncompensated spin- $\frac{1}{2}$ at large fields $g\mu_B H \gg k_B T_K$, where g is the g-factor of the magnetic impurity. The zero-field magnetic susceptibility shows a Curie-like increase for $T > T_K$, and then saturates until it reaches a temperature-independent value well below T_K . A maximum associated with the Schottky anomaly of the specific heat appears around T_K for $g\mu_B H/k_B T_K = 2$ [30]. Its temperature position increases, while its magnitude decreases with increasing field.

2.4 Anisotropic Kondo Model

The anisotropic Kondo model (AKM) [31, 32] refers to the problem of a single magnetic impurity coupled to the conduction electrons via an anisotropic exchange interaction $J \rightarrow J_{\parallel}, J_{\perp}$, where $J_{\parallel} \gg J_{\perp}$. The Hamiltonian is given by

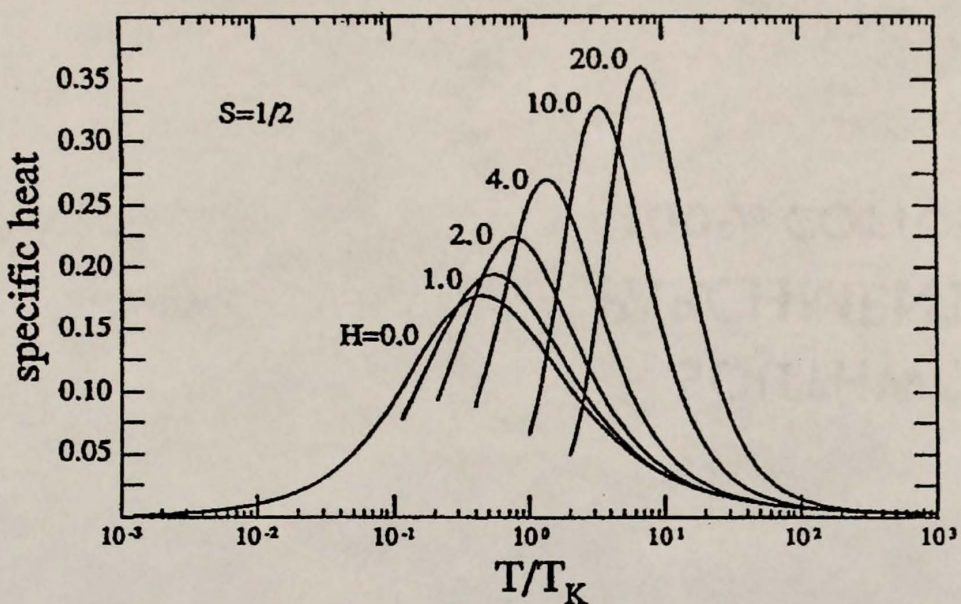


Figure 2.2: Specific heat of a $S = \frac{1}{2}$ Kondo impurity as a function of T/T_K for different magnetic fields ($H \rightarrow g\mu_B H/k_B T_K$) [30].

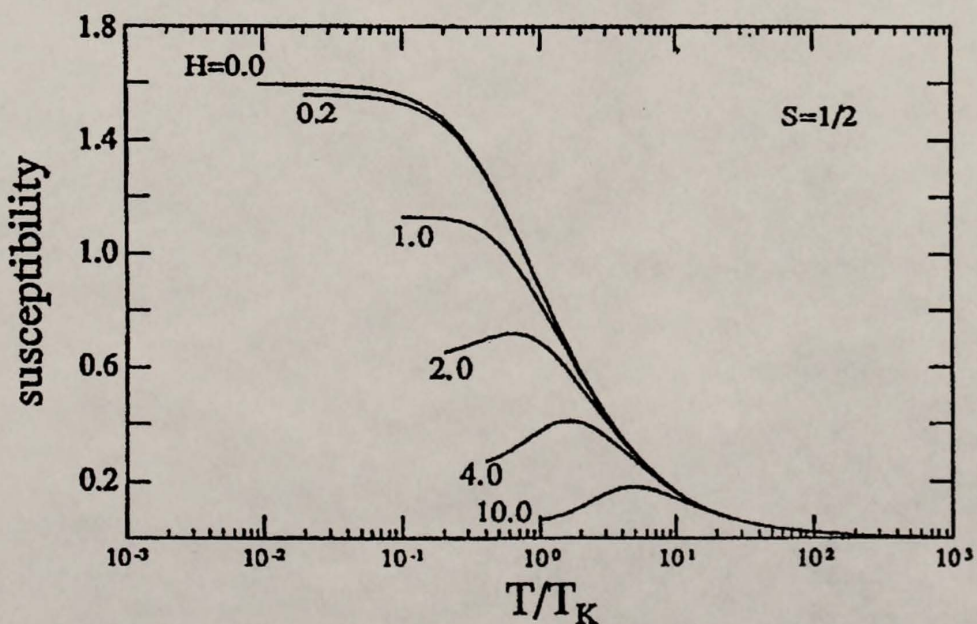


Figure 2.3: Magnetic susceptibility of a $S = \frac{1}{2}$ Kondo impurity as a function of T/T_K for different magnetic fields ($H \rightarrow g\mu_B H/k_B T_K$) [30].

$$\mathcal{H}_{\text{AKM}} = \sum_{k,\sigma} \epsilon_k c_{k,\sigma}^\dagger c_{k,\sigma} + \frac{J_\perp}{2} \sum_{kk'} (c_{k\uparrow}^\dagger c_{k'\downarrow} S^- + c_{k\downarrow}^\dagger c_{k'\uparrow} S^+) + \frac{J_\parallel}{2} \sum_{kk'} (c_{k\uparrow}^\dagger c_{k'\uparrow} - c_{k\downarrow}^\dagger c_{k'\downarrow}) S_z + g\mu_B h S_z, \quad (2.38)$$

where $c_{k\sigma}^\dagger$ and $c_{k\sigma}$ are the conduction electron creation and annihilation operators, S^+ and S^- are the impurity spin raising and lowering operator eigenvalues, and S_z is the impurity spin value in the z direction. The first term in \mathcal{H}_{AKM} represents the conduction-electron energies, the second and third terms represent the in-plane (J_\perp) and easy-axis (J_\parallel) exchange interactions between a localized spin and the conduction electrons, respectively, and the last term corresponds to the Zeeman energy due to a local magnetic field h applied only to the impurity spin S . The Kondo temperature for an anisotropic exchange interaction ($J_\parallel < 0$) is given in terms of J_\parallel and J_\perp as [21, 33]

$$k_B T_K = D \exp \left[\frac{-1}{N(0) \sqrt{J_\parallel^2 - J_\perp^2}} \times \tanh^{-1} \frac{\sqrt{J_\parallel^2 - J_\perp^2}}{-J_\parallel} \right], \quad (2.39)$$

where $N(0)$ is the density of states and D is the bandwidth. The exponential dependence of the Kondo temperature in the parameter J_\parallel is qualitatively similar to the J dependence of T_K in the isotropic case.

The Hamiltonian for an anisotropic Kondo interaction has been used successfully to evaluate the properties of the spin-boson Hamiltonian [34, 35, 36, 37], which describes the dissipation in the dynamics of a two-level system by an Ohmic bosonic bath. A mapping of the spin-boson model [38] onto the AKM has been exploited to calculate the thermodynamic properties of the former model. Furthermore, the parameters of the spin-boson model have recently been used to describe the properties of the AKM applied to the heavy-fermion system $\text{Ce}_{1-x}\text{La}_x\text{Al}_3$ [15]. The spin-boson Hamiltonian has the form

$$\begin{aligned}\mathcal{H}_{\text{SB}} = & -\frac{1}{2} \Delta \sigma_x + \frac{1}{2} \epsilon \sigma_z + \sum_{\alpha} \omega_{\alpha} \left(a_{\alpha}^{\dagger} a_{\alpha} + \frac{1}{2} \right) + \\ & \frac{1}{2} q_0 \sigma_z \sum_{\alpha} \frac{C_{\alpha}}{\sqrt{2m_{\alpha} \omega_{\alpha}}} (a_{\alpha} + a_{\alpha}^{\dagger}).\end{aligned}\quad (2.40)$$

Here σ_x and σ_z are Pauli matrices, Δ is the tunneling energy between the two states and ϵ is an external bias applied to the system. The third term corresponds to the energy of the bosonic bath and the last term represents the coupling of the two-level system to the bath, with coupling constants C_{α} . In the case of Ohmic dissipation, the spectral function of the system is $J(\omega) = 2\pi \alpha \omega$ for $\omega \ll \omega_c$, where α is a measure of the strength of the dissipation and ω_c is a cutoff frequency. For $\alpha \neq 0$, the tunneling energy Δ ($\hbar = 1$) is renormalized into

$$\Delta_r = \Delta \left(\frac{\Delta}{\omega_c} \right)^{\frac{\alpha}{1-\alpha}}, \quad (2.41)$$

with Δ_r/k_B equivalent to the Kondo temperature T_K in the AKM.

The low temperature behavior of both spin-boson and AKM systems is that of a Fermi liquid. The linear coefficient of the specific heat per total mole is given by [35, 36]

$$\gamma = \alpha \frac{\pi^2 k_B^2}{3\Delta_r} N_A = \alpha \frac{\pi^2 R}{3T_K}, \quad (2.42)$$

where N_A is Avogadro's number and $R = k_B N_A$ is the gas constant, and the magnetic susceptibility of the spin-boson model per total mole at $T = 0$ is

$$\chi_{\text{SB}} = \frac{g^2 \mu_B^2 N_A}{2\Delta_r} = \frac{g^2 \mu_B^2 N_A}{2k_B T_K}, \quad (2.43)$$

where g is the g -factor of the impurity spin. The susceptibility of the AKM at $T = 0$ differs from χ_{SB} by a factor of α : $\chi_{\text{AKM}} = \alpha \chi_{\text{SB}}$. The Wilson ratios for both models are related as follows:

$$R_{\text{AKM}} = \frac{4}{3} \frac{\pi^2 k_B^2}{(g\mu_B)^2} \frac{\chi_{\text{AKM}}}{\gamma} = 2$$

$$R_{\text{SB}} = \frac{4}{3} \frac{\pi^2 k_{\text{B}}^2}{(g\mu_{\text{B}})^2} \frac{\chi_{\text{SB}}}{\gamma} = \frac{2}{\alpha}, \quad (2.44)$$

where $R_{\text{AKM}} = \alpha R_{\text{SB}}$.

The thermodynamic properties of the AKM are given in terms of the exchange interactions (J_{\parallel}) and (J_{\perp}), and therefore can also be expressed in terms of the parameters α and Δ_r of the spin-boson model [35, 36]:

$$\begin{aligned} \Delta_r &= \rho J_{\perp}, \\ \alpha &= \left[1 + \frac{2}{\pi} \tan^{-1} \left(-\frac{\pi \rho J_{\parallel}}{4} \right) \right]^2. \end{aligned} \quad (2.45)$$

Figure 2.4 illustrates the temperature dependence of the static susceptibility and specific heat as C/T for different values of the dissipation α and $\epsilon = 0$. The parameter α is a good measure of the Kondo anisotropy of the system, since it decreases sharply with increasing J_{\parallel} . Both curves are universal functions of $(T/\Delta_r) \sim (T/T_K)$. For $\epsilon = 0$, the electronic coefficient of the specific heat is given by $\gamma = \alpha/\Delta_r$, and C/T reaches a maximum at a temperature corresponding to Δ_r for $\alpha < 0.3$. This maximum is reduced in magnitude with increasing α . The susceptibility expressed as $k_{\text{B}}T\chi_{\text{SB}}$ has a finite value at $T = 0$, as in the isotropic Kondo model, and reaches the free-spin value at high temperatures. The main effect of α is to increase the temperature at which this latter value is attained. The temperature Δ_r indicates the crossover between Kondo and free-spin behavior.

The behavior for a finite bias $\epsilon > 0$ is described in Fig. 2.5 for $\alpha = 0.2$. The quantity ϵ is equivalent to a magnetic energy $g\mu_{\text{B}}h$ acting on the impurity spin in the AKM. The temperature Δ_r is renormalized by ϵ , and becomes [37]

$$\tilde{\Delta}_r = \sqrt{\Delta_r^2 + \epsilon^2}. \quad (2.46)$$

The effects of a field on the specific heat are a strong reduction of γ , an attenuation of the maximum in C/T , and an increase of its temperature position given by $\tilde{\Delta}_r$. The low-temperature susceptibility strongly decreases as a function of the

parameter ϵ . It also shows a maximum for fields of order Δ_r and above, with a temperature position that increases with $\tilde{\Delta}_r$.

2.5 Kondo Lattice

Certain types of metallic compounds, including heavy-fermion systems, can be described as a lattice of Kondo impurities embedded in a metallic host [39, 40, 41]. This class of materials is commonly referred to as concentrated Kondo systems. In these alloys, a giant Abrikosov-Suhl resonance of width T_K appears in the density of states near the Fermi level for $T \ll T_K$. In the case of spin- $\frac{1}{2}$ Kondo scatterers, the resonance lies right at the Fermi energy. This feature indicates the crossover to a strong-coupling regime in the scattering between f and conduction electrons, growing in size as the number of impurities approaches Avogadro's number N_A . Consequently, there is a substantial increase in the density of states at ε_F . Figure 2.6 illustrates the evolution of the Abrikosov-Suhl resonance for different temperatures. In heavy-fermion compounds, the $4f$ level is located well below the Fermi energy. As a result, the localized orbital has integer valence. The large resonance in the density of states has an effect on the effective mass m^* , as indicated by Fermi-liquid theory. At high temperatures ($T \gg T_K$), the Abrikosov-Suhl resonance disappears, and the system behaves as an ensemble of classical free spins.

Two other characteristics of the Kondo lattice are the appearance of coherence effects and interactions between magnetic impurities. Below a temperature T_{coh} , the electronic properties change from those described by scattering off independent Kondo impurities to those reflecting the periodicity of the lattice via Bloch's theorem. This crossover is usually described in terms of a maximum in the temperature dependence of the specific heat as C/T and the electrical resistivity around $T \approx T_{coh}$. A consequence of coherence is an increase of indirect exchange interactions between impurity spins. At distances larger than the $4f$ radius ($r_{4f} < 0.5\text{\AA}$) but less than

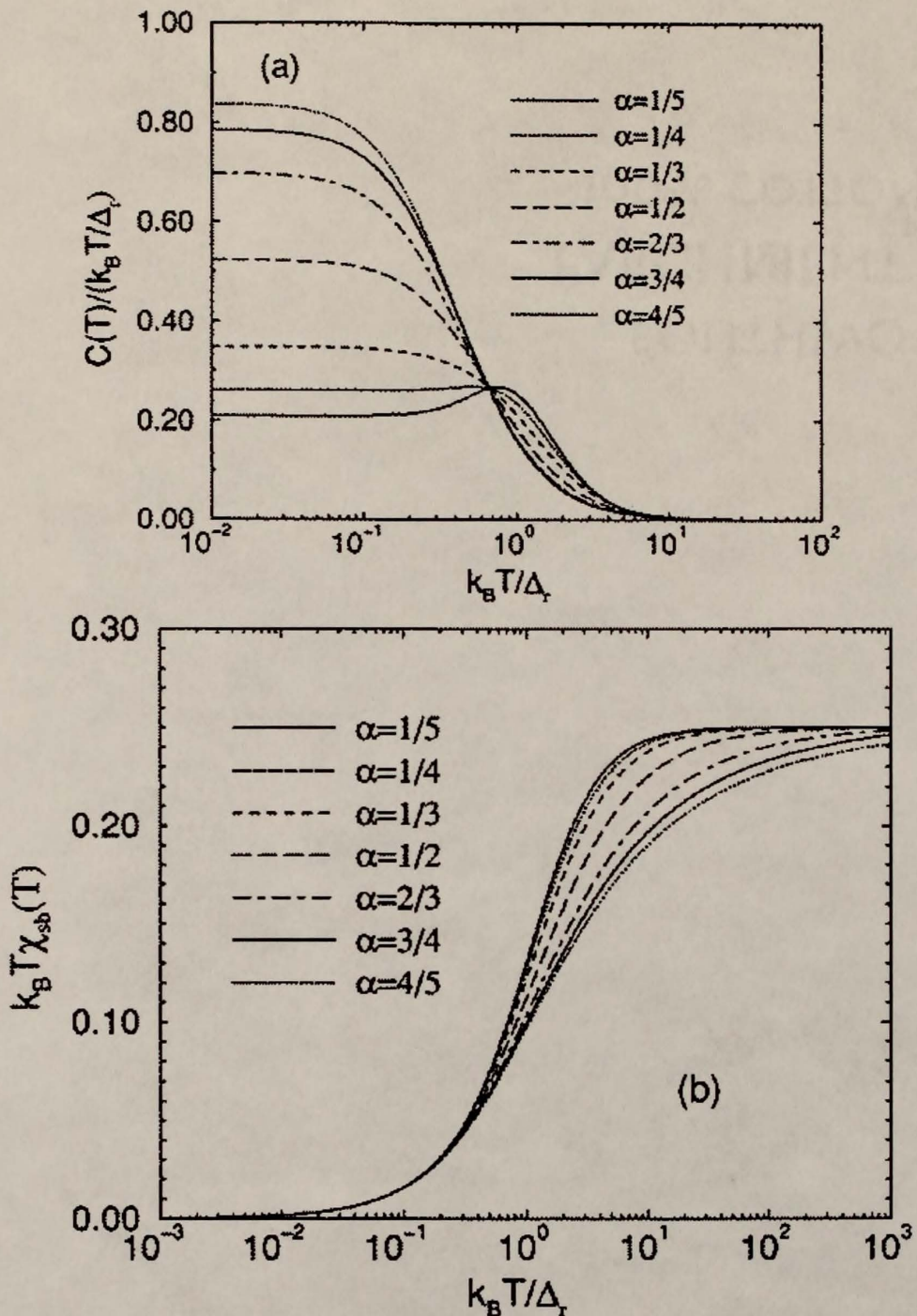


Figure 2.4: Thermodynamic properties of the anisotropic Kondo model for $\epsilon = 0$ and different values of α . a) Specific heat expressed as $\Delta_r C/k_B T$ vs T/Δ_r . b) Universal static susceptibility curves expressed as $k_B T \chi_{sb}$ vs T/Δ_r [37].

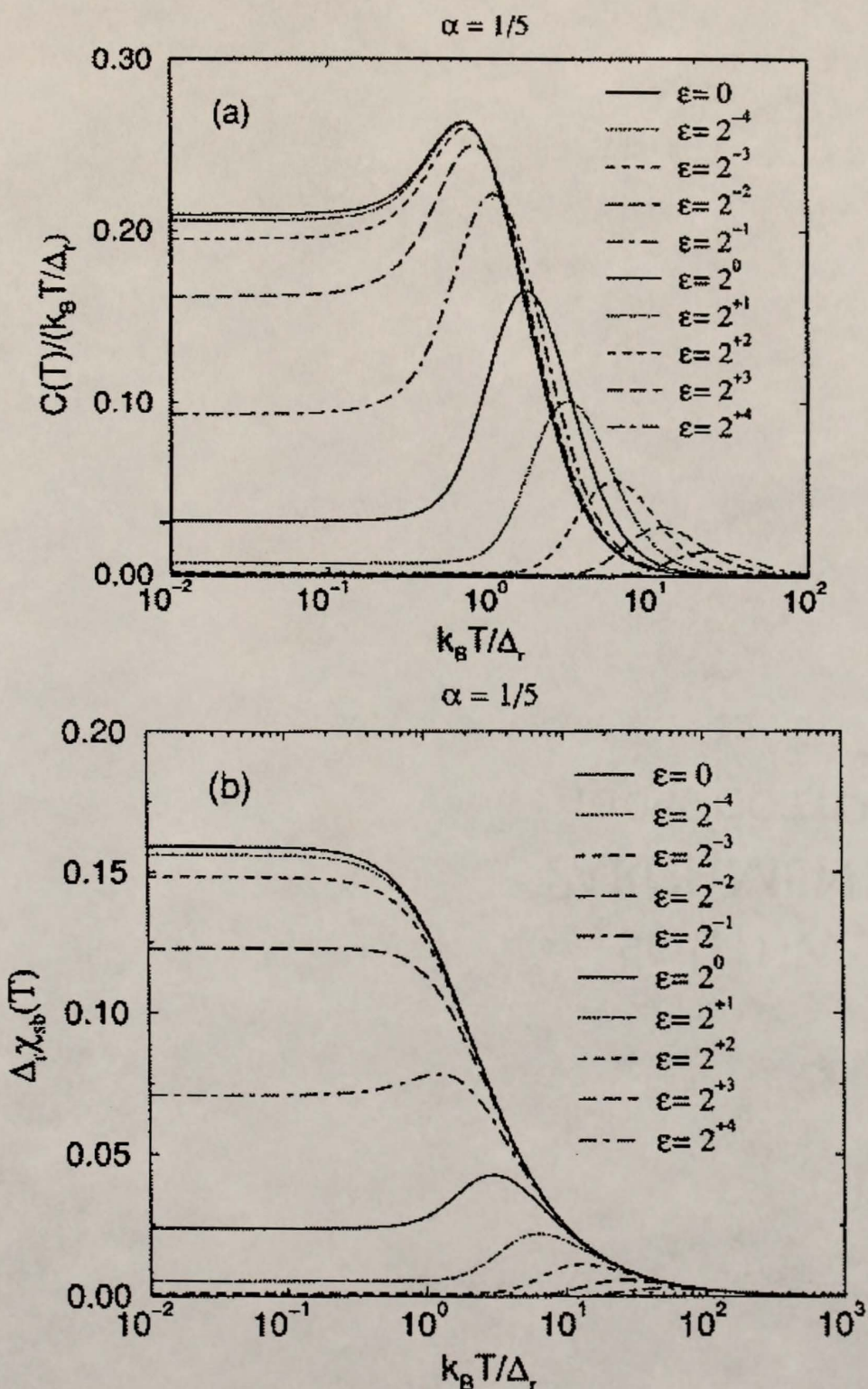


Figure 2.5: Thermodynamic properties of the AKM for $\alpha = 0.2$ and different values of ϵ (in units of Δ_r). a) Specific heat as $\Delta_r C / k_B T$ vs $k_B T / \Delta_r$. b) Susceptibility curves expressed as $\Delta_r \chi_{sb}$ vs $k_B T / \Delta_r$ [37].

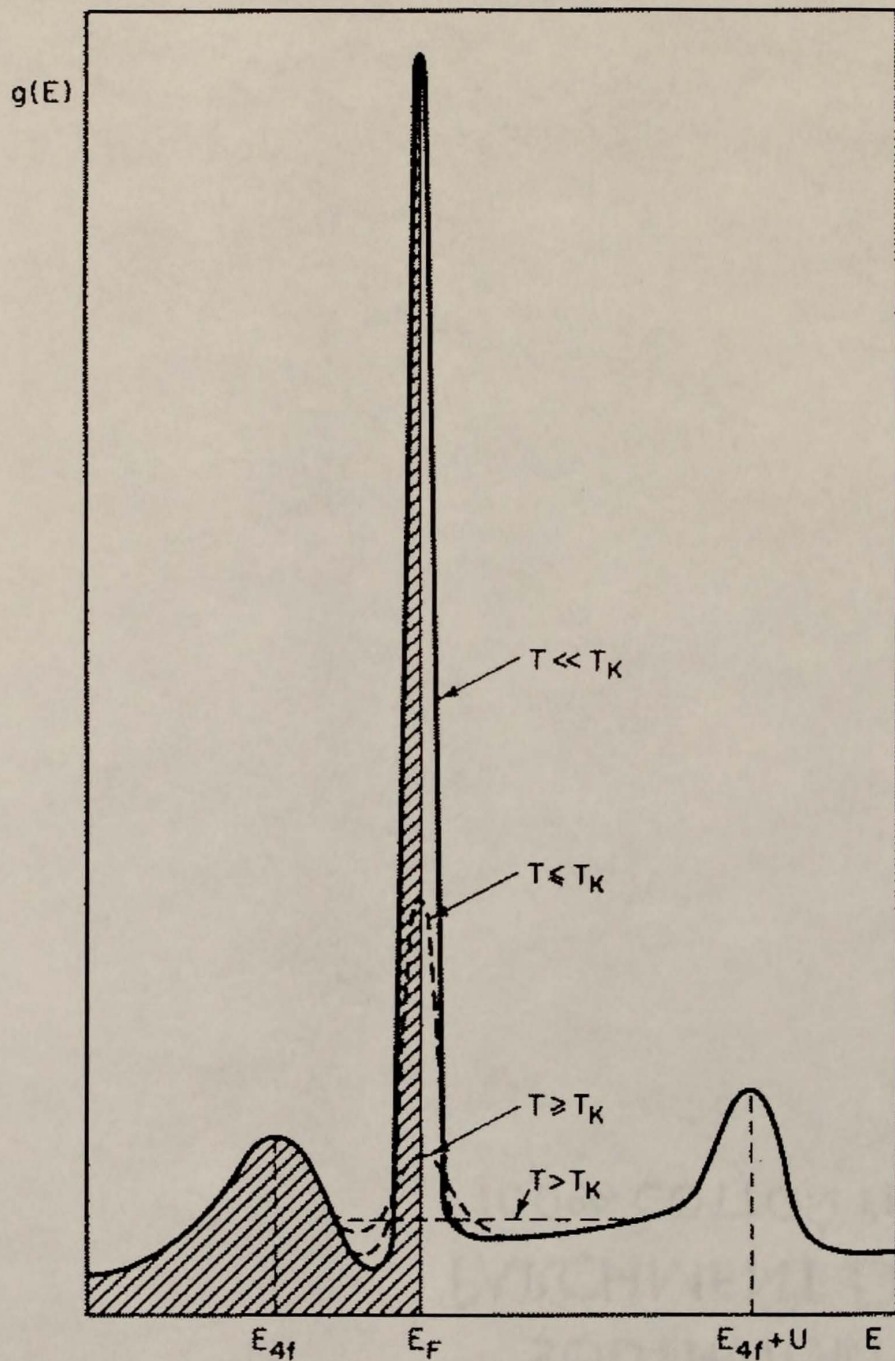


Figure 2.6: Density of states of a nonmagnetic Kondo lattice at different temperatures, showing the evolution of the giant Abrikosov-Suhl resonance [39].

the size of the Kondo compensation cloud for a single impurity, the presence of closely-spaced uncompensated spins leads to the Ruderman-Kittel-Kasuya-Yosida (RKKY) interaction between localized f orbitals

$$\mathcal{H}_{\text{RKKY}} = \mathcal{J}(r) \mathbf{S}_i \cdot \mathbf{S}_j, \quad (2.47)$$

where

$$\mathcal{J}(r) \sim \frac{J \cos(2k_F r)}{(2k_F r)^3} \quad (2.48)$$

is the RKKY coupling at large distances, J is the Kondo coupling, and k_F is the Fermi wavevector. In most heavy-fermions $\mathcal{J}(r)$ leads to antiferromagnetic coupling between impurity spins.

The state of a concentrated Kondo system depends on the competition between the two energies represented by the Kondo and RKKY temperatures T_K and T_{RKKY} . This competition has been described in a simple form through the Kondo necklace model, developed by Doniach [42, 43]. Both T_K and T_{RKKY} depend on the Kondo coupling J and the concentration of magnetic impurities. The Doniach model relies on the assumption that the ground state of the system depends on the relative magnitude of the coupling J only. The phase diagram for this model is shown in Fig. 2.7. The Kondo temperature depends exponentially on the parameter J , as discussed previously, while $T_{\text{RKKY}} \sim J^2 N(0)$. At low values of J , $T_{\text{RKKY}} > T_K$, the material is a magnetic $4f$ metal, and the Kondo effect is absent. As J increases, $T_K > T_{\text{RKKY}}$, the Kondo effect appears before magnetic order, and the material is a magnetic Kondo lattice. At even larger values of J ($T_K \gg T_{\text{RKKY}}$), magnetic order disappears altogether and the material is a nonmagnetic Kondo lattice. Heavy-fermion compounds exist in the region around the magnetic-nonmagetic phase boundary, and those with a magnetic ground state exhibit mostly antiferromagnetic order.

A modified form of the Doniach diagram has been recently proposed [44, 45] to account for the effect of intersite magnetic correlations on the Kondo temperature in the nonmagnetic region. Instead of continuing to increase exponentially as in the single-impurity case, T_K reaches a saturation value, after which it decreases slightly with increasing J . Thus, T_K in nonmagnetic Kondo lattices may not necessarily follow single-impurity behavior. On the other hand, a complete theoretical explanation of the effect of magnetic interactions on the Kondo temperature has yet to be developed.

At a value of the Kondo coupling $J = J_c$, the magnetic ordering temperature T_M approaches zero at a critical point. The ground state of some heavy fermions at or near J_c is neither magnetically ordered nor Fermi-liquid-like. A large number of intermetallics falling in this category are commonly referred to as non-Fermi-liquid (NFL) systems. Their thermodynamic and transport properties can in some cases be described by either logarithmic divergences or power-law behavior according to different theoretical models [3, 12].

2.6 Non-Fermi-Liquid Effects

Current models of non-Fermi-liquid phenomena can be divided into two groups: theories describing a possible single-ion origin to these effects and those attributing them to intersite interactions. A member of the first group is the two-channel quadrupolar Kondo effect [46], a particular scenario within the more general multichannel Kondo problem [47]. The quadrupolar Kondo effect consists of the quenching of a nonmagnetic quadrupolar level by two degenerate conduction-electron bands, and has been used to explain the properties of heavy-fermion systems like $U_{1-x}Th_xBe_{13}$ [48]. In this model, NFL behavior is associated with fluctuations of the quadrupolar degrees of freedom, rather than spin fluctuations.

Another possible single-ion mechanism towards non-Fermi-liquid behavior is Kondo disorder [49, 50, 51]. The material exhibits a random distribution of

the quantity ρJ , where ρ is the density of states and J is the Kondo coupling constant. Thus, variations in either the Kondo couplings or the local density of states gives as a result a distribution of Kondo temperatures. The probability distribution function $P(T_K) = P(\rho J) d(\rho J)/dT_K$ acquires a log-normal form for strong disorder:

$$P(T_K) = (4\pi u)^{-\frac{1}{2}} \frac{1}{T_K \ln(\varepsilon_F/T_K)} \exp \left\{ -\frac{1}{4\pi u} \ln^2[\rho_0 J e^{-u} \ln(\varepsilon_F/T_K)] \right\}, \quad (2.49)$$

where ρ_0 is the average density of states, and u is a dimensionless parameter corresponding to the amount of disorder in the system. For weak disorder, $P(T_K)$ takes the form of a Gaussian. At a given temperature T , there are regions where the local Kondo temperature $T_K \ll T$, and the local spin is uncompensated. If the probability of having uncompensated spins at $T = 0$, $P(T_K = 0) \neq 0$, the thermodynamic properties are dominated by the contribution from free spins, leading to non-Fermi-liquid behavior.

The first model involving collective behavior applied to NFL alloys was based on a description of the physical properties in terms of their proximity to a quantum critical point (QCP). The system exhibits critical fluctuations of the order parameter in the vicinity of a quantum phase transition at $T \rightarrow 0$ [52, 53, 54, 55, 56]. At finite temperatures, the characteristic frequency ω^* associated with the critical fluctuations of the order parameter is much smaller than the transition temperature T_c , so that the system behaves classically at $\hbar\omega^* \ll k_B T_c$ [56]. A quantum phase transition at $T = 0$ is not achieved by a change in temperature, but rather by a change in a parameter of the Hamiltonian. Under this model, non-Fermi-liquid effects in heavy-fermion systems arise as a consequence of a near-zero anti-ferromagnetic transition temperature, so that a quantum-mechanical treatment is necessary. The thermodynamic properties are dominated by the collective modes due to critical fluctuations rather than by Fermi-liquid-like elementary excitations, and are described by various scaling laws [53, 54] depending on the effective dimen-

sionality and the nature of the magnetic transition. As a result, the system is said to have a ‘generalized’ (non-Landau) Fermi-liquid ground state, with an enhanced quasiparticle mass m^* due to the presence of long-range spin fluctuations [57].

A recent explanation for NFL behavior relies on the competition between anisotropic Kondo and RKKY interactions in a disordered system [58, 59]. Around the QCP corresponding to J_c , for $T_K > T_{\text{RKKY}}$, free spins arrange into clusters, which increase in size as $T_K \rightarrow T_{\text{RKKY}}$. The spin clusters form a granular magnetic phase, coexisting with the metallic phase, and the system exhibits a Griffiths singularity at zero temperature [60]. Non-Fermi-liquid effects are attributed to the dynamics of large spin clusters in the Griffiths phase. A percolation limit for these clusters is reached at the QCP, which for $T_c \neq 0$ leads to an antiferromagnetic, spin-glass, or ferromagnetic transition [58]. The temperature dependences of the thermodynamic properties obey power laws, with exponents determined by the crystal symmetry and the values of the local exchange constants. The nonuniversal nature of these exponents offers a common description of NFL effects in heavy-fermion alloys within the Griffiths phase model.

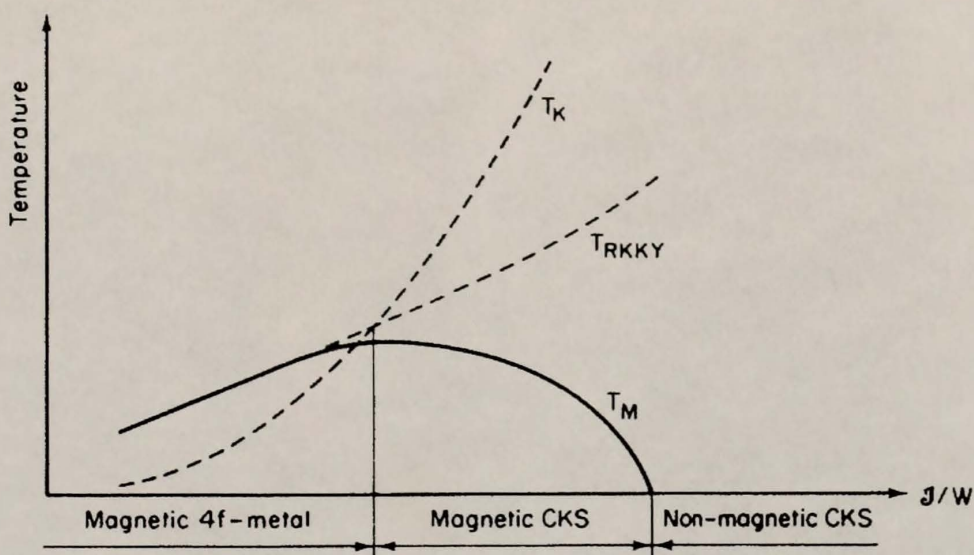


Figure 2.7: Phase diagram of the Kondo lattice [39], illustrating the different dependences of T_K and T_{RKKY} on the parameter J/W , where J represents the Kondo coupling and W is the bandwidth. The dependence of the magnetic ordering temperature T_M on J/W dictates the regions corresponding to magnetic metal, magnetic concentrated Kondo system (CKS), and nonmagnetic CKS.

CHAPTER 3

PROPERTIES OF CeAl₃ AND CePb₃

This chapter gives an overview of structural, thermodynamic, transport, and magnetic properties of CeAl₃ and CePb₃ alloys that are relevant to the problems addressed in this dissertation.

3.1 Properties of CeAl₃

3.1.1 Crystal Structure

The compound CeAl₃ crystallizes in the hexagonal Ni₃Sn structure (DO₁₉), Pearson symbol *hP8*, space group *P6₃/mmc*, number 194. This structure consists of two alternating hexagonal layers. The most recently published lattice parameter measurements give $a = 6.547 \text{ \AA}$ and $c = 4.608 \text{ \AA}$ [61]. The above values correspond to a c/a ratio of 0.704, much smaller than the close packed ratio (0.816), and a lattice volume $V = 171.05 \text{ \AA}^3$. A study of the structure of rare-earth trialuminides[62] attributed the formation of a particular structure and its c/a ratio to the rare-earth/aluminum ratio $R_{\text{RE}}/R_{\text{Al}}$. This ratio is largest for the hexagonal LaAl₃, PrAl₃, and CeAl₃, and smallest for Yb, Tm and Sc trialuminides, which crystallize in the cubic Cu₃Au structure. As $R_{\text{RE}}/R_{\text{Al}}$ decreases, the crystal structure is modified from hexagonal to cubic, the layer stacking changes, and the c/a ratio increases.

Figure 3.1 shows the idealized (Ni₃Sn) unit cell of CeAl₃. The cell contains two formula units. The atom positions with respect to the origin are given in Table 3.1 in terms of the lattice parameters a (x, y axes) and c (z axis). Figure 3.2 is an extended scheme showing the hexagonal stacking and the periodicity of the

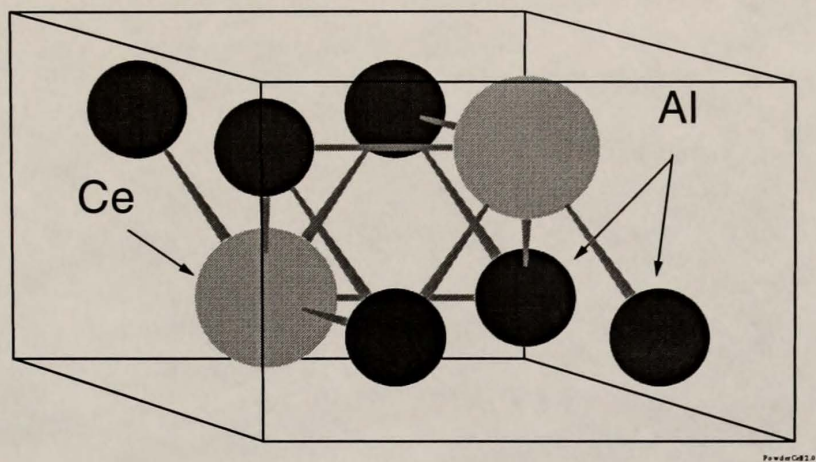


Figure 3.1: Hexagonal Ni₃Sn structure of CeAl₃.

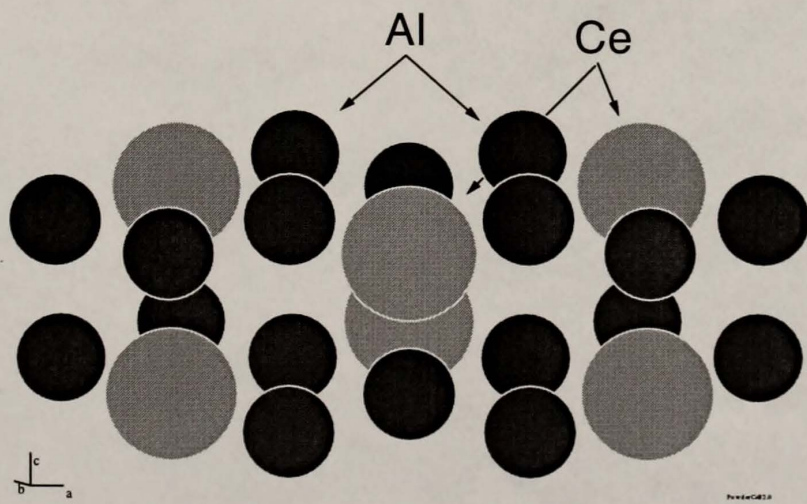


Figure 3.2: Hexagonal Ni₃Sn structure of CeAl₃ (extended scheme).

Table 3.1: Cell Content of Ni₃Sn structure of CeAl₃ [64].

Atom	Multiplicity (Wyckoff notation)	Coordinates		
		x	y	z
Ce	2c	1/3	2/3	1/4
		2/3	1/3	3/4
Al	6h	0.833	0.666	1/4
		0.833	0.167	1/4
		0.334	0.167	1/4
		0.167	0.334	3/4
		0.666	0.833	3/4
		0.167	0.833	3/4

unit cell. Each Ce atom has 6 Al nearest neighbors, at a distance $d_{\text{Ce-Al}} = 3.27 \text{ \AA}$, and 6 Ce nearest neighbors at a distance $d_{\text{Ce-Ce}} = 4.428 \text{ \AA}$ [63]. The central Ce atom is surrounded by six nearest neighbors (3 Al and 3 Ce atoms) above and six below the basal plane. It is important to point out that all nearest neighbors are located in the layers above and below the central Ce atoms, and their distances are not along the *c*-axis direction, but rather at an angle. These off-axis neighboring distances might have some implications regarding the hybridization between Ce and Al atoms, as well as the effects of the RKKY interaction on the magnetic properties of CeAl₃ (see Chapter 7).

3.1.2 Specific Heat

Early measurements of the specific heat of CeAl₃ below 10 K proved to be unreliable [65, 66] due to anomalies caused by the presence of the secondary phases. Later measurements by Brodale *et al.* [67] demonstrated a significant reduction of these anomalies. In their study, the low temperature specific heat showed a maximum around 0.4 K when plotted as C/T vs T . The value of the electronic specific heat coefficient γ extrapolated from C/T vs T^2 is $\gamma = 1250 \text{ mJ/K}^2 \text{ mol}$. This maximum in C/T has been the subject of intense controversy about the ground state of CeAl₃. It was initially proposed that its origin is due to the formation of a Kondo

lattice state in which the conduction electrons undergo coherent scattering [68]. Later experiments [69, 70, 71] suggested that the maximum was due to either magnetic correlations or a possible antiferromagnetic order in this compound.

The anomaly in C/T has also been studied at different pressures and magnetic fields. Magnetic field measurements up to 4 T [68] showed that both the maximum and its temperature position decrease in field, while there is an increase of C/T values below 0.2 K (see Fig. 3.3). Measurements above 1 K and at 23 T [72] indicated a decrease in C/T values below 4-5 K (more than 15% at 1 K) and an increase in values above the same temperature (around 20% near 10 K). These results seem to indicate an initial increase of the electronic coefficient γ with field, followed by a marked decrease at higher fields. The pressure dependence of the specific heat as C/T vs T is shown in Fig. 3.3 [73]. The specific heat is very sensitive to pressure. C/T values at 0.4 K were found to decrease with pressure as $P^{1/6}$. There is no sign of the specific heat anomaly at a pressure of 0.4 kbar. The coefficient γ is reduced from 1250 mJ/K² mol at atmospheric pressure to about 550 mJ/K² mol at 8.2 kbar. Values of C/T are essentially constant below 1 K for pressures around and above 2 kbar.

An attempt was also made to measure specific heat on very small single crystals of CeAl₃ [74]. The results proved to be sample-dependent. Some of the crystals showed peaks in the specific heat resembling antiferromagnetic phase transitions. It remains to be understood whether there is any relationship between these peaks in the specific heat and the maximum observed in C/T for polycrystalline samples.

3.1.3 Magnetic Susceptibility

Avenel *et al.* [75] measured the magnetic susceptibility of polycrystalline CeAl₃ down to 0.8 mK. The results show a broad maximum around 0.5 K, resembling the anomaly in C/T near 0.4 K (see Fig. 3.4). The susceptibility becomes temperature independent below 40 mK ($\chi(T = 0) \approx 29.5$ memu/mol), consistent

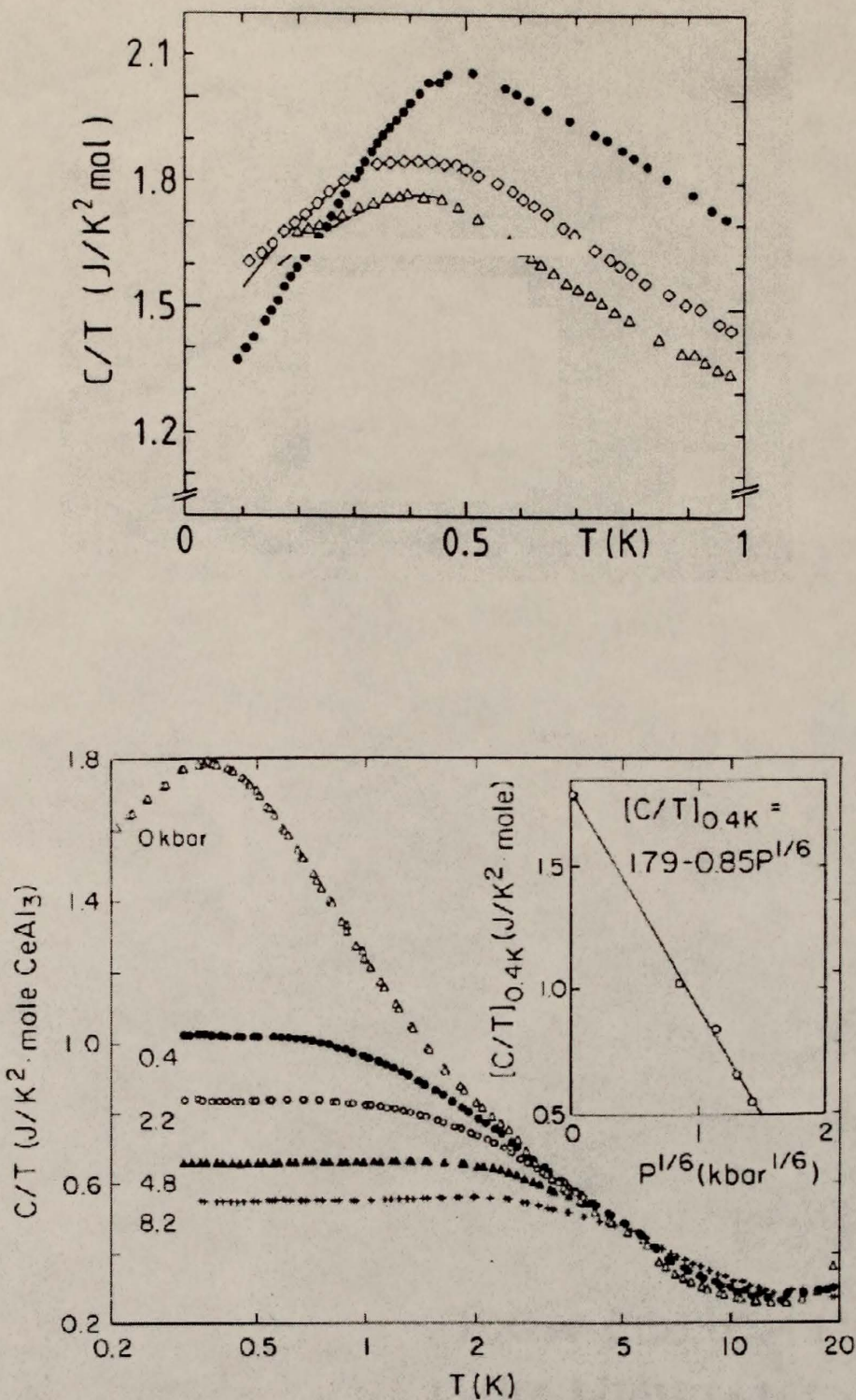


Figure 3.3: Magnetic field and pressure dependence of the specific heat of $CeAl_3$. Upper part: C/T vs T of $CeAl_3$ in magnetic fields up to 4 T (0 T: circles, 2 T: diamonds, and 4 T: triangles) [68]. Lower part: Pressure dependence of C/T vs T for $CeAl_3$ up to 8.2 kbar [73].

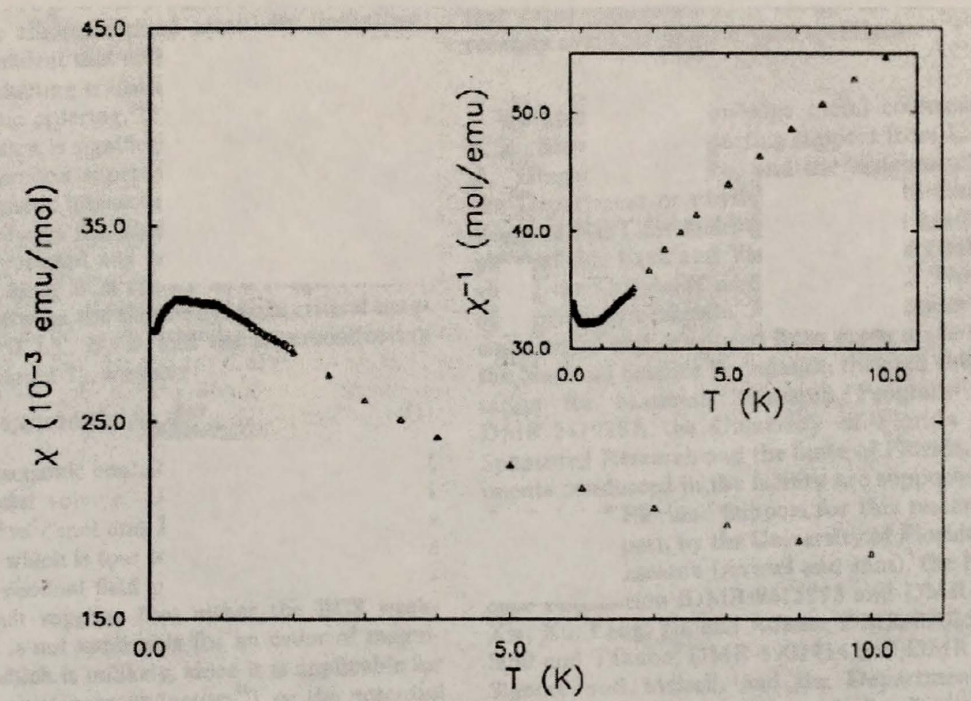


Figure 3.4: Magnetic susceptibility of CeAl_3 below 10 K [75]. The inset shows the inverse susceptibility.

with Fermi-liquid behavior. The inverse susceptibility follows Curie-Weiss law above 150 K, with an effective magnetic moment close to that of a free Ce³⁺ ion, $\mu_{\text{eff}} = 2.54\mu_B$, and $\Theta_{\text{cw}} = -30 \pm 6$ K. The susceptibility of single crystals above 4 K was also measured with the field parallel (χ_{\parallel}) and perpendicular (χ_{\perp}) to the *c*-axis [76]. The susceptibility along the *c*-axis χ_{\parallel} is at least three times as large as χ_{\perp} around 4 K, indicating a large anisotropic magnetic behavior.

3.1.4 Transport Measurements

Figure 3.5 shows the electrical resistivity of CeAl₃ below 300 K. It can generally be described by a Kondo-like increase down to 50 K, a maximum around 35 K, possibly signaling the crossover from single-impurity to Kondo-lattice behavior, and a sharp decrease below 10 K. At temperatures below 100 mK, the resistivity has the form of a Fermi-liquid, with a coefficient $A = 35 \mu\Omega\text{cm}/\text{K}^2$ (see Fig. 3.5). No sign of a magnetic phase transition (i.e. kink in the resistivity curve) has been detected in electrical resistivity measurements around 0.4-0.5 K. When pressure is applied, there is an increase in both the temperature and magnitude of the maximum [77]. In addition, the A coefficient decreases, and resistivity values above the temperature of the maximum are enhanced as pressure increases.

The low temperature magnetoresistance of polycrystalline samples was found to change sign at a field of 2 T, becoming positive at lower fields [79, 80]. The results are shown in Fig. 3.6. The resistivity values are dependent on the field direction with respect to the current. This anisotropic behavior increases with applied field and at low temperatures. The magnetoresistance at 4.2 K and field perpendicular to the current becomes less negative with increasing pressure for fields larger than 2 T [77]. In single-crystal measurements, the electrical resistivity in zero field along the basal plane is more than twice that along the *c*-axis [76, 81]. The field dependence of the A coefficient parallel to the *c*-axis shows a peak around

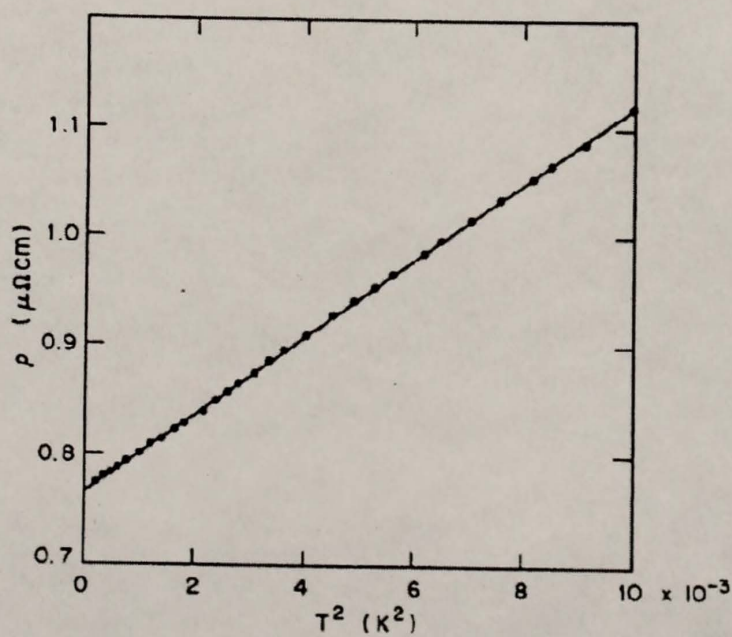
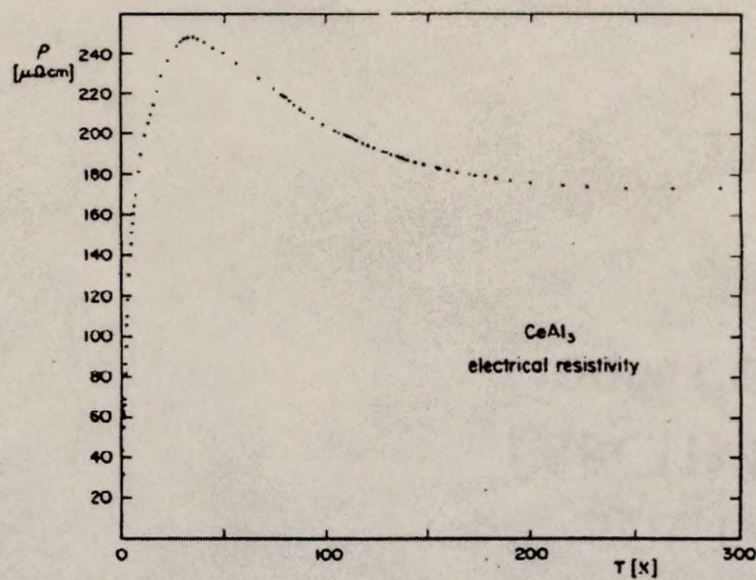


Figure 3.5: Transport measurements on CeAl_3 . Upper part: Electrical resistivity below 300 K [78]. Lower part: ρ vs T^2 below 100 mK [20].

2 T. The authors found this result to be in qualitative agreement with theoretical models describing weakly-antiferromagnetic metals.

3.1.5 Nuclear Magnetic Resonance

Measurements on ^{27}Al nuclear magnetic resonance (NMR) on CeAl_3 down to 0.3 K by Nakamura *et al.*[82] are part of a series of microscopic measurements arguing against the coherence interpretation of the anomalies in C/T and the magnetic susceptibility. The temperature dependence of the spin-lattice relaxation rate at 0.98 MHz increases by one order of magnitude at the lowest temperatures in a nonlinear fashion. The relaxation rate reaches a maximum at 1.2 K. The authors attributed this maximum to the onset of antiferromagnetic order at this temperature. Later measurements by Wong and Clark [83] and Gavilano *et al.* [70] revealed not only the absence of a maximum in the relaxation rate at low temperature, but a Korringa-like ($T_1 T = \text{const.}$) behavior below 0.6 K as well. The reason for these discrepancies might be related to a large sensitivity of the ground state to lattice strains and sample preparation for NMR measurements. Powdered samples have grains with typical linear dimensions around $50\ \mu\text{m}$. The nonuniform strains created by preparing the powder can have a dramatic effect on the physical properties of CeAl_3 below 1 K. The presence of secondary phases can also have an effect on the results, since it is more probable to find entire grains of either CeAl_2 or $\text{Ce}_3\text{Al}_{11}$, as proposed by Wong and Clark [83]. Gavilano *et al.* also measured the NMR spectra of partially oriented powder (c -axis along the direction of the applied field) at 6.968 MHz, and observed two distinct components (Fig. 3.7). They concluded that these components correspond to two different regions of the sample being studied: the spectral lines seen in Fig. 3.7 were attributed to a normal paramagnetic phase, while the broad structure was ascribed to a phase where static magnetic correlations take place. The Ce moments of this latter phase were estimated to be

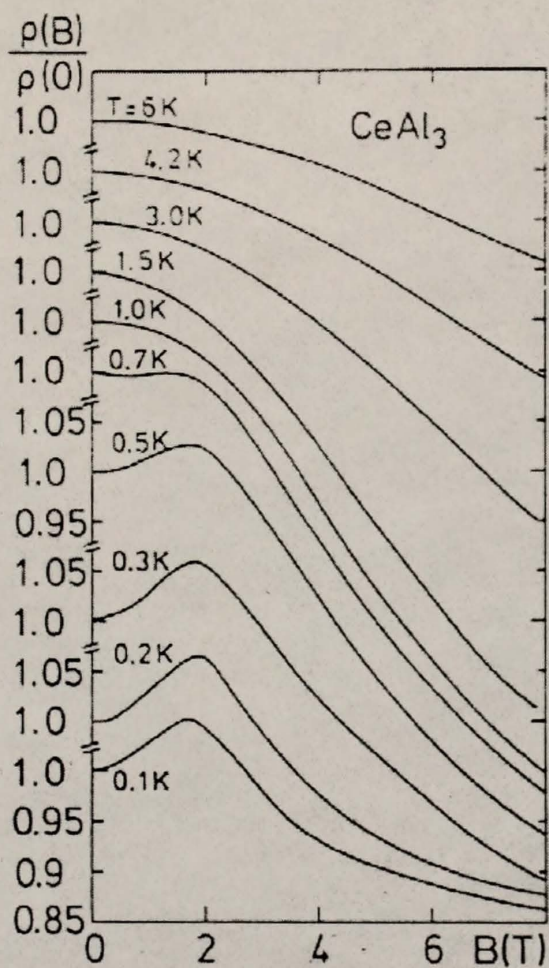


Figure 3.6: Magnetoresistance of CeAl_3 down to 100 mK [79].

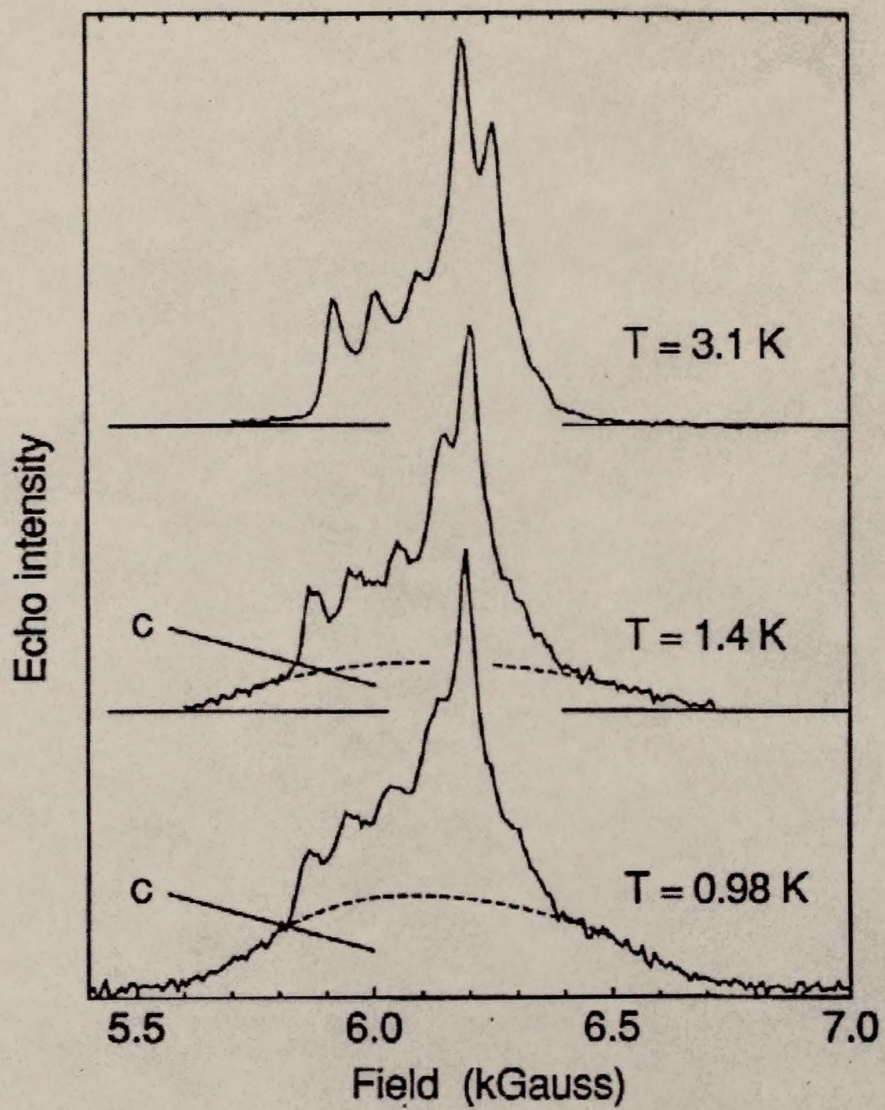


Figure 3.7: NMR spectra of partially oriented powder at 6.968 MHz for different temperatures [70].

less than $0.05\mu_B$. The presence of magnetic correlations in CeAl₃ argues against a simple interpretation of its ground state in terms of a non-magnetic Fermi-liquid.

3.1.6 Muon Spin Rotation

The only muon spin rotation (μ SR) experiments on pure CeAl₃ available to date are those of Barth *et al.* [69, 84]. The authors measured the time-dependent muon polarization on two polycrystalline samples, as seen in Fig. 3.8. The muon polarization signal was described as the sum of several time-dependent components, two of which correspond to the response of muons from different magnetic environments. The most significant finding was the detection of a spontaneous muon spin precession frequency in zero field below 0.7 K from one of these components. This Larmor frequency, proportional to the local magnetic field, has a very small temperature dependence below 0.7 K. Its extrapolated value at $T = 0$ is just above 3 MHz, which corresponds to an average local field of 220 G. In agreement with this estimate, the muon precession signal could not be observed at an external applied field of 750 G. Both the oscillating component and the fast relaxation of the muon polarization are commonly associated with spin-density-wave behavior [85]. The presence of the local field at the muon sites was interpreted as the development of short-range, quasistatic magnetic correlations in CeAl₃ below 0.7 K. As the temperature decreases, these correlated moments, estimated to be around $0.5\mu_B$, develop some coherence in a spatially inhomogeneous manner. The appearance of this almost percolative effect was attributed to magnetic frustration. Electron paramagnetic resonance (EPR) measurements by Coles *et al.* on GdAl₃ (Ni₃Sn structure) [86], also contributed to the development of this idea, arguing that the magnetic behavior in CeAl₃ might be mediated by frustrated antiferromagnetism in the triangular sublattice of the hexagonal *a-b* planes.

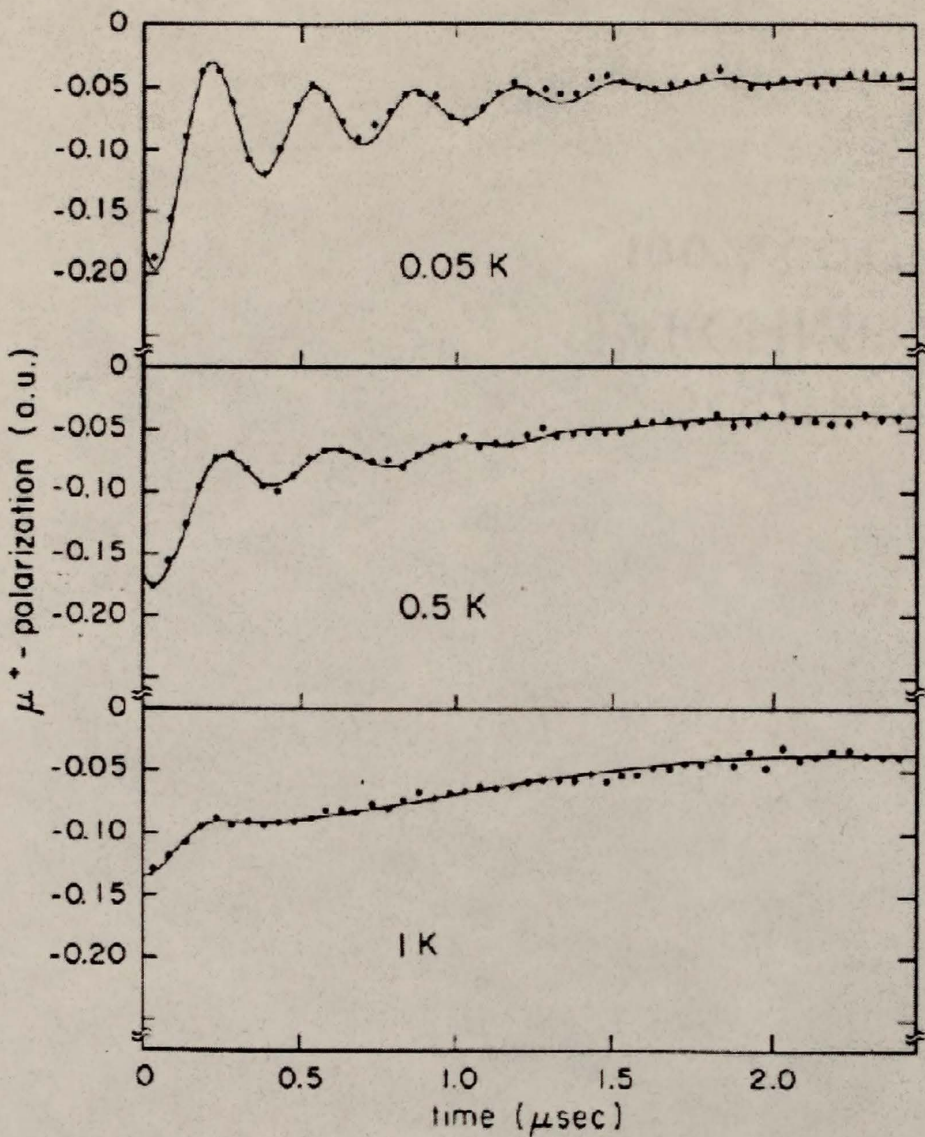


Figure 3.8: Muon polarization as a function of time in zero external field for $T = 0.05, 0.5$, and 1K [69].

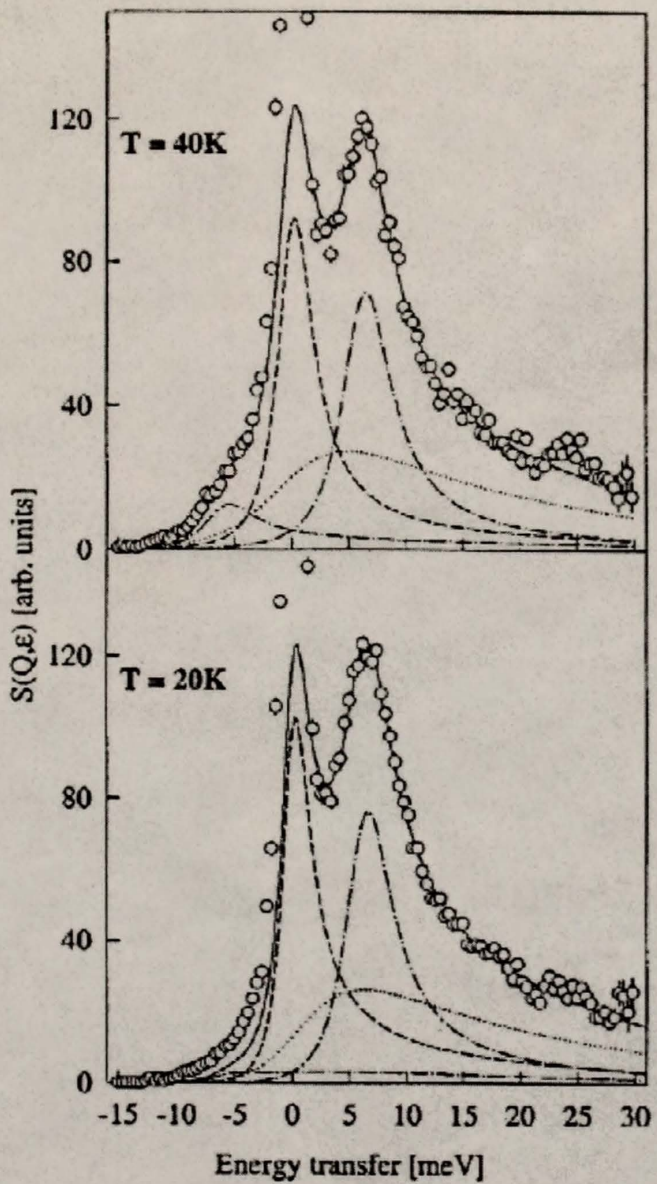


Figure 3.9: Magnetic contribution to the inelastic scattering function of CeAl_3 at $T = 20$ and 40K [87]. The solid line is a fit to a three-Lorentzian model. The dotted lines represent the individual fit components.

3.1.7 Neutron Scattering

Inelastic neutron scattering is one of the most direct methods of determining electronic energies and crystal fields in metallic compounds. In CeAl₃, the cerium ions occupy positions of low point symmetry. In hexagonal structures, the Ce³⁺ $|J = \frac{5}{2}\rangle$ multiplet splits into three doublets under the influence of a crystalline electric field (CEF): $\Gamma_7 : |\pm \frac{1}{2}\rangle$, $\Gamma_8 : |\pm \frac{5}{2}\rangle$, and $\Gamma_9 : |\pm \frac{3}{2}\rangle$. In cerium heavy-fermion compounds, the neutron scattering spectrum can be described in terms of two components: a quasielastic peak around zero energy transfer and a width of order T_K at $T \approx 0$, and an inelastic peak at an energy that coincides with the characteristic energy of crystal-field excitations.

In addition to the quasielastic peak, the most recent measurements [87] displayed a single inelastic peak at an energy $\epsilon \sim 6.4$ meV for $T = 20$ K (Fig. 3.9). With the help of previous single-crystal magnetic susceptibility data [76], the authors calculated the crystal-field parameters for CeAl₃ and determined the ground state to be $\Gamma_9 : |\pm \frac{3}{2}\rangle$, followed by $\Gamma_8 : |\pm \frac{5}{2}\rangle$ at 6.1 meV ($T = 71$ K), and $\Gamma_7 : |\pm \frac{1}{2}\rangle$ at 6.4 meV ($T = 74$ K). By comparing the parameters to those of other rare-earth trialuminides with Ni₃Sn structure, they concluded that the hybridization of Ce 4f electrons with the conduction band is the dominant contribution to the CEF potential, as proposed by some theories of the Kondo effect in crystal fields [88]. Thus, the hybridization is responsible for both Kondo and CEF energy scales.

3.1.8 Chemical Substitution Studies

By far the most interesting doping studies on CeAl₃ to date are those of La impurities on the Ce sites. Recent specific heat studies of Ce_{1-x}La_xAl₃, performed after evidence for magnetic correlations was found for the pure compound [69, 84], added to the already existing controversy about the nature of the anomalies in CeAl₃. An enhancement of the anomaly in C/T was found for $0 \leq x \leq 0.2$ [71], and a corresponding peak appears in the specific heat, as seen in Fig. 3.10. The

magnetic susceptibility also shows an enhancement in its corresponding maximum, with a temperature around 2.5 K for $x = 0.2$. A T^3 dependence of the specific heat below this maximum for the La-doped alloys led to the conclusion that the anomalies represented the development of an antiferromagnetic transition. Two reasons for this development were proposed. The first one is the application of a negative chemical pressure by the larger La atoms and a subsequent decrease in hybridization between f ions and conduction electrons. This effect is in accordance with the Kondo necklace model (see Chapter 2). The second possibility is the reduction of magnetic frustration in the basal-plane triangular lattice of Ce ions [86, 89]. As the Ce ions are substituted by non-magnetic La atoms in the triangular sites, a number of the Ce moments are relieved from the frustration constraint and are free to interact with others. This explanation relies on the assumption that the in-plane interactions are much stronger than the interactions between two adjacent planes.

More recent neutron scattering and μ SR studies on $\text{Ce}_{1-x}\text{La}_x\text{Al}_3$ [15, 90] have shown that the temperature at which the maximum in the specific heat for $x = 0.2$ develops coincides with both the appearance of an inelastic peak in the neutron scattering function and the divergence of the μ SR relaxation rate. The divergence of the muon relaxation rate was interpreted as evidence for either short-range magnetic correlations, as found for pure CeAl_3 [69, 84], or long-range magnetic order of small moments. Bragg scattering on powdered samples did not show evidence of long range order within the resolution of the measurement. The magnitude of the Ce moments was estimated as $\leq 0.05\mu_B$. The position of the inelastic peak for $x = 0.2$ is weakly temperature-dependent, with an estimated energy of 0.54 meV at $T = 0$. It was argued that the magnetic correlations in this sample were too small to be responsible for the behavior of both the inelastic peak and the thermodynamics below 2 K. In the search for an alternate explanation, the specific heat

and the inelastic peak were described in terms of the anisotropic Kondo model (discussed in Chapter 2), which shows a similar response function and a maximum in C/T for specific parameter values. This interpretation was not able to account for the magnetic behavior inferred from the μ SR results. Instead, the AKM proved to be useful in providing an explanation for the anomalies in terms of a single-ion mechanism, rather than cooperative behavior. Numerical results for the specific heat of the AKM will be compared to specific heat measurements in magnetic field of La-doped CeAl_3 alloys in Chapter 6.

Only one study reports doping of CeAl_3 -based alloys on the Al ligand sites [61]. Corsépius *et al.* found that the alloys were single-phased for doping levels less than $x = 0.1$, and that substitution of Ga, Si, and Ge contracts the lattice, while Sn expands it. All of the above elements have the same effect on the specific heat and the magnetic susceptibility. The anomaly in C/T for the pure compound is shifted to higher temperatures, as much as 4.2 K for $\text{Ce}(\text{Al}_{0.9}\text{Sn}_{0.1})_3$. A maximum at a slightly higher temperature is also seen in the susceptibility between 0.1 and 70 kG. The maxima were attributed to the development of an antiferromagnetic phase transition. All samples except those with Ga impurities exhibit discrepancies between zero-field-cooled and field-cooled susceptibilities, and only those above $x = 0.1$ show a time-dependent maximum (spin-glass-like). The development of an apparent phase transition in the thermodynamic properties does not seem to be exclusively related to an isotropic volume change of the hexagonal lattice, since these features were seen in alloys with both smaller and larger lattice parameters than those of CeAl_3 . Instead, the authors argued that the change in the temperature position of the anomaly in C/T is related to the absolute-value change (increase or decrease) in the c/a ratio.

Table 3.2: Cell Content of Cu₃Au structure of CePb₃ [64].

Atom	Multiplicity (Wyckoff notation)	Coordinates		
		x	y	z
Ce	1a	0	0	0
Pb	3c	1/2	1/2	0
		1/2	0	1/2
		0	1/2	1/2

3.2 Properties of CePb₃

3.2.1 Crystal Structure

The compound CePb₃ crystallizes in the face-centered cubic Cu₃Au structure, Pearson symbol *cP4*, space group *Pm3m*, number 221. The Ce sites correspond to the corners of the cube, while the Pb atoms occupy the face-centered positions. The structure forms directly from the melt at 1170°C on the Ce-Pb phase diagram [91]. Unlike CeAl₃, there are no secondary phases that might affect the physical properties and the formation of single crystals of this compound. The lattice constant is $a = 4.876 \pm 0.002 \text{ \AA}$ [92], corresponding to a lattice volume $V = 115.93 \text{ \AA}^3$.

Figure 3.11 shows the Cu₃Au unit cell of CePb₃. The cell contains one formula unit. The atomic coordinates with respect to the origin are given in units of a in Table 3.2. In an fcc structure, the Ce atoms have 6 Ce nearest neighbors at a distance equal to the lattice constant, and 12 Pb nearest neighbors at a distance $d_{\text{Ce-Pb}} = a/\sqrt{2} = 3.448 \text{ \AA}$.

3.2.2 Specific Heat

The low-temperature specific heat, plotted as C/T vs T^2 , is shown in Fig. 3.12. It has a peak around 1.1 K due to an antiferromagnetic transition. The magnitude of the peak is close to 3.5 J/K² mol, and the extrapolated electronic coefficient γ reaches a value around 1000 mJ/K² mol. The effect of high magnetic fields was

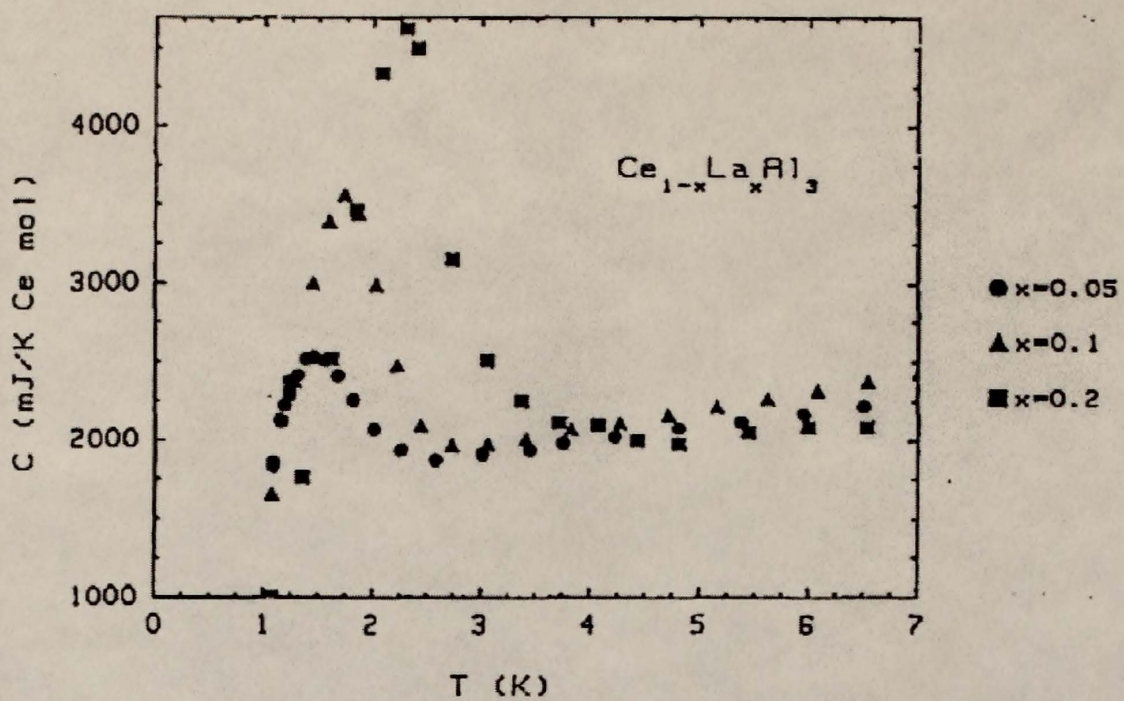


Figure 3.10: Specific heat of $\text{Ce}_{1-x}\text{La}_x\text{Al}_3$ alloys ($x = 0.05, 0.1$, and 0.2) [71].

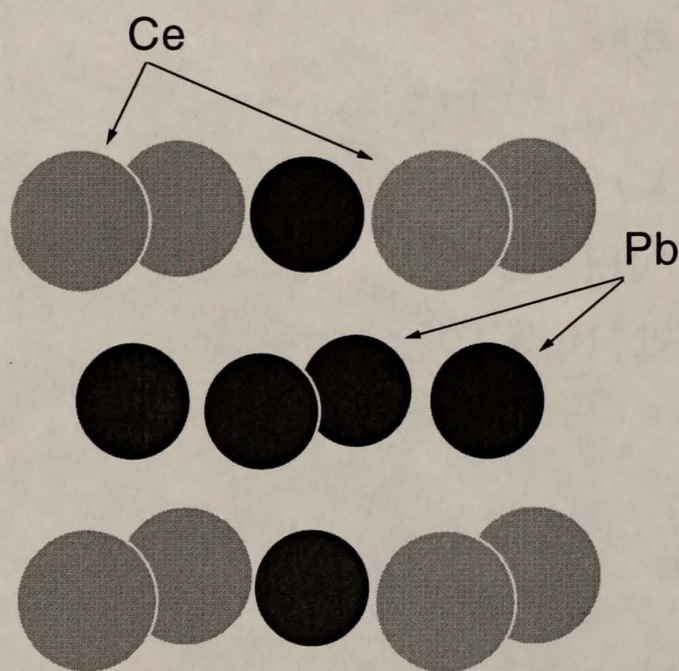


Figure 3.11: Cubic Cu_3Au structure of CePb_3 .

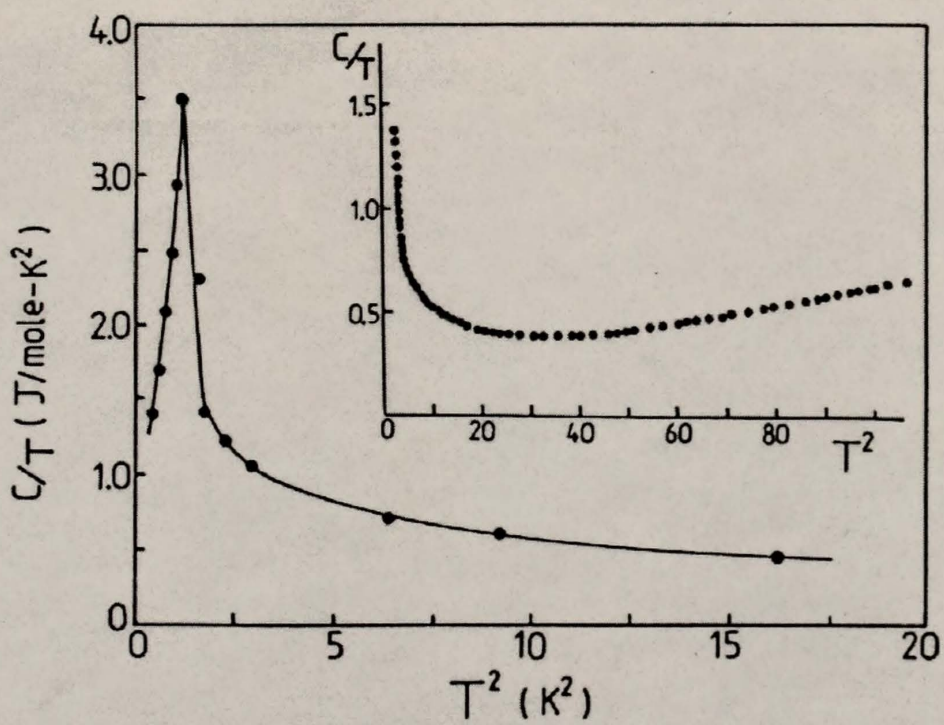


Figure 3.12: Specific heat plotted as C/T vs T^2 of CePb_3 between 0.6 and 4 K. The inset shows C/T vs T^2 from 1.5 to 10 K [93].

first studied by Fortune *et al.* [94]. Magnetic fields between 10 and 20 T were found to suppress the antiferromagnetic state and reduce the electronic coefficient.

Specific heat studies under pressure [95] revealed the existence of a pressure-induced magnetic phase above 0.7 GPa. Below the critical pressure, the antiferromagnetic temperature T_N is suppressed down to 0.6 K; above 0.7 GPa, the temperature of this pressure-induced type-II antiferromagnetic phase increases from 0.6 K to 1 K at 1.3 GPa. Figure 3.13 illustrates the temperature-pressure phase diagram, with T_N decreasing up to 0.7 GPa and increasing at higher pressures. This behavior is rather unusual since a continuous decrease of T_N with pressure is expected for Kondo lattices, especially when the Kondo temperature T_K is about three times as large as the transition temperature, as in CePb₃ [96]. In addition, contrary to other Ce Kondo lattices like CeCu_{6-x}Au_x ($x > 0.1$) [97], and CeRu₂Ge₂ [45], no pressure-induced suppression of T_N to zero was observed for this compound.

3.2.3 Sound Velocity Measurements

The temperature dependence of elastic constants was determined from measurements on a CePb₃ single crystal along the (1 0 0) and (1 1 0) directions [98]. Figure 3.14 illustrates the magnetic field dependence of the relative change in velocity of an elastic mode in the (1 1 0) direction at 10 MHz. Two phase boundaries (indicated by arrows) can be distinguished at 0.38 K. The lower one signals the antiferromagnetic phase transition. The high-field boundary corresponds to an unknown phase, possibly a spin-flop state [98]. The exact nature of this field-induced phase remains to be determined by neutron diffraction experiments. Nevertheless, the discovery of this field-induced transition in the (1 1 0) direction motivated further investigation of the properties of CePb₃ single crystals in magnetic fields.

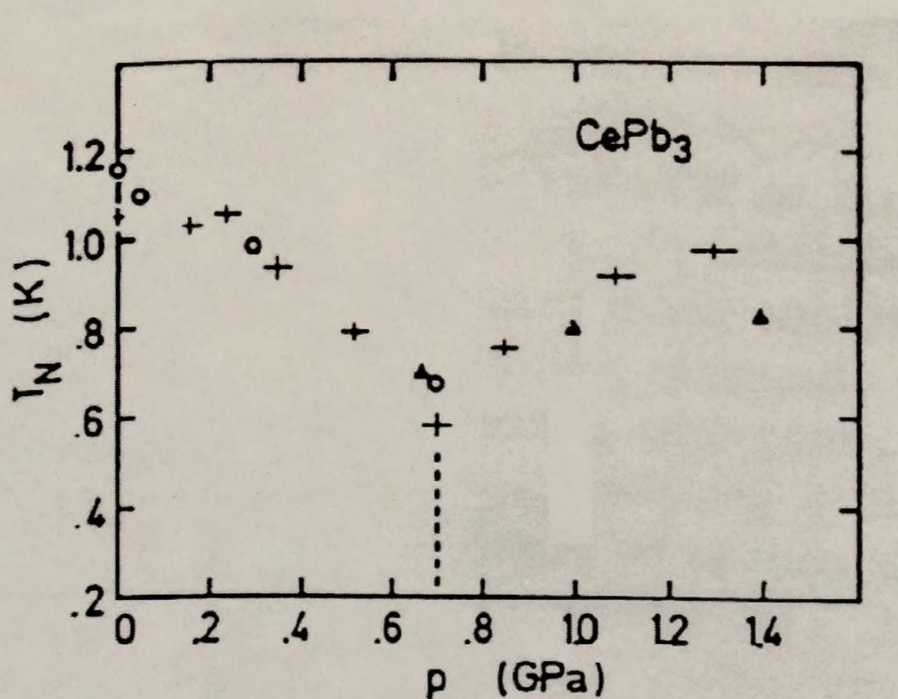


Figure 3.13: Transition temperature-pressure phase diagram for CePb₃ up to 1.4 GPa [95]; the graph shows specific heat measurements (crosses), neutron scattering (circles), and transport measurements (triangles). The broken line indicates a crossover between two distinct magnetic phases (see text).

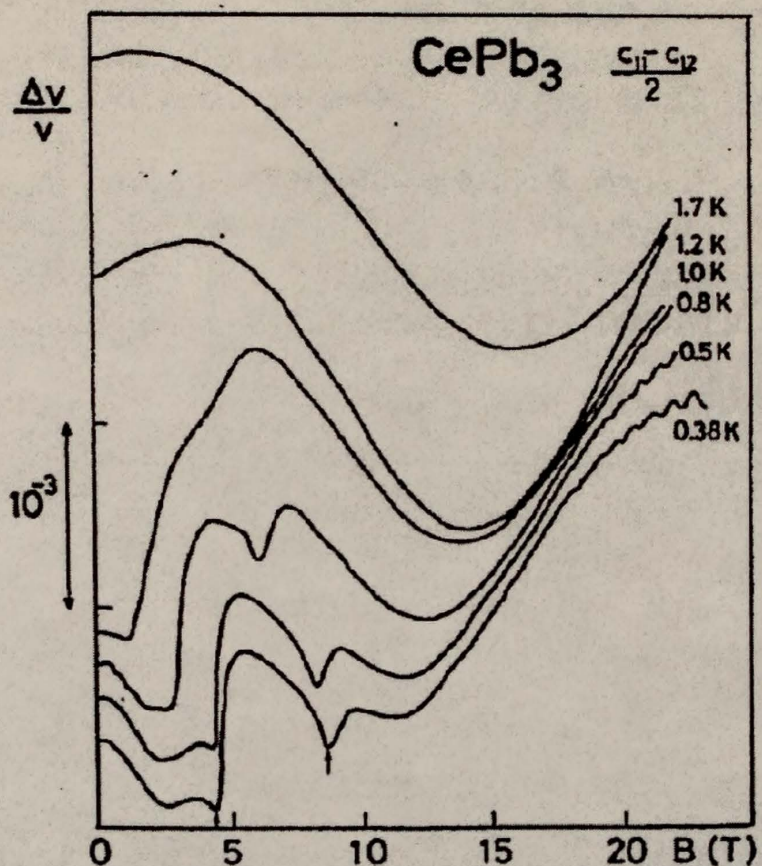


Figure 3.14: Magnetic field dependence of the relative change in sound velocity for the $(c_{11} - c_{12})/2$ elastic mode at 10 MHz [98].

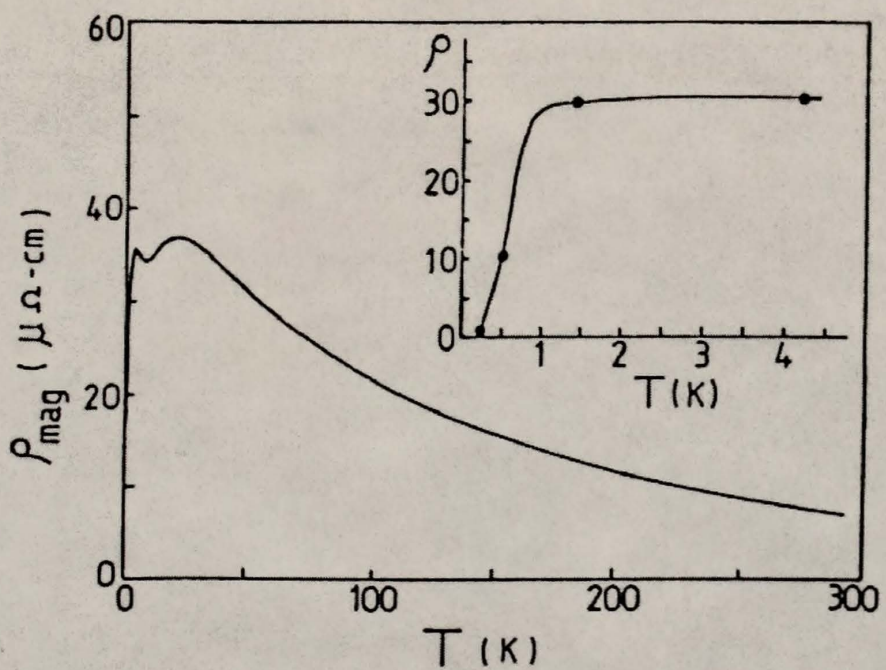


Figure 3.15: Magnetic contribution to the electrical resistivity of CePb_3 at $H = 1 \text{ T}$ below room temperature. The inset shows the resistivity between 0.2 and 4 K at $H = 0.93 \text{ T}$ [93].

3.2.4 Transport Measurements

In order to measure the electrical resistivity of CePb_3 , it is important to measure in magnetic fields of order 1 T in order to suppress the superconducting transition due to the presence of Pb on the surface of the sample [93]. The reaction of CePb_3 with oxygen from air causes the separation of the two elements, eventually followed by oxidation of Ce and Pb. Figure 3.15 displays the magnetic resistivity between 0.2 and 4 K. It shows a logarithmic, Kondo-like increase from room temperature down to 40 K, followed by two maxima, and finally by a drop below 2 K. The maximum around 20 K has been attributed to the decrease in Kondo scattering due to a depopulation of the excited crystal-field levels [99]. The maximum at 3.3 K is thought to be due to a coherence effect of the Kondo lattice. There is also a rapid change in slope around 1 K, indicative of the antiferromagnetic phase transition, as shown in the inset to the figure.

The pressure dependence of the magnetic resistivity was measured on a single crystal [99]. There is a shift of the maximum at 3.3 K toward higher temperatures. Only one broad maximum was detected for pressures above 11.5 kbar. This result is consistent with an increase of the Kondo temperature T_K . The magnetoresistance was recently measured along the (1 1 0) crystallographic direction [100]. Two field-induced anomalies were found for the magnetoresistance curves below 400 mK at 5 and 9.5 T, respectively (see Fig. 3.16). The resistivity increases up to 5 T, decreasing sharply above the first transition, and becoming almost field-independent after the second. A magnetic field-temperature phase diagram was constructed, in good agreement with previous sound velocity measurements. The angle dependence near the (1 1 0) direction was also measured in order to verify the orientational dependence of the field-induced phase above 5 T, detected by sound velocity measurements. A large increase in the magnetoresistance was observed as the field direction was rotated toward the (1 0 0) direction, at which point the sharp

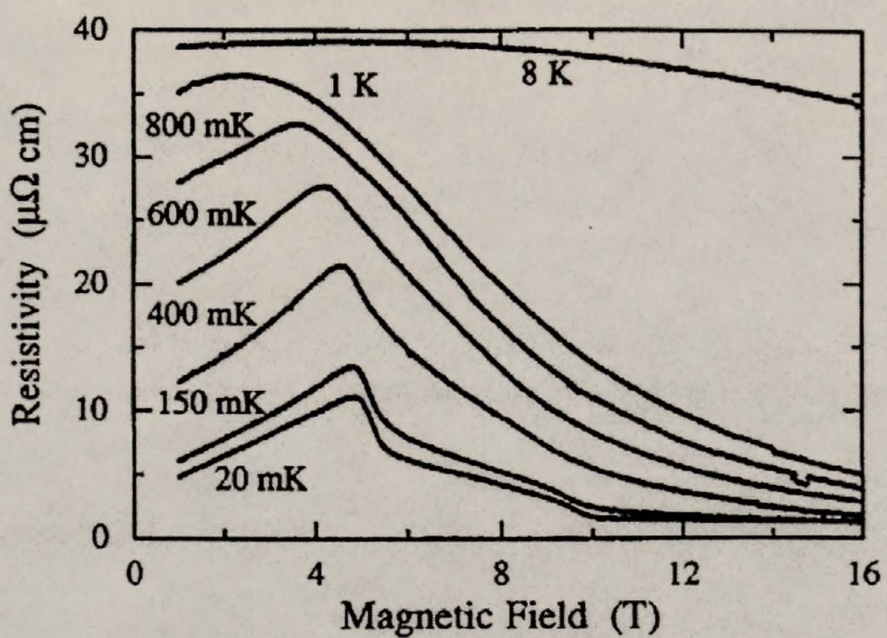


Figure 3.16: Magnetoresistance curves between 1 and 16 T for temperatures in the range 20 mK to 8 K. The magnetic field is along the (1 1 0) direction [100].

drop at 5 T could not be detected. The low-temperature resistivity was found to be proportional to T^2 with a field-dependent A coefficient. At 5 T, A reaches a maximum, the range of T^2 dependence becomes smaller, and the resistivity acquires a linear term, all coinciding with the field-induced transition. This enhancement of A with field points to a corresponding enhancement of the specific heat coefficient γ , as the ratio A/γ^2 is expected to remain constant for heavy fermions [101]. At 10 T, there is a small bump in the A coefficient, indicating a transition to a ferromagnetically-polarized paramagnetic state [100].

3.2.5 Magnetic Susceptibility

Measurements of the magnetic susceptibility on a CePb₃ polycrystal below 4 K [102] revealed a maximum at 1.25 K, similar to that found for the specific heat at 1.1 K. Figure 3.17 shows the data measured at 2.6 kG. This maximum is reminiscent of an antiferromagnetic phase transition, and coincides with the appearance of a maximum in the specific heat at 1.1 K. The estimated value of $\chi(T = 0)$ is somewhere between 32 and 33 memu/mol. The inverse susceptibility follows a Curie-Weiss behavior, and gives a high temperature effective moment $\mu_{\text{eff}} = 2.5 \mu_B$, and a Curie-Weiss temperature $\Theta_{\text{cw}} = -25$ K. An investigation of the pressure dependence of the inverse susceptibility [99] found an increase of Θ_{cw} from 0 to 15 kbar, a trend consistent with an increase of T_K .

Recently, the ac susceptibility of a CePb₃ single crystal was measured as a function of crystallographic direction to verify the phase diagram and the field-induced (presumably spin-flop) phase transition [103]. Their phase diagrams along the (1 0 0) and (1 1 0) directions indicated that the range of the field-induced phase depends on the crystallographic direction. Between 20 and 600 mK, with $H \parallel (1 0 0)$, the range is about 1 T, while for $H \parallel (1 1 0)$, it is close to 5 T. The phase diagram determined from ac susceptibility data along (1 1 0) is in agreement with previous studies, as shown in Fig. 3.18.

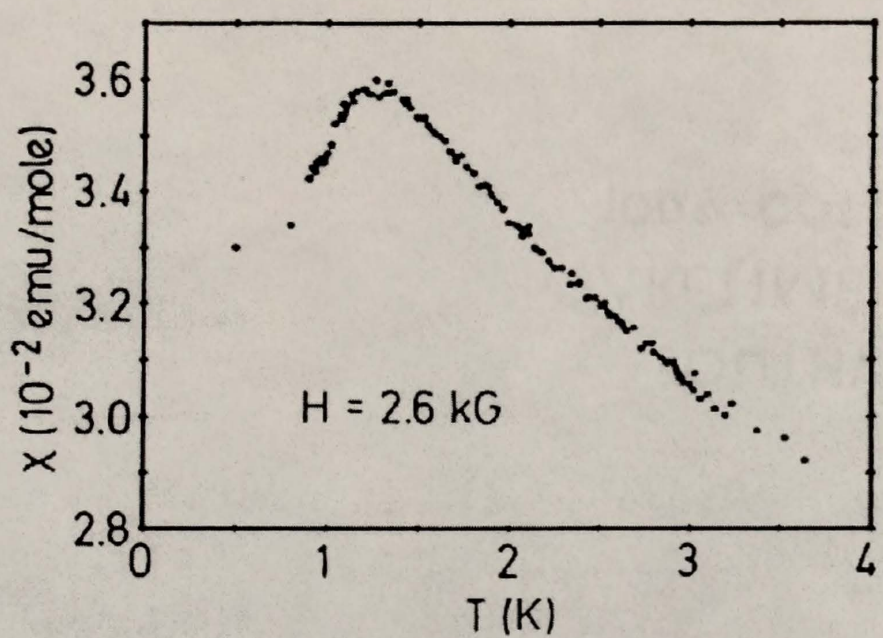


Figure 3.17: Magnetic susceptibility of a CePb_3 polycrystal below 4 K at $H = 2.6$ kG [102].

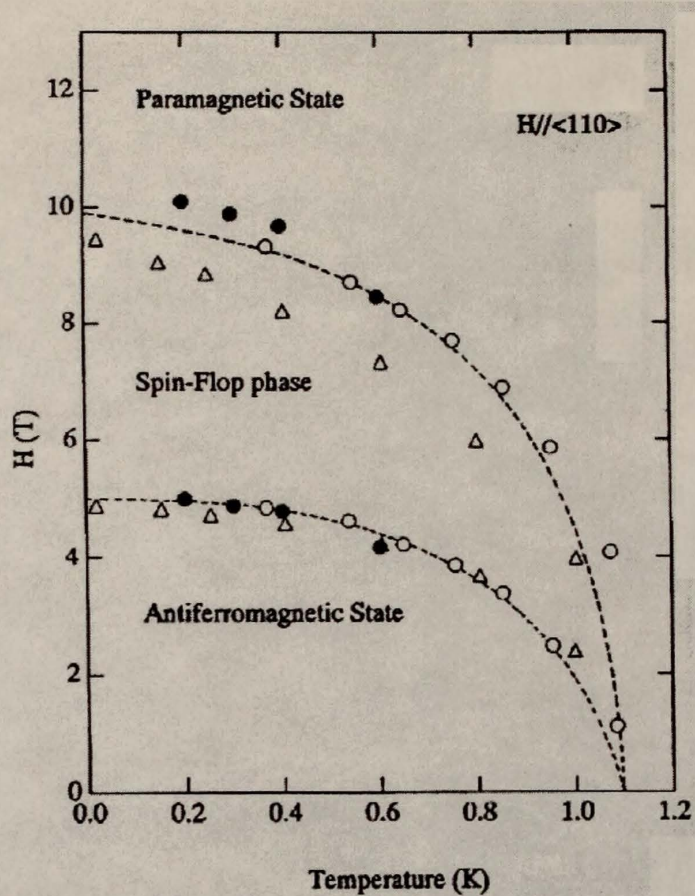


Figure 3.18: Phase diagram ($H - T$) for CePb₃, with the field along the (110) direction (Solid circles: ac susceptibility [103], open circles: sound velocity [98], and open triangles: magnetoresistance [100]).

3.2.6 Neutron Scattering

Neutron scattering studies are essential in the determination of the ordered moment at low temperatures and the crystal-field parameters of heavy-fermion systems. The Cu₃Au cubic structure of CePb₃ provides a high degree of crystal symmetry. In the cubic environment of Ce³⁺ ions in CePb₃, the crystal-field (CEF) potential splits the $|J = \frac{5}{2}\rangle$ multiplet into a Γ_7 doublet and a Γ_8 quartet [104]:

$$|\Gamma_7\rangle = a|\pm\frac{5}{2}\rangle - b|\mp\frac{3}{2}\rangle$$

$$|\Gamma_8\rangle = \begin{cases} |\pm\frac{1}{2}\rangle \\ b|\pm\frac{5}{2}\rangle + a|\mp\frac{3}{2}\rangle \end{cases}, \quad (3.1)$$

where $a = (\frac{1}{6})^{1/2}$ and $b = (\frac{5}{6})^{1/2}$.

The magnetic scattering function of polycrystalline CePb₃ is shown in Fig. 3.19, which shows the inelastic, quasielastic, and elastic peaks. A fit to the scattering function [105] determined that the ground state is the Γ_7 doublet. The CEF splitting between the doublet and the first excited state is around 72 K [106]. Bragg scattering studies on a single crystal led to the conclusion that the magnetic structure of CePb₃ is antiferromagnetic, and that the moments are aligned along the (1 0 0) direction [106]. The magnetism is incommensurate, with a modulation amplitude of $0.55\mu_B$ at 30 mK. A similar incommensurate structure has also been detected for CeAl₂ [107], another cubic heavy-fermion compound. Vettier *et al.* [106] concluded from a comparative study of Ce Kondo lattices that cubic compounds are more magnetic than those with a large crystal anisotropy, like CeAl₃, CeCu₆, and CeCu₂Si₂. This statement has important implications regarding a possible role of crystalline anisotropy in regulating the competition between the Kondo and RKKY energy scales.

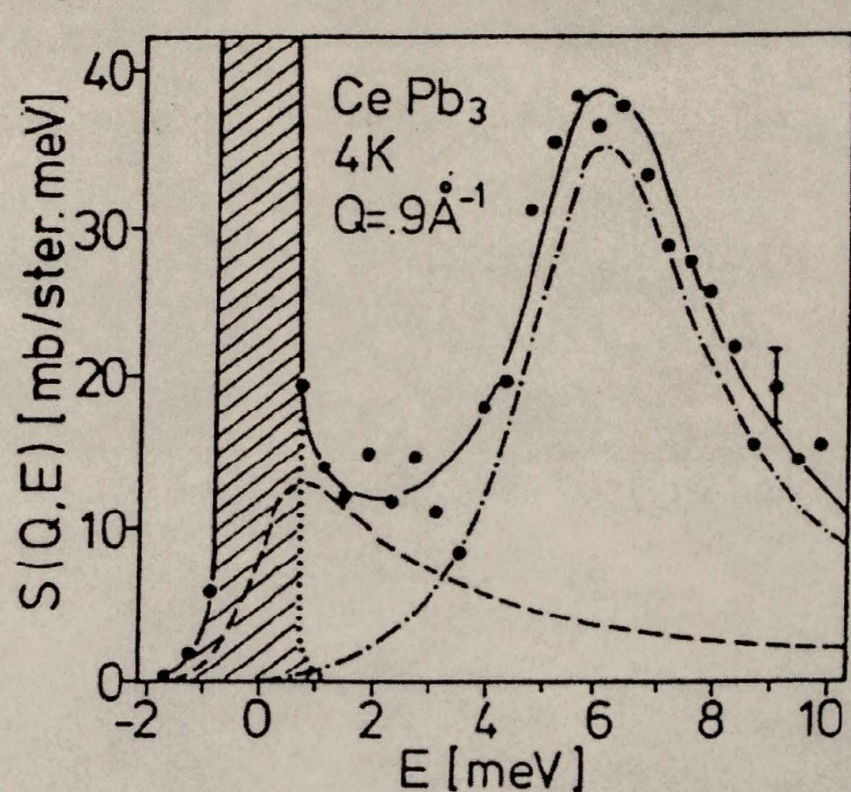


Figure 3.19: Magnetic neutron scattering function of a CePb_3 polycrystal [105]. The solid line is a fit to the data. The dashed line represents the determined quasielastic component, and the dash-dotted line corresponds to the inelastic component.

3.2.7 Chemical Substitution Studies

Alloying studies on the Ce sites of CePb_3 were first reported using La [96]. These studies are particularly important and have fundamental significance, because they constitute evidence of single-impurity effects in a concentrated heavy-fermion system. The specific heat, magnetic susceptibility, and electrical resistivity all scale with Ce concentration. Electrical resistivity measurements revealed that the crystal-field splitting is also unaffected by La doping. The electronic specific heat data for alloys with La $x = 0.4, 0.6$, and 0.96 are shown in Fig. 3.20, along with the theoretical prediction for $S = \frac{1}{2}$. The Kondo temperature is constant throughout the series, implying a constant value of J . The transition temperature T_N goes to zero near a La concentration $x = 0.2$. The suppression of magnetism as a result of a lattice expansion upon La substitution seems to indicate that the decrease in T_{RKKY} with respect to T_K is due to an increase in the average Ce-Ce distance, rather than to an overall change in J . Indeed, $\text{Ce}_{1-x}\text{La}_x\text{Pb}_3$ is a unique system in the sense that T_K and the coupling J seem to remain unaffected by La doping.

While thermodynamic and transport properties of $\text{Ce}_{1-x}\text{La}_x\text{Pb}_3$ seem to be unaffected by the electronic environment surrounding the Ce^{3+} ions, experiments on $\text{Ce}_{1-x}\text{M}_x\text{Pb}_3$ ($\text{M} = \text{Y}, \text{Th}$) [109] confirmed that the single-impurity scaling observed by La doping on the Ce sites is the exception rather than the rule. Instead, a rather unusual behavior is observed upon either Y or Th doping. The magnetic susceptibility at 1.8 K increases with Y concentration. The Kondo susceptibility is inversely proportional to T_K , so this result implies an unusual decrease of the Kondo temperature as the lattice contracts (increasing J). Substitution of Th on the Ce sites also contracts the lattice, and at the same time leads to magnetic-like anomalies in both specific heat and susceptibility for $x = 0.3, 0.5$. The differences in the outer electronic structure between Ce, Y, and Th seem to play an important role in the evolution of the ground state properties of $\text{Ce}_{1-x}\text{M}_x\text{Pb}_3$.

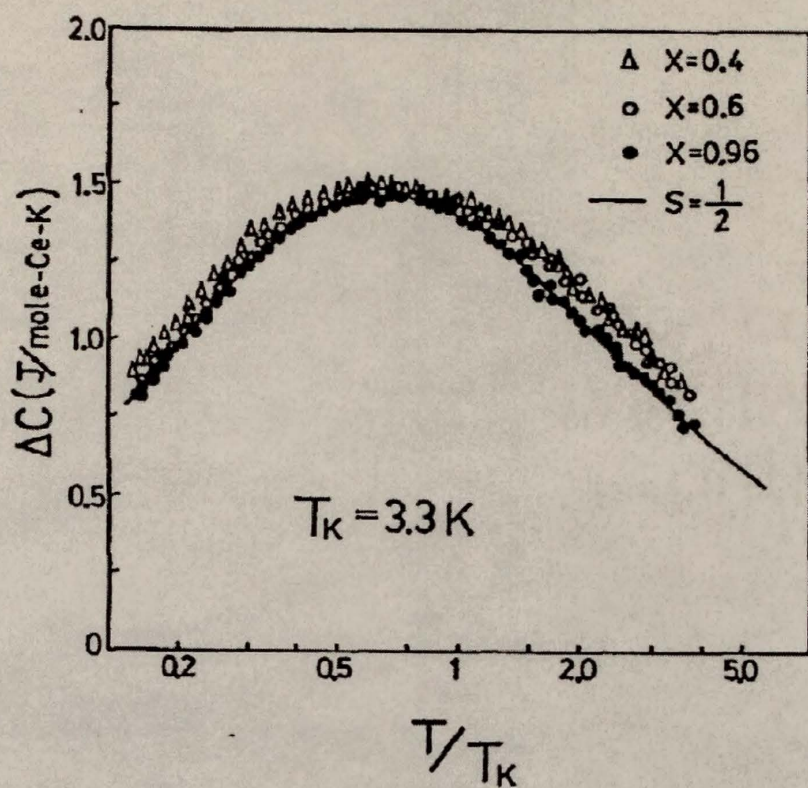


Figure 3.20: Electronic specific heat vs T/T_K for $\text{Ce}_{1-x}\text{La}_x\text{Pb}_3$ alloys, $x = 0.4, 0.6$, and 0.96 [96]. The data are in good agreement with the prediction from the spin- $\frac{1}{2}$ Kondo specific heat [108]. The only adjustable parameter is $T_K = 3.3\text{ K}$.

Chemical substitution studies were also performed on both *f*-ion and ligand sites of the CePb₃ structure. In Ce(Pb_{1-x}M_x)₃ studies with M = Tl, In, and Sn [110, 111], the antiferromagnetic transition temperature decreased toward zero for a Sn concentration $x = 0.4$, and increased for both Tl and In. For the latter two dopants, there is a maximum towards the center of the $T_N - x$ phase diagram. Substitution of Sn for Pb on the ligand sites suppresses T_N and greatly increases the Kondo temperature [112, 113].

CHAPTER 4

MOTIVATION

This chapter begins with a discussion on the importance of the study of CeAl_3 and CePb_3 , followed by a presentation of the objectives of the current study.

4.1 Importance of CeAl_3 and CePb_3

Both CeAl_3 and CePb_3 are canonical, well-documented heavy-fermion systems, with values of the γ coefficient surpassing $1 \text{ J/K}^2 \text{ mol}$, crystal-field doublet ground states, and a low temperature resistivity characteristic of Kondo lattices. Studies on these compounds over the last 25 years made a substantial contribution to the standard interpretation of heavy-fermion systems, based on the Kondo effect and Fermi-liquid theory. However, deviations from this standard model have been observed in these and other compounds through the coexistence of magnetic order and heavy electrons, the presence of unaccountable anomalies in the thermodynamic properties, and non-Fermi-liquid effects. These are all topics of current interest, yet they are among the least understood aspects of heavy-fermion physics. Any information obtained from the study of the above two compounds might be utilized in the development of new interpretations for the heavy-fermion state. The current work will concentrate on the coexistence of heavy fermions and magnetic order in CePb_3 , the nature of the anomaly seen in the specific heat (plotted as C/T) of CeAl_3 , and the heavy-fermion behavior of both compounds in magnetic fields.

In 1975, specific heat and electrical resistivity measurements below 100 mK by Andres, Graebner, and Ott led to the discovery of CeAl_3 as the first heavy-

fermion compound [20]. Despite its significance in the field of strongly-correlated electron systems, CeAl₃ is probably one of the least understood among these compounds. Ever since its discovery, it has been considered a canonical, nonmagnetic heavy-fermion system. Yet later experimental results (see Chapter 3) challenged its nonmagnetic status, and pointed to a possible magnetically-ordered ground state for CeAl₃. Whether the ground state in this compound is magnetic or not has been a long-standing debate, and remains an important topic in the study of heavy-fermion systems.

The compound CePb₃ ranks among the most extensively studied magnetic Kondo lattices. The magnetic transition has little effect in reducing the large value of the electronic specific heat coefficient, $\gamma \approx 1000 \text{ mJ/K}^2 \text{ mol}$. The electrical resistivity has a large T^2 coefficient, $A = 45 \mu\Omega \text{ cm/K}^2$, and the ratio A/γ^2 is around $4 \times 10^{-5} \Omega \text{ cm K}^2 \text{ mol}^2/\text{J}^2$. When taking into account the relatively large value of γ for this compound, the above suggests that the ground state is some superposition of ordered local moments and heavy electrons. Very little is known about the nature of the magnetic ground state of heavy-fermion materials. Measurements of thermodynamic properties of paramagnetic and magnetic states in this compound may be useful to understand the coexistence of magnetic order and heavy electrons.

Another important characteristic of CePb₃ is the observation of single-ion scaling of thermodynamic and transport properties in a concentrated 4f system. The study of Ce_{1-x}La_xPb₃ by Lin *et al.* [96] revealed that the normal state of alloys over the range ($0 \leq x \leq 1$) can be described in terms of a single-ion picture (see Chapter 3). It is the only Ce heavy-fermion system to date exhibiting such behavior. The reason why such a concentrated system can exist with apparently noninteracting 4f sites remains unclear.

4.2 Objectives

4.2.1 Magnetism and Heavy-Fermion Behavior in Ce Kondo Lattices

The studies on CeAl_3 and CePb_3 alloys presented in this dissertation are motivated by a fundamentally important topic in heavy-fermion research: the need for a full understanding of the interdependence between magnetic correlations and/or magnetic order and the heavy-fermion state. The ground state of rare-earth intermetallics is generally described in terms of the competition between two energy scales, T_K and T_{RKKY} , discussed in Chapter 2. The former represents a single-ion effect due to the local Kondo interaction between conduction electrons and the f orbital. The latter portrays a collective effect due to indirect exchange interactions between ionic spins. The schematics of this delicate balance were shown in Fig. 2.7. For $T_{\text{RKKY}} > T_K$, magnetic order occurs and the moments are unquenched at zero temperature. The size of the moments is close to that corresponding to the crystal-field ground state. Concentrated Kondo systems falling into this category have relatively low values of γ , of order $100 \text{ mJ/K}^2 \text{ mol}$ (e.g., CeCu_2 and CeAl_2 [6]). Whenever $T_K \gg T_{\text{RKKY}}$, the Kondo effect develops without magnetic order. This regime corresponds to most nonmagnetic Kondo lattices, with Kondo temperatures larger than 10 K . For $T_K \geq T_{\text{RKKY}}$, the formation of heavy electrons occurs, with γ values in excess of several hundred $\text{mJ/K}^2 \text{ mol}$. This is the least understood area of the Doniach phase diagram. The applicability of this model to heavy-fermion Kondo lattices, in particular to CeAl_3 alloys, will be discussed as part of a study on the anomaly present in this system.

Two empirical correlations have been postulated in order to distinguish between magnetic and nonmagnetic heavy-fermion ground states: the Wilson ratio R and the Kadowaki-Woods ratio. The experimental Wilson ratio R [5] is defined as $\pi^2 k_B^2 \chi_0 / \mu_{\text{eff}}^2 \gamma$, where χ_0 is the zero-temperature susceptibility and μ_{eff} is the effective moment at room temperature. Values of R are usually much larger for magnetically-

ordered than for nonmagnetic Kondo lattices [5]. Nevertheless, the experimental ratios for CeAl_3 and CePb_3 are both around 0.7, a value within the range corresponding to nonmagnetic heavy fermions. Thus, this ratio does not seem to account for the magnetic order observed in CePb_3 , as well as for a possible magnetic order in CeAl_3 .

In most heavy-fermion compounds, the empirical relation A/γ^2 lies somewhat close to the Kadowaki-Woods ratio $A/\gamma^2 = 1 \times 10^{-5} \Omega \text{ cm K}^2 \text{ mol}^2/\text{J}^2$ [101]. This ratio is about an order of magnitude larger than that corresponding to transition-metal alloys. The magnetic field dependence of this relation has not been extensively studied. The ratio A/γ^2 has been observed to remain constant with field in nonmagnetic $\text{CeCu}_{5.9}\text{Au}_{0.1}$ [114], the only published study of the field dependence of this ratio. In order to verify whether A/γ^2 remains the same for both paramagnetic and ordered states, it would be of interest to explore the field dependence of this ratio in a magnetically-ordered heavy-fermion system.

Previous thermodynamic and transport measurements on $\text{Ce}_{0.6}\text{La}_{0.4}\text{Pb}_3$ [96] suggested a single-ion mechanism for the heavy-fermion behavior in this system. A study of the specific heat in magnetic field of $\text{Ce}_{0.6}\text{La}_{0.4}\text{Pb}_3$, a nonmagnetic counterpart of CePb_3 , was conducted in this dissertation to search for further evidence of a single-ion Kondo origin for the heavy-fermion state in Ce-based systems.

4.2.2 Ground State of CeAl_3

The experiments on CeAl_3 alloys presented in this dissertation are motivated by the existing controversy about the ground state of CeAl_3 . The nature of the anomalies in the thermodynamic properties of CeAl_3 systems below 1 K is not well understood. It is a major topic of interest in the field of strongly-correlated electron systems. There are at least three competing interpretations for the origin of these anomalies. One explanation is that the weak maxima seen in C/T and in the magnetic susceptibility between 0.3 and 0.5 K is due to a reduction in the density

of states caused by the formation of coherent states in the Kondo lattice [68]. Another interpretation argues for an unconventional ground state in which heavy electrons coexist with either magnetic correlations or magnetic order. There is now enough evidence [61, 70, 69, 71] for the existence of magentic correlations below 1 K in CeAl₃ through NMR and μ SR studies, casting serious doubt on the so-called coherence interpretation [68]. However, it is not clear at the present time whether the magnetic correlations are short-ranged, frustrated, or whether they lead to long range order. The third and most recent interpretation suggests that the anisotropic Kondo model provides an alternative explanation to the ground state properties, as driven by single-ion dynamics, and dependent on the anisotropy of the Kondo interaction [15, 90]. Under this point of view, the question remains of how to reconcile the presence of magnetic correlations in CeAl₃ with a single-ion Kondo description of its thermodynamic features.

CHAPTER 5 EXPERIMENTAL METHODS

5.1 Sample Preparation

5.1.1 Synthesis

Alloys used in this dissertation were synthesized by melting its respective constituents in an Edmund-Bühler arc furnace under a high-purity argon atmosphere. The arc-melting apparatus consisted of a stainless-steel vacuum chamber with a water-cooled copper crucible at the bottom and a hydraulic mechanism supporting an electrode at the top. The tip of the electrode is made out of a tungsten alloy, and it is capable of carrying well over 100 A of current.

Prior to melting, each of the constituent elements was carefully cleaned to eliminate any oxide layer on the surface, and later weighed to an accuracy of ± 0.03 mg. Their molecular weights and stoichiometric ratios were used to calculate the appropriate relative masses. The total mass of an average sample was about 500 mg, and the diameter of a sample bead ranged between 0.5 and 1 cm. The Cu hearth on the arc-melter was thoroughly cleaned to avoid the presence of unwanted impurities during sample preparation. The element with the highest vapor pressure was placed on the Cu crucible below those with lower vapor pressures. This procedure minimizes direct contact between the Ar arc and the material with highest vapor pressure, therefore reducing its mass loss, and minimizing the discrepancy between predicted and actual stoichiometries for the alloy being synthesized. The chamber was then pumped and subsequently flushed with high-purity Ar. After this procedure was repeated three to four times, the cham-

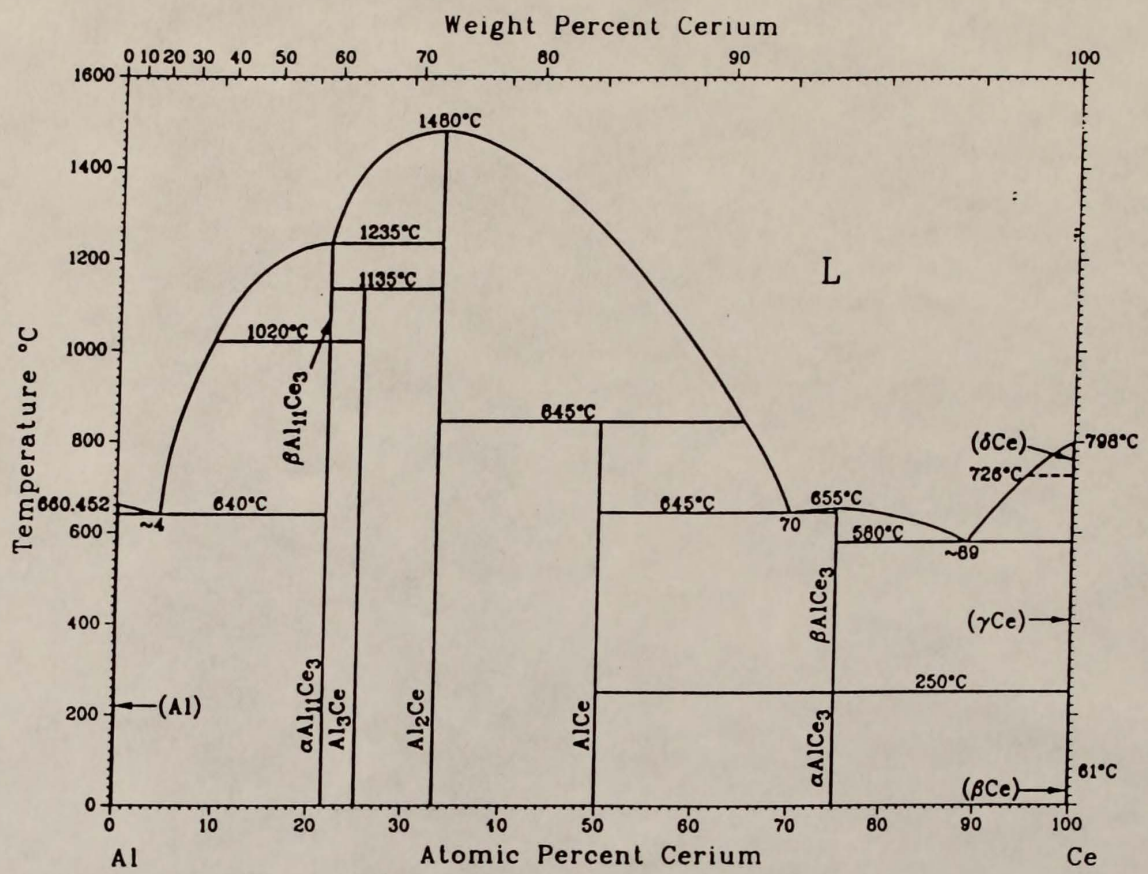


Figure 5.1: Phase diagram of Ce-Al [91].

ber was filled to 0.5 atm of Ar gas. In order to avoid the unwanted presence of oxygen and water vapor, two measures were taken. First, the high-purity Ar goes through a purifier before entering the arc-furnace. Second, a zirconium bead is placed inside the furnace and melted before sample synthesis. Zirconium is known for its high absorbing capacity for oxygen.

At the start of the melting process, a relatively low current was sent through the tungsten electrode. The arc was moved slowly towards the elements to avoid any thermal stresses and motion or splashing of material due to the arc pressure. During melting, enough time was allowed for the liquid components to mix via arc pressure. To ensure homogeneity, the above process was repeated several times and the sample bead was turned over after each melt. The mass loss during melting was obtained as a percentage difference (typically $< 0.1 - 0.3\%$) between the total masses before and after sample synthesis.

Alloys of CeAl₃

Alloys of Ce_{1-x}M_xAl₃ (M = La, Y) were synthesized using the purest available materials: cerium and lanthanum from Ames Laboratory, and Johnson Matthey (AESAR) aluminum (99.999% purity). The weighing of constituents required special attention due to the sensitivity of the crystal structure of CeAl₃ to small changes in the relative concentration of Ce and Al atoms. The synthesis of CeAl₃ alloys is always accompanied by the formation of a large amount of the secondary phases CeAl₂ and Ce₃Al₁₁. The presence of these unwanted phases is substantially reduced by proper annealing conditions.

The cerium-aluminum phase diagram has been studied by several groups [91], its latest addition being CeAl₃ [62]. It contains four other compounds: Ce₃Al₁₁, CeAl₂, CeAl, and Ce₃Al (see Fig. 5.1). Both CeAl₂ and Ce₃Al form directly from the liquid solution, CeAl and Ce₃Al₁₁ form peritectically, and CeAl₃ forms peritectoidally at 1135°C. A peritectic reaction is one in which the compound

melts incongruently [115], that is, the composition of the liquid just above the melting point has a different composition than the solid before melting. Only part of the solid forms a liquid solution, with the remaining part forming crystallites floating around in the liquid. As the temperature reaches the melting point, the mixture solidifies into a single phase. The peritectoid reaction in CeAl₃ is similar to a peritectic reaction, except that the compound does not melt into a liquid-crystallite mixture. Rather, it separates into a solid phase mixture of CeAl₂ and β -Ce₃Al₁₁, which in turn melts into CeAl₂ crystallites embedded in a liquid solution matrix.

The transformation of a mixture of Ce-Al neighboring phases into the CeAl₃ phase upon cooling has a marked effect on the way samples crystallize. The presence of secondary phases is the cause of many sample dependences of thermodynamic and transport measurements. Polycrystals synthesized by arc melting consist of a mixture of CeAl₃ with large amounts of CeAl₂ and Ce₃Al₁₁. Annealing has been found to reduce the proportion of secondary phases to the point of becoming undetectable by conventional x-ray diffraction methods. Magnetic susceptibility measurements on annealed samples are an efficient way of detecting the above second phases, since CeAl₂ is antiferromagnetic below 3.8 K, and Ce₃Al₁₁ is ferromagnetic with transitions at 3.2 and 6.2 K [116]. Specific heat data has also been used successfully by some groups to detect irregularities at these temperatures.

Alloys of CePb₃

Lanthanum-doped CePb₃ alloys were made using Ames Laboratory Ce and La, and Johnson Matthey Pb with 99.9999% purity. Special care was also taken in the making of both CePb₃ and Ce_{0.6}La_{0.4}Pb₃ due to the large vapor pressure of lead. Therefore, Ce should be melted first, then Pb. Unfortunately, this procedure was not enough to significantly reduce Pb mass loss due to vapor pressure at

0.5 atm of Ar gas. In order to compensate for this mass loss, an additional 3% of the calculated mass for Pb was added to the constituents before the first melt. The mass loss for each bead after melting was mostly due to lead, usually around 3%. The sample was remelted in case the mass loss was less than the extra amount of Pb. Correspondingly, more Pb was added in the event that the mass loss was greater than expected. After melting the sample, the stoichiometry was verified by recalculating the atomic percentages based on the final mass of the sample. CePb₃-based alloys are generally free of any secondary phases except pure Pb, which can precipitate in the surface as the alloys react with air. As a result, the samples were kept in a vacuum container along with Drierite acting as a moisture absorber.

5.1.2 Annealing

Annealing helps relieve stresses inside the samples not removed during crystallization. It also reduces the amount of unwanted secondary phases in the final melt. Typical annealing temperatures range between 2/3 and 3/4 of the melting point of the alloy.

The final beads were broken into smaller pieces using a ceramic mortar instead of a metal crusher to avoid the presence of iron impurities in the samples. Part of each original bead was wrapped in a clean tantalum foil and placed inside a quartz tube. The tubes were pumped and flushed with Ar gas several times. Right before sealing, the Ar pressure inside was reduced to 100 mtorr. The quartz tubes were then placed inside a Lindberg furnace and annealed according to a previously tested prescription. Alloys of Ce_{1-x}La_xAl₃ were annealed at 830°C for two weeks, while those of Ce_{1-x}Y_xAl₃ were annealed at 800°C for two weeks, then 850°C for five days. Both CePb₃ and Ce_{0.6}La_{0.4}Pb₃ were annealed at 800°C for one week. In all cases, annealing started with the furnace already at annealing temperature. At

the end of the prescribed annealing period, the samples were immediately removed from the furnace and left to cool down at ambient temperature.

5.2 Diffraction of X-Rays

Measurements of x-ray diffraction were used as a means to verify whether the arc melting and annealing processes led to the formation of the desired crystal structure. From the diffraction pattern, it was also possible to determine the lattice parameters and the presence of secondary phases in the sample. The principle behind the diffraction of x-rays in crystals is based on Bragg's Law:

$$\lambda = 2d \sin \theta, \quad (5.1)$$

which for a first order ($n = 1$) spectrum relates the known Cu K_{α} wavelength to the diffraction angle θ and the distance between lattice planes d . The lattice constants are then calculated from d and the intersection points of the lattice planes for the desired space group number, given in terms of the Miller indices $(h k l)$.

The experimental setup consisted of a Phillips APD 3720 diffractometer, an x-ray source with a water-cooled power supply, and a computer for data acquisition. The APD 3720 consists primarily of x-ray beam slits, the sample holder, and an electronic counter. Both the counter and the sample holder rotate about a horizontal axis so that the angle of rotation of the counter is always twice that of the holder. This latter angle corresponds to the angle of incidence/reflection from the sample plane θ . The x-ray beam is of known wavelength: a Cu K_{α} line with $\lambda = 1.540562 \text{ \AA}$.

Powder samples were ground out of annealed pieces from the original beads using a ceramic mortar. About 1 cm^2 of powder was then glued to a glass slide using a 7:1 amyl acetate – collodion mixture. With the slide in place, the diffractometer power supply was set to 40 kV and 20 mA. The detector angular speed was set

to $6^\circ/\text{min}$, and its range to $5^\circ \leq 2\theta \leq 120^\circ$. The counting rate was set to 1000 counts/sec. All measurements were performed at room temperature.

The angular positions of the resulting intensities were compared to the theoretical positions and reflection indices obtained from a structure-generating software. This procedure allows for identification of secondary-phase intensity lines larger than the background intensity ($\sim 5\%$ of maximum intensity line). For a cubic system (i. e. CePb₃ alloys), the indices for primary-phase lines are obtained from the following equation [117]:

$$\sin^2 \theta = \frac{\lambda^2}{4a^2} (h^2 + k^2 + l^2). \quad (5.2)$$

Similarly, for a hexagonal system (CeAl₃ alloys),

$$\sin^2 \theta = \frac{\lambda^2}{4} \left[\frac{4}{3} \cdot \frac{(h^2 + k^2 + l^2)}{a^2} + \frac{l^2}{c^2} \right]. \quad (5.3)$$

The indices $(h k l)$ and the angles 2θ for the highest and narrowest intensity lines were entered as data points into a least-squares fitting program, along with the wavelength and structure type. The room-temperature lattice parameters and their uncertainties were then obtained from a least-squares fit using one of the above two equations, depending on the structure type of the sample.

5.3 Magnetic Measurements

All magnetization and magnetic susceptibility measurements were conducted using a Quantum Design Magnetic Property Measurement System (MPMS) SQUID magnetometer. The apparatus consisted of a liquid He dewar, the sample probe assembly, the electronic console with temperature and gas controllers, the He gas handling system, and a Hewlett Packard computer. The probe assembly is inserted inside the dewar; it contains the sample space, thermometers, the sample heater, an impedance controlling He flow, a superconducting magnet producing fields up to 5.5 T, and the sample transport mechanism. The temperature is regulated by the flow of He gas through the sample space and by the sample heater. Below

approximately 4.2 K, the liquid-helium vapor inside a pot is pumped in order to reach temperatures down to 2 K.

The technique used for magnetization measurements on the MPMS detects the change in flux induced by the sample under an applied field using a superconducting quantum interference device (SQUID) amplifier. The sample is first enclosed in a 0.5 cm-long plastic straw segment, which is slid into a drinking straw at the end of the support tube, serving as the sample holder. During each measurement, the sample is moved upward along the axis of a series of pick-up coils connected to the SQUID. The SQUID voltage is read at different position intervals across the scan length. This voltage is proportional to the change in flux detected by the coils, which in turn is proportional to the magnetization of the sample. The accuracy of magnetization measurements is generally around 3%, while the precision at a fixed temperature can be as low as 0.01%.

Magnetization curves as a function of magnetic field can also be obtained by measuring at the lowest temperature (2 K) and measuring at each field, sweeping the field from 0 to 5 T. The magnetization (in emu/mol) is obtained by multiplying the signal by the molecular weight of the sample and dividing by its mass. The magnetic susceptibility $\chi = M/H$ (in memu/mol) is calculated from the signal measured at a fixed field (typically 1 kG), multiplied by the molecular weight of the alloy, and divided by its mass and the applied field. Each measurement sequence is fully automated, and uses a version of the MPMS software from Quantum Design. The convention used for units of magnetization and magnetic susceptibility in this dissertation follows from the literature on heavy-fermion systems (e.g., Refs. [5] and [6]).

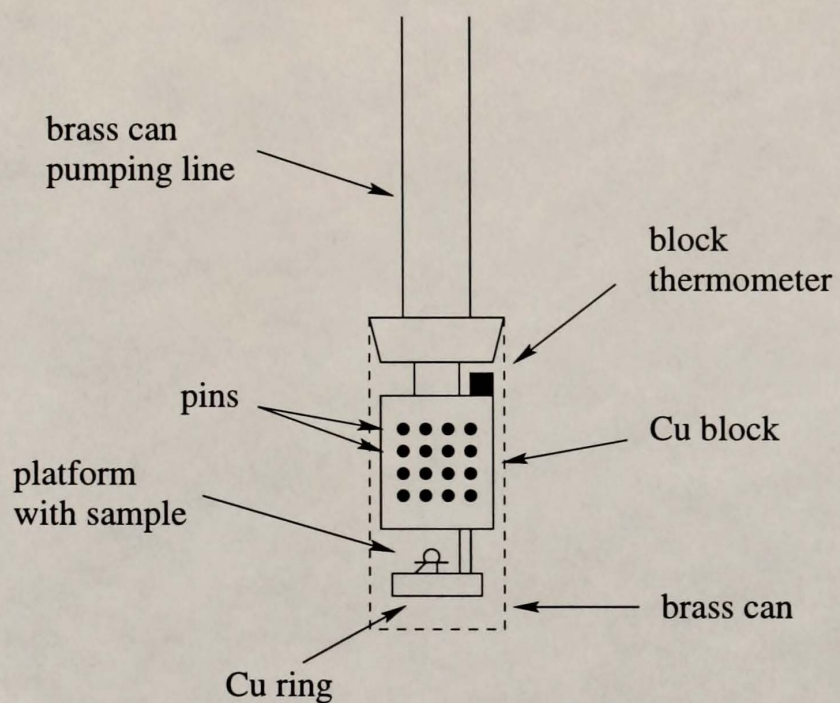


Figure 5.2: View of the cryostat used for zero-field specific heat measurements between 1 and 10 K.

5.4 Specific Heat Measurements

This section will discuss the necessary cryogenic and electrical equipment to measure specific heat of small samples (< 100 mg) with large heat capacity, and the thermal relaxation method [118, 119, 120] used for this purpose.

5.4.1 Equipment

Electronic

The experimental setup for the measurement of specific heat in both zero and magnetic fields by the thermal relaxation method consisted of three cryostats, a liquid-He dewar, two Keithley 220 and a Keithley 224 programmable current sources, a Keithley 195A, 196 digital multimeter for thermometer voltage measurements, an EG&G Model 124A lock-in amplifier for platform thermometer current detection, a variable decade resistor and a resistance box with three internal resistances. The resistance box is connected to the decade resistor in a Wheatstone bridge configuration. A more detailed explanation of the equipment is provided elsewhere [118, 119, 120, 121]. A Dell PC was used for data acquisition and analysis. The computer was interfaced to the digital equipment using an AT-TNT Plug and Play GPIB board from National Instruments. A 12-bit resolution Keithley Metrabyte DAS-1402 A/D converter board interfaced the PC to the lock-in amplifier. The data acquisition was monitored using two PC-based programs for thermal conductance and specific heat measurements, respectively. The software was designed by the author using LabVIEWTM version 5.1 for Windows 95/98.

Cryogenic

The cryostats used for zero-field measurements are illustrated in Figs. 5.2 and 5.3. Figure 5.2 shows the probe used in the temperature range 1-10 K. The electrical connections are enclosed by a brass can attached to a taper joint by pumping on the enclosure. The cooldown procedure consisted of precooling in

liquid nitrogen for about 15 to 60 minutes, insertion into a dewar, and subsequent transfer of liquid He into the dewar, which reduces the temperature to 4.2 K. A temperature of 1 K was achieved by pumping the He vapor out of the dewar/probe assembly for about an hour.

Measurements in the range 0.4-2 K were conducted using the cryostat described in Fig. 5.3. After reaching a temperature of 4.2 K following the procedure above, the ^4He pot was filled with liquid He from the bath by opening the needle valve, and ^3He gas was transferred into the ^3He pot. The needle valve was then closed, and the ^4He pot was pumped out to reach a temperature between 1 and 2 K. Although this temperature can be sustained for many hours, the ^4He pot can be easily refilled if necessary. In order to reach a temperature of 0.4 K, the following method was used. A Cu container full of activated charcoal resides at the lower end of a rod inside the ^3He -gas enclosure. At 1 K, the ^3He gas condenses inside. As the charcoal container is lowered towards the ^3He pot, the condensed ^3He is attracted to the charcoal, which acts as an adsorption pump. Temperatures below 1 K could be achieved in 20 minutes and sustained up to several hours with this technique. Once the charcoal saturates with ^3He , it was warmed up to release the gas and the above process was repeated.

Specific heat measurements in magnetic field were conducted in a specially-designed dewar from Cryogenic Consultants Limited (CCL). The additional electronic equipment consisted of a GenRad 1689M RLC DigiBridge, used to measure the capacitance of a thermometer used above 1 K, a CCL superconducting magnet and a magnet power supply. The magnet is made of two inner coil sections of niobium-tin wire and two outer coil sections of niobium-titanium wire. The cryostat used below 1 K is the same as in Fig. 5.3, and the one used between 1-10 K is illustrated in Fig. 5.4. The main difference between them is the lack of a ^3He enclosure for the higher-temperature probe.

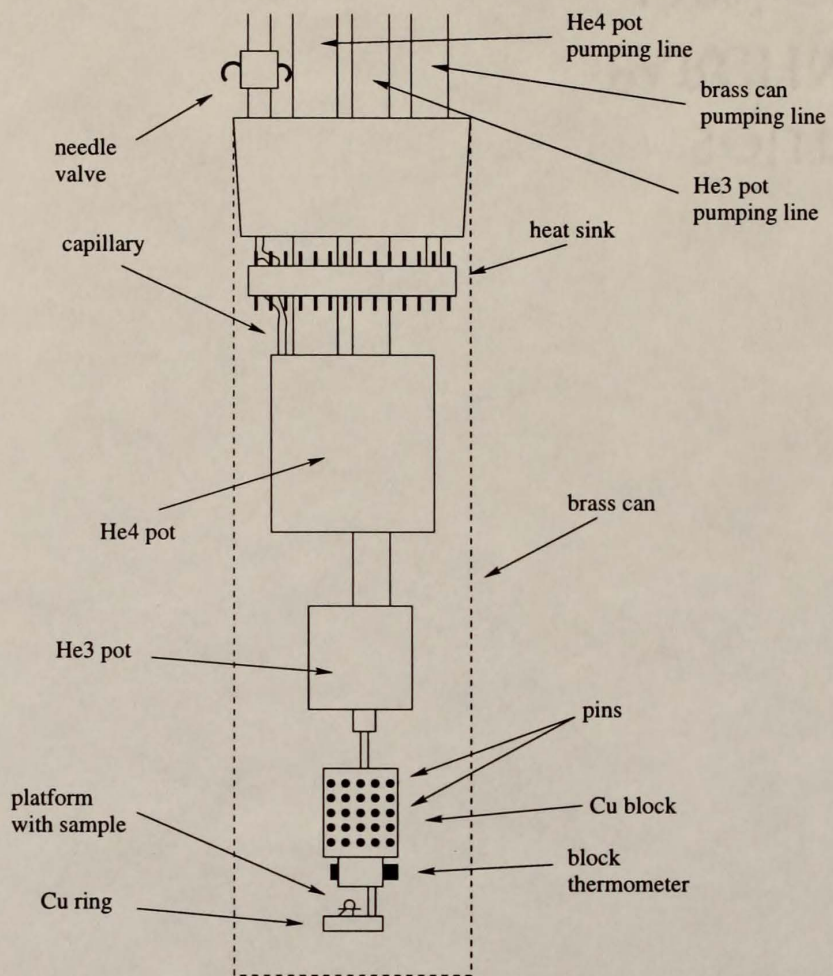


Figure 5.3: View of the ${}^3\text{He}$ inner pot cryostat used in both zero and magnetic field specific heat measurements between 0.4 and 2 K.

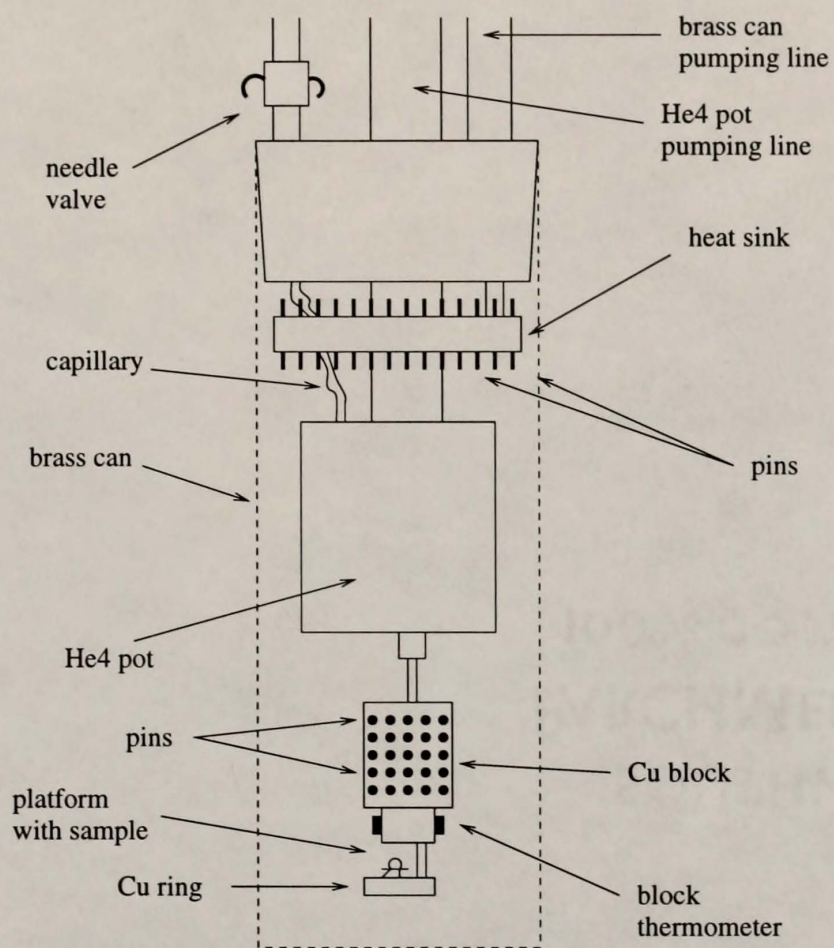


Figure 5.4: View of the ^4He inner pot cryostat used for specific heat measurements in magnetic fields at temperatures between 2 and 10 K.

All cryostats have a similar electronic design. They are equipped with radiation shields from top to bottom, and the wires are coupled to the He bath by a heat sink, as shown in Figs. 5.3, and 5.4. Additional wires are soldered from the heat sink to the Cu block, and wrapped around the ^4He pot to ensure thermal equilibrium. The temperature of the block is regulated by a heater made of wrapped manganin wire. It is monitored by a Lake Shore calibrated Ge thermometer in the range 1-10 K, and by a Speer carbon resistor between 0.4 and 2 K. In magnetic fields, a Lake Shore capacitance thermometer was used above 1 K due to its negligible field dependence, and the Speer resistor was used from 0.4-2 K for its known magnetoresistance [122]. All thermometers are linked to the block using thermally-conductive Wakefield grease.

Sample Platform

The sample resides at the bottom of the cryostat, attached to a sapphire platform by Wakefield grease. A flat surface at the bottom of the sample is important in order to establish optimum thermal contact between platform and sample. The platform is thermally linked to a copper ring, as shown in Fig. 5.5. Two types of platforms were used in this study. Each platform has four wires soldered to silver pads attached to the ring by thermally-conductive Styrocast. The two pairs of wires are connected to the platform heater and thermometer, respectively, using EpoTek H31LV silver epoxy. The platform heater is an evaporated layer of 7%Ti-Cr alloy. For measurements between 1-10 K, the platform thermometer used was an elongated piece of doped Ge, and the platform wires were made of a Au-7%Cu alloy. A thin piece of Speer carbon resistor and Pt-10%Rh platform wires were used for measurements between 0.4 and 2 K.

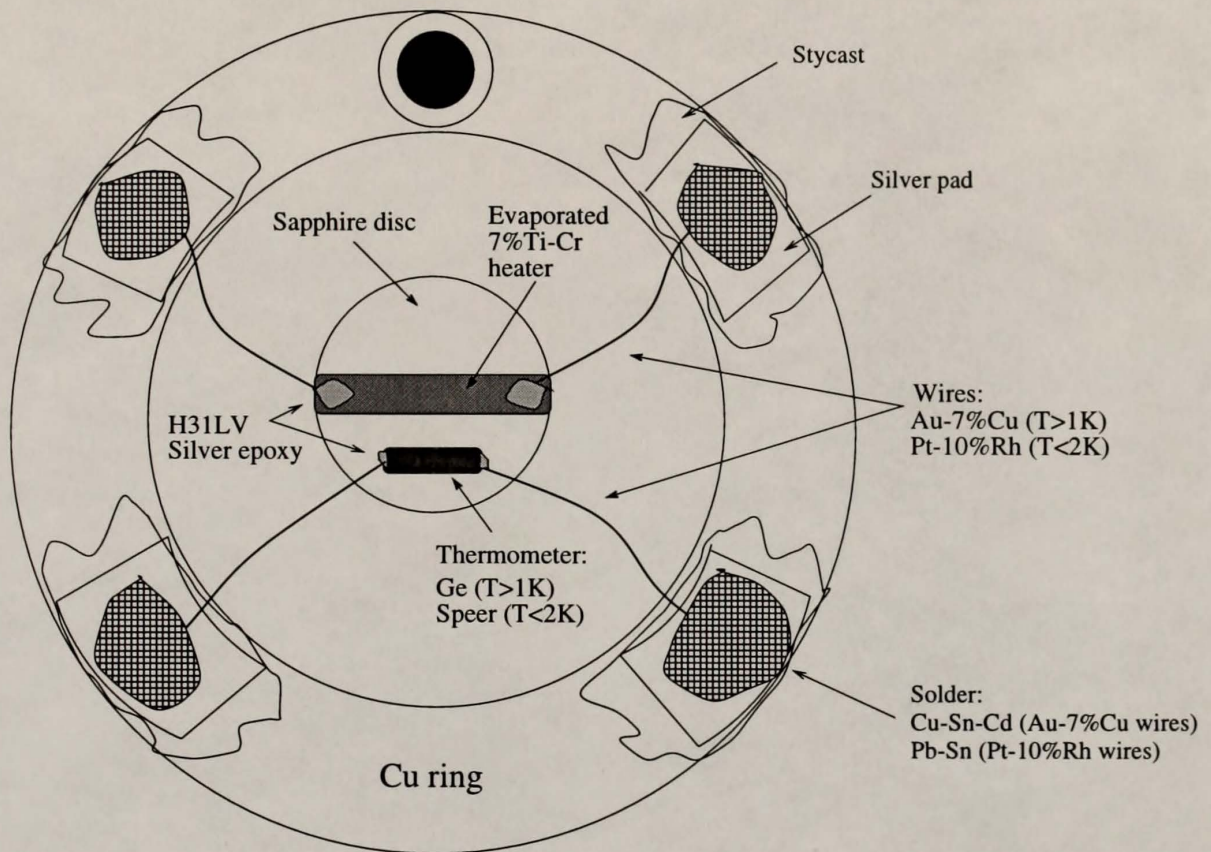


Figure 5.5: Top view of the sample-platform/Cu-ring assembly at the bottom of the cryostat.

5.4.2 Thermal Relaxation Method

A thermal relaxation technique consists of calculating the time constant of the temperature decay of the sample linked to a heat bath by a small thermal resistance [118, 119, 120]. The electrical analog of the system is that of an RC circuit, where the time constant is proportional to the capacitance. When heat is applied to the platform-sample system by means of a small current (in μA), the temperature increases from a base value T_0 by an amount ΔT . When the current is turned off, the system temperature $T(t)$ decays exponentially to T_0 :

$$T(t) = T_0 + \Delta T e^{-t/\tau_1}. \quad (5.4)$$

The time constant τ_1 is proportional to the total heat capacity (sample plus platform) C_{total} :

$$\tau_1 = \frac{C_{\text{total}}}{\kappa}, \quad (5.5)$$

where κ is the thermal conductance of the wires linking both platform and sample at $T = T_0 + \Delta T$, and the Cu ring at $T = T_0$. The time constant was obtained by measuring the time decay of the off-null voltage signal from a Wheatstone bridge using a lock-in amplifier. Two arms of the Wheatstone bridge consisted of a resistance box and the platform thermometer. By adjusting the resistance of the box it is possible to balance the bridge and obtain the platform thermometer resistance. The platform temperature is extracted from a previous calibration of the platform thermometer. The accuracy of the time constant measurement in the temperature range 0.4-10 K is 1-3%. The thermal conductance is given by

$$\kappa = \frac{P}{\Delta T}. \quad (5.6)$$

Here, $P = IV$ is the power applied to the platform heater. The above equations are valid under the assumption of an ideal thermal contact ($\kappa_{\text{sample}} \sim \infty$) between sample and platform. In the event of a poor thermal contact between the sample

and the sapphire ($\kappa_{\text{sample}} \sim \kappa$) the temperature decay can generally be described as the sum of two exponentials

$$T(t) = T_0 + Ae^{-t/\tau_1} + Be^{-t/\tau_2}, \quad (5.7)$$

where A and B are measurement parameters and τ_2 is the time constant between sample and platform temperatures. The total heat capacity can be calculated from τ_1 , τ_2 , and κ . The thermal conductance is measured separately by applying a current to the platform heater, calculating the power $P = IV$, and calculating ΔT as a result of the power applied to the heater. The accuracy of this measurement between 0.4-10 K is $\pm 5\%$. The sample heat capacity is calculated by subtracting the heat capacity of the addenda (sapphire platform, wires, silver epoxy, platform thermometer, and thermal grease) from the total heat capacity. Finally, the specific heat is obtained by multiplying by the molecular weight and dividing by the sample mass.

5.5 Experimental Probes

In order to accomplish the objectives discussed in the previous chapter, two mechanisms for the study of thermodynamic properties were used in this dissertation: alloying and magnetic fields. Alloying is a powerful tool that allows for changes in the electronic structure, the lattice constants, and the properties of a system. Magnetic fields allow to probe the energy scales relevant to heavy-fermion systems at low temperatures and test their thermodynamic properties against theoretical predictions.

The two main types of doping on heavy-fermion compounds are Kondo-hole and ligand-site doping. The first one consists of replacing the magnetic ion by a nonmagnetic counterpart (e.g., La or Y instead of Ce). In this method, there is a reduction of the number of magnetic moments in the sample and some disorder in their electronic environment. In addition, the lattice structure changes significantly

due to an atomic size difference between the *f* ion and the dopant ion. Doping with La usually leads to a lattice volume expansion, while Y substitution corresponds to the application of a positive chemical pressure. Ligand-site doping consists of substituting the ligand atoms of one species by another. The main effect here is a dramatic change in the electronic environment of the magnetic ions, changing the value of the local exchange constants. Maximum atomic disorder is introduced using this method, which could complicate the analysis of properties. It is of current interest to investigate the extent to which each method of doping affects the electronic properties.

The measurement of thermodynamic properties as a function of applied magnetic field is an important, though not often implemented tool in the study of heavy fermions. The relevant energy scales, both single-site and cooperative, are small enough that magnetic fields easily accessible in a laboratory can help determine their overall magnitude and their role in determining physical properties. The magnetic behavior of heavy-fermion compounds ranges from short-range correlations to non-Fermi-liquid behavior to long-range antiferromagnetic order. Magnetic fields are useful in understanding the different types of magnetic behavior through a comparative study of changes in the density of states, the entropy, the specific heat, and the magnetic characteristic temperature. Various theoretical models, including the single-impurity Kondo description, have different predictions for the magnetic field response of thermodynamic properties. Therefore, the use of magnetic fields as an external parameter is a convenient way of testing the applicability of these models. Specific heat measurements in magnetic field on CePb₃ and CeAl₃ alloys will be presented in this dissertation in order to study the trends followed by parameters relevant to both Kondo and magnetic degrees of freedom in these systems.

5.5.1 Experiments on CeAl₃

A doping study of the lattice parameters, specific heat, and magnetic susceptibility of Ce_{1-x}M_xAl₃ alloys has been conducted, with M = La concentrations 0 ≤ x ≤ 1, and M = Y concentrations 0 ≤ x ≤ 0.2. The evolution of the lattice parameters and their ratio c/a with La/Y concentration x was investigated to determine how the relative variation of a with respect to c and changes in the lattice volume are related to trends in the thermodynamic properties. In addition, the specific heat, the anomaly in C/T , the magnetic susceptibility, and the Wilson ratio expressed as χ/γ of Ce_{1-x}La_xAl₃ were studied over the whole concentration range to search for evidence for a magnetic origin of the anomaly in this system by comparing the concentration dependence of T_K and the temperature T_m of the anomaly in C/T , with their dependence on the parameter J based on Doniach's Kondo necklace model. The coupling J is proportional to the hybridization, which is expected to decrease with La concentration (expansion of the lattice).

The specific heat of Ce_{0.8}La_{0.2}Al₃ and Ce_{0.3}La_{0.7}Al₃ was measured in magnetic fields up to 14 T to compare to the predictions of the anisotropic Kondo model [15, 36, 37] and to search for clues regarding the magnetic character of the ground state in these alloys. The measured field dependence will allow to determine a connection between the maxima in C/T and those of the AKM. The specific heat data of Y-doped samples will be compared to data as a function of pressure for CeAl₃ to distinguish between the effects of chemical and hydrostatic pressure on the anomaly in C/T .

Additional Ce_{0.8}(La_{1-x}Y_x)_{0.2}Al₃ samples with $x = 0.09, 0.4$ were also prepared for specific heat and magnetic susceptibility studies. In this system, yttrium doping of Ce_{0.8}La_{0.2}Al₃ was conducted to create a similar hybridization environment to that of CeAl₃ by reducing the lattice volume to that of the undoped compound. Thermodynamic measurements will allow to test the magnetic inter-

pretation of the anomaly in C/T by assuming a constant coupling J , yet reducing T_{RKKY} by increasing the Ce-Ce distance with respect to CeAl₃.

5.5.2 Experiments on CePb₃

In CePb₃, the increase in the A coefficient of the electrical resistivity along (110) points to a possible enhancement of the heavy-fermion state in magnetic fields based on the proportionality between A and γ . A study of the specific heat of a CePb₃ polycrystal in magnetic fields will be presented in order to describe the changes of the Fermi-liquid parameters γ and A/γ^2 as a function of magnetic field. The phase diagram obtained from these measurements will be compared to previous magnetoresistance results along (110) to search for evidence of the field-induced transition detected by previous sound velocity and magnetoresistance measurements, and for possible non-Fermi-liquid effects. The data should be helpful in understanding the effects of a magnetic transition on the nature of the heavy-fermion state.

Results from measurements of the heat capacity of Ce_{0.6}La_{0.4}Pb₃ in magnetic fields up to 14 T will also be discussed in order to investigate further the single-impurity nature of the paramagnetic heavy-fermion state of CePb₃. The electronic contribution to the specific heat below 10 K will be compared to predictions for the $S = \frac{1}{2}$ single-impurity Kondo model in magnetic fields. The above measurements on CePb₃ and Ce_{0.6}La_{0.4}Pb₃ allow for an analysis of the electronic coefficient γ and the Kondo state in both nonmagnetic and magnetic heavy-fermion systems.

CHAPTER 6

STRUCTURAL AND THERMODYNAMIC PROPERTIES OF CeAl₃ ALLOYS

6.1 Lattice Parameter Study of CeAl₃ Alloys

Samples for x-ray diffraction were prepared according to the procedure described in the previous chapter. All data were taken at room temperature. The diffraction pattern for a CeAl₃ sample is shown in the upper half of Fig. 6.1. The data shown are normalized to the intensity of the largest peak (201) and compared to the calculated intensities for CeAl₃. The residuals are shown in the lower half of Fig. 6.1. The average background intensity per degree is about 5% of the maximum intensity, corresponding to the (201) peak. Both positive and negative values larger than 5% correspond to the subtraction of theoretical peaks from experimental data. A comparison between the residual plot and calculated intensities for the secondary phases CeAl₂ and Ce₃Al₁₁ was conducted in order to detect peaks associated with these phases. After a careful analysis, no diffraction lines from any of these two phases could be distinguished from the background data. As mentioned in section 5.2, this does not rule out the presence of a smaller (<5% of maximum intensity) amount of secondary phases, which could have an effect on other sample properties. The lattice parameters obtained from the diffraction pattern were $a = 6.543 \pm 0.003 \text{ \AA}$ and $c = 4.611 \pm 0.004 \text{ \AA}$, with a lattice volume $V = 170.97 \pm 0.16 \text{ \AA}^3$ and a c/a ratio of 0.7047 ± 0.0007 . All of these values are within one uncertainty of the original values published by Buschow *et al.* [62], and those of Corsépius *et al.* [61].

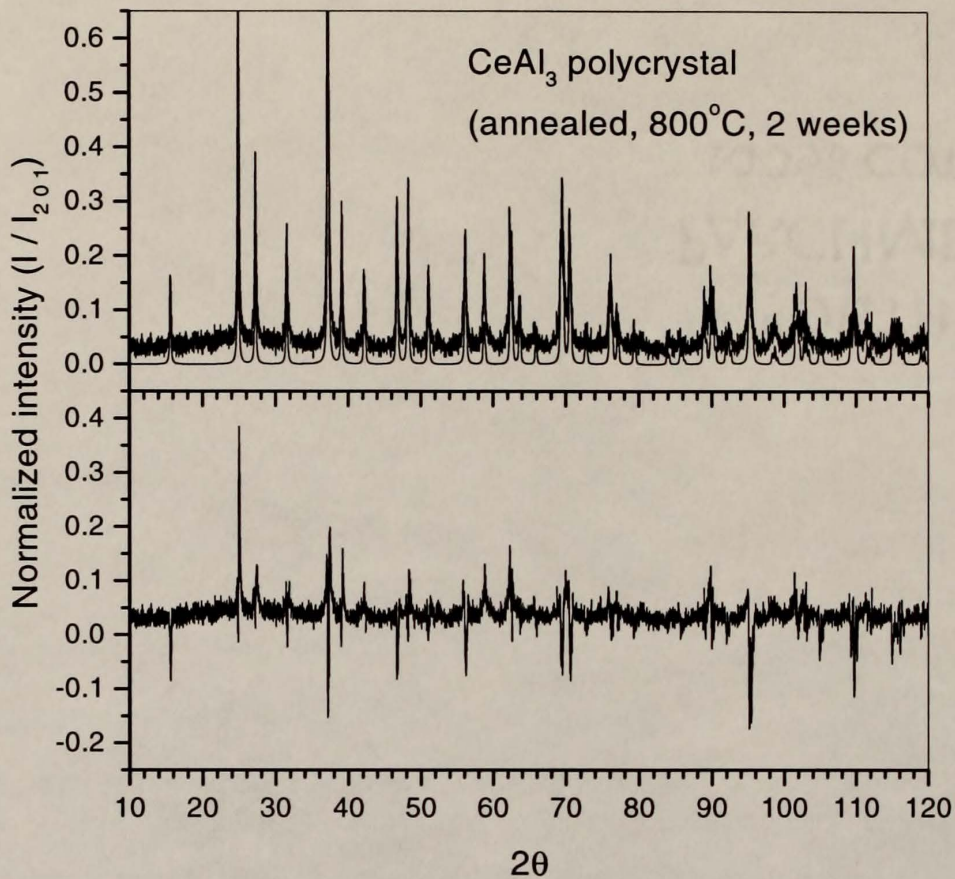


Figure 6.1: Diffraction pattern of an annealed CeAl₃ polycrystal (data taken at room temperature). Top: Experimental intensities of CeAl₃, along with the calculated intensities for a Ni₃Sn structure using the lattice parameters of Ref. [61]. The two largest intensities, around $2\theta = 25^\circ$ and 37° , correspond to (101) and (201) reflections, respectively. Bottom: Difference between calculated and experimental normalized intensities (see text).

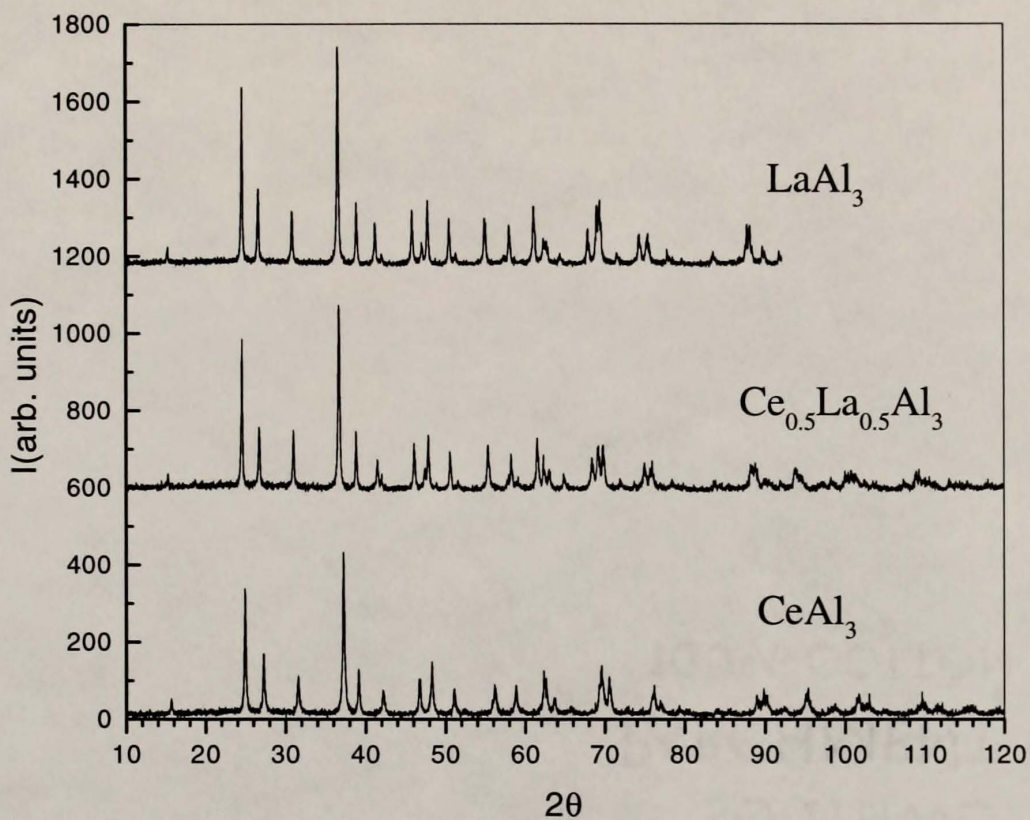


Figure 6.2: Room-temperature x-ray diffraction patterns for annealed $\text{Ce}_{1-x}\text{La}_x\text{Al}_3$ alloys ($x = 0, 0.5$, and 1).

6.1.1 Lanthanum Doping: $\text{Ce}_{1-x}\text{La}_x\text{Al}_3$

The chemical substitution of Ce by La atoms in the hexagonal Ni_3Sn structure is possible because of their similar electronic structure and atomic radii. Substitution of La for the smaller Ce atoms leads to a lattice expansion. Furthermore, the present study revealed that properly annealed $\text{Ce}_{1-x}\text{La}_x\text{Al}_3$ alloys crystallize in the Ni_3Sn structure across the entire concentration range ($0 \leq x \leq 1$). This result indicates that the Ce and La atoms are present in solid solution, and that no ternary phases were found. The x-ray diffraction patterns for $\text{Ce}_{1-x}\text{La}_x\text{Al}_3$ ($x = 0$, 0.5, and 1) are shown in Fig. 6.2. All three data sets exhibit the same pattern (hexagonal Ni_3Sn). The diffraction peaks shift to lower 2θ values with increasing La concentration. According to Bragg's Law, a shift to lower angles implies an increase of the interplane distance d , and also suggests an expansion of the lattice.

The lattice parameters for $\text{Ce}_{1-x}\text{La}_x\text{Al}_3$ are shown as a function of La concentration x in Fig. 6.3. The error bars for these and all other lattice parameter data were extracted from the least-squares fits to crystallographic reflections for each sample. The volume increase as a function of La doping is anisotropic. The a parameter increases with x , while c remains essentially constant. The a parameter experiences a larger increase (almost 10 times larger) than the c parameter. The increase in lattice volume V is therefore mostly due to the increase in a vs x . Figure 6.4 illustrates the linear dependence of V with La doping. Due to the larger rate of expansion of a , the c/a ratio decreases (by about 1.6%) between $x = 0$ and $x = 1$. This linear decrease as a function of x can be seen in Fig. 6.5. Thus, the effects of La doping on the Ce sites of the hexagonal structure of CeAl_3 are an expansion of the basal plane and a decrease in the c/a ratio. This ratio moves further away from the ideal close-packed ratio (0.816) due to a rapid increase in a with respect to c for $c/a < 1$. This anisotropic volume change could have a significant effect on the electronic environment of the Ce f ions and the exchange

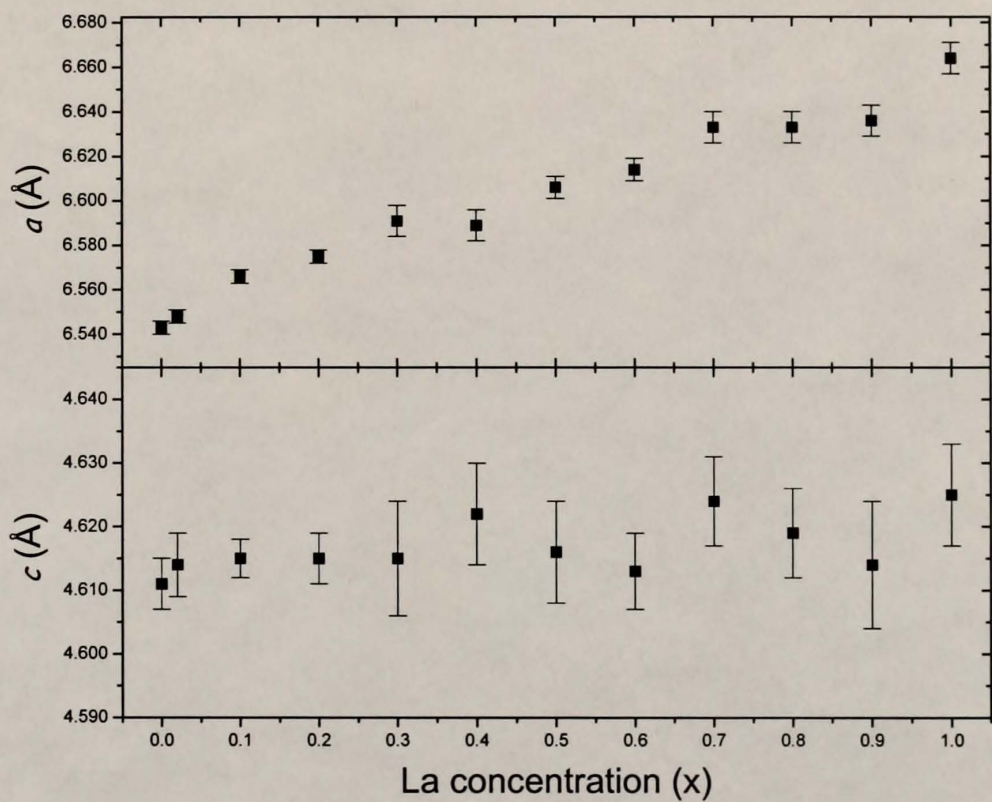


Figure 6.3: Lattice parameters a and c as a function of La concentration x for $\text{Ce}_{1-x}\text{La}_x\text{Al}_3$ ($0 \leq x \leq 1$).

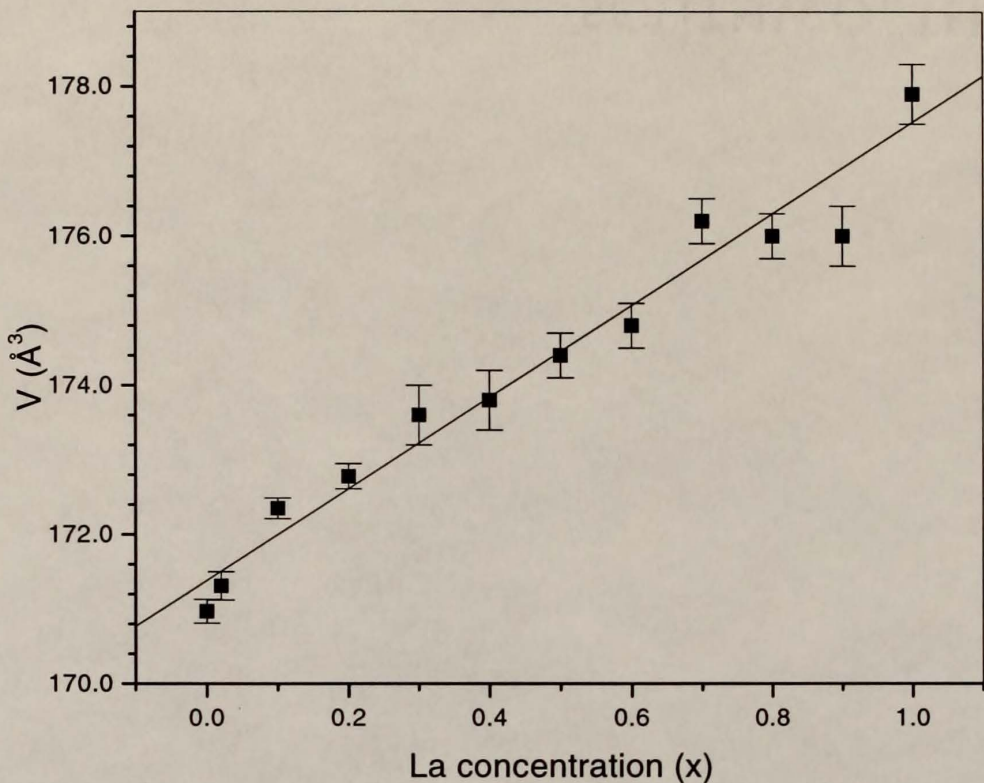


Figure 6.4: Lattice volume V as a function of La concentration x for $\text{Ce}_{1-x}\text{La}_x\text{Al}_3$ ($0 \leq x \leq 1$). The solid line is a least-squares fit to the data.

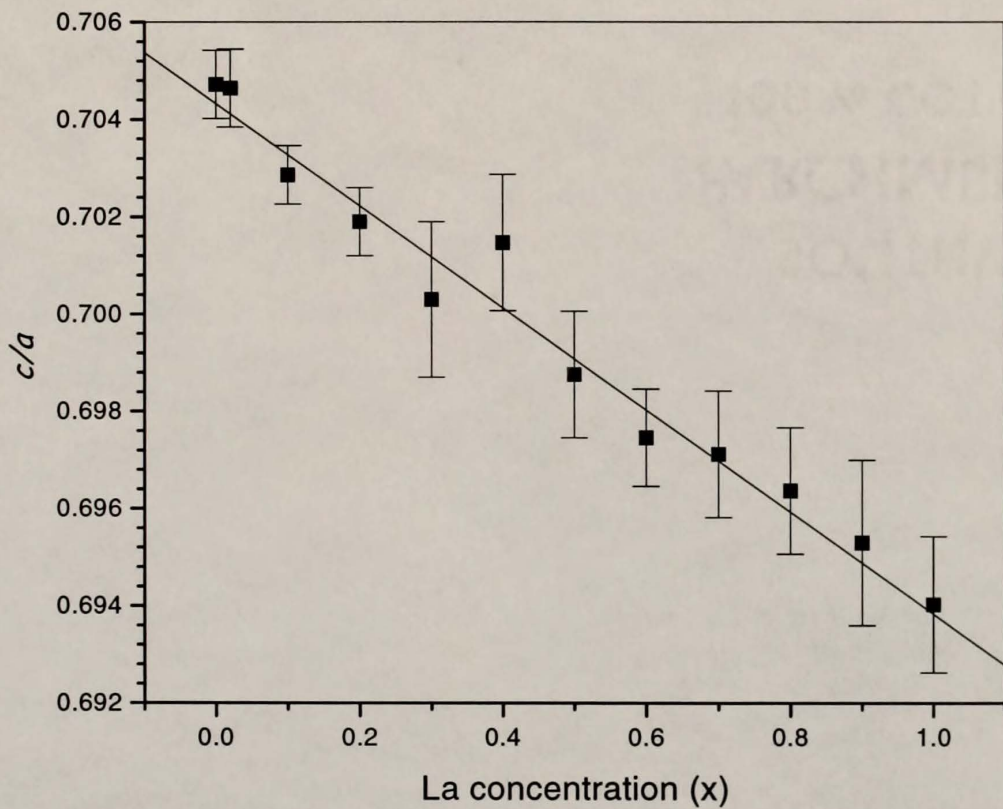


Figure 6.5: Ratio c/a as a function of La concentration x for $\text{Ce}_{1-x}\text{L}_{\text{a}}_x\text{Al}_3$ ($0 \leq x \leq 1$). The solid line is a least-squares fit to the data.

constants in the c axis and the hexagonal plane. In fact, it has been argued that in $\text{Ce}_{1-x}\text{La}_x\text{Al}_3$ alloys, the magnetic anisotropy due to a c/a ratio with $c < a$ leads to an anisotropic Kondo scenario [15, 36, 37]. This aspect will be discussed later in the chapter.

The above room-temperature lattice parameter data, especially the values of c/a , can be interpreted along with results for the low temperature properties of doped CeAl_3 alloys if both $a(x)$ and $c(x)$ show a small-enough temperature dependence. At the present time there are no published results on the temperature dependence of the lattice parameters for CeAl_3 . Nevertheless, the temperature dependence of the thermal expansion coefficient was measured by Kagayama and Oomi [123] on a polycrystalline sample down to 6 K. These values represent an average over all crystallographic directions. A rough estimate of the strain $\Delta l/l$ between 6 and 300 K, extracted by integrating the thermal expansion coefficient $\alpha(T)$ of Ref. [123], corresponds to a decrease of the order of 0.1% in the lattice parameters. This value is 3-4 times smaller than the average increase in volume caused by a change in La concentration equal to 0.1 (see Fig. 6.4). The increase in V is mostly due to the increase in a upon La doping (Fig. 6.3). Since the increase of a between $x = 0$ and $x = 1$ ($\sim 2\%$) is larger than the average decrease with temperature suggested by $\Delta l/l$ between 300 and 6 K, a change in the trends observed in Figs. 6.3, 6.4, and 6.5 is not expected at low temperatures.

6.1.2 Yttrium Doping: $\text{Ce}_{1-x}\text{Y}_x\text{Al}_3$

The substitution of Y for Ce atoms in the hexagonal Ni_3Sn structure of CeAl_3 induces a positive chemical lattice pressure due to the smaller atomic radius of Y. Doping studies with Y can be used along with pressure studies on pure CeAl_3 [124] to compare the effects of both methods on the lattice parameters a and c . Samples of YAl_3 have been reported to crystallize in the Ni_3Sn structure [125], which allows

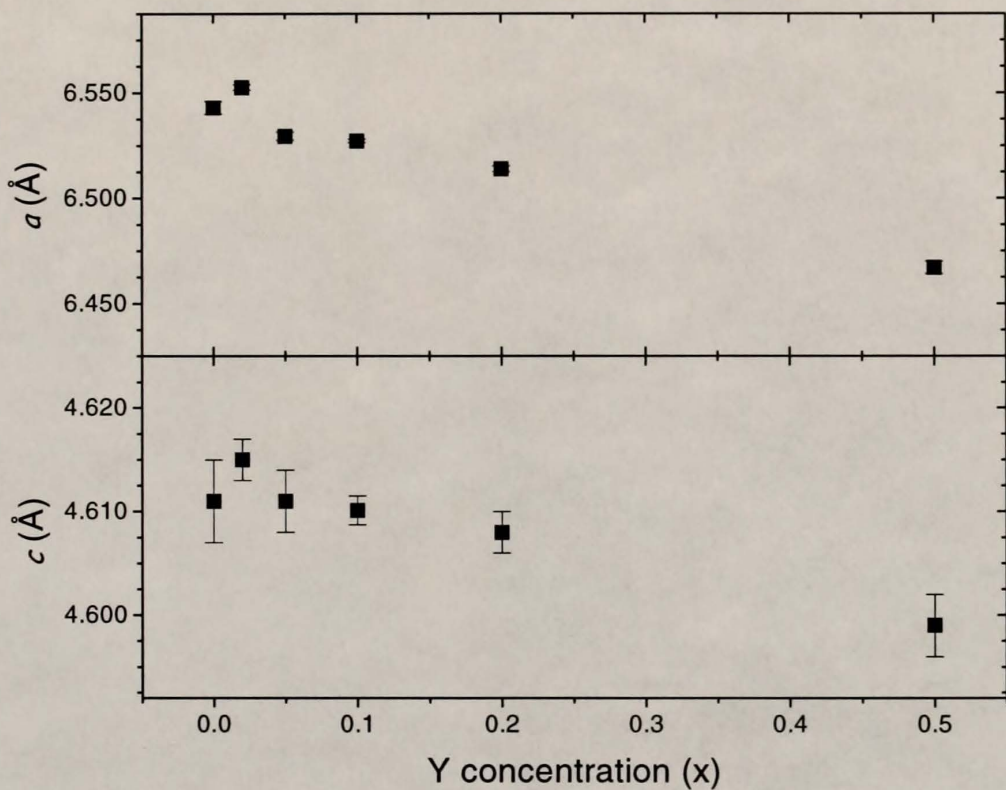


Figure 6.6: Lattice parameters a and c as a function of Y concentration x for $\text{Ce}_{1-x}\text{Y}_x\text{Al}_3$ alloys ($x = 0, 0.02, 0.05, 0.1, 0.2$, and 0.5). The $x = 0.5$ value was obtained from C. S. Jee and G. R. Stewart (unpublished).

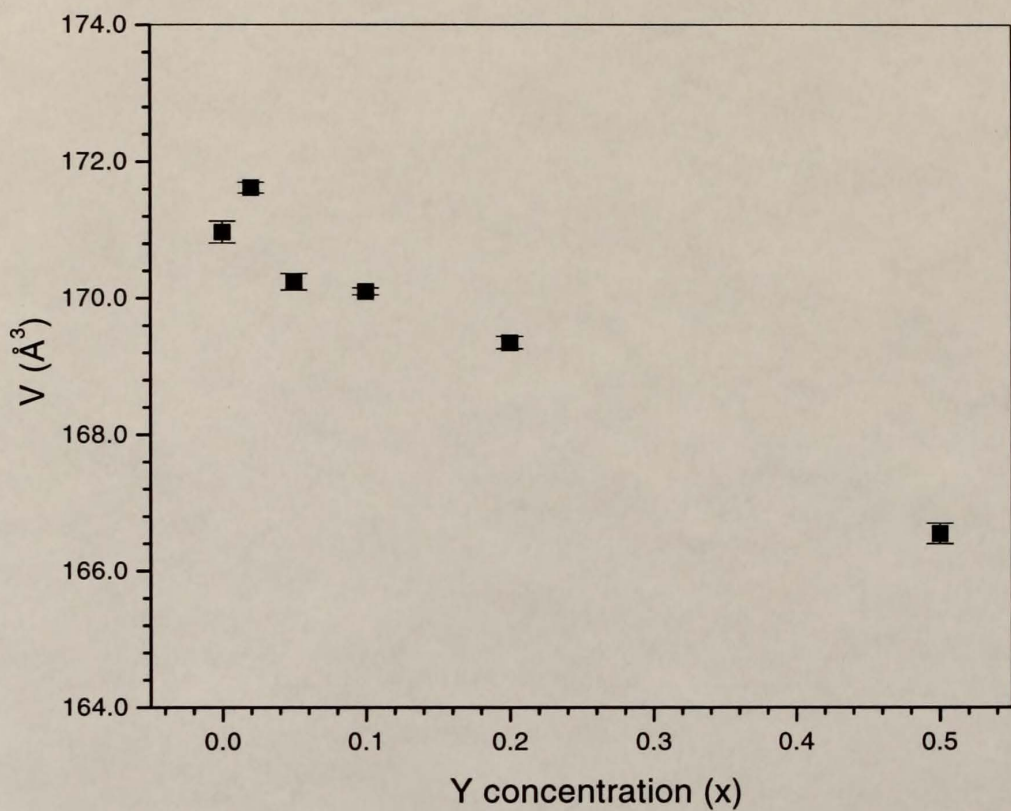


Figure 6.7: Lattice volume V as a function of Y concentration x for $\text{Ce}_{1-x}\text{Y}_x\text{Al}_3$ alloys ($x = 0, 0.02, 0.05, 0.1, 0.2$, and 0.5). The $x = 0.5$ value was obtained from C. S. Jee and G. R. Stewart (unpublished).

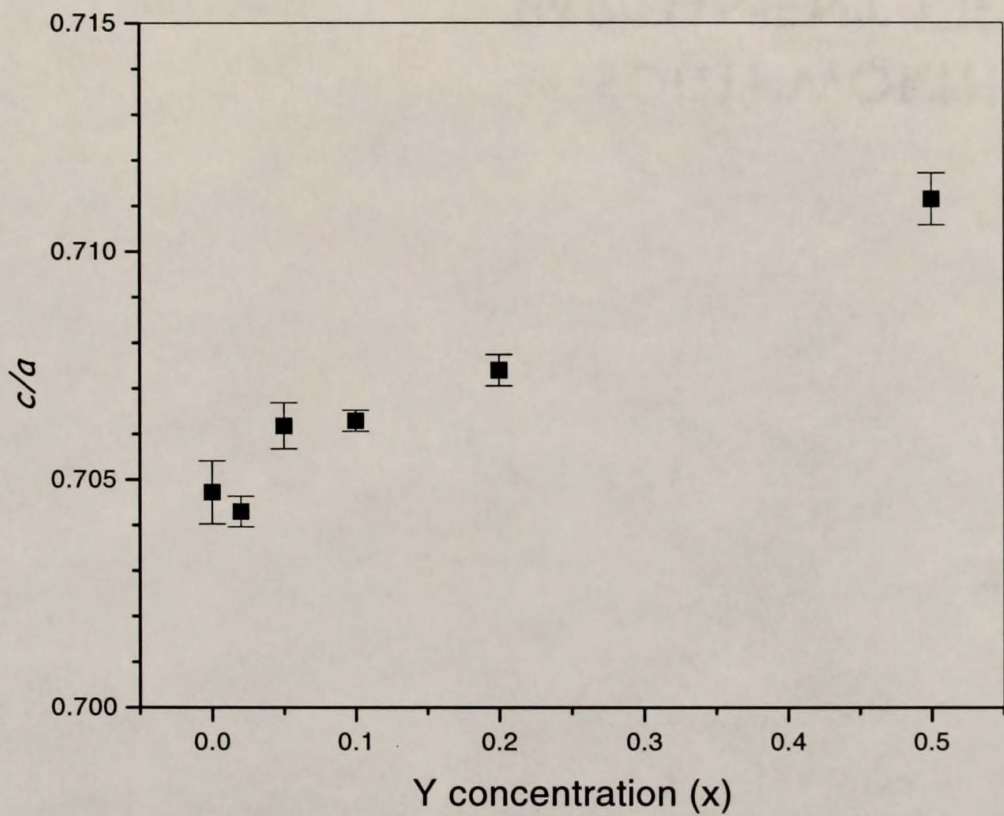


Figure 6.8: The ratio c/a as a function of Y concentration x for $\text{Ce}_{1-x}\text{Y}_x\text{Al}_3$ alloys ($x = 0, 0.02, 0.05, 0.1, 0.2$, and 0.5). The $x = 0.5$ value was obtained from C. S. Jee and G. R. Stewart (unpublished).

for the possibility of obtaining solid-solution $\text{Ce}_{1-x}\text{Y}_x\text{Al}_3$ alloys between $x = 0$ and $x = 1$.

However, YAl_3 undergoes a phase transformation to a rhombohedral, BaPb_3 type structure around 644°C [91]. Studies by D. M. Bailey [125] and R. L. Snyder [126] confirmed that the low-temperature hexagonal structure occurs in furnace-cooled needle-shaped crystals, and that attempts to obtain the Ni_3Sn structure from a bulk sample were unsuccessful, even after some annealing below the transformation temperature. Moreover, there have been reports of a third, cubic structure associated with this compound [62]. Due to the shortcomings in preparing pure YAl_3 , the annealing procedures for Y-rich $\text{Ce}_{1-x}\text{Y}_x\text{Al}_3$ alloys might prove to be fairly complex.

Diffraction patterns for Y concentrations up to $x = 0.1$ did not reveal the presence of secondary phases. On the other hand, patterns corresponding to $x = 0.2$ and particularly $x = 0.5$ (C. S. Jee and G. R. Stewart, unpublished) showed some broadening of Bragg peaks when compared to data from La doped samples for the same concentrations. In addition, these two concentrations revealed the presence of extra reflections of low intensity that could not be identified with either the hexagonal or rhombohedral variation of YAl_3 . These results point toward difficulties in obtaining single-phase hexagonal $\text{Ce}_{1-x}\text{Y}_x\text{Al}_3$ alloys for $x > 0.2$.

As Fig. 6.6 illustrates, a large decrease in both a and c was observed up to $x = 0.5$. A plot of lattice volume V vs x indicates the expected compression of the lattice with Y doping (see Fig. 6.7). There is a significant increase in the c/a ratio for the Y-doped samples, as a consequence of a larger compression rate in the basal plane (Fig. 6.8). This increase in c/a is much larger than the decrease observed with La doping. As a result, both Y and La studies have confirmed that the a parameter is the most sensitive to alloying on the Ce sites.

A comparison of the change in lattice parameters as a function of Y concentration with previous pressure studies on CeAl₃ lattice constants [124] seemed appropriate since doping with Y atoms contracts the lattice, therefore applying an effective chemical pressure on the alloy. It is also important because of a suggestion that the thermodynamic properties of these alloys, in particular the anomaly in C/T , are dependent on values of c/a , and therefore on the anisotropy of the exchange constants along the c axis and in the $a-b$ plane of the Ni₃Sn structure [61]. The difference between alloying and the application of hydrostatic pressure is influenced by the degree of disorder, the changes in the electronic structure, and the reduction in the number of Ce f ions introduced by alloying. Kagayama and Oomi [124] found an anisotropic change in a and c in their high-pressure lattice constant measurements of CeAl₃. At 17 GPa, the lattice volume change V/V_0 with respect to the pure compound corresponded to a 20% decrease, and the ratios a/a_0 and c/c_0 were 9% and 4%, respectively. The c/a ratio increased with applied pressure by as much as 5% at 17 GPa. No pressure-induced transitions were observed.

Kagayama and Oomi established a relation between pressure and lattice volume change from a least-squares fit of their data to a first-order Murnaghan's equation of state [124]:

$$P_V = \left(\frac{B_0}{B'_0} \right) \left[\left(\frac{V_0}{V} \right)^{B'_0} - 1 \right], \quad (6.1)$$

where B_0 is the bulk modulus at ambient pressure, and B'_0 its rate of change with pressure,

$$\begin{aligned} B_0 &= -\frac{\partial P}{\partial \ln V} \Big|_{P=0}, \\ B'_0 &= -\frac{\partial B}{\partial P} \Big|_{P=0} - 1. \end{aligned} \quad (6.2)$$

Table 6.1: Fractional changes (in %) in the lattice parameters, the change in c/a , and their corresponding chemical pressures (in GPa) P_V , P_a , P_c , and $P_{c/a}$ for Y concentrations $x = 0.02, 0.05, 0.1, 0.2$, and 1 (see text for details). The $x = 0.5$ and $x = 1$ values were obtained from C. S. Jee and G. R. Stewart (unpublished) and Van Vucht *et al.* [62], respectively. The pressure data correspond to lattice-parameter changes at room temperature.

Y x	V/V_0	a/a_0	c/c_0	c/a	P_V	P_a	P_c	$P_{c/a}$
0.02	0.0016	0.015	0.01	0.705(0)	8.58×10^{-4}	0.02	0.03	0.32
0.05	0.16	0.085	0.026	0.705(4)	0.09	0.11	0.08	0.45
0.1	0.44	0.208	0.052	0.706	0.24	0.27	0.16	0.69
0.2	1.06	0.482	0.108	0.708	0.58	0.64	0.34	1.22
0.5	3.5	1.55	0.3	0.714	2.01	2.14	0.97	3.46
1.0	8.9	4.0	0.7	0.730	5.58	6.08	2.35	10.13

This treatment was extended heuristically to find similar relations between pressure and the lattice constants a and c . The data for a/a_0 and c/c_0 as a function of pressure are in good agreement with the following equations [124]:

$$\begin{aligned} P_a &= \left(\frac{B_{a0}}{B'_{a0}} \right) \left[\left(\frac{a_0^3}{a^3} \right)^{B'_{a0}} - 1 \right], \\ P_c &= \left(\frac{B_{c0}}{B'_{c0}} \right) \left[\left(\frac{c_0^3}{c^3} \right)^{B'_{c0}} - 1 \right], \end{aligned} \quad (6.3)$$

where

$$\begin{aligned} B_{i0} &= -\frac{\partial P}{\partial \ln i} \Big|_{P=0}, \\ B'_{i0} &= -\frac{\partial B_i}{\partial P} \Big|_{P=0} - \frac{1}{3}, \end{aligned} \quad (6.4)$$

the index i corresponding to either a or c . The c/a ratio was fitted to the following equation, in fair agreement with the data:

$$\frac{c}{a} = \left(\frac{c_0}{a_0} \right) \left(\frac{V_0}{V} \right)^\gamma, \quad (6.5)$$

where $\gamma = 0.24$.

A relation between pressure and Y concentration (corresponding to chemical pressure) was obtained in this dissertation combining the above results with the concentration dependence of the lattice parameters. First, the fractional changes V/V_0 , a/a_0 , c/c_0 with respect to published values for CeAl₃ [61], and the c/a ratio were plotted for Y concentrations between $x = 0$ and pure YAl₃ (VanVucht *et al.* [62]). The data were fitted to a square polynomial to determine an approximate concentration dependence over the range $0 \leq x \leq 1$. The following equations were obtained:

$$\begin{aligned} V/V_0 &= 1.00 - 0.05x - 0.04x^2, \\ a/a_0 &= 1.00 - 0.02x - 0.02x^2, \\ c/c_0 &= 1.000 - 0.005x - 0.002x^2, \\ c/a &= 0.705 + 0.012x + 0.013x^2. \end{aligned} \quad (6.6)$$

A square polynomial, rather than a linear fit, was used because the increase in c/a as a function of doping does not imply an isotropic lattice volume change, described by Vegard's Law, and characteristic of cubic alloys. When compared to data for YAl₃ ($x = 1$), the results for $x \leq 0.2$ follow a different slope with respect to values for CeAl₃ ($x = 0$).

The above equations allow for a consistent determination of the fractional changes in V , a , and c and the change in c/a with x . Values from the fit were substituted into their respective Murnaghan equations above to determine a chemical pressure associated with the fractional change for a given Y concentration. In this manner, each concentration is associated with a change in volume V/V_0 , and a corresponding chemical pressure P_V . The same argument applies to all other parameters. The fractional changes in the lattice parameters for all concentrations investigated, along with their associated chemical pressures are given in Table 6.1. The most striking fact is that Y doping induces a much smaller chemical pressure along the c -axis than along the hexagonal plane, compared to the application of

hydrostatic pressure. Therefore, the anisotropic character of the change in lattice parameters is stronger as a function of Y concentration than as a function of pressure. A pressure – concentration diagram is illustrated in Fig 6.9. It can be seen from the graph that the parameter most strongly affected by doping is the c/a ratio. This result might have strong implications as far as the role of anisotropy in determining the ground state properties of this system, as mentioned later in the chapter along with specific heat studies of Y-doped samples.

6.1.3 Mixed Doping: $\text{Ce}_{0.8}(\text{La}_{1-x}\text{Y}_x)_{0.2}\text{Al}_3$

The two main effects associated with alloying on the Ce sites are a reduction in the number of magnetic ions, resulting in an increase of the effective distance between them, and a change in the average f -ion to ligand-atom hybridization. The former has a direct influence on the strength of RKKY interactions, while the latter affects the local Kondo coupling constants. The present alloying study on $\text{Ce}_{0.8}\text{La}_{0.2}\text{Al}_3$ combines both Y and La on the Ce sites to keep the average hybridization constant with respect to CeAl_3 , while reducing the Ce concentration. Assuming that the hybridization is dependent only on the value of the lattice constants, this study may help distinguish between the effects of changes in the concentration of magnetic impurities and changes in their electronic environment.

In $\text{Ce}_{0.8}(\text{La}_{1-x}\text{Y}_x)_{0.2}\text{Al}_3$, it was found that yttrium doping on the Ce/La sites induces a compression of the lattice. As shown in Fig. 6.11, the change in volume is linear in Y concentration, and is mainly due to a decrease in the a parameter (Fig. 6.10). Therefore, there is an overall increase of the c/a ratio with x (Fig. 6.12). The lattice parameters for $x = 0.4$ are within the error bars of those of CeAl_3 . Thus, this experiment demonstrates that by chemically substituting a certain proportion of Y and La atoms on the Ce sites it is possible to obtain the same lattice parameters as in the undoped compound.

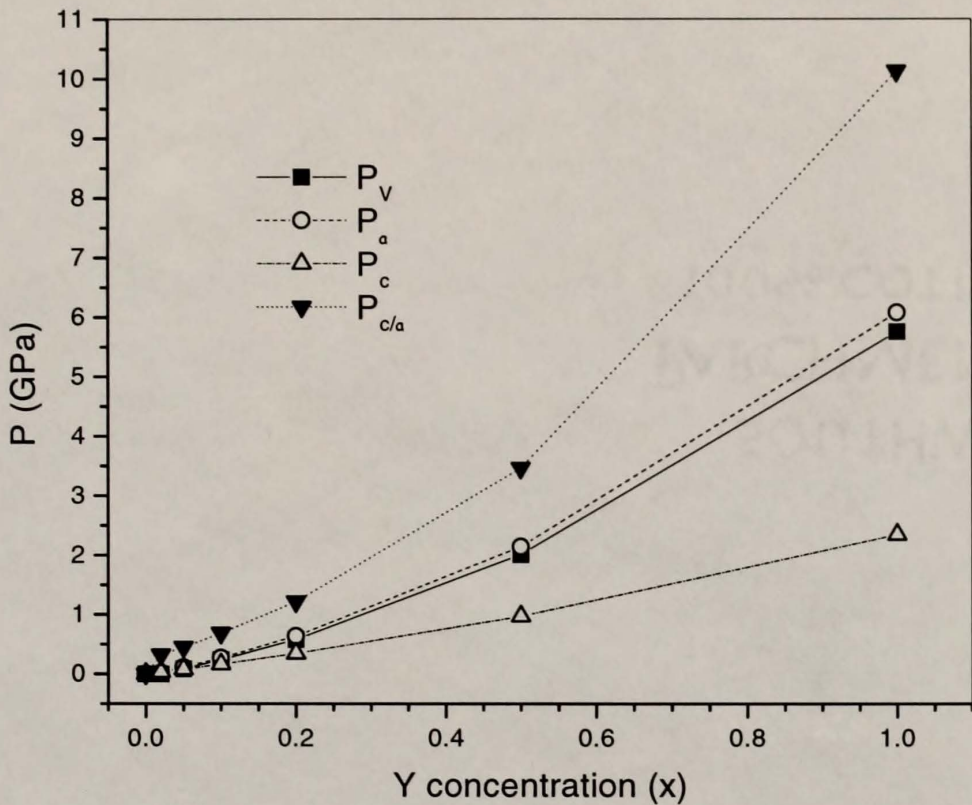


Figure 6.9: Chemical pressures P_V , P_a , P_c , and $P_{c/a}$ as a function of Y concentration x for $\text{Ce}_{1-x}\text{Y}_x\text{Al}_3$ alloys ($x = 0, 0.02, 0.05, 0.1, 0.2, 0.5$, and 1 ; see text for details). The lattice parameters for $x = 0.5$ and $x = 1$ were obtained from C. S. Jee and G. R. Stewart (unpublished) and Van Vucht *et al.* [62], respectively. The lines are guides to the eye.

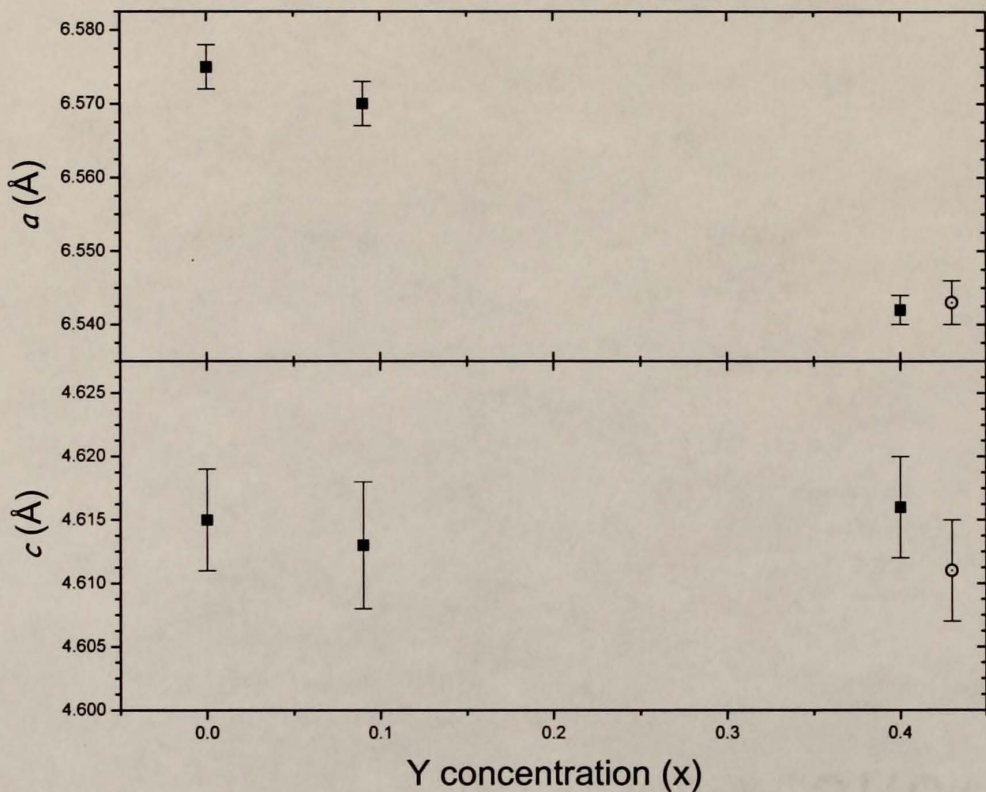


Figure 6.10: Lattice parameters a and c as a function of Y concentration x for $\text{Ce}_{0.8}(\text{La}_{1-x}\text{Y}_x)_{0.2}\text{Al}_3$ ($x = 0, 0.09$, and 0.4). The open circles indicate the corresponding y -axis values for CeAl_3 .

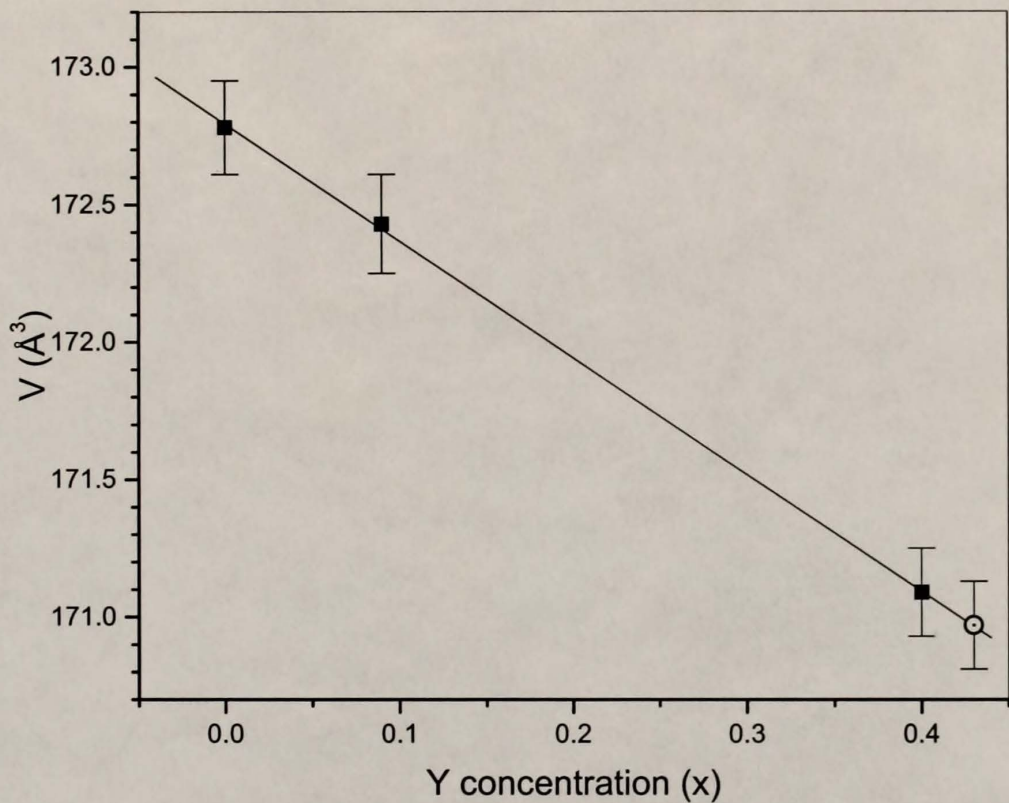


Figure 6.11: Lattice volume V as a function of Y concentration x for $\text{Ce}_{0.8}(\text{La}_{1-x}\text{Y}_x)_{0.2}\text{Al}_3$ ($x = 0, 0.09$, and 0.4). The open circle indicates the corresponding y -axis value for CeAl_3 . The solid line is a least-squares fit to the data.

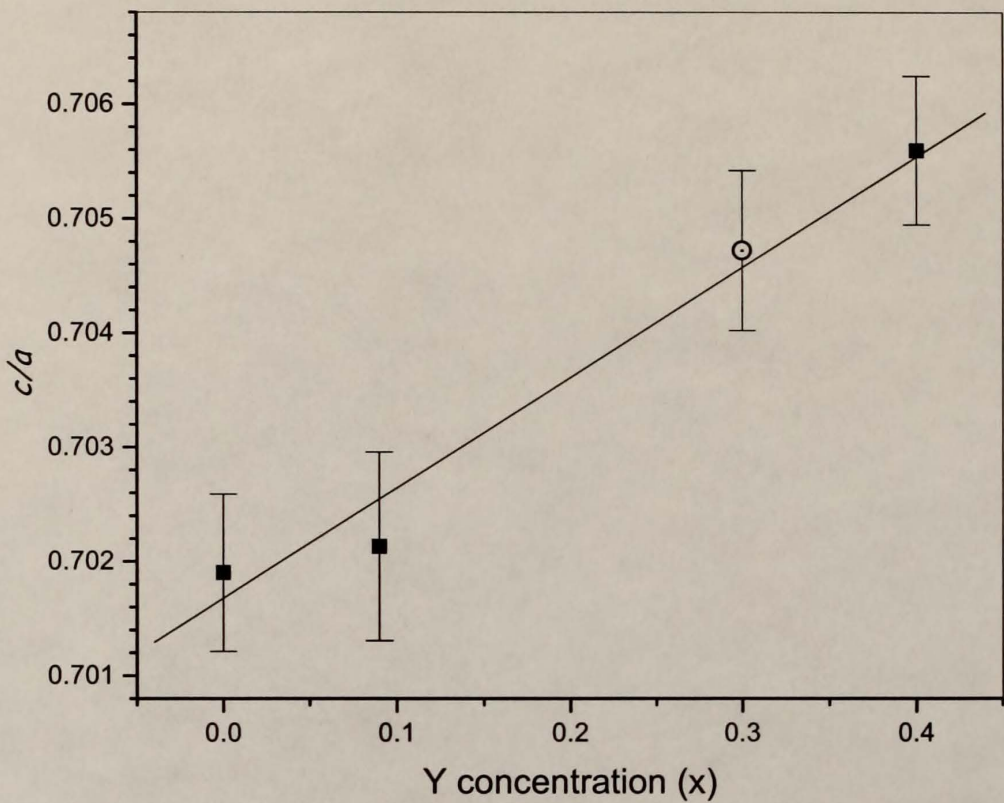


Figure 6.12: Ratio c/a as a function of Y concentration x for $\text{Ce}_{0.8}(\text{La}_{1-x}\text{Y}_x)_{0.2}\text{Al}_3$ ($x = 0, 0.09$, and 0.4). The open circle indicates the corresponding y -axis value for CeAl_3 . The solid line is a least-squares fit to the data.

6.1.4 Summary

Chemical substitution of La in CeAl_3 causes an expansion of the lattice and a decrease in c/a , while Y doping on both $\text{Ce}_{0.8}(\text{La}_{1-x}\text{Y}_x)_{0.2}\text{Al}_3$ and $\text{Ce}_{1-x}\text{Y}_x\text{Al}_3$ alloys results in a contraction of the lattice and an increase in c/a . The overall changes in the structure are more drastic for Y than for La substitution. For example, the change in V between $\text{Ce}_{0.8}\text{Y}_{0.2}\text{Al}_3$ and pure CeAl_3 is more than twice as large as that using the same amount of La. In addition, the corresponding decrease in c/a caused by La is less than half the increase in c/a from Y doping.

A comparison of $\text{Ce}_{1-x}\text{Y}_x\text{Al}_3$ data to the pressure dependence of V , a , and c for CeAl_3 revealed that both alloying and pressure affect the a parameter more than c , yet the difference in the rates of reduction for a and c is largest in the case of alloying. Therefore, c is more affected by hydrostatic pressure than by chemical substitution. The presence of Y in the Ce sites induces an anisotropic lattice contraction that could have a significant effect in the electronic environment surrounding the Ce f ions.

Another comparison can be made between f -ion and ligand-doping lattice parameter results. A previous study by Corsépius *et al.* [61] determined that substitution of Ga, Si and Ge on the Al sites causes a net contraction of the lattice, while doping with Sn expands the lattice. In this case, the relative changes between a and c were found to depend on the choice of dopant. For example, both Si and Ge affect a more than c , while Ga and Sn affect c more than a . Therefore, ligand-site doping seems to affect both a and c more than Kondo-hole (La, Y) doping of the Ce sites, which mainly affects the a parameter.

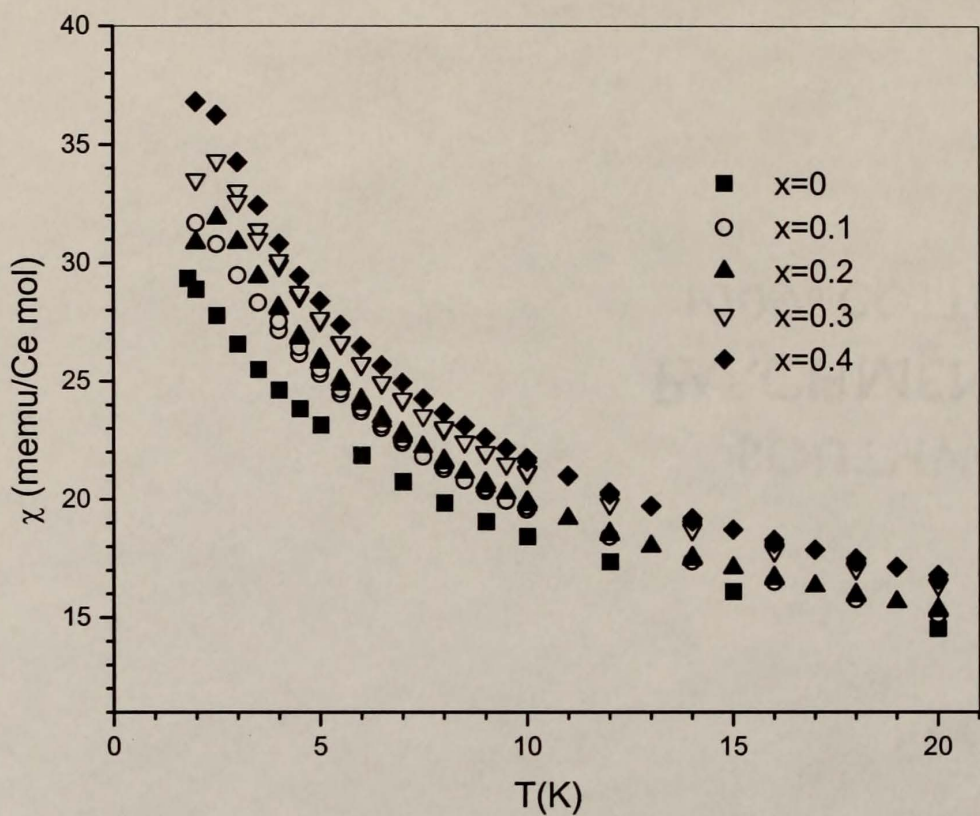


Figure 6.13: Low temperature magnetic susceptibility χ vs T for $\text{Ce}_{1-x}\text{La}_x\text{Al}_3$ alloys, $0 \leq x \leq 0.4$ ($H = 1$ kG).

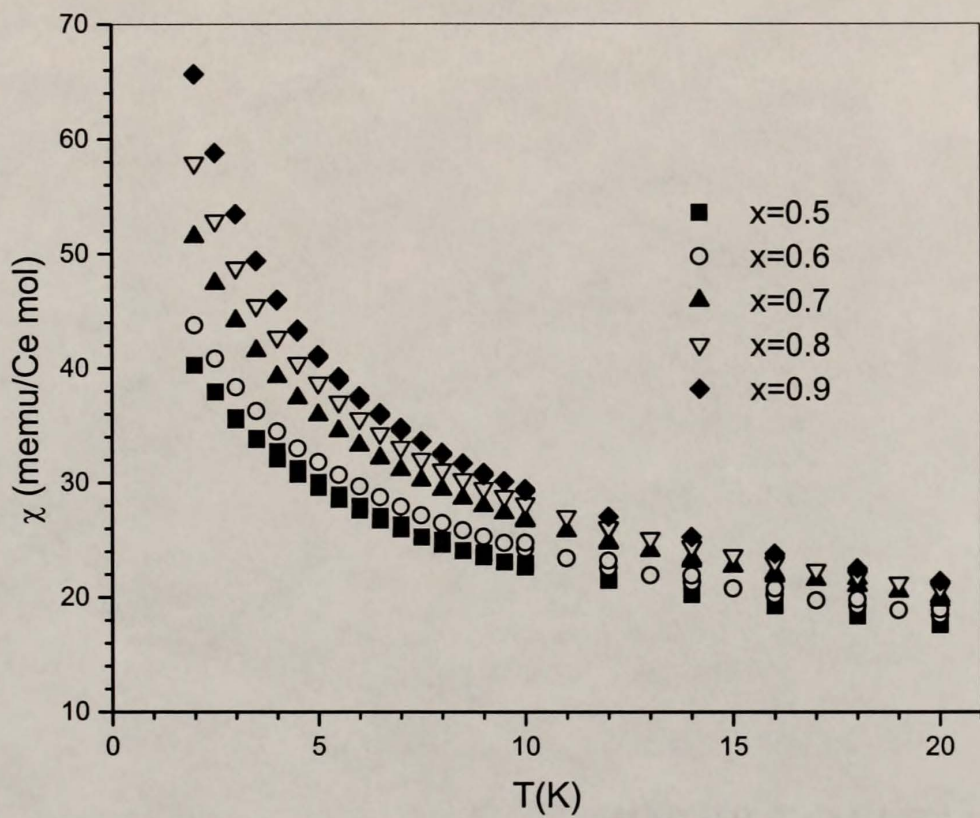


Figure 6.14: Low temperature magnetic susceptibility χ vs T for $\text{Ce}_{1-x}\text{La}_x\text{Al}_3$ alloys, $0.5 \leq x \leq 0.9$ ($H = 1\text{ kG}$).

6.2 Thermodynamic Measurements of $\text{Ce}_{1-x}\text{La}_x\text{Al}_3$ Alloys

6.2.1 Magnetic Susceptibility

The magnetic susceptibility of $\text{Ce}_{1-x}\text{La}_x\text{Al}_3$ alloys was measured between 2 and 300 K, and was normalized per Ce mole by first subtracting the susceptibility of LaAl_3 , then dividing by the Ce concentration. Figure 6.13 shows the low temperature susceptibility of samples with La concentrations $0 \leq x \leq 0.4$. The anomaly in the susceptibility, which occurs around 0.5 K in CeAl_3 , is visible at 2.5 K for $x = 0.2$ and 0.3, while a shoulder can be detected at the same temperature for $x = 0.4$. Measurements performed on $x = 0.2$ found no discrepancy between zero-field-cooled and field-cooled measurements at temperatures around the anomaly. Values for the susceptibility at 2 K increase from about 29 memu/Ce mol for $x = 0$ to almost 37 memu/Ce mol for $x = 0.4$. The susceptibility for higher La concentrations ($0.5 \leq x \leq 0.9$) is shown in Fig. 6.14. The rate of increase of χ values at 2 K is larger than for $x \leq 0.4$, from 40 memu/Ce mol for $x = 0.5$ to about 66 memu/Ce mol for $x = 0.9$, as illustrated in Fig. 6.14. This enhancement of low-temperature susceptibility values might be an indication of an enhancement of the zero-temperature susceptibility χ_0 between $x = 0$ and $x = 0.9$, consistent with a decrease of the Kondo temperature T_K (see Chapter 2). It is not certain from these measurements that similar anomalies are present for other concentrations at temperatures below 2 K. An upturn in the susceptibility does not always lead to a phase transition; it could also indicate an increase in magnetic correlations without leading to a maximum in χ vs T . Nevertheless, despite the apparent non-monotonic dependence of the temperature of this anomaly with La concentration, the continuous increase of susceptibility values at 2 K with x suggests a decrease of T_K , as seen in Fig. 6.15.

The inverse susceptibility data of various $\text{Ce}_{1-x}\text{La}_x\text{Al}_3$ alloys are shown in Fig. 6.16. The temperature dependence of χ followed a Curie-Weiss form above

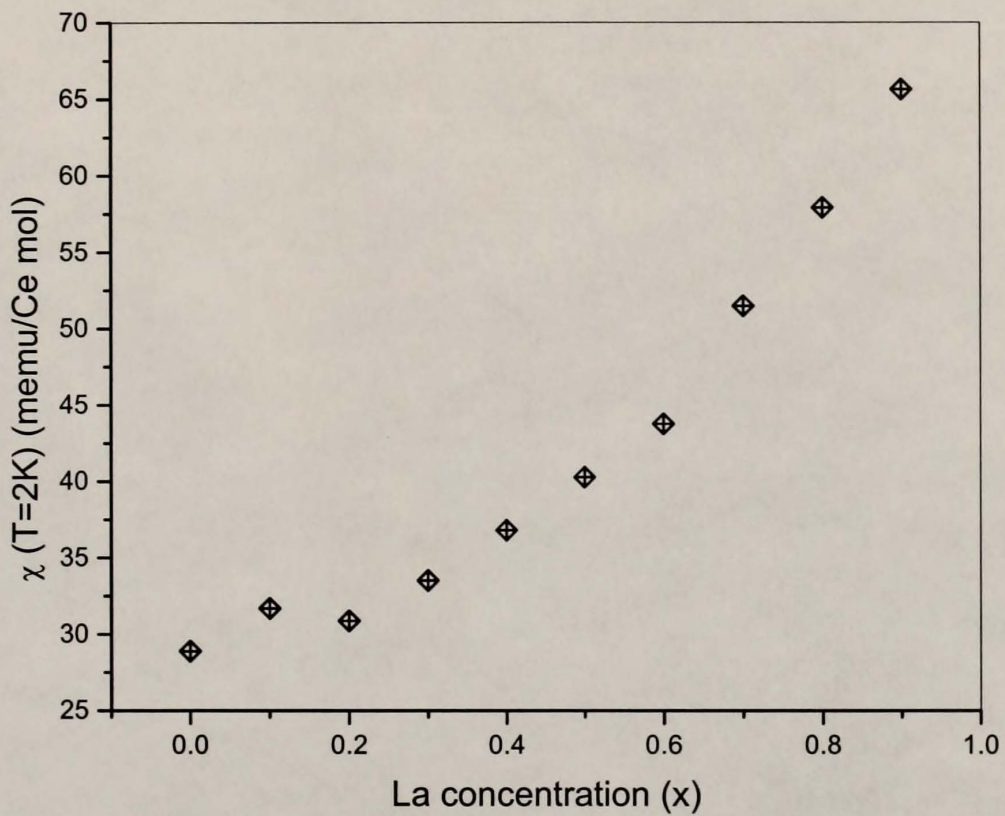


Figure 6.15: Low temperature susceptibility χ ($T = 2\text{ K}$) vs La concentration x for $\text{Ce}_{1-x}\text{La}_x\text{Al}_3$, $0 \leq x \leq 0.9$ ($H = 1\text{ kG}$).

Table 6.2: Magnetic susceptibility parameters for $\text{Ce}_{1-x}\text{La}_x\text{Al}_3$ alloys, $0 \leq x \leq 0.9$.

La x	χ_0 (2 K) (memu/Ce mol)	μ_{eff} (μ_B)	Θ_{cw} (K)
0	28.9	2.53	29
0.1	31.7	2.57	33
0.2	30.9	2.52	29
0.3	33.5	2.54	25
0.4	36.8	2.59	25
0.5	40.3	2.53	23
0.6	43.8	2.58	24
0.7	51.5	2.44	11
0.8	57.9	2.53	18
0.9	65.6	—	—

150 K, with the exception of $x = 0.9$. The calculated effective moments were around the Hund's rule value $\mu_{\text{eff}} = 2.54 \mu_B$ for the $4f^1$ configuration of Ce^{3+} . Table 6.2 shows the variation in the susceptibility at 2 K, the high-temperature effective moment, and the magnitude of the Curie-Weiss temperature Θ_{cw} with La concentration. Values of the effective moment range between $2.44 \mu_B$ and $2.59 \mu_B$ per Ce ion, with most of them around $2.54 \mu_B$.

The random errors in μ_{eff} might be due to its extraction over a short temperature range ($100 \text{ K} \leq T \leq 300 \text{ K}$) for this system, in particular the narrow range between 300 K and the excited crystal-field levels ($\sim 70 \text{ K}$). Nonetheless these measurements point to a stable trivalent configuration of the Ce ions at higher temperatures. The extracted values of Θ_{cw} are negative, consistent with both antiferromagnetic RKKY interactions between the Ce ions and the Kondo effect. The calculated Θ_{cw} shows a trend towards decreasing values with x . This decrease is usually associated with the decrease of T_K in Kondo alloys, where $\Theta_{\text{cw}} \propto T_K$ [32, 127].

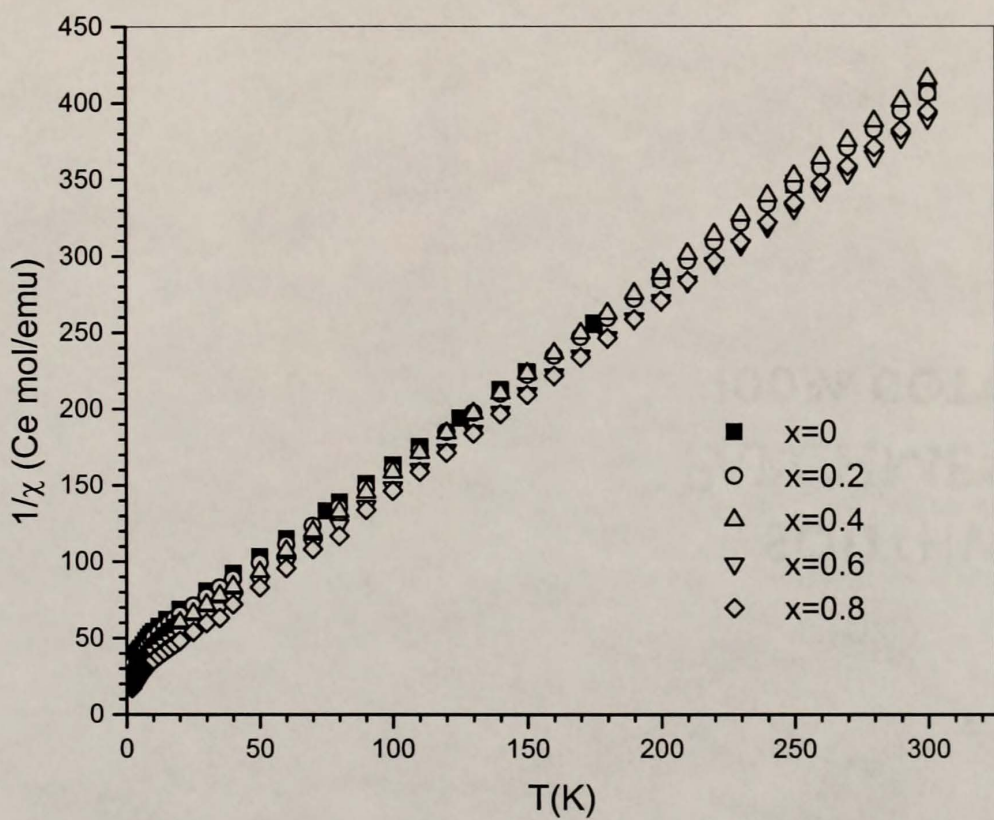


Figure 6.16: Inverse susceptibility vs temperature for $\text{Ce}_{1-x}\text{La}_x\text{Al}_3$, $x = 0, 0.2, 0.4, 0.6$, and 0.8 .

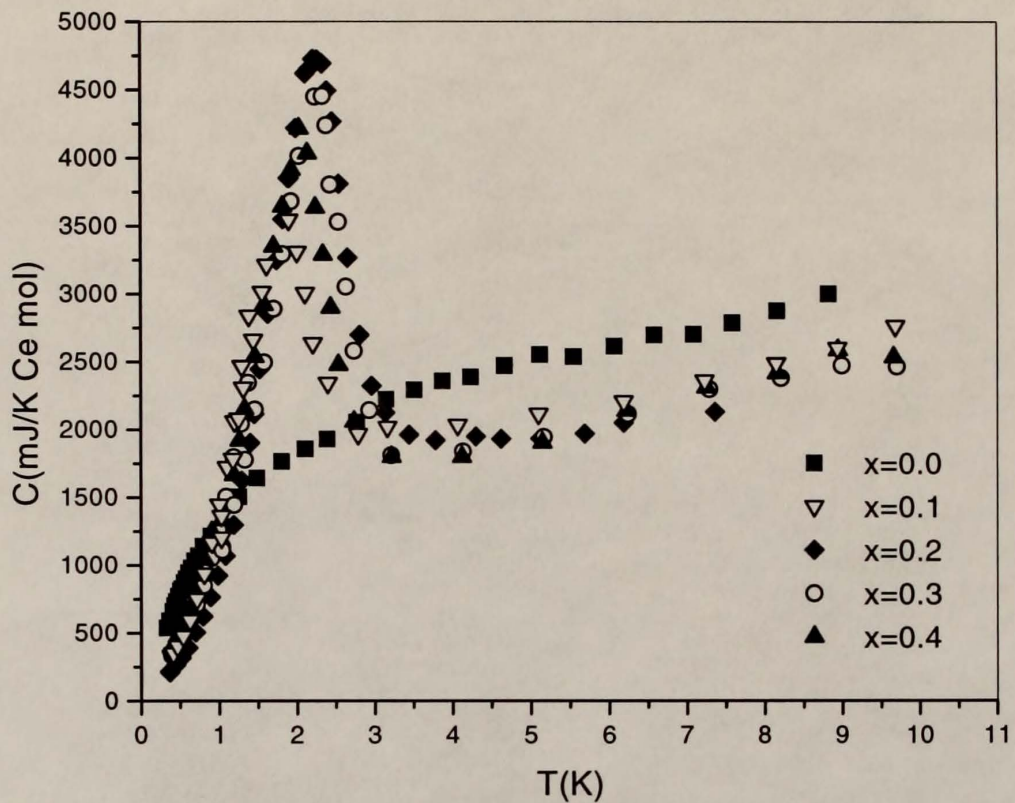


Figure 6.17: Specific heat vs temperature of $\text{Ce}_{1-x}\text{La}_x\text{Al}_3$ alloys, $0 \leq x \leq 0.4$. Data below 1 K for CeAl_3 is from Andraka *et al.* [71].

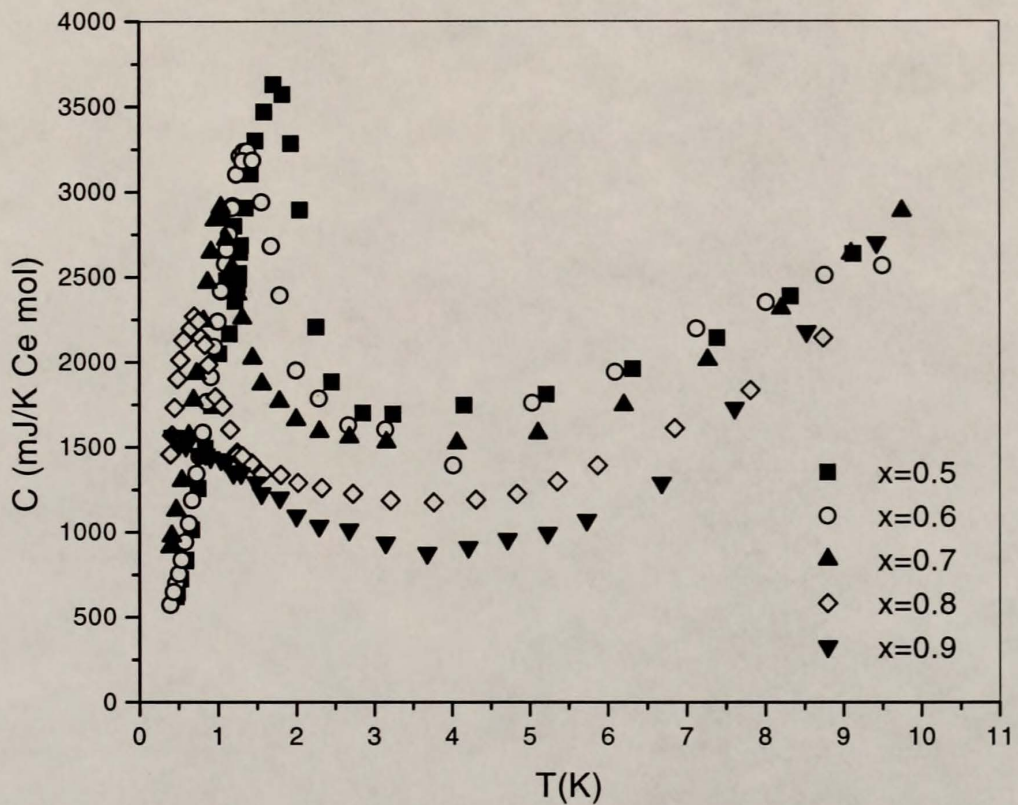


Figure 6.18: Specific heat vs temperature of $\text{Ce}_{1-x}\text{La}_x\text{Al}_3$ alloys, $0.5 \leq x \leq 0.9$.

6.2.2 Specific Heat

The specific heat curves of $\text{Ce}_{1-x}\text{La}_x\text{Al}_3$ alloys are shown in Figs. 6.17 and 6.18. The specific heat of LaAl_3 was subtracted from the data to account for the phonon contribution. It is represented by the following formula between 0.35 and 20 K [128]:

$$C(T) = 4.95T + 0.1213T^3 + 4.13 \times 10^{-4}T^5 - 3.88 \times 10^{-7}T^7. \quad (6.7)$$

Substitution by La induces the development of a maximum in C vs T at a temperature T_M , as was previously seen for low concentration levels ($x \leq 0.2$) [71]. This temperature reaches a maximum around 2.3-2.4 K for $x = 0.3$, and it is reduced to 2 K for $x = 0.4$. The magnitude of this anomaly initially increases with increasing La concentration. It achieves a value around 4750 mJ/K Ce mol for $x = 0.2$, before decreasing to 3600 mJ/K Ce mol for $x = 0.4$. The increases in both T_M and the magnitude of the maximum in C support the idea of Andraka *et al.* [71] that this anomaly evolves smoothly as a function of doping from the weak maximum seen in C/T of CeAl_3 at 0.4 K. Both T_M and the magnitude of the maximum continue decreasing at higher La concentrations. The lowest temperature T_M detected within the range of measurement was about 0.7 K for $x = 0.8$. The anomaly for this concentration has a magnitude of 2250 mJ/K Ce mol. Values of the specific heat for the more dilute $x = 0.9$ seem to saturate below 0.4 K, suggesting the presence of a broad maximum at lower temperatures for this concentration.

Figure 6.19 shows the specific heat as C/T vs T per mole of Ce for $0 \leq x \leq 0.4$. The temperature of the anomaly in C/T , T_m , shifts continuously towards higher values with La doping for $x \leq 0.3$. The maximum increases in magnitude ($\sim 2200 \text{ mJ/K}^2 \text{ Ce mol}$ for $x = 0.2$), and T_m reaches a maximum value of 2.3 K at $x = 0.3$, similar to that of T_M from the specific heat data. Values of C/T at 0.4 K decrease significantly compared to that of CeAl_3 , while those above 4 K

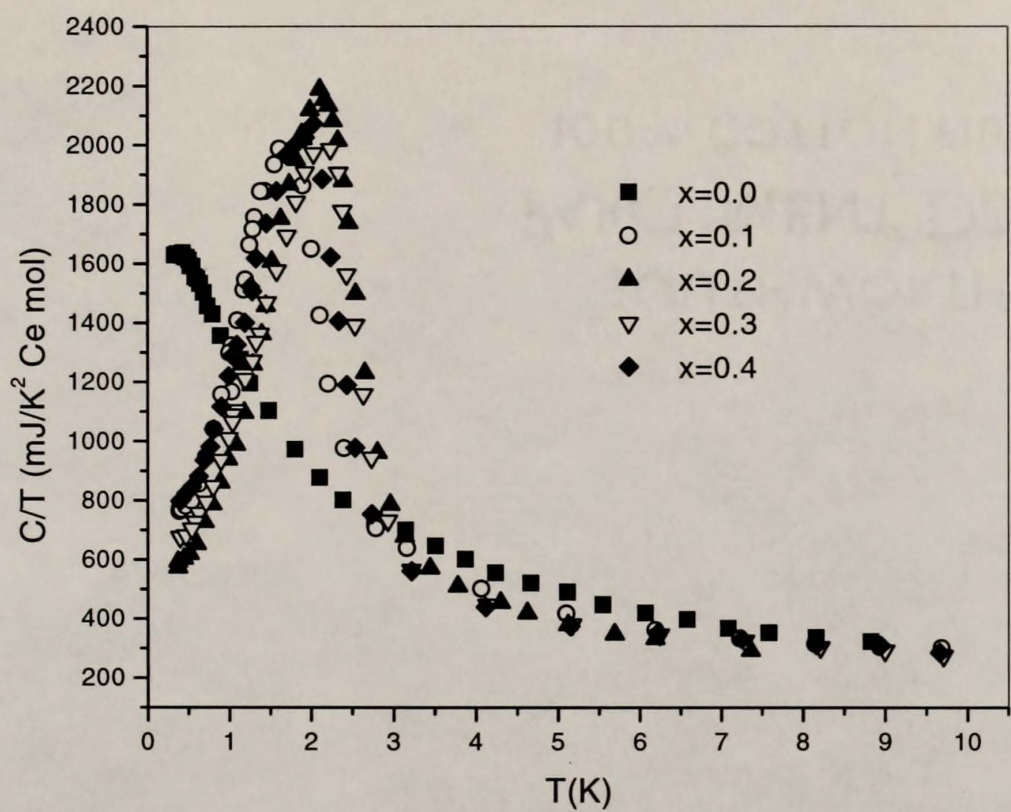


Figure 6.19: Specific heat plotted as C/T vs T for $\text{Ce}_{1-x}\text{La}_x\text{Al}_3$ alloys, $0 \leq x \leq 0.4$. Data below 1 K for CeAl_3 is from Andraka *et al.* [71].

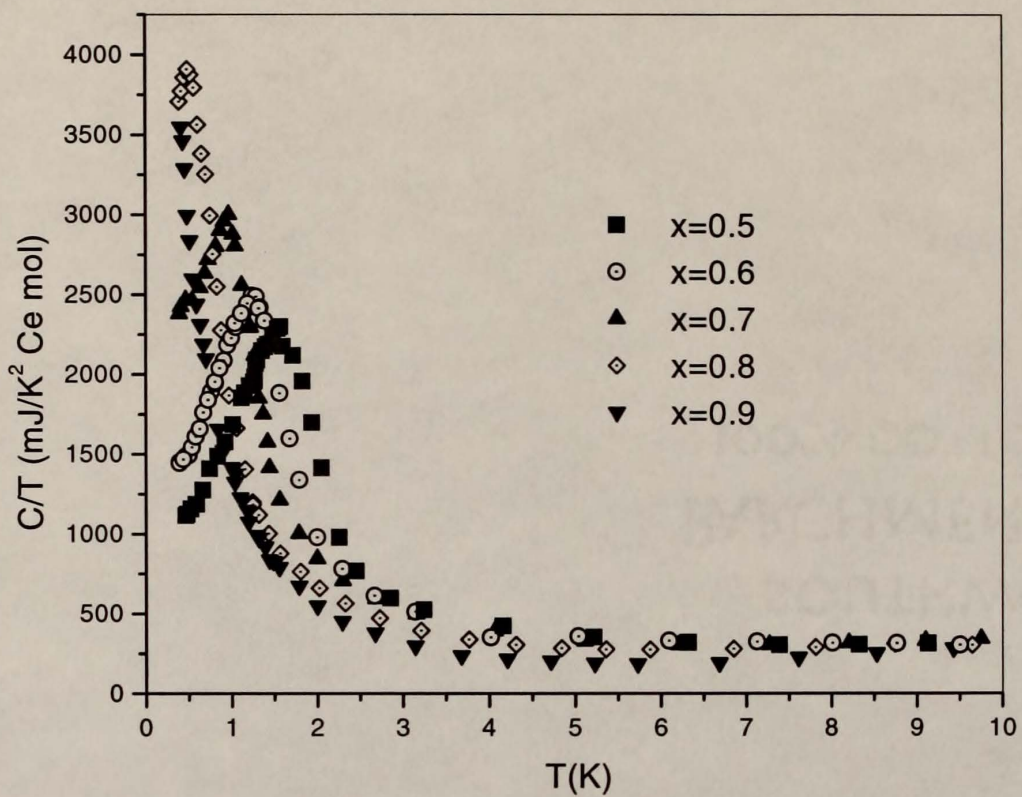


Figure 6.20: Specific heat plotted as C/T vs T for $\text{Ce}_{1-x}\text{La}_x\text{Al}_3$ alloys, $0.5 \leq x \leq 0.9$.

appear to be less dependent on La concentration. It is possible that the merging of the curves points to a characteristic temperature for the development of magnetic correlations. At higher concentrations, the temperature T_m decreases, following the trend of T_M . The magnitude of the anomaly in C/T momentarily decreases between $x = 0.3$ and $x = 0.4$, but increases dramatically for larger values of x , as shown in Fig. 6.20. The entropy is redistributed to lower temperatures, with values of C/T at 0.4 K increasing to more than six times that of $x = 0.2$ for $x = 0.9$. The largest maximum detected above 0.4 K has a value of 3900 mJ/K² Ce mol and corresponds to $x = 0.8$. If $x = 0.9$ has a similar maximum in C/T , its magnitude could easily surpass 4 J/K² Ce mol, due to a very large slope in C/T vs T below 1 K. In fact, recent μ SR studies on $\text{Ce}_{1-x}\text{La}_x\text{Al}_3$ alloys [15] found that the divergence of the muon damping rate, signaling the presence of magnetic correlations, occurs around the same temperature as the anomaly in C/T for at least $x = 0.2$. The damping rate for $x = 0.9$ diverges around 0.1 K, so it is likely that this sample exhibits an anomaly in C/T near this temperature.

The electronic specific heat coefficient γ was extracted for $\text{Ce}_{1-x}\text{La}_x\text{Al}_3$ alloys from a linear fit of the data below T_m in C/T vs T^2 form, where γ corresponds to the intercept. The main sources of error are the relatively large values of C/T at the lowest temperature (0.4 K) and the uncertainty in the true form of the temperature dependence of this quantity down to $T = 0$. Brodale *et al.* determined that C/T is linear in temperature between 0.06 K and 0.25 K for CeAl_3 [67]. The calculated values of γ in this section assume $C/T \propto T^2$ down to $T = 0$. Other sources of error include experimental and regression uncertainties. Figure 6.21 displays the evolution of γ as a function of La concentration. The value of 1250 mJ/K² mol for pure CeAl_3 decreases to a minimum of 520 mJ/K² Ce mol for $x = 0.2$. A very large increase in the electronic coefficient is then observed for $x \geq 0.3$, with γ reaching 3400 mJ/K² Ce mol for $x = 0.8$. This minimum in the γ vs x curve might indicate

the competition of two effects in the determination of the ground state properties of the system.

Another result possibly indicating the competition between two contributions to the ground state properties is the change of the temperature of the anomaly in C/T with x , shown in Fig. 6.22. Data for $x = 0.01$ and $x = 0.05$ was obtained from the previous low-level doping study of Andraka *et al.* [71]. A rapid increase in T_m can be seen for $x \leq 0.2$. What was previously unknown is that a maximum in T_m around 2.3 K is reached at $x = 0.3$, followed by an almost linear decrease all the way to $x = 0.8$. This behavior is similar to that observed for the antiferromagnetic anomalies in the specific heat of $\text{Ce}_{1-x}\text{Th}_x\text{Cu}_2\text{Si}_2$ [129], where the associated temperature position reaches a maximum value also at $x = 0.3$. An extrapolation of the $\text{Ce}_{1-x}\text{La}_x\text{Al}_3$ data to higher concentrations gives a value of T_m near 0.1 K for $x = 0.9$. The maximum in the data is asymmetric, due to a sudden increase in T_m values at lower La concentrations. Clearly, this is a sign of two competing interactions taking place in $\text{Ce}_{1-x}\text{La}_x\text{Al}_3$.

Finally, the Wilson ratio $R = 218.7\chi/(\gamma\mu_{\text{eff}}^2)$ [5] was calculated for La concentrations up to $x = 0.8$ using the susceptibility values at 2 K (Fig. 6.15), the extrapolated γ values from the C/T data, and the high-temperature effective moment $\mu_{\text{eff}} = 2.54\mu_B$. Figure 6.23 illustrates the trend of R vs x , which is very similar to that of T_m vs x . The ratio rises sharply from $x = 0$ to $x = 0.2$. The maximum at $x = 0.2$ is then followed by a slower decrease up to $x = 0.8$. The highest values of both R and T_m are in the range $0.2 \leq x \leq 0.4$. When compared to the Wilson ratio of other magnetic heavy-fermion systems (e.g., $R(\text{U}_2\text{Zn}_{17})=0.79$, $R(\text{UCd}_{11})=1.55$ -1.82 [5]), the large values of R (1.8-2.2) for $\text{Ce}_{1-x}\text{La}_x\text{Al}_3$ within this doping range suggest an increase in the magnetic character of this system.

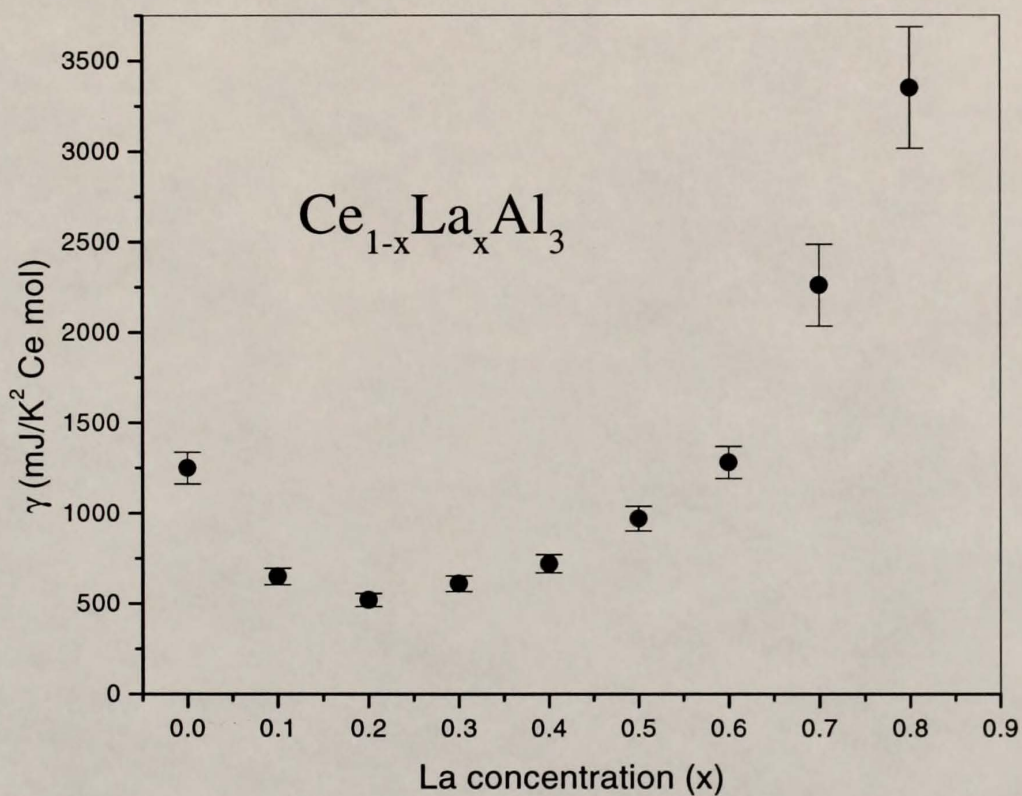


Figure 6.21: Electronic specific heat coefficient γ vs La concentration x for $\text{Ce}_{1-x}\text{La}_x\text{Al}_3$.

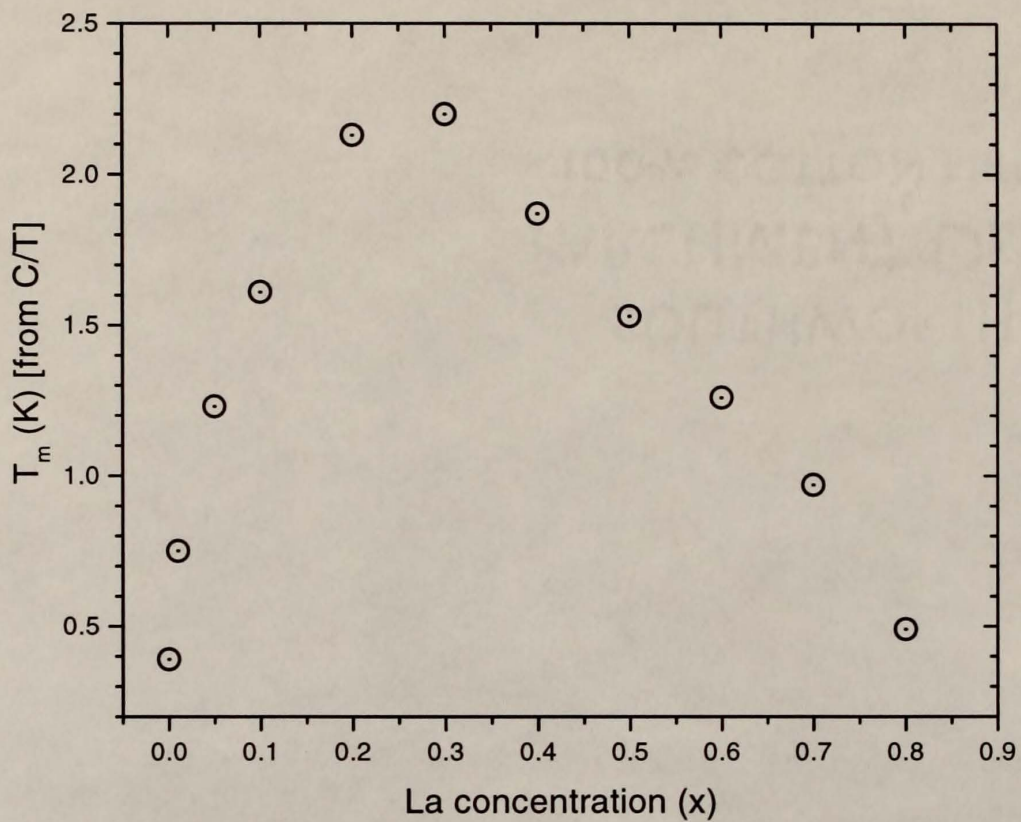


Figure 6.22: Temperature of the maximum in C/T (T_m) vs La concentration x for $\text{Ce}_{1-x}\text{L}_x\text{Al}_3$. Data for $x = 0.01, 0.05$ was obtained from Andraka *et al.* [71].

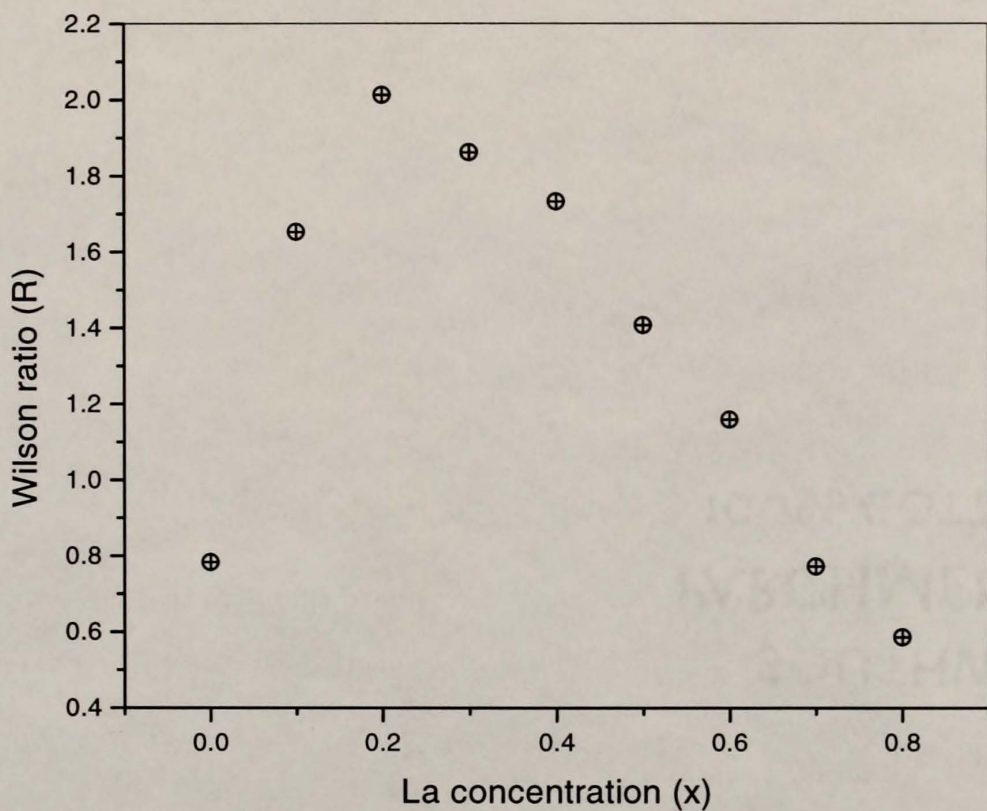


Figure 6.23: Wilson ratio R [5] vs La concentration x for $\text{Ce}_{1-x}\text{La}_x\text{Al}_3$, $0 \leq x \leq 0.8$.

6.2.3 Discussion

The behavior of lattice parameters and thermodynamic properties of the $\text{Ce}_{1-x}\text{La}_x\text{Al}_3$ system are very similar to those found by La substitution of another heavy-fermion Kondo lattice, CeCu_2Si_2 . The properties of $\text{Ce}_{1-x}\text{La}_x\text{Cu}_2\text{Si}_2$ alloys seem to be consistent with Doniach's Kondo necklace model [130, 40]. $\text{Ce}_{1-x}\text{La}_x\text{Al}_3$ alloys have a hexagonal structure with $c < a$, while La-doped CeCu_2Si_2 alloys have a tetragonal structure with $c > a$. When comparing the change in lattice parameters between the two systems, it was found in both cases that the a parameter is the most affected by La substitution. The change in lattice volume is mostly due to the change in a , and the c/a ratio decreases linearly by a similar amount across the whole series: 1.2% for $\text{Ce}_{1-x}\text{La}_x\text{Cu}_2\text{Si}_2$ [130] and 1.5% for $\text{Ce}_{1-x}\text{La}_x\text{Al}_3$.

The electronic specific heat coefficient of $\text{Ce}_{1-x}\text{La}_x\text{Al}_3$ alloys has a minimum around $x = 0.2$. A similar nonmonotonic dependence of the electronic coefficient γ with La doping was also found in $\text{CeCu}_{2.2}\text{Si}_2$ [130]. Studies in which Ce is substituted by La revealed that γ has a minimum at a La concentration $x = 0.5$, and achieves a value close to that of pure $\text{CeCu}_{2.2}\text{Si}_2$ at $x = 0.9$. Magnetic susceptibility values around 2 K for this system also have a minimum for $x = 0.5$. The observed similar trends for the changes in γ and low-temperature susceptibility values point to a common origin of their behavior as a function of La concentration.

The non-single-ion-like changes in γ upon dilution with La in the above systems are of general interest in the study of strongly-correlated electron systems. The increase in γ with La concentration observed in dilute samples can be explained by a decrease in the Kondo temperature T_K and in the hybridization between $4f$ and conduction electrons. On the other hand, the observed increase of this coefficient with decreasing La concentration could be interpreted in two different ways. The first interpretation attributes the change to the development

of a paramagnetic heavy-fermion state. The second explanation is based on the suppression of magnetic order with increasing Ce concentration.

The development of the heavy-fermion state from a collection of noninteracting Kondo scatterers is one of the major unresolved issues in heavy-fermion physics. This problem is linked to the “Kondo exhaustion” paradox [131]. In such a concentrated system at low temperatures, there are not enough conduction electrons within a narrow band around the Fermi level ($\sim k_B T_K$) to individually compensate all of the impurity spins at the lowest temperatures. Yet each electron is involved in the simultaneous screening of many local moments. This state develops at a characteristic lattice temperature lower than the single-impurity Kondo temperature T_K . The decrease in T_K with the development of the heavy-fermion state has been experimentally observed in $U_{1-x}M_xBe_{13}$ [132] ($M =$ nonmagnetic dopant) and $Ce_{1-x}La_xCu_{2.2}Si_2$ [130]. From these observations, it is possible that the behavior of γ in Ce-rich $Ce_{1-x}La_xAl_3$ alloys can also be explained in terms of the formation of a coherent Kondo lattice state.

However, assuming that the maximum in C/T is indicative of a magnetic phase transition, the electronic coefficient in $Ce_{1-x}La_xAl_3$, extracted from C/T at the lowest temperatures, does not correspond to the heavy-fermion paramagnetic state, but to an antiferromagnetic (or spin-glass) state. The phase transition leads to a decrease in the value of the electronic specific heat coefficient. Therefore, it is quite unreliable to extract a measure of the lattice Kondo temperature from the inverse of the electronic coefficient of magnetic heavy-fermion alloys. In order to estimate the concentration dependence of a characteristic lattice Kondo temperature for the $Ce_{1-x}La_xAl_3$ alloys studied, values of T_K were extracted instead using the magnetic entropy $S_m(T_0)$, defined as

$$S_m(T_0) = \int_0^{T_0} \frac{C_m(T)}{T} dT, \quad (6.8)$$

where $C_m(T)/T$ is the specific heat contribution per Ce mole after subtracting the phonon contribution (LaAl_3), and $T_0 > T_m$, the characteristic magnetic transition temperature. In Ce heavy-fermion compounds, the magnetic entropy at low temperatures includes contributions from the Kondo effect as well as magnetic interactions, while at $T \rightarrow \infty$ it reaches the value $R \ln 2$ for a mole of $S = \frac{1}{2}$ magnetic moments. At a temperature T_0 sufficiently larger than the magnetic ordering temperature, magnetic interactions represent only a minor contribution to the specific heat [133, 134], and the entropy $S_m(T_0)$ is essentially the difference between $R \ln 2$ and that removed by the Kondo effect at T_0 . In the range $T_0 \leq T \leq \infty$, the entropy removed is a function of T_K only, so that $S_m(T \geq T_0)$ provides a good measure of T_K .

All C/T vs T curves between $x = 0$ and $x = 0.8$ were numerically integrated up to $T_0 = 3\text{K}$. This temperature is above all T_m values between $x = 0$ and $x = 0.8$. Values of T_K were extracted by comparing the results for $S_m(3\text{K})$ with the Bethe Ansatz solution for the $S = \frac{1}{2}$ Kondo entropy curve [30]. Calculating the entropies at values of $T_0 < 5v\text{K}$ was found to have little effect on the values of T_K determined from the curves. In addition, the contributions and concentration dependences of higher crystal-field levels at this temperature were assumed to be negligible. The calculated entropies at 3K and values of the Kondo temperature are shown in Table 6.3. As the La content increases in $\text{Ce}_{1-x}\text{La}_x\text{Al}_3$, $S_m(3\text{K})$ increases, which implies a decrease in T_K .

A characteristic temperature – Ce concentration phase diagram, shown in Fig. 6.24, was constructed using the calculated values of T_K for $(0 \leq x \leq 0.8)$ and assuming that the maxima in C/T at T_m are indicative of a magnetic transition. The resulting diagram is similar to that of the Kondo-necklace model shown in Fig. 2.7 [42, 43]. Yet, it is important to keep in mind that changes in both T_K and T_m with Ce concentration might not only reflect the effect of reducing J , but also

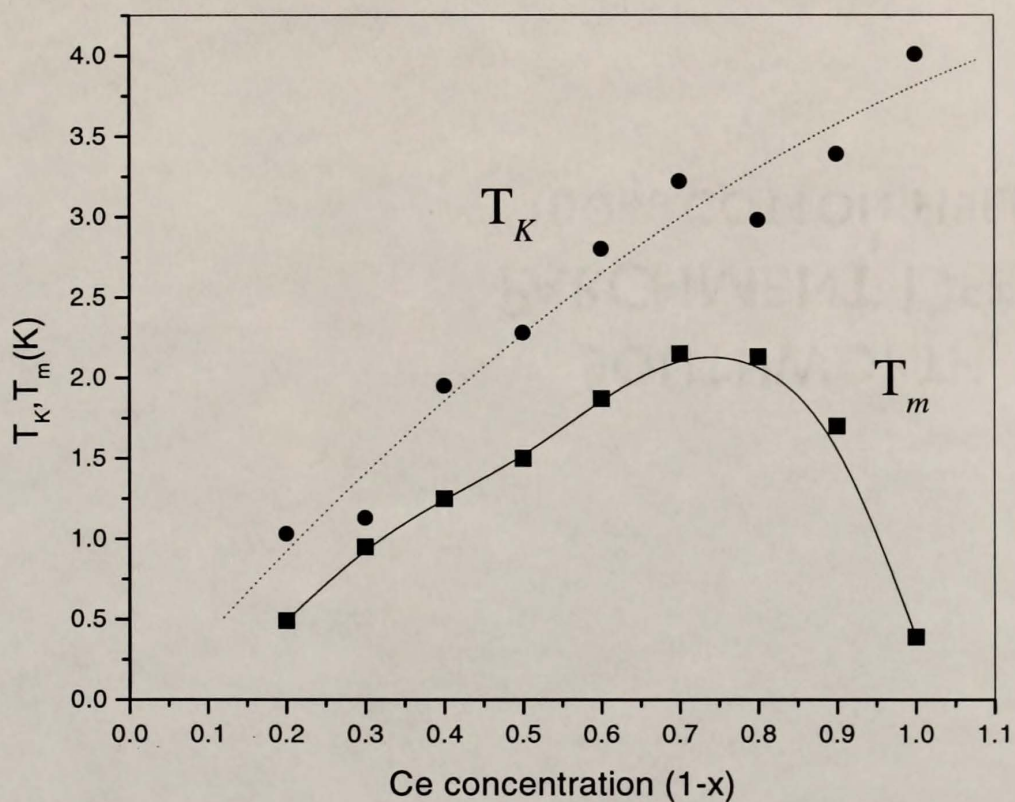


Figure 6.24: Phase diagram illustrating both the temperature of the anomaly in C/T , T_m and the calculated Kondo temperature T_K (see text) as a function of Ce concentration. The lines are guides to the eye.

Table 6.3: Values of the magnetic entropy S_m (in units of $R \ln 2$), $(T = 3 \text{ K})/T_K$, the Kondo temperature T_K , and T_K normalized to that of CeAl_3 ($T_K \sim 4 \text{ K}$ [6]) for $\text{Ce}_{1-x}\text{La}_x\text{Al}_3$ alloys.

La x	$S_m(3 \text{ K}) (R \ln 2)$	$(T = 3 \text{ K})/T_K$	$T_K(\text{K})$	$T_K/T_K^{\text{CeAl}_3}$
0	0.586	0.749	4.0	1.00
0.1	0.624	0.884	3.4	0.85
0.2	0.652	1.008	3.0	0.74
0.3	0.636	0.933	3.2	0.80
0.4	0.660	1.071	2.8	0.70
0.5	0.704	1.319	2.3	0.57
0.6	0.735	1.541	2.0	0.49
0.7	0.813	2.650	1.1	0.28
0.8	0.826	2.901	1.0	0.26

the effect due to an increase in the average distance between Ce $4f$ moments. This Doniach-like diagram positions CeAl_3 at the end of the magnetic temperature curve in the region corresponding to $T_K > T_{\text{RKKY}}$. The description of CeAl_3 in terms of the Doniach model places it in the proximity of a critical point at $T_m = 0$, consistent with current views on heavy-fermion systems [135, 136, 137, 138].

6.3 Thermodynamic Measurements on $\text{Ce}_{1-x}\text{Y}_x\text{Al}_3$ Alloys

6.3.1 Magnetic Susceptibility

The magnetic susceptibility of $\text{Ce}_{1-x}\text{Y}_x\text{Al}_3$ alloys was measured between 1.8 and 400 K at a field $H = 5 \text{ kG}$. Figure 6.25 shows data for $x = 0, 0.02, 0.05, 0.1$, and 0.2 per Ce mole below 20 K. The main consequence of Y doping is a decrease in the magnitude of the susceptibility at this temperature range. The magnetic susceptibility at 1.8 K, $\chi(T = 1.8 \text{ K})$, is reduced by about 40% for $x = 0.2$ from the value of pure CeAl_3 . A decrease in low-temperature susceptibility values with compression of the lattice is usually associated with an increase of the Kondo temperature T_K , since the zero temperature susceptibility is inversely proportional to T_K . The inverse susceptibility as a function of temperature is

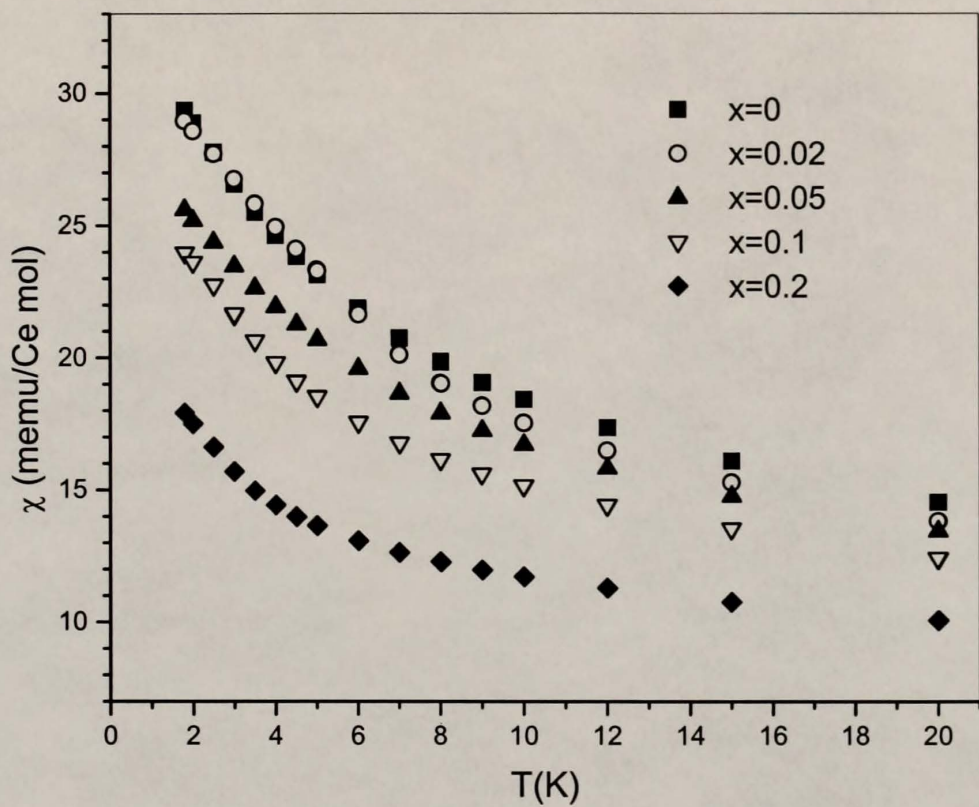


Figure 6.25: Magnetic susceptibility vs temperature of $\text{Ce}_{1-x}\text{Y}_x\text{Al}_3$ alloys, $1.8 \leq T \leq 20 \text{ K}$, $H = 5 \text{ kG}$.

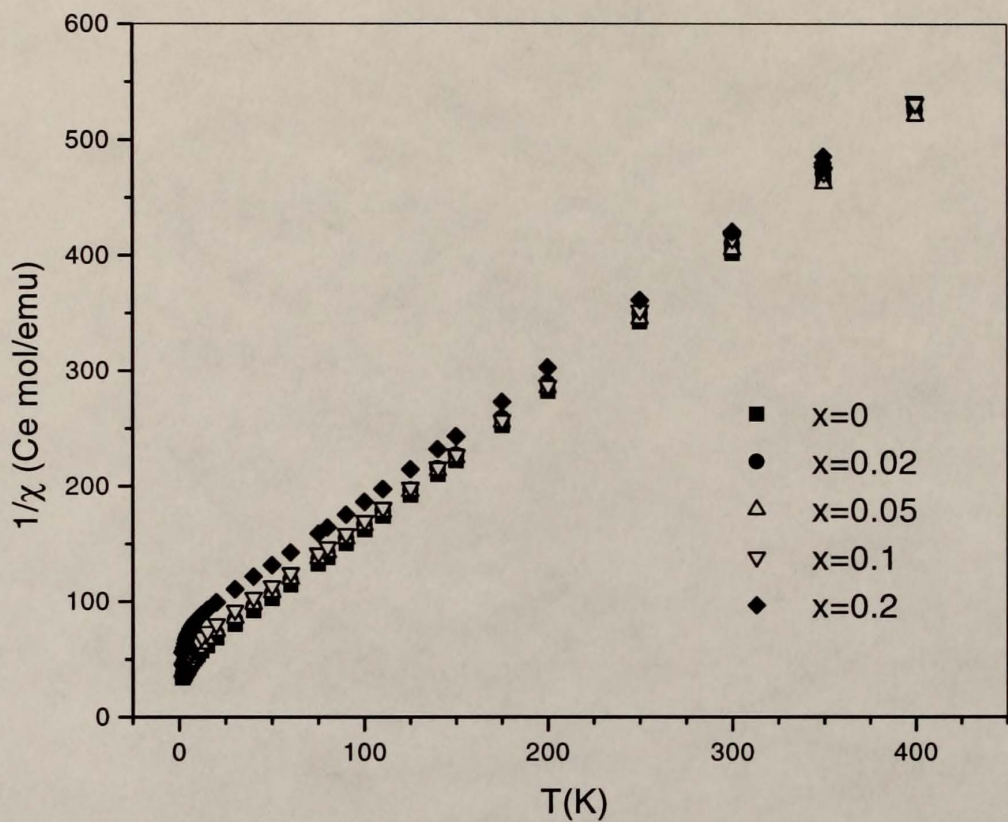


Figure 6.26: Inverse magnetic susceptibility vs temperature of $\text{Ce}_{1-x}\text{Y}_x\text{Al}_3$ alloys, $1.8 \leq T \leq 400$ K, $H = 5$ kG.

Table 6.4: Magnetic susceptibility parameters for $\text{Ce}_{1-x}\text{Y}_x\text{Al}_3$ alloys, $0 \leq x \leq 0.2$.

Y	x	χ_0 (2 K) (memu/Ce mol)	μ_{eff} (μ_B)	Θ_{cw} (K)
	0	28.89	2.53	29
	0.02	28.56	2.58	41
	0.05	25.19	2.60	41
	0.1	23.61	2.57	40
	0.2	17.49	2.60	55

illustrated in Fig. 6.26. Data for $x = 0.2$ are noticeably higher than the rest, especially below 150 K. All concentrations show linear behavior, following a Curie-Weiss law, above 100 K. The Curie-Weiss parameters were extracted from a least-squares fit of the data above 100 K (see Table 6.4). The calculated values for the high temperature effective moment μ_{eff} are in the vicinity of the Ce^{3+} free-ion value, $\mu_{\text{eff}} = 2.54 \mu_B$. The negative Curie-Weiss temperature Θ_{cw} increases with x , which is also consistent with an increase of the Kondo temperature T_K .

6.3.2 Specific Heat

The specific heat of $\text{Ce}_{1-x}\text{Y}_x\text{Al}_3$ alloys ($0 \leq x \leq 0.2$), plotted as C/T vs T per mole of Ce, is shown in Fig. 6.27. The temperature of the anomaly T_m is slightly larger for $x = 0.02$ than for CeAl_3 . It remains around 0.6 K between $x = 0.02$ and $x = 0.1$, and increases toward 1 K for $x = 0.2$. At the same time, the magnitude of the anomaly decreases gradually, from about 1650 mJ/K² Ce mol for $x = 0$ to 540 mJ/K² Ce mol for $x = 0.2$. Values of C/T around 0.4 K, just below T_m , decrease monotonically within this range of concentration, from above 1600 mJ/K² Ce mol to 420 mJ/K² Ce mol. This trend in C/T values indicates a decrease in values of the electronic coefficient γ at $T = 0$. Values of γ could not be extracted from the C/T curves with reasonable accuracy due to the small difference between 0.4 K, the lowest temperature of the measurement, and T_m . A larger temperature range and number of data points is needed to determine γ from

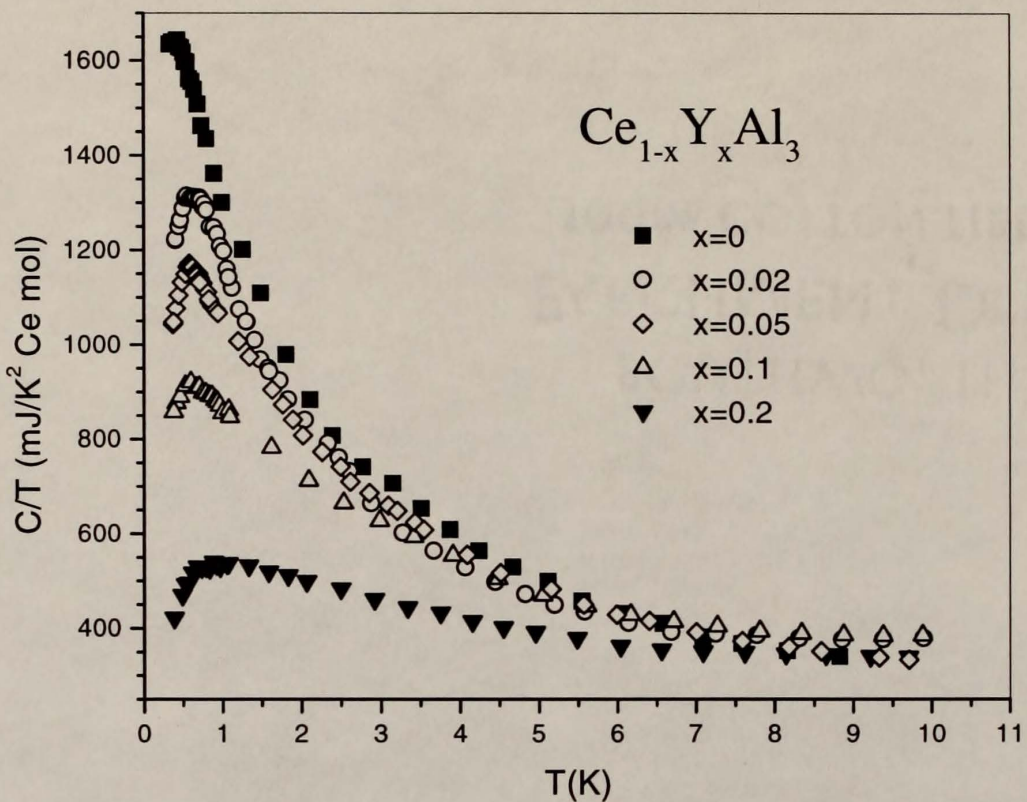


Figure 6.27: Specific heat plotted as C/T vs T for $\text{Ce}_{1-x}\text{Y}_x\text{Al}_3$ alloys, $0 \leq x \leq 0.2$. Data below 1 K for CeAl_3 is from Andraka *et al.* [71].

a linear fit of C/T vs T^2 below T_m . In addition, the area under the C/T curves up to 7 K, equal to the entropy $S_m(T_0 \sim 7 \text{ K})$, clearly decreases with Y concentration. Both the apparent decrease in γ and the decrease in $S_m(T_0 \sim 7 \text{ K})$ with x point to an increase of the Kondo temperature. A decrease in the Kondo entropy, which is the dominant contribution to S_m , is consistent with a decrease of $(T_0 = 7 \text{ K})/T_K$ [30], as previously discussed in the context of $\text{Ce}_{1-x}\text{La}_x\text{Al}_3$ alloys.

6.3.3 Discussion

Both specific heat and magnetic susceptibility results for $0 \leq x \leq 0.2$ point towards an increase in the hybridization between Ce and Al atoms, and therefore to an enhancement of the Kondo effect, with increasing Y concentration. The increase of T_K is manifested in the increase of Θ_{cw} , in the reduction of the magnetic entropy S_m around 7 K, and in the decrease in χ and C/T values at the lowest measured temperatures. The specific heat data can be compared in this regard with previous results for the heat capacity as a function of pressure of CeAl_3 (see Fig. 3.3) [67]. According to the comparison between Y doping and pressure dependence of the lattice parameters of $\text{Ce}_{1-x}\text{Y}_x\text{Al}_3$ and CeAl_3 , respectively, presented earlier, an Y doping level of $x = 0.1$ induces a change in the lattice volume corresponding to a chemical pressure P_V of 2.4 kbar (0.24 GPa). This sample shows an anomaly at 0.46 K, with $C(0.4 \text{ K})/T = 860 \pm 40 \text{ mJ/K}^2 \text{ Ce mol}$. A similar pressure (2.2 kbar) was applied on CeAl_3 by Brodale *et al.* [67], suppressing the anomaly in C/T and reducing both $C(0.4 \text{ K})/T$ and the extrapolated γ to 838 mJ/K² Ce mol. It is interesting that the values of $C(0.4 \text{ K})/T$ are the same within uncertainty in both cases, while the anomaly only appears in the Y doped sample. Also interesting is that values of C/T above the temperature of the anomaly T_m are more strongly reduced by Y substitution. The main differences between the application of chemical and hydrostatic pressures are a reduction in the number of Ce moments and a much slower decrease of the c lattice parameter with Y doping. Since the anomaly is still

present despite a reduction in Ce concentration, its rapid suppression in the case of CeAl₃ may be related to a stronger reduction of the *c* parameter with pressure.

The almost constant value of T_m for Y concentrations between $x = 0$ and $x = 0.2$, when compared to its rapid suppression between ambient pressure and 2.2 kbar in CeAl₃, cannot be reconciled in terms of Doniach's Kondo necklace model, and lacks a complete explanation. However, these results seem to indicate that interactions between the hexagonal planes strongly affect the magnetism in this system. In fact, magnetic susceptibility measurements in single crystals [76] revealed a large magnetic anisotropy, with χ below 40 K being larger along the *c* direction. The decrease in *c* is larger with pressure than as a function of Y concentration, significantly reducing the distance between hexagonal planes, increasing the hybridization between Ce and Al atoms in adjacent planes, and therefore suppressing magnetic order. A similar argument has been proposed for the hexagonal heavy-fermion compounds CePd₂Al₃ [139, 140] and CeCu₅ [141, 142] based on annealing, pressure, and doping studies on the Ce sites. In these two compounds, the intraplane hybridization is larger than that between planes ($J_{\perp} \gg J_{\parallel}$), while the opposite is true of CeAl₃, according to previous susceptibility and neutron scattering studies [76, 87]. Despite this difference, the strength of magnetic interactions in both cases seems to be dependent on the hybridization between hexagonal planes.

On the other hand, the lack of a suppression of T_m with Y doping appears to be consistent with recent ligand-site doping measurements on CeAl₃ by Corsépius *et al.* [61], where both an expansion and contraction of the lattice were found to enhance the anomaly in C/T . The authors argued that the absolute-value change in *c/a* was responsible for the development of this maximum. This ratio is related to the hybridization angles between Ce and Al atoms. Assuming that *c/a* in CeAl₃ roughly corresponds to the angle with optimum screening of *f* moments,

any variation in c/a will disturb the screening and will give rise to larger moments. The interactions between these moments then increases, allowing the development of magnetic anomalies in the specific heat.

6.4 Thermodynamic Measurements on $\text{Ce}_{0.8}(\text{La}_{1-x}\text{Y}_x)_{0.2}\text{Al}_3$ Alloys

6.4.1 Magnetic Susceptibility

In order to explore further the magnetic nature of the C/T anomaly in $\text{Ce}_{1-x}\text{La}_x\text{Al}_3$ alloys, an yttrium doping study was conducted on $\text{Ce}_{0.8}\text{La}_{0.2}\text{Al}_3$. The motivation was to determine the effect of keeping the lattice volume at a value close to that of CeAl_3 , while keeping the number of Ce moments at a constant, but reduced value, and to search for changes in properties due to intersite interactions. The lattice parameters for an Y concentration $x = 0.4$ are $a = 6.542 \pm 0.002 \text{ \AA}$ and $c = 4.616 \pm 0.004 \text{ \AA}$, both within error bars of those of pure CeAl_3 . Figure 6.28 shows the magnetic susceptibility per Ce mole of $\text{Ce}_{0.8}(\text{La}_{1-x}\text{Y}_x)_{0.2}\text{Al}_3$ alloys for Y concentrations $x = 0$, 0.09, and 0.4, along with data for CeAl_3 , up to 20 K. The maximum seen for $x = 0$ appears to shift towards lower temperatures (below 2 K), and the susceptibility values above the anomaly ($\geq 3 \text{ K}$) decrease with increasing Y concentration. There is also a small increase of $\chi(2 \text{ K})$ between $x = 0$ and $x = 0.09$ (see Table 6.5). This increase might be due to the observed decrease in the temperature position of the maximum, which will be discussed in the following section. Values of $\chi(2 \text{ K})$ for $x = 0.4$ and for CeAl_3 are very similar (differ by 2%). It seems that the similarity between the two values is coincidental, since data for $x = 0.4$ show a larger decrease between 2 and 10 K than that of the pure compound.

The inverse susceptibility of $\text{Ce}_{0.8}(\text{La}_{1-x}\text{Y}_x)_{0.2}\text{Al}_3$ ($x = 0$, 0.09, and 0.4) is illustrated in Fig. 6.29. The data follow a Curie-Weiss law above 150 K, and the calculated high-temperature effective moments are close to the Ce^{3+} value,

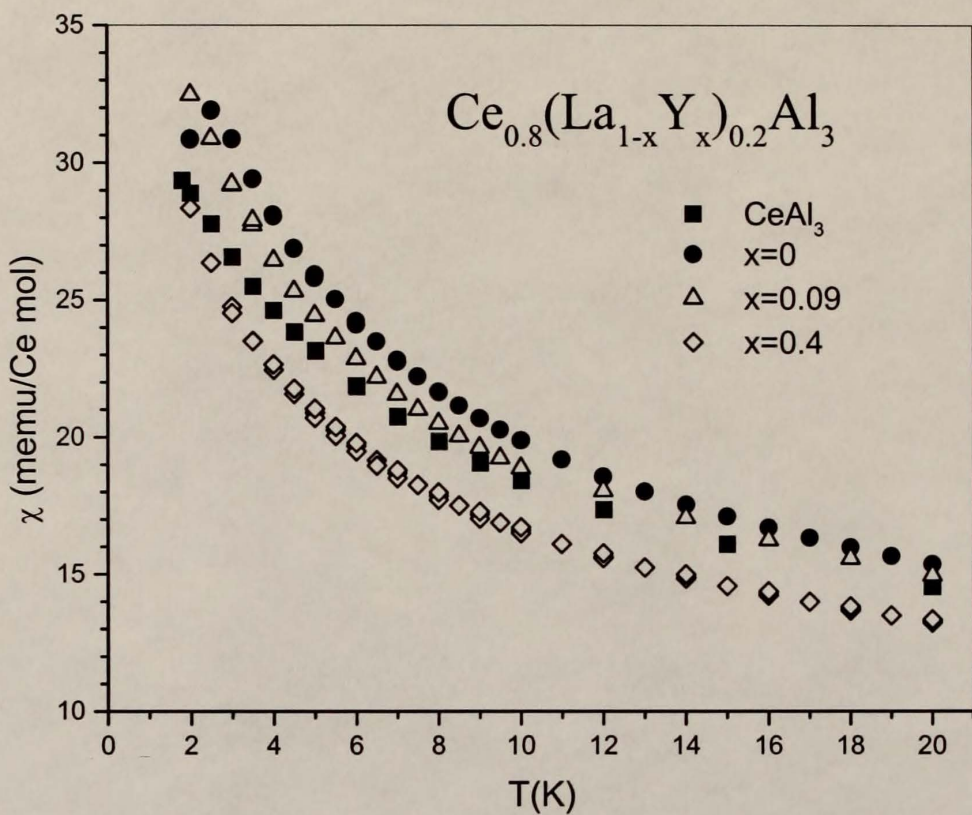


Figure 6.28: Low temperature magnetic susceptibility χ vs T for $\text{Ce}_{0.8}(\text{La}_{1-x}\text{Y}_x)_{0.2}\text{Al}_3$ alloys, $x = 0$, 0.09, and 0.4 ($H = 1 \text{ kG}$). Data for CeAl_3 are shown for comparison.

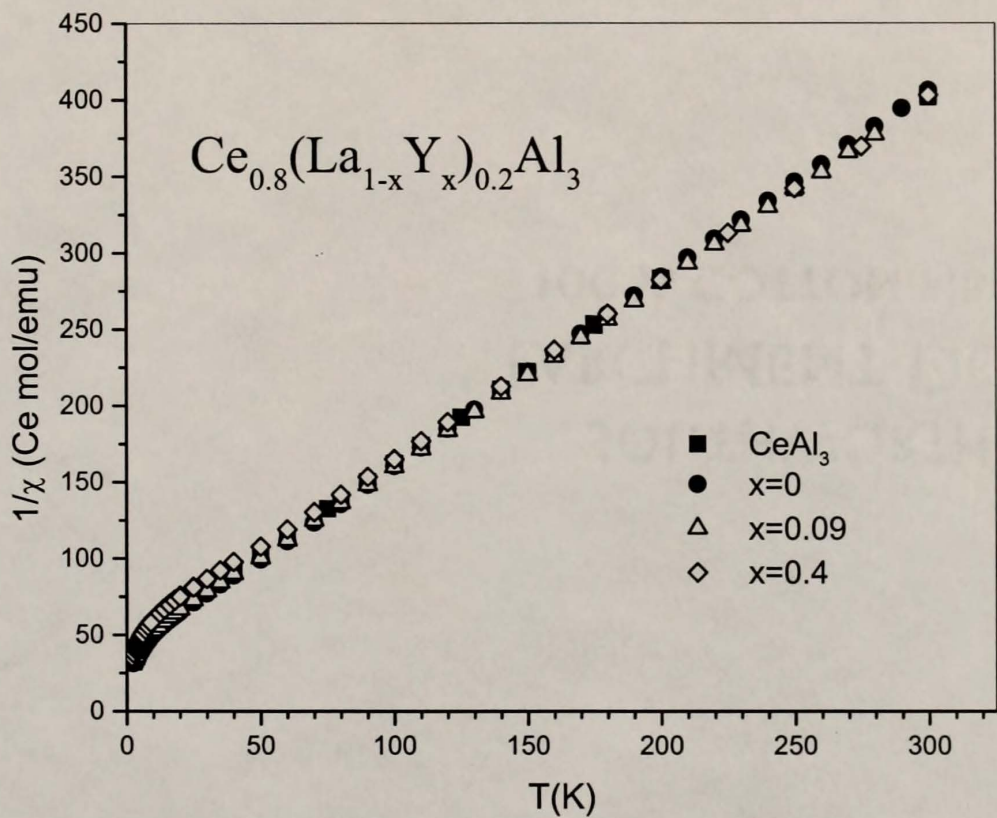


Figure 6.29: Inverse susceptibility vs temperature for $\text{Ce}_{0.8}(\text{La}_{1-x}\text{Y}_x)_{0.2}\text{Al}_3$ alloys, $x = 0, 0.09$, and 0.4 ($H = 1\text{ kG}$). Data for CeAl_3 are shown for comparison.

Table 6.5: Magnetic susceptibility parameters for $\text{Ce}_{0.8}(\text{La}_{1-x}\text{Y}_x)_{0.2}\text{Al}_3$ alloys, $x = 0, 0.09$, and 0.4 . Data for CeAl_3 are shown for comparison.

La x	χ (2 K) (memu/Ce mol)	μ_{eff} (μ_{B})	Θ_{cw} (K)
0	30.9	2.52	29
0.09	32.5	2.57	32
0.4	28.4	2.60	40
CeAl_3	28.9	2.53	29

$\mu_{\text{eff}} = 2.54 \mu_{\text{B}}$. The parameters obtained from a linear fit of $1/\chi$ vs T above 150 K are shown in Table 6.5. The negative Curie-Weiss temperature Θ_{cw} increases with Y concentration. Yttrium doping contracts the crystalline lattice, increasing the coupling between conduction and f electrons in the Kondo necklace model, and therefore increasing T_K . It should be noted that CeAl_3 has the same lattice volume as $x = 0.4$, and consequently a similar average hybridization. Yet, the larger value of Θ_{cw} obtained for $x = 0.4$ seems to indicate a higher T_K for this sample.

6.4.2 Specific Heat

Figure 6.30 shows the specific heat as C/T vs T for $\text{Ce}_{0.8}(\text{La}_{1-x}\text{Y}_x)_{0.2}\text{Al}_3$ ($x = 0, 0.09, 0.4$). Data for CeAl_3 is also shown for comparison. The behavior of C/T with Y concentration is somewhat analogous to that of $\text{Ce}_{1-x}\text{La}_x\text{Al}_3$ alloys between $x = 0$ and $x = 0.2$ with decreasing La content. The anomaly at 2.1 K is attenuated in magnitude and its temperature reduced with Y concentration. Yet, the C/T curve for $x = 0.4$ does not have a maximum down to the lowest temperature measured (0.4 K). Values of C/T at this temperature increase dramatically, approaching that of CeAl_3 at $x = 0.4$. The inset to the figure indicates that the specific heat at $x = 0.4$ shows no sign of the anomaly, as in pure CeAl_3 . The entropy between 0.4 and 4 K (area under the C/T vs T curves) clearly decreases from $x = 0$ to $x = 0.4$. A crossing of the C/T curves for the Y-doped samples can be observed around 4 K upon closer inspection of the data. Values of this quantity

above 4 K are highest for $x = 0.4$, which seems to indicate that the lost entropy is recovered at temperatures much larger than 10 K.

Based on the similarities between their lattice parameters, it is assumed that both CeAl_3 and $\text{Ce}_{0.8}(\text{La}_{0.6}\text{Y}_{0.4})_{0.2}\text{Al}_3$ also have a similar Kondo temperature. An estimate of T_K for the alloy with $x = 0.4$ can be obtained using the procedure described earlier for La-doped alloys, then compared to $T_K = 4 \text{ K}$ for CeAl_3 . The entropy $S_m(3 \text{ K})$ was obtained by fitting the data below 3 K to a power law and analytically integrating this function using the fit coefficients. A power-law behavior assumes a divergent value for γ . Therefore, the area calculated would correspond to an upper-limit value of $S_m(3 \text{ K})$, and a lower-limit value of T_K . The value obtained was $T_K = 4.4 \text{ K}$, slightly larger than T_K for CeAl_3 . This result is consistent with the larger value of Θ_{cw} obtained from the inverse susceptibility of $\text{Ce}_{0.8}(\text{La}_{0.6}\text{Y}_{0.4})_{0.2}\text{Al}_3$, and suggests that this alloy has a larger Kondo temperature than the undoped compound. A larger Kondo temperature for $x = 0.4$, despite having the same values of a and c as CeAl_3 , indicates that the average coupling J may not be exclusively dependent upon changes in the lattice constants.

Alloying of $\text{Ce}_{0.8}\text{La}_{0.2}\text{Al}_3$ with Y introduces random microstresses in the lattice which could change the average hybridization and suppress the specific heat anomaly. In order to investigate whether the suppression of this anomaly is indeed due to lattice stress, the specific heat of a pressed pellet made out of $\text{Ce}_{0.8}\text{La}_{0.2}\text{Al}_3$ powder was measured down to 1 K. Grinding of a sample into powder causes microscopic tensile and compressive stresses that can simulate effects associated with alloying and can also contribute to changes in the physical properties of a system with a pressure-sensitive ground state. Data for C/T on $\text{Ce}_{0.8}\text{La}_{0.2}\text{Al}_3$ bulk and pellet samples are shown in Fig. 6.31. The effects of grinding the sample are a broadening and an attenuation of the magnitude of the anomaly. The broadening of the anomaly indicates that simultaneous tension and compression

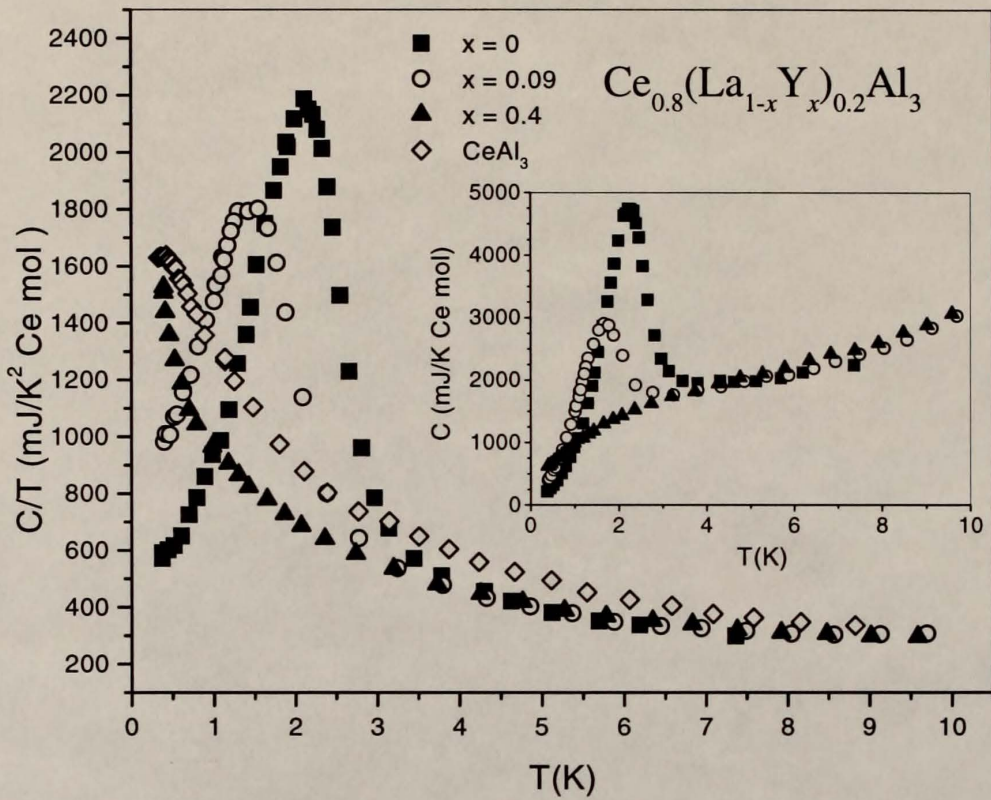


Figure 6.30: Specific heat plotted as C/T vs T for $\text{Ce}_{0.8}(\text{La}_{1-x}\text{Y}_x)_{0.2}\text{Al}_3$ ($x = 0, 0.09$ and 0.4). The specific heat of CeAl_3 in C/T form is also shown for comparison (data below 1 K for CeAl_3 by Andraka *et al.* [71]). The inset shows C vs T for $x = 0, 0.09$ and 0.4 .

of the lattice can be found at the microscopic level, leading to a possible distribution of temperatures T_m . The temperature of the maximum is slightly increased by about 0.2-0.3 K. Subsequent annealing of the pellet at 600°C for 24 hours partially restores the shape of the anomaly for the bulk sample. Therefore, the anomaly does not seem to be related to random stresses due to alloying. Rather, the reduction of such stresses by annealing was found to enhance the size of the anomaly.

Previous specific heat measurements have also been conducted on pellets of isostructural UPt₃ [143], CeAl₃ (B. Andraka and R. Pietri, unpublished), and Ce(Al_{0.97}Ga_{0.03})₃ [61]. An increase in temperature of the related anomaly in C was found in the latter two cases. In particular, when comparing the pellet data on Fig. 6.31 with measurements on a pressed pellet of CeAl₃, it is found that C/T values at 0.4 K for the pellet are significantly lower than those of bulk CeAl₃, while the corresponding values for Ce_{0.8}La_{0.2}Al₃ for both bulk and pellet samples remain essentially the same. This comparison suggests that values of γ for the more magnetic state of La $x = 0.2$ are less sensitive to random lattice stresses than those of CeAl₃, which has both a lower T_m and a higher T_K .

6.4.3 Discussion

Doping of Y on the Ce/La sites of Ce_{0.8}La_{0.2}Al₃ was found to be successful in restoring the lattice parameters corresponding to CeAl₃, as reported at the beginning of the chapter. The effect of reducing the number of Ce impurities while keeping the same lattice parameters as in the pure compound has been observed in both specific heat and susceptibility. The anomaly was suppressed towards lower temperatures by attempting to keep the hybridization constant (assuming J depends on a , c only) while increasing the distance between Ce atoms, therefore decreasing the RKKY interaction (see end of section). There seems to be an overall increase in both C/T and χ values at the lowest temperatures ($T \rightarrow 0$). The C/T

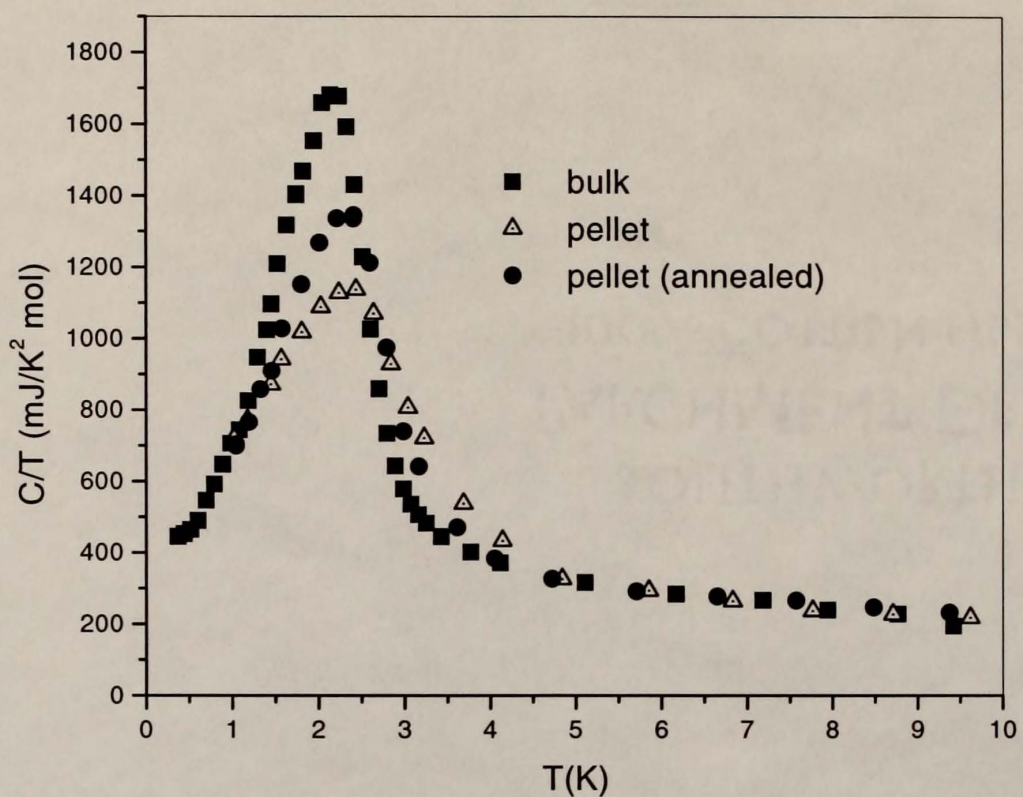


Figure 6.31: Specific heat plotted as C/T vs T for $\text{Ce}_{0.8}\text{La}_{0.2}\text{Al}_3$ bulk, pressed pellet, and post-annealed pellet samples.

anomaly visible in CeAl₃ at 0.4 K either completely disappears or shifts towards lower temperatures for an Y concentration $x = 0.4$. It seems that the intersite magnetic correlations, which depend on the overall number of Ce moments, play a crucial role in determining the strength of the energy scale giving rise to the anomaly in CeAl₃.

A uniform rise in C/T at the lowest measured temperatures is a signature commonly associated with non-Fermi-liquid behavior [12], where C/T is either a logarithmic function of the temperature, as in the Kondo disorder model [50, 49], or obeys a power law T^ν as in quantum critical ($\nu = 0.5$) [53, 55] and Griffiths phase ($0 \geq \nu \geq -1$) [58, 59] models. Specific heat results for $x = 0.4$ show no sign of a maximum in C/T down to 0.4 K, suggesting the presence of non-Fermi-liquid effects. In order to verify whether the temperature dependence of C/T for this alloy is consistent with any of the predictions from the above models, the data were plotted in semilog and log-log forms, and as C/T vs $T^{1/2}$. The data for C/T did not follow linear behavior on both semilog and $T^{1/2}$ forms. It rather roughly followed a power-law dependence in the limited temperature range of 0.4-1.7 K, with an exponent close to -0.5 (see Fig. 6.32). The magnetic susceptibility was also plotted in log-log form, with the data following linear behavior up to 30 K, as shown in Fig. 6.33. A fit of the data to a power-law dependence yielded an exponent of -0.33 .

In the Griffiths phase model [58], the specific heat is related to the magnetic susceptibility by a power law:

$$\frac{C(T)}{T} \propto \chi(T) \propto T^{-1+\lambda}, \quad (6.9)$$

where the parameter $\lambda < 1$ can be determined by a best fit through the data. A value of $\lambda = 1$ indicates Fermi-liquid behavior. The corresponding parameters

obtained from fits to C/T (0.4-1.7 K) and χ data, shown in Figs. 6.32 and 6.33, respectively, are $\lambda_C = 0.54$ and $\lambda_\chi = 0.67$.

The above values for λ are fairly close to each other, indicating a possible relation between C/T and χ . A similar analysis has been performed for two canonical non-Fermi-liquid systems: UCu_4Pd ($\lambda_C = 0.71$; $\lambda_\chi = 0.72$) and $\text{U}_{0.6}\text{Th}_{0.4}\text{Pd}_2\text{Al}_3$ ($\lambda_C = 0.84$; $\lambda_\chi = 0.63$) [59]. The former is a disordered ligand system with a cubic structure [144]; the latter a Kondo hole system with a hexagonal structure [145]. It is worth noting that the difference $|\lambda_C - \lambda_\chi|$ is larger in the hexagonal alloy, and may be due to anisotropy in its magnetic properties. The authors attributed this larger discrepancy to the polycrystalline nature of the sample, so that the measured susceptibility represents the average over different crystalline directions, and expected better agreement on single crystalline measurements. The difference of 0.21 observed for $\text{U}_{0.6}\text{Th}_{0.4}\text{Pd}_2\text{Al}_3$ is larger than that of polycrystalline $\text{Ce}_{0.8}(\text{La}_{0.6}\text{Y}_{0.4})_{0.2}\text{Al}_3$ ($|\lambda_C - \lambda_\chi| = 0.13$), indicating that a Griffiths phase model may describe the observed dependence in C/T and χ down to 0.4 K, provided that C/T follows a power law down to temperatures much lower than 0.38 K.

The validity of this description also depends on whether the alloy in question reproduces the physical scenario required for the formation of a Griffiths phase [58, 59]: magnetic anisotropy, disorder due to alloying, and the competition between Kondo and RKKY energy scales. The alloy $\text{Ce}_{0.8}(\text{La}_{0.6}\text{Y}_{0.4})_{0.2}\text{Al}_3$ seems to fulfill all of these requirements, since a strong magnetic anisotropy has been deduced from neutron scattering data [87] and magnetic susceptibility studies on single crystals [76]. Yet, measurements at lower temperatures (especially for C/T) are necessary in order to verify this interpretation.

The alloying procedure described in this section potentially demonstrates a novel method of inducing non-Fermi-liquid effects in antiferromagnetic Kondo lattices. The standard method consists of using alloying, pressure, or magnetic

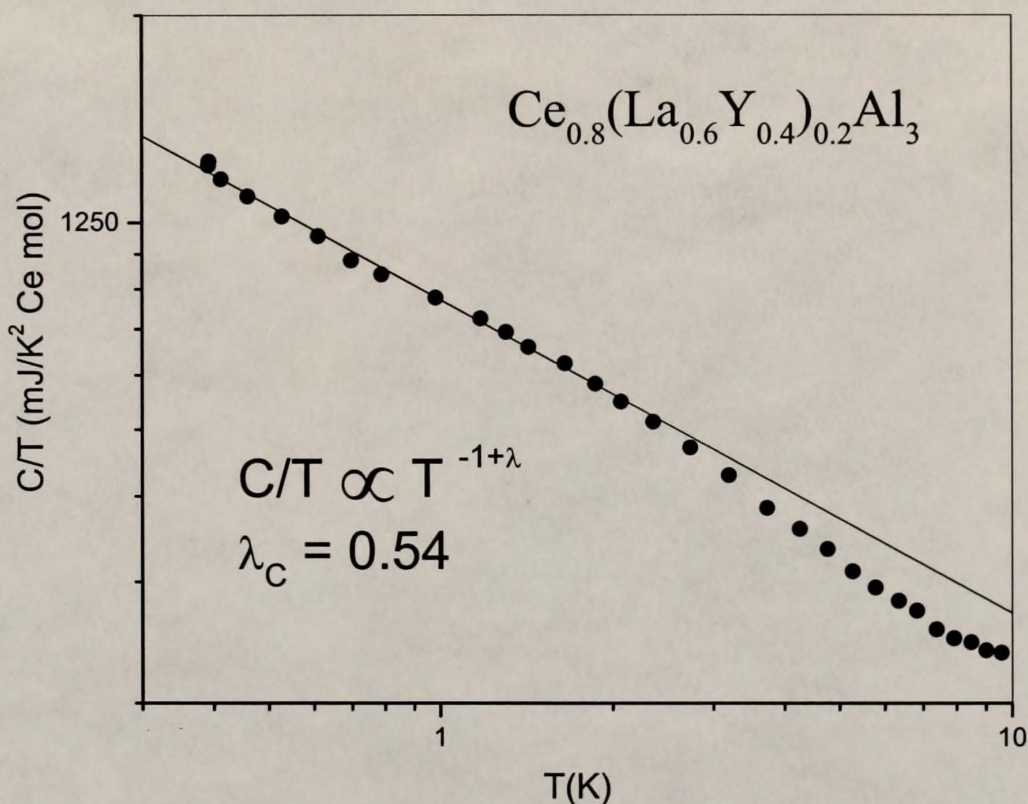


Figure 6.32: Log-log plot of C/T vs T for $\text{Ce}_{0.8}(\text{La}_{0.6}\text{Y}_{0.4})_{0.2}\text{Al}_3$. The solid line is a fit of the data below 1.7 K to the power-law equation shown in the graph.

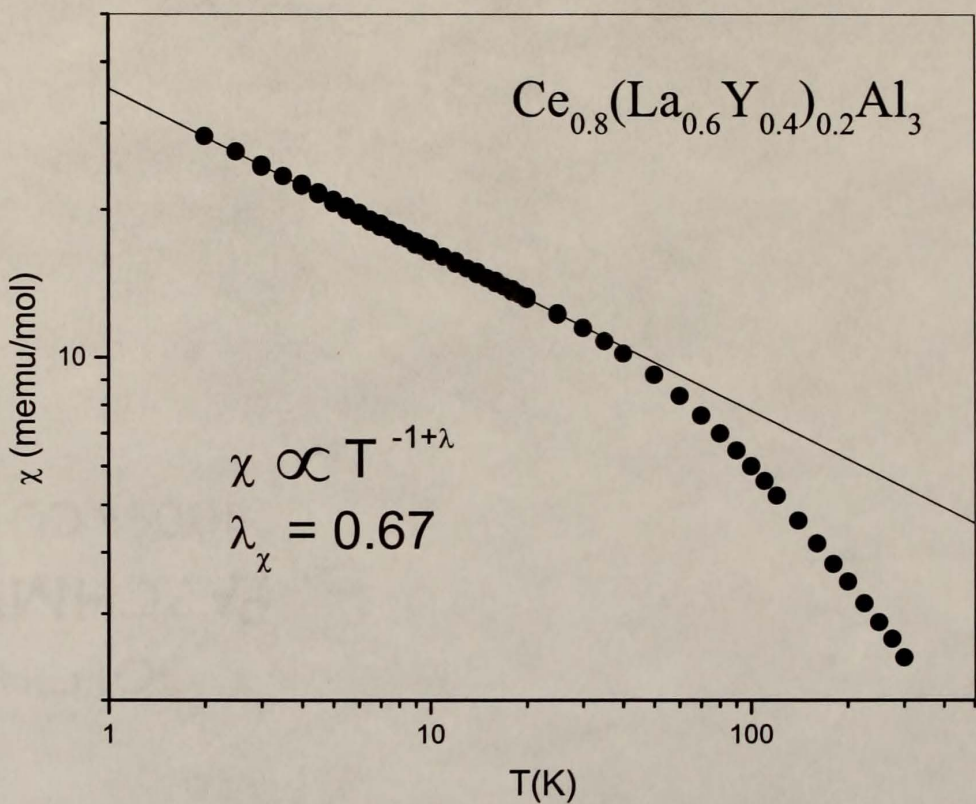


Figure 6.33: Log-log plot of χ vs T for $\text{Ce}_{0.8}(\text{La}_{0.6}\text{Y}_{0.4})_{0.2}\text{Al}_3$ at $H = 1\text{ kG}$. The solid line is a fit of the data below 30 K to the power-law equation shown in the graph.

fields as external parameters to significantly change the coupling J in order to drive T_m to zero. This novel method uses alloying on the impurity site, but with a combination of dopants that keeps the lattice parameters fairly constant with respect to the pure compound. Assuming J depends only on the value of a and c , changes in this quantity are minimized by using atoms with both smaller/larger atomic radii than that of f ions. At the same time, the reduction in the number of f ions increases the average distance R between them. The latter causes a decrease in the RKKY temperature ($T_{\text{RKKY}} \propto J^2/R^3$, see Chapter 2) with respect to the Kondo temperature, thus driving the system through a quantum critical point. In this manner, non-Fermi-liquid effects might be observed by only changing the distance between impurities without significantly affecting the value of J .

6.5 Heat Capacity of $\text{Ce}_{0.8}\text{La}_{0.2}\text{Al}_3$ and $\text{Ce}_{0.3}\text{La}_{0.7}\text{Al}_3$ in Magnetic Fields

As mentioned previously, recent neutron scattering and μ SR studies by Goremychkin *et al.* [15] on $\text{Ce}_{0.8}\text{La}_{0.2}\text{Al}_3$ revealed the absence of magnetic Bragg peaks, and estimated the upper limit of any possible ordered moment to be $0.05\mu_B$. The response function deduced from time-of-flight measurements changes from a quasi-elastic form to an inelastic form around 3 K, below which features develop in the specific heat and the magnetic susceptibility. This result [15] was attributed to weakly dissipative dynamics consistent with the anisotropic Kondo model (AKM) [35]. Data from μ SR experiments showed Lorentzian damping, with a temperature-dependent damping rate. The temperature at which the damping rate starts to diverge coincides with the temperature T_m of the maxima in C/T for $x = 0.2$, 0.7, and 0.9 samples, as previously described. The divergence was attributed to the development of static magnetic correlations, indicating the possibility of magnetic order of small moments, as seen in URu_2Si_2 [146]. In order to investigate further the applicability of the AKM to both CeAl_3 and $\text{Ce}_{0.8}\text{La}_{0.2}\text{Al}_3$, the effect of

magnetic fields up to 14 T on the linear coefficient γ and on the temperatures T_M and T_m of the maxima in C and C/T , respectively, was studied by specific heat measurements. Magnetic field measurements were also performed on $\text{Ce}_{0.3}\text{La}_{0.7}\text{Al}_3$ to study the effects on a more dilute $4f$ system.

6.5.1 Results

Figure 6.34 shows the specific heat of $\text{Ce}_{0.8}\text{La}_{0.2}\text{Al}_3$ in fields of 0, 5, 10, and 14 T. The phonon contribution was subtracted using the specific heat of LaAl_3 [128], and the remainder has been normalized to a mole of Ce. Data plotted as C/T vs T can be seen in Fig. 6.35. The main effect of the field is a strong reduction in the magnitude of the anomalies in C and C/T , but probably the most striking fact is the very weak field dependence of the temperature position of the anomalies. A pronounced peak in C located at $T_M \simeq 2.3$ K for $H = 0$ is replaced by a shoulder near 2.1 K for $H = 14$ T. The peak in C/T also shifts slowly with field, with T_m decreasing from 2.1 K at 0 T to 1.7 K at 14 T (see Fig. 6.36). The difference between T_M and T_m grows with applied field. A difference of the same order has been observed in zero field for $\text{Ce}_{1-x}\text{La}_x\text{Al}_3$ alloys with $x < 0.2$, where $T_M - T_m$ grows with decreasing La concentration x [71]. In this respect, an increase in the magnetic field has a similar effect to a decrease in x .

Another important result is an increase with field of C/T values at temperatures below 1 K, suggesting a partial restoration of the heavy-fermion state present in pure CeAl_3 . The large nuclear moments of ^{27}Al and ^{139}La ($\mu_n = 3.64$ and $2.76 \mu_N$, respectively) contribute in part to the enhancement of C/T at the lowest temperatures and the largest fields. In fact, the 14-tesla C/T data display a low-temperature tail which is due in part to a nuclear hyperfine contribution $C_n/T = N_A \mu_n H^2 / 3k_B T^3$ (e.g., see Ref. [147]). The combined hyperfine contribution from ^{27}Al and ^{139}La at 0.4 K and $H = 14$ T is around 25 mJ/K² mol (per total mole). None of the curves at lower fields show a similar upturn. The linear specific

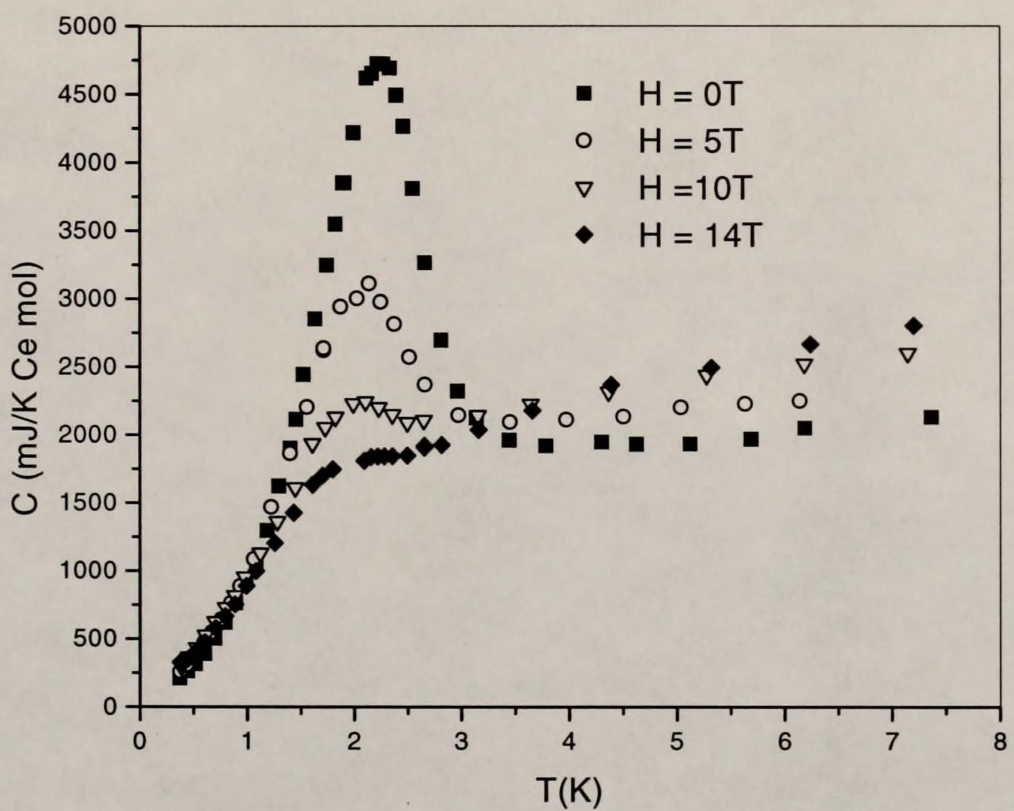


Figure 6.34: Specific heat vs temperature for $\text{Ce}_{0.8}\text{La}_{0.2}\text{Al}_3$ at $H = 0, 5, 10$, and 14 T .

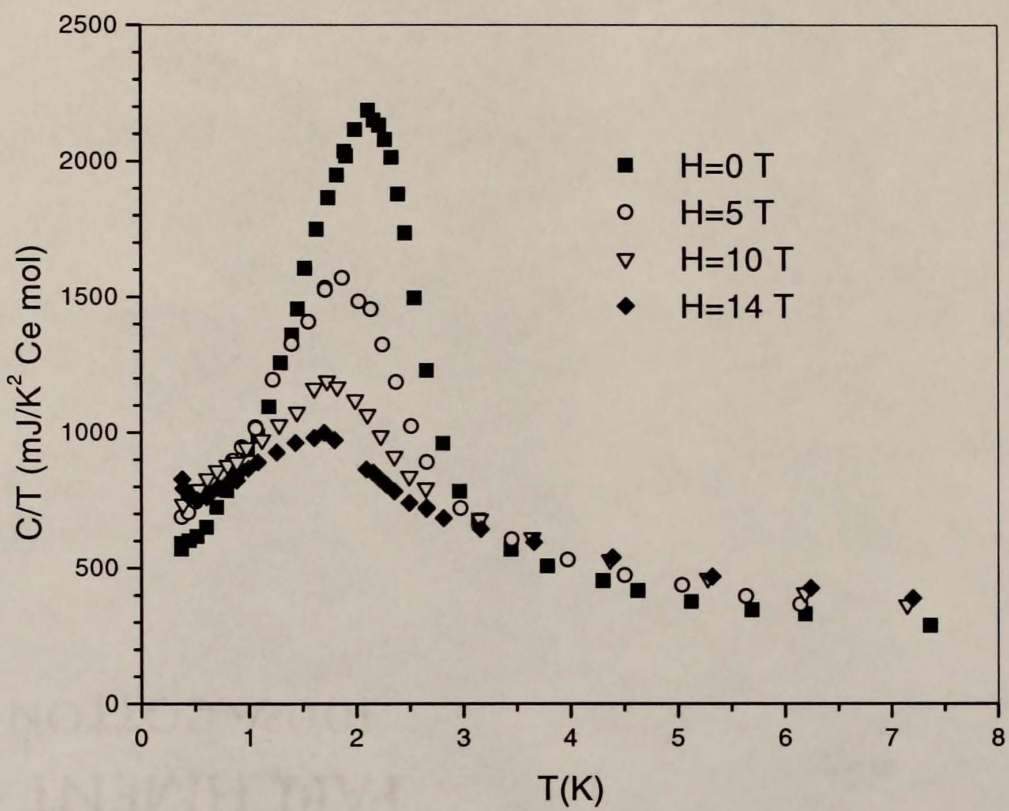


Figure 6.35: Specific heat plotted as C/T vs T for $\text{Ce}_{0.8}\text{La}_{0.2}\text{Al}_3$ at $H = 0, 5, 10$, and 14 T .

heat coefficient γ was extracted from a linear fit to C/T vs T^2 below 1 K, except for the data at 14 T, where γ was determined from the slope of CT^2 vs T^3 below 1 K. As illustrated in Fig. 6.36, γ seems to saturate above $H \geq 10$ T. The error bars for γ were calculated by taking into account the effect of both experimental and linear regression uncertainties.

The specific heat of $\text{Ce}_{0.3}\text{La}_{0.7}\text{Al}_3$, plotted as C/T vs T , is shown in Fig. 6.37. In this sample, the magnitude of the peak is strongly attenuated at $H = 6$ T, and it completely disappears at larger fields. The temperature of the maximum T_m is reduced by about 0.2 K in a 6 T field, a relatively larger rate than for $x = 0.2$. A similar trend has been observed in the field dependence of the anomaly of pure CeAl_3 [68], where γ was found to increase slightly and the anomaly was found to disappear at fields of order 5 T. In contrast to the data for $x = 0.2$, C/T values at 0.4 K for this sample with a lower T_m are significantly reduced, from about 2400 mJ/K² Ce mol at $H = 0$ to almost 1000 mJ/K² Ce mol at 14 T. The small rise in C/T values below 0.6 K for the 10 and 14 T data may be described in terms of a Schottky contribution from the ²⁷Al nuclei. The observed reduction of $C(0.4\text{ K})/T$ with field points to a possible decrease of γ in magnetic field. All C/T curves seem to cross above 1.5 K, suggesting that the entropy associated with the maximum shifts toward higher temperatures. Finally, a shallow maximum appears around 1 K for $H = 10$ T, and at 1.3 K for $H = 14$ T. A possible explanation for this feature will be provided in Chapter 7.

6.5.2 Discussion

The magnetic-field specific heat for $x = 0.2$ was analyzed in terms of the anisotropic Kondo model (AKM) for a single magnetic impurity. The data was compared to numerical results for the specific heat of the AKM. The model, previously introduced in Chapter 2, assumes an anisotropic exchange interaction $J_z S_z s_z + J_{\perp} (S_x s_x + S_y s_y)$ between the impurity spin \mathbf{S} and the net conduction-

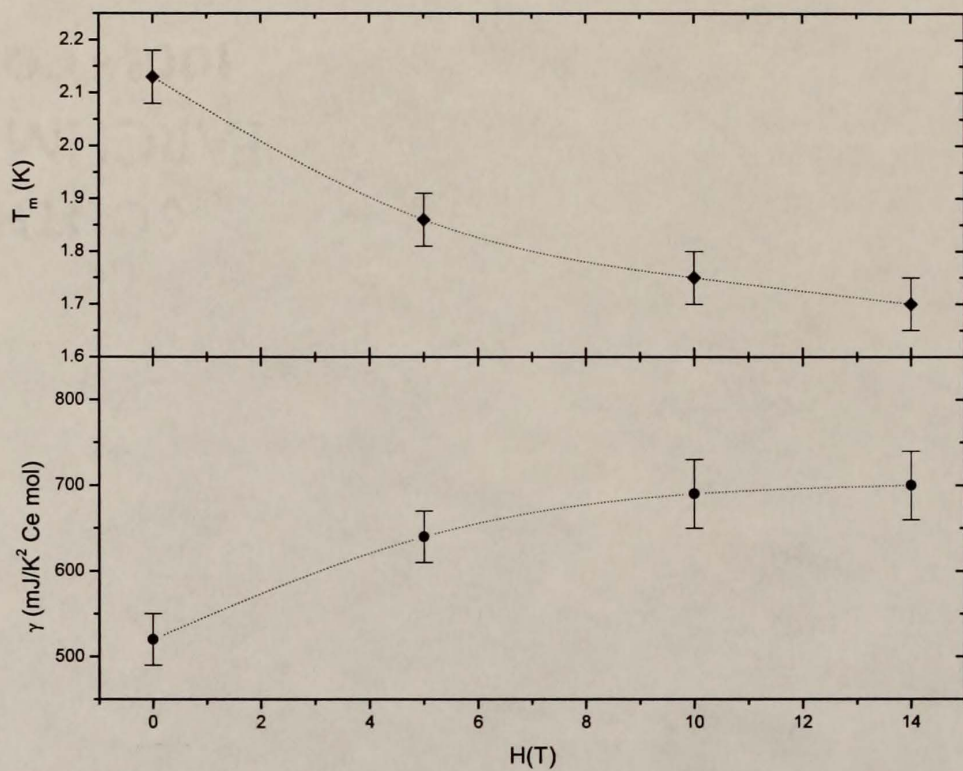


Figure 6.36: Temperature of the maximum in C/T , T_m vs H and γ vs H for $\text{Ce}_{0.8}\text{La}_{0.2}\text{Al}_3$, where T_m is the temperature of the maximum in C/T . The dotted lines are guides to the eye.

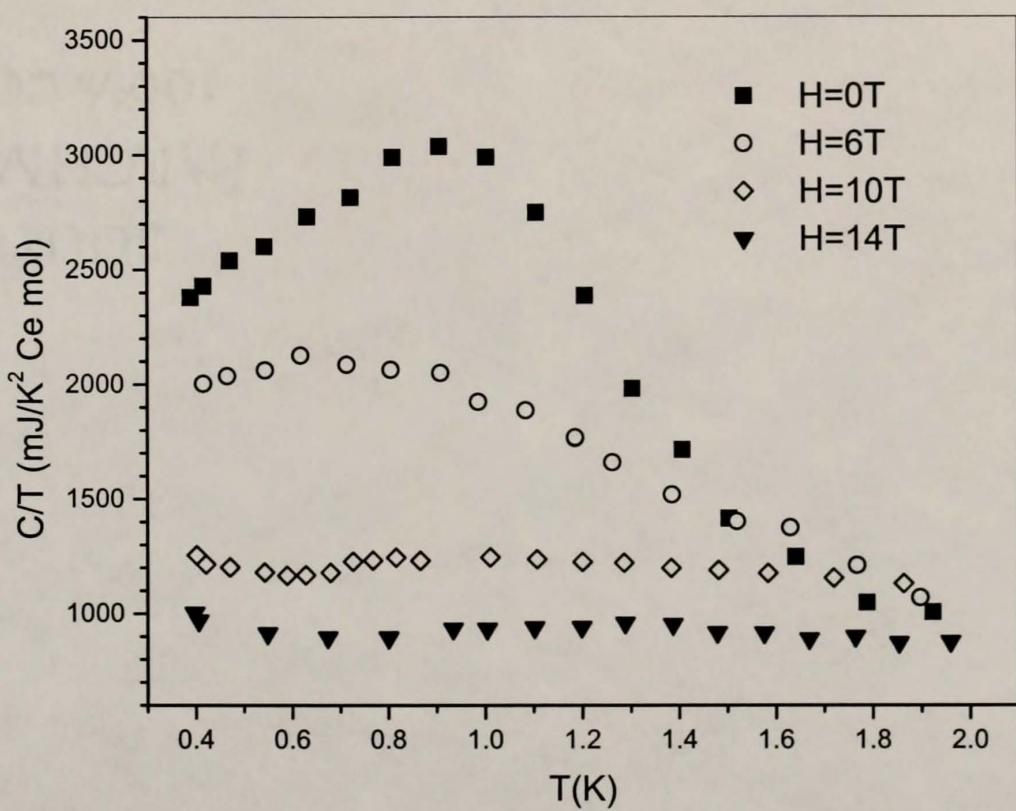


Figure 6.37: Specific heat plotted as C/T vs T for $\text{Ce}_{0.3}\text{La}_{0.7}\text{Al}_3$ at $H = 0, 6, 10$, and 14T .

electron spin \mathbf{s} at the impurity site. The AKM has been proposed as a description for the thermodynamic properties of both $\text{Ce}_{0.8}\text{La}_{0.2}\text{Al}_3$ and CeAl_3 . A strong dependence on field orientation in the magnetic susceptibility of some CeAl_3 single crystals [76] suggests anisotropic behavior corresponding to $J_z \gg J_{\perp} > 0$, with the magnetic z direction along the crystallographic c axis. Assuming that the couplings J_z and J_{\perp} are dependent only on the values of a and c , the above scenario corresponds to $c < a$ ($c/a < 1$; recall $c/a = 0.705$ for CeAl_3).

The AKM is known to be equivalent to a number of other models in the limit of low energies. For more than a decade, a mapping [148] of the spin-boson model with Ohmic dissipation onto the AKM has been used [35, 36, 37] to deduce physical properties of dissipative two-level systems [34] from numerical calculations originally performed for the AKM. These studies have shown that under certain conditions, the impurity contribution to the zero-field heat capacity of the AKM exhibits a peak in both C and C/T , resembling the anomalies described in Figs. 6.34 and 6.35. The temperature of the peak in C/T is given by $T_m = \alpha^* R/\gamma$, where R is the gas constant and α^* is a function of $\varrho_0 J_z$ (see Chapter 2).

The value $\alpha^* = \gamma T_m/R = 0.13$ for $\text{Ce}_{0.8}\text{La}_{0.2}\text{Al}_3$ in zero field is in agreement with the estimate of Ref. [15]. It was calculated from the observed peak position $T_m = 2.1$ K and the linearly extrapolated $\gamma = 520$ J/K²Ce mol. Both α^* and T_m were used as inputs for a numerical renormalization-group calculation [149] of the specific heat of the AKM. Figure 6.38 shows the predicted behavior of C/T with applied magnetic field along the z axis, under the assumption that the impurity and the conduction electrons have g factors $g_i = g_e = 2$ [149].

The numerical data show three main trends with increasing field. First, the anomaly in C/T becomes broader and lower. Second, there is a marked shift of the maximum toward higher temperatures. Third, C/T decreases significantly at temperatures below the zero-field value of T_m . The effect in γ is greater than that

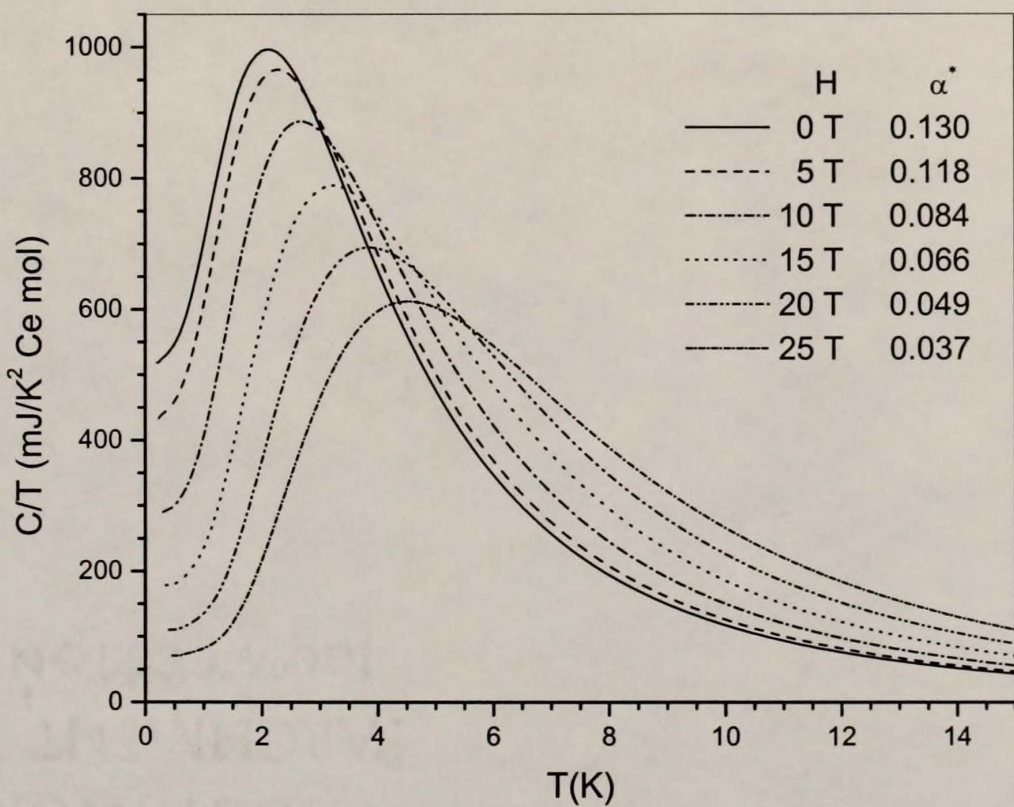


Figure 6.38: Numerical solutions of C/T vs T for the anisotropic Kondo model in various magnetic fields H [149], with model parameters chosen so that $\alpha^* = 0.130$ for $H = 0$ (see text for details).

Table 6.6: Values of the specific heat coefficient γ , the peak temperature T_m , and $\alpha^* = \gamma T_m / R$ (where R is the gas constant) for $\text{Ce}_{0.8}\text{La}_{0.2}\text{Al}_3$ in different magnetic fields H .

$H(\text{T})$	γ (mJ/K ² Ce mol)	$T_m(\text{K})$	α^*
0	520 ± 30	2.13 ± 0.05	0.133 ± 0.008
5	640 ± 30	1.86 ± 0.05	0.143 ± 0.008
10	690 ± 40	1.75 ± 0.05	0.145 ± 0.009
14	700 ± 40	1.70 ± 0.05	0.143 ± 0.009

in the peak position, so that $\alpha^*(H) = \gamma(H)T_m(H)/R$ decreases monotonically with increasing magnetic field, as shown in the legend of Fig. 6.38.

It is important to keep in mind that these numerical results are applicable only to single-crystal $\text{Ce}_{0.8}\text{La}_{0.2}\text{Al}_3$, with a magnetic field along the c axis. The justification for comparing to the polycrystalline data assumes a basal-plane g factor $g_i = 0$ for the Ising-like, crystal-field ground state of Ce^{3+} in CeAl_3 [87]. The specific heat data for the polycrystal then constitutes a weighted average of single-crystal results over fields $H \geq 0$ [149].

Both the shift of T_m to higher temperatures and the decrease in low temperature C/T values are in stark contrast with experiment. The temperature T_m is weakly depressed in $\text{Ce}_{0.8}\text{La}_{0.2}\text{Al}_3$, while C/T increase slightly below 1 K. Moreover, these two trends keep α^* relatively constant up to a field of 14 T (see Table 6.6), which goes against the prediction of the AKM.

The specific heat data of $\text{Ce}_{0.3}\text{La}_{0.7}\text{Al}_3$ also do not seem to follow the predicted field dependence of C/T for the AKM. The suppression of the maximum in this sample towards lower temperatures from $H = 0$ to $H = 6$ T is in disagreement with Fig. 6.38, and tends to rule out a description solely in terms of the AKM. On the other hand, there is a significant decrease in the electronic coefficient, a trend which is at least in qualitative agreement with the model. This behavior is quite different from that observed in $\text{Ce}_{0.8}\text{La}_{0.2}\text{Al}_3$.

The preceding comparisons question the reliability of the AKM as a sole description of $\text{Ce}_{1-x}\text{La}_x\text{Al}_3$ alloys in magnetic fields. The lack of a description exclusively in terms of this model may be due to the neglect of magnetic correlations around the temperature of the maximum, as identified in recent μSR studies [15]. The presence of magnetic correlations could point towards long-range order of small moments, as seen in URu_2Si_2 [146]. This latter compound has an ordered moment $\mu_{\text{eff}} = 0.04 \pm 0.01 \mu_B$. In addition, the peak associated with its T_N does not broaden in magnetic fields, and the Néel temperature T_N follows a power-law field dependence, $|T_N(0) - T_N(H)| \propto H^\nu$, where $\nu = 2$. Another explanation might be that the magnetic correlations are short-ranged, and therefore not easily detected by neutron diffraction. Nevertheless, the above results support a theoretical scenario based on small-moment magnetism instead of on the AKM.

The extremely low rate of reduction of the temperature position of the anomaly in the specific heat of $\text{Ce}_{0.8}\text{La}_{0.2}\text{Al}_3$ with field remains to be understood. The temperature T_m follows a field dependence with an exponent $\nu < 1$ (see Fig. 6.36), and the anomaly broadens significantly between 0 and 14 T, indicating a different behavior than the one expected for long range order of small moments in heavy fermions, according to studies on URu_2Si_2 . In addition, both T_M and T_m are depressed in an applied field at a much lower rate than is the Néel temperature in antiferromagnetic, Ce-based heavy-fermion systems. For example, in $\text{CeCu}_{5.2}\text{Ag}_{0.8}$, T_N is reduced from 0.7 K to 0 K in a field of about 2.5 T [150]. On the other hand, magnetic fields have a stronger effect on both the magnitude and the temperature of the anomaly in $\text{Ce}_{0.3}\text{La}_{0.7}\text{Al}_3$ than for $x = 0.2$. An estimate of the exact rate of change of T_m with field in this sample proved to be rather difficult, since its maximum broadens significantly between $H = 0$ and 6 T, and its temperature position is very close to the low temperature limit of the data.

Finally, values of C/T at the lowest measured temperatures (0.4 K) showed different behavior in $\text{Ce}_{0.8}\text{La}_{0.2}\text{Al}_3$ and $\text{Ce}_{0.3}\text{La}_{0.7}\text{Al}_3$ for the range of fields studied. These results suggest that the electronic coefficient γ for $x = 0.2$ has a different field dependence than that for $x = 0.7$. The magnetic field dependence of γ in heavy-fermion antiferromagnets has not been thoroughly studied in the past. Both an increase and a decrease in field have been reported in different compounds. Of particular interest are systems which show an initial increase in γ followed by a decrease at high fields (e.g. CePb_3 , see Chapter 7). Non-Fermi-liquid behavior has been observed in some alloys at fields corresponding to a maximum in this coefficient.

The variation of γ with applied field depends on the relative strength of the energy scales T_K and T_{RKKY} with respect to the Zeeman energy μH . Small values of γ in antiferromagnetic heavy fermions are due to changes in the excitation spectrum with respect to the nonmagnetic Fermi liquid. The application of a magnetic field leads to both a suppression of antiferromagnetic order, which favors an increase in γ , and a Zeeman splitting of the Kondo resonance, which favors a reduction of γ . The relative magnitude of these two effects with respect to μH determines the observed trend in γ vs H . In particular, if $T_K \ll T_{\text{RKKY}}$, as in $\text{Ce}_{0.3}\text{La}_{0.7}\text{Al}_3$, the smaller Kondo temperature leads to a large decrease in field, enough to overwhelm the expected increase due to suppression of magnetic order. On the other hand, if $T_K \sim T_N$, as in $\text{Ce}_{0.8}\text{La}_{0.2}\text{Al}_3$, the increase in γ due to the suppression of magnetic order is larger than the decrease from the suppression of the Kondo effect at low fields, so that an initial increase, followed by a decrease of the electronic coefficient at high fields (of order 20 T), is expected.

CHAPTER 7

MAGNETIC FIELD STUDY OF CePb₃ ALLOYS

The goal of this chapter is to address the subjects discussed in Chapter 4 through the study of CePb₃ alloys in magnetic fields. An investigation of the magnetic state of CePb₃ would help describe the role of magnetic order in the formation of the heavy-fermion state through the evolution of the Fermi-liquid parameters A and γ . Also, specific heat measurements of nonmagnetic Ce_{0.6}La_{0.4}Pb₃ would provide insight into the single-ion properties in magnetic fields. The chapter starts with results on the specific heat of CePb₃ in magnetic fields. The magnetic field dependence of the specific heat of Ce_{0.6}La_{0.4}Pb₃ will then be compared to the predictions of existing single-impurity models to further explore the feasibility of such a description on a concentrated system.

7.1 Specific Heat of CePb₃ in Magnetic Fields

The CePb₃ polycrystal used for specific heat measurements was synthesized by arc-melting following the procedure described in Chapter 5. No additional secondary phases were found by x-ray diffraction. Special care was taken to minimize exposure of the sample to air before x-ray diffraction measurements. Contact with oxygen in air causes Pb tends to segregate on the surface. This segregation has been detected from the formation of time-dependent diffraction peaks corresponding to the structure of Pb [151]. The calculated lattice parameter was $a = 4.868 \pm 0.001$ Å, in agreement with previously published values [92]. Magnetic susceptibility and specific heat data in zero field were also consistent with previous results.

The specific heat data below 2 K in magnetic fields from 0 to 14 T are shown as C/T vs T in Fig. 7.1. The specific heat of LaPb_3 , mostly due to the lattice, was not subtracted from the CePb_3 data since its contribution is negligible over this temperature range. The antiferromagnetic peak is suppressed up to a field of 6 T, with T_N reduced from 1.1 K to around 0.7 K. There is no clear sign of the transition for fields above 7 T. The rate of suppression of T_N decreases significantly between 5 and 6 T, so the absence of a maximum for 7 T implies that it is strongly attenuated at these fields, rather than shifted towards lower temperatures. The field-induced transition, which is strongest in the (110) direction, [98, 100, 103] could not be detected on this polycrystal measurement. A broad shoulder above 1 K was found on the 10 and 14 T data. It is apparently unrelated to the field-induced transition and shifts to higher temperatures with applied field. A similar structure was detected at 16.1 T by Fortune *et al.* [94]. A possible origin of this feature will be discussed at the end of the chapter.

An $H - T$ phase diagram can be constructed using the temperature of the maximum in C/T , as illustrated in Fig. 7.2. The corresponding temperature of the maximum in C vs T is slightly larger for $H \neq 0$, the difference between them increasing with field. Figure 7.2 also compares the phase diagram from specific heat measurements with that obtained from the magnetoresistance along the (110) direction on a single crystal [100]. The dashed line represents the first-order transition between an incommensurate antiferromagnetic (AF) phase and the field-induced so-called ‘spin-flop’ (SF) phase. At higher fields, the field-induced phase gives way to a ferromagnetically-polarized paramagnetic (PM) phase at low temperatures. The error bars on the data points represent the estimated uncertainty in the determination of the temperature of the maxima at different fields, increasing with the width of the peak. As the figure illustrates, measurements on a polycrystal differ from those taken along (110) since the former constitute an average

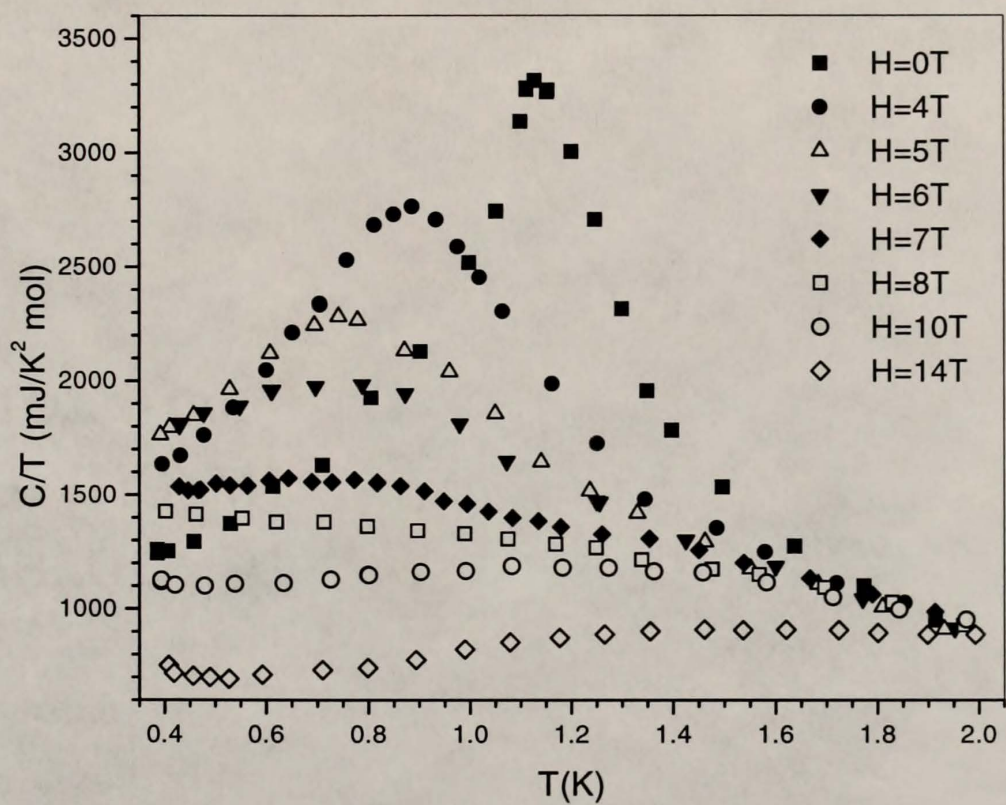


Figure 7.1: Specific heat plotted as C/T vs T for CePb₃ below 2 K in magnetic fields $H = 0, 4, 5, 6, 7, 8, 10$, and 14 T.

over all crystallographic directions. Since the field-induced transition is strongly detected only along (1 1 0), its transition temperature could not be found on these measurements.

The field dependence of the electronic specific heat coefficient γ is shown in Fig. 7.3. Values of γ were determined from a linear fit to C/T vs T^2 data below the maximum for $H \leq 6$ T, and from the values of C/T at 0.4 K for $H \geq 7$ T. Above this field, C/T values do not vary appreciably below 0.8 K. The error bars were extracted from the propagation of both regression and experimental uncertainties. Data for 10 and 14 T both exhibit a small tail below 0.5 K. The temperature dependence of this feature can be described by the nuclear Schottky contribution from Pb, $C_n/T \propto T^{-3}$. This contribution is still smaller than the uncertainty in the measurement at high fields ($\sim 10\%$). The electronic coefficient initially increases with field, reaching a maximum of 1770 mJ/K² mol at 6 T. The small decrease obtained for γ at 1 T is within the uncertainty of the results. The maximum in γ vs H coincides with the attenuation of the antiferromagnetic transition, as seen in Fig. 7.1. The coefficient then decreases for higher fields, with a value around 600 mJ/K² mol at 14 T.

The trend followed by the field dependence of γ is very similar to that of the square coefficient of the resistivity A in magnetic fields obtained from magnetoresistance measurements along (1 1 0) [100]. As seen in Fig. 7.4, A follows an initial increase with applied field, reaching a maximum at 5 T instead of 6 T as in γ vs H . This discrepancy might be due to differences between single-crystal and polycrystalline measurements. The obtained specific heat coefficients represent averages over all crystallographic directions. As the field is rotated 10° away from (1 1 0), the maximum in A becomes less pronounced and its field position slightly increases, consistent with an attenuation of the AF-SF transition. There is also a small maximum in A vs H observed at 10 T. A similar maximum could

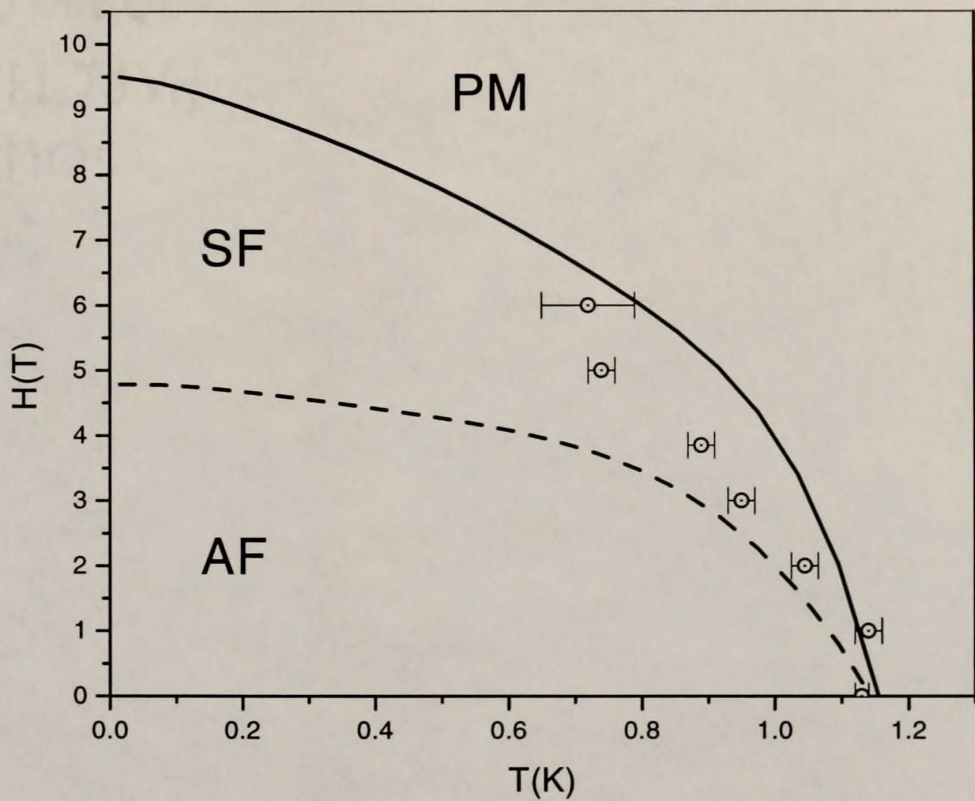


Figure 7.2: Phase diagram ($H - T$) for CePb₃. The data points are obtained from the temperature of the maximum in C/T vs T . The solid and dashed lines follow the phase diagram obtained from single-crystal magnetoresistance measurements along the (1 1 0) direction [100].

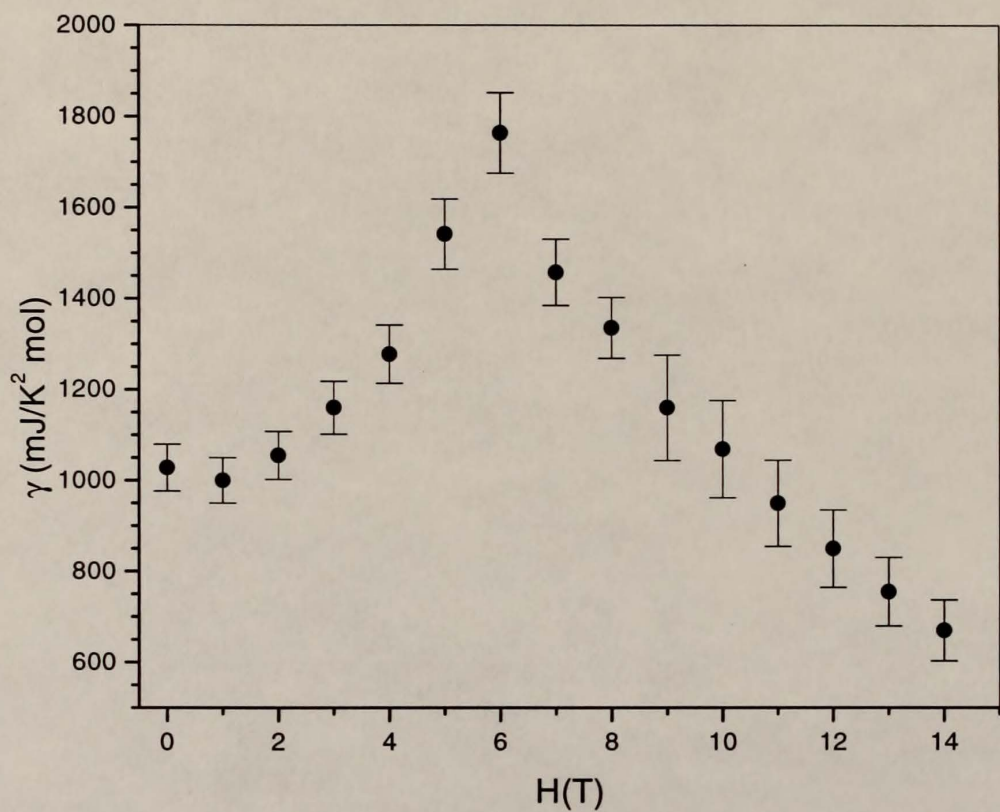


Figure 7.3: Magnetic field dependence of the electronic specific heat coefficient γ of polycrystalline CePb_3 .

not be deduced from the determination of γ at different fields. The two maxima in the field dependence of the A coefficient coincide with the AF-SF (5 T) and SF-PM (10 T) phase transitions detected in the magnetoresistance curves below 150 mK.

The preceding discussion assumes that the increase in A with field is due to the proximity to a spin-flop transition. In fact, the sharpness of the maximum in A vs H along (110) is consistent with the appearance of a phase transition. However, a field-induced spin-flop phase has not yet been confirmed by neutron scattering experiments. The maximum in γ vs H can also be related to the competition between relevant energy scales in heavy-fermion antiferromagnets (see Chapter 6, section 6.5.2). At small fields compared to T_K , the antiferromagnetic and Kondo entropies redistribute in such a way to enhance the values of γ . At higher fields, the antiferromagnetic state is suppressed, and the electronic coefficient decreases due to Zeeman splitting of the Kondo resonance.

The A coefficients obtained from magnetoresistance data along (110) were used to obtain the field dependence of the ratio A/γ^2 . A plot of A/γ^2 vs H is shown in Fig. 7.5. The dotted line corresponds to the average value for heavy-fermion systems obtained by Kadowaki and Woods [101], $A/\gamma^2 = 1 \times 10^{-5} \Omega \text{ cm K}^2 \text{ mol}^2/\text{J}^2$. This value has been postulated as a universal value for nonmagnetic heavy-fermion materials. The figure reveals that A/γ^2 is nearly constant for fields $H \geq 6 \text{ T}$, and that these values are only slightly higher than the Kadowaki-Woods ratio. A similar result was obtained for CeCu_{5.9}Au_{0.1} [114]. This alloy exhibits non-Fermi-liquid behavior in zero field, but for $H \neq 0$ the ratio A/γ^2 is constant and close to the postulated universal value. Figure 7.5 also shows a significant increase of A/γ^2 in the antiferromagnetic state ($H < 6 \text{ T}$), with a value around $4.6 \times 10^{-5} \Omega \text{ cm K}^2 \text{ mol}^2/\text{J}^2$ at 1 T.

The enhancement of A/γ^2 in CePb₃ for $H < 6 \text{ T}$ is comparable to values reported for systems in which heavy electrons coexist with magnetic order (see

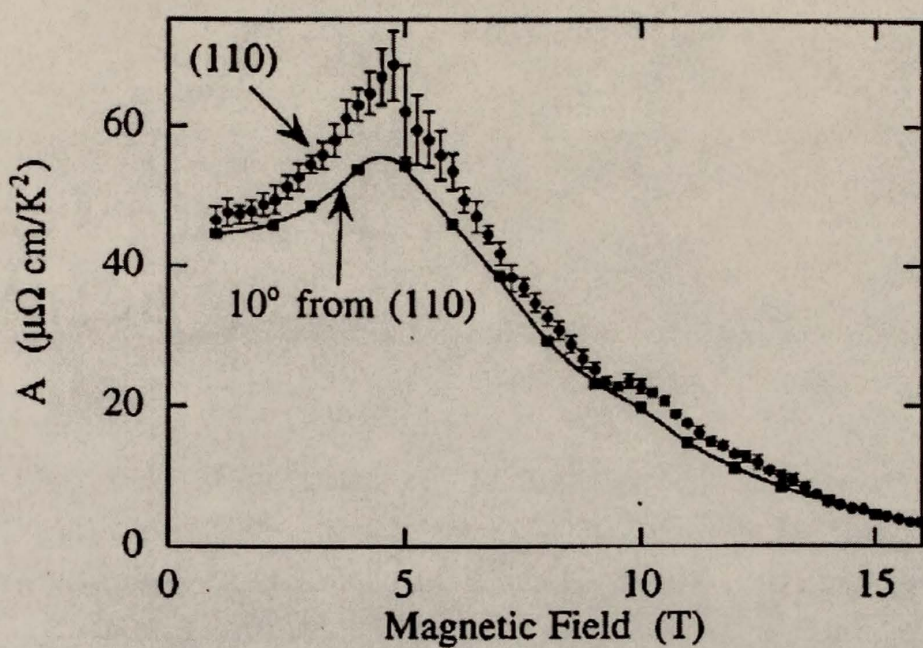


Figure 7.4: Magnetic field dependence of the square coefficient of the resistivity A , with the field along (110) and 10° away from (110) [100].

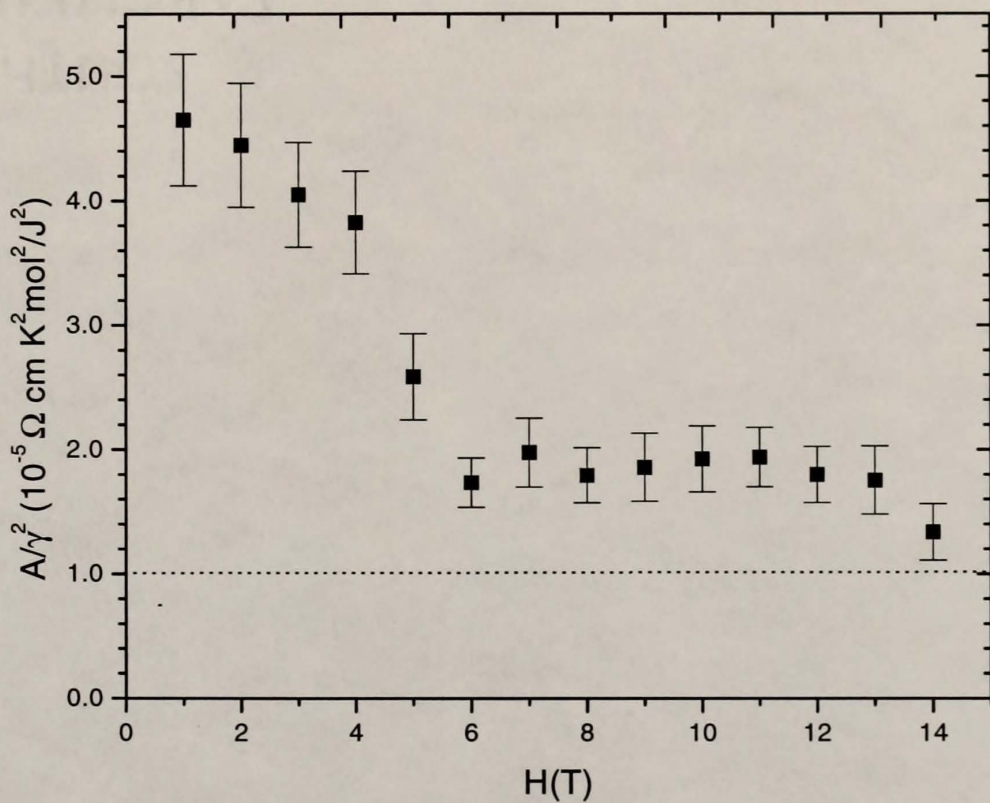


Figure 7.5: Magnetic field dependence of A/γ^2 . Values of A were extracted from previous magnetoresistance studies [100].

Table 7.1: Values of A/γ^2 for several magnetically ordered $4f$ heavy-fermion compounds (T_N of order 1 K).

Compound	A/γ^2 ($\Omega \text{ cm K}^2 \text{ mol}^2/\text{J}^2$)
CeAl ₂	5×10^{-5} [153]
CeAuAl ₃	10×10^{-5} [154]
CePd ₂ In	3×10^{-5} [155]
YbPdBi	30×10^{-5} [156]

Table 7.1). A model based on antiferromagnetic spin fluctuations [152] predicts a constant A/γ^2 ratio except in the vicinity of a magnetic instability ($T_N = 0$), where it diverges. Magnetic correlations clearly have a strong effect on this ratio. It is important to point out that if the zero-field γ were to be calculated from the Kondo temperature $T_K = 3.3$ K [96] ($\gamma = 1700 \text{ mJ/K}^2 \text{ mol}$), as proposed by current models [108], the corresponding A/γ^2 ratio for $H = 0$ would not be consistent with experiment ($A/\gamma^2 = 1.6 \times 10^{-5} \Omega \text{ cm K}^2 \text{ mol}^2/\text{J}^2$), but would be close to the postulated value by Kadowaki and Woods. From this comparison, it can be concluded that the electronic specific heat coefficient exhibits a larger field dependence in the antiferromagnetic phase ($H \leq 6$ T) than the A coefficient of the resistivity. As a consequence, the proportionality relations between γ and T_K and between A and γ^2 fail to apply in this region.

Finally, no field-induced non-Fermi liquid properties were observed in the specific heat of polycrystalline CePb₃. Non-Fermi-liquid effects triggered by the suppression of T_N towards zero have been reported, for example, in CeCu_{4.8}Ag_{1.2} at 3 T [157]. Theoretical models based on quantum phase transitions attribute non-Fermi liquid behavior to critical fluctuations corresponding to $T_N \rightarrow 0$ [12]. Thermodynamic signatures of magnetic order in the specific heat disappear long before T_N reaches zero under the influence of an external field, so that the system may not reach the quantum critical point.

7.2 Single-Ion Kondo Behavior of $\text{Ce}_{0.6}\text{La}_{0.4}\text{Pb}_3$ in Magnetic Fields

A previous study on $\text{Ce}_{1-x}\text{La}_x\text{Pb}_3$ [96] demonstrated that the thermodynamic and transport properties of this system show single-impurity scaling in zero applied magnetic field, with a Kondo temperature $T_K = 3.3$ K. This is a unique behavior among concentrated Kondo systems. In the search for understanding the Kondo effect in Ce-based heavy-fermion systems, it would be useful to study the specific heat of a nonmagnetic analog to CePb_3 , $\text{Ce}_{0.6}\text{La}_{0.4}\text{Pb}_3$, in order to compare to the numerical solutions for the $S = \frac{1}{2}$ Kondo model in magnetic field, as well as to describe the behavior of the electronic specific heat coefficient with applied field. Data for the field dependence of the electronic specific heat and the coefficient γ for this alloy will be presented in this section.

7.2.1 Results

The specific heat was measured between 0.4 and 10 K in magnetic fields up to 14 T. The electronic contribution was obtained using the following procedure: A cubic (lattice) term was obtained by using the zero-field specific heat data of $\text{Ce}_{0.6}\text{La}_{0.4}\text{Pb}_3$ from Lin *et al.* [96], and subtracting their electronic contribution from the total specific heat. The resulting coefficient is equal to 5.24 ± 0.03 mJ/K⁴ mol. This cubic function was then subtracted from the measured specific heat, and the difference was divided by the Ce concentration.

The electronic specific heat ΔC of $\text{Ce}_{0.6}\text{La}_{0.4}\text{Pb}_3$ at fields between 0 and 14 T is illustrated in Fig. 7.6. Numerical renormalization group (NRG) solutions for different ratios of $g_i\mu_B H/k_B T_K$ (provided by K. Ingersent, to be published) are also shown for comparison. The parameter g_i corresponds to the g-factor of the impurity, and was chosen to be equal to one. The error bars take into account the uncertainty in the measurement, as well as a temperature-dependent term due to the subtraction of the large lattice contribution. Around 10 K, the electronic specific heat is $\sim 10\%$ of the sample specific heat, hence the large error at this

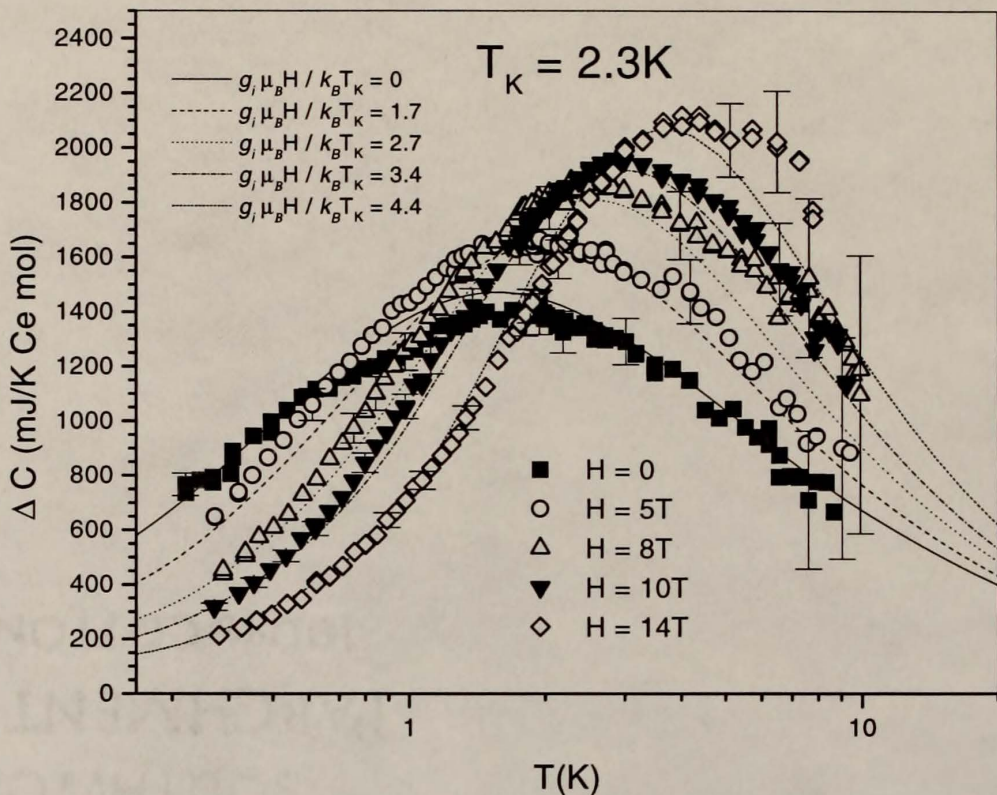


Figure 7.6: Single-ion specific heat ΔC vs T of $\text{Ce}_{0.6}\text{La}_{0.4}\text{Pb}_3$ for $H = 0, 5, 8, 10$, and 14 T . The lines correspond to NRG solutions of the $S = \frac{1}{2}$ Kondo model for various ratios $g_i \mu_B H / k_B T_K$ (R. Pietri, K. Ingersent, and B. Andraka, to be published). The estimated Kondo temperature at all fields is $T_K = 2.3\text{ K}$. The error bars represent the propagated uncertainties including experimental errors and the error from the subtraction of the lattice term (see text for details).

temperature. The zero-field data are somewhat different from those of Lin *et al.* The maximum in ΔC is about 6% lower than in the previous study. Also, the zero-field data are described by the $S = \frac{1}{2}$ Kondo specific heat curve with $T_K = 2.3$ K, instead of the previously obtained value of 3.3 K [96].

The low-temperature specific heat is suppressed in a magnetic field, as seen in Fig. 7.6. The maximum becomes larger and narrower, and its position shifts toward higher temperatures. Assuming that the Kondo temperature $T_K = 2.3$ K, and the impurity g-factor $g_i = 1$, the numerical solutions for $g_i\mu_B H/k_B T_K = 1.7, 2.7, 3.4$, and 4.4 correspond to magnetic fields $H = 5.8, 9.3, 11.7$, and 15.1 T, respectively. These curves resemble the temperature dependence of the experimental data at $H = 5, 8, 10$, and 14 T.

The specific heat was also plotted as $\Delta C/T$ between 0.4 and 10 K (Fig. 7.7) in order to extract a value of the electronic coefficient γ at each field. This quantity shows a significant discrepancy between the data and the available NRG solutions at the lowest temperatures. The adjustment of parameters like $g_i\mu_B H$ and T_K could lead to a better agreement between theory and experiment. The closest matches found between the NRG solution and the data were for $H = 0$ and at 14 T using the curve for $g_i\mu_B H/k_B T_K = 4.4$.

The experimental results show a significant decrease of low-temperature values of $\Delta C/T$, pointing to an expected decrease of γ with field. But the most striking result is the appearance of broad maxima for fields larger than 5 T. These anomalies become more distinct with increasing magnetic field. The temperature position of each maximum T_m shifts toward higher temperatures between 5 and 14 T. Also within the same field range, the decrease in $\Delta C/T$ values below T_m at each field is accompanied by an increase in such values above this temperature up to 10 K.

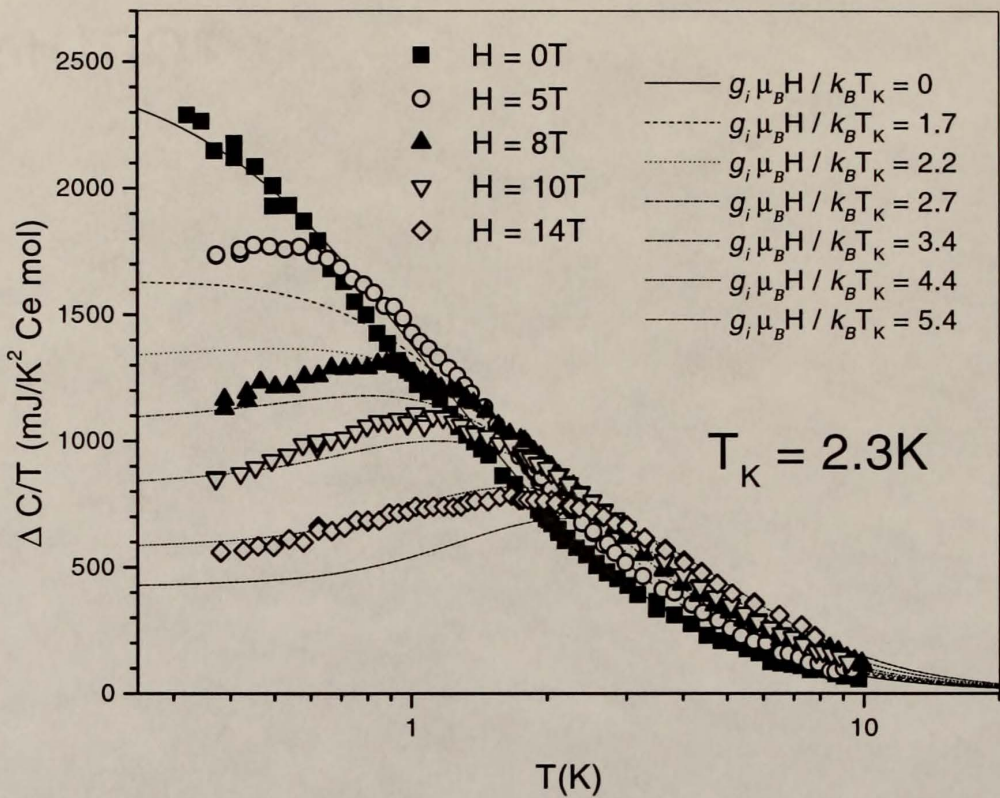


Figure 7.7: Single-ion specific heat, plotted as $\Delta C/T$ vs T , of $\text{Ce}_{0.6}\text{La}_{0.4}\text{Pb}_3$ for $H = 0, 5, 8, 10$, and 14T . The lines correspond to NRG solutions of the $S = \frac{1}{2}$ Kondo model for various ratios $g_i \mu_B H / k_B T_K$ (R. Pietri, K. Ingersent, and B. Andraka, to be published). The estimated Kondo temperature is $T_K = 2.3\text{ K}$.

In order to rule out the possibility that the maxima in $\Delta C/T$ might be due to extraneous phases, the specific heat was also measured on a second $\text{Ce}_{0.6}\text{La}_{0.4}\text{Pb}_3$ sample from a different batch, as well as on a $\text{Ce}_{0.55}\text{La}_{0.45}\text{Pb}_3$ sample. Plots of $\Delta C/T$ vs T at all of the above fields confirmed the presence of anomalies for both $\text{La } x = 0.4$ and $x = 0.45$. Both the magnitude and the temperature position of these maxima at each field did not vary appreciably between the three samples studied.

A more likely explanation is that the maxima are an intrinsic feature of the electronic specific heat. A comparison of the data with NRG solutions for $\Delta C/T$ at various ratios $g_i\mu_{\text{B}}H/k_{\text{B}}T_K$ led to the conclusion that the maxima seem to be a previously unidentified characteristic of the $S = \frac{1}{2}$ Kondo specific heat in magnetic fields. As revealed in Fig. 7.7, the data are in qualitative agreement with the numerical solutions, which show maxima at similar temperatures. The NRG solutions also show a similar decrease in low-temperature values of $\Delta C/T$.

7.2.2 Discussion

In a Kondo-impurity system, the zero-field $\Delta C/T$ increases monotonically with decreasing temperature. However, at significantly larger fields, the appearance of a maximum in this quantity is expected based on the following argument. It is well known that in the limit $\mu H \gg k_{\text{B}}T_K$, where μ is the magnetic moment in the direction of H , the Kondo effect is suppressed and the single-ion specific heat takes the shape of the free-spin Schottky anomaly due to the Zeeman splitting of the lowest-lying crystal-field level. The Schottky specific heat for a two-level system has the following form [158]:

$$C_{\text{Sch}} = R \left(\frac{\delta}{T} \right)^2 \frac{g_0}{g_1} \frac{\exp(\delta/T)}{[1 + (g_0/g_1)\exp(\delta/T)]^2}, \quad (7.1)$$

where R is the gas constant, δ is the energy separation between the two levels in degrees Kelvin ($\delta = 2\mu H/k_{\text{B}}$), and g_0 and g_1 are the degeneracies of the lowest and

Table 7.2: Values of the specific heat coefficient $\gamma = \Delta C(T \approx 0.4 \text{ K})/T$, and the temperatures of the maxima in ΔC and $\Delta C/T$ (T_M and T_m , respectively) for $\text{Ce}_{0.6}\text{La}_{0.4}\text{Pb}_3$ in different magnetic fields H ; also shown are T_M and T_m values for NRG solutions at different ratios $g_i\mu_B H/k_B T_K$ (R. Pietri, K. Ingersent, and B. Andraka, to be published).

$H(\text{T})$	$\gamma(\text{mJ/K}^2 \text{Ce mol})$	$T_M(\text{K})$	$T_m(\text{K})$	$g_i\mu_B H/k_B T_K$	$T_M^{\text{NRG}}(\text{K})$	$T_m^{\text{NRG}}(\text{K})$
0	2290 ± 180	1.6 ± 0.1	--	0	1.56	--
5	1740 ± 120	1.9 ± 0.1	0.50 ± 0.03	1.7	1.98	0.30 ± 0.05
8	1150 ± 70	2.5 ± 0.2	0.84 ± 0.03	2.7	2.55	0.80 ± 0.03
10	850 ± 50	3.0 ± 0.2	1.06 ± 0.10	3.4	2.99	1.18 ± 0.03
14	560 ± 50	4.2 ± 0.2	1.65 ± 0.10	4.4	3.68	1.76 ± 0.04

highest levels, respectively. For the Γ_7 doublet in Ce^{3+} , $g_0/g_1 = 1$. The Schottky specific heat C_{Sch} has a peak at a temperature T_M proportional to the splitting δ . The quantity C_{Sch}/T also has a peak at a temperature $T_m < T_M$. Therefore, for a Kondo impurity, a maximum in $\Delta C/T$ should develop at sufficiently large fields.

The temperatures of the maxima in ΔC and $\Delta C/T$ vs T (T_M and T_m , respectively) for $\text{Ce}_{0.6}\text{La}_{0.4}\text{Pb}_3$ were compared to the corresponding temperatures for the NRG solutions. Values for these temperatures at different fields H and ratios $g_i\mu_B H/k_B T_K$ are shown in Table 7.2. The temperatures T_m were found to be lower than T_M in both numerical and experimental results. Also, the NRG calculations suggest that the maxima in $\Delta C/T$ appear above a certain field value, as in the experimental data.

The electronic specific heat coefficient γ was defined as the value of $\Delta C/T$ at the lowest temperature measured ($\sim 0.4 \text{ K}$). The coefficients $\gamma(H)$ of $\text{Ce}_{0.6}\text{La}_{0.4}\text{Pb}_3$ are shown in Fig. 7.8 and Table 7.2. A continuous decrease (75%) is observed between $H = 0$ and $H = 14 \text{ T}$. The error bars include contributions from measurement uncertainties. The observed decrease of $\gamma(H)$ in heavy-fermion systems has been previously described in terms of a broadening of the Kondo resonance in magnetic fields [159]. In this phenomenological model, the width of the Kondo resonance $\Gamma(0)$ is affected by magnetic fields as follows:

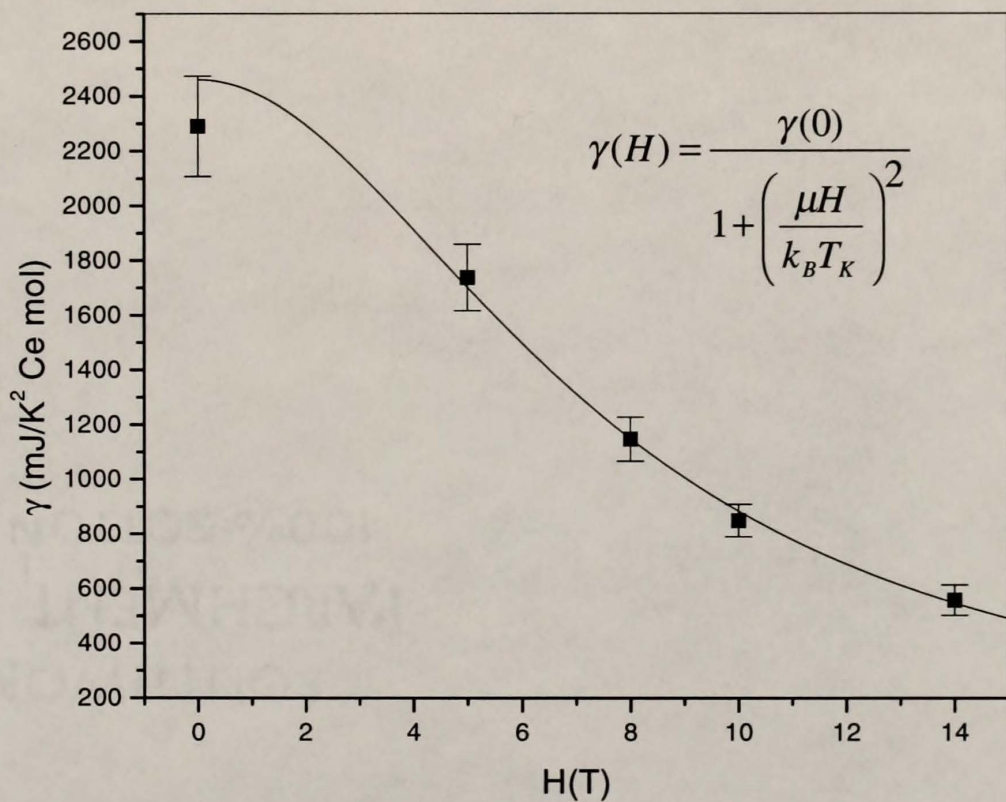


Figure 7.8: Electronic specific heat coefficient γ vs H for $\text{Ce}_{0.6}\text{La}_{0.4}\text{Pb}_3$. Error bars account for experimental uncertainties. The fit to the data corresponds to Eq. 7.4 (shown above).

$$\Gamma(H)^2 = \Gamma(0)^2 + \mu^2 H^2, \quad (7.2)$$

where $\Gamma(0) \propto T_K \propto 1/\gamma(0)$, and the magnetic moment of the impurity $\mu = \mu_z = g_i \mu_B s$, with $s = 1/2$. Therefore,

$$\gamma(H) = \frac{\gamma(0)}{\sqrt{1 + (\mu H/k_B T_K)^2}}, \quad (7.3)$$

with $\gamma(0)$ being the electronic coefficient in zero field. This description is based on the field dependence of the electronic specific heat of the resonant level model by Schotte and Schotte [160]. Even though this model agrees with the exact solutions of the $S = \frac{1}{2}$ Kondo model in zero field (Bethe Ansatz, NRG) [161], there are significant discrepancies between the magnetic field solutions of the resonant level model and the $S = \frac{1}{2}$ Kondo model.

The extrapolated values of γ from NRG solutions follow a somewhat different magnetic field dependence (courtesy of K. Ingersent, to be published):

$$\gamma(H) = \frac{\gamma(0)}{1 + (\mu H/k_B T_K)^2}. \quad (7.4)$$

A fit to the data is shown in Fig. 7.8.

The ordered moment for the crystal-field Γ_7 doublet ground state of CePb₃ is equal to $0.71 \mu_B$ [106]. This moment corresponds to a g-factor $g_i = \frac{10}{7}$ [162]. Remarkably, the field dependence of the maximum in the specific heat and its temperature position seem to be described fairly well by the NRG solutions with ratios $g_i \mu_B H/k_B T_K$ using an impurity g-factor $g_i = 1$. The NRG curves in Figs. 7.6 and 7.7 correspond to a moment $\mu = g_i \mu_B s = 0.5 \mu_B$, somewhat smaller than the expected value of $0.71 \mu_B$. The generation of numerical solutions using $g_i = \frac{10}{7}$ and values of H closer to the experimental values may lead to better agreement between the model and the specific heat data.

Another estimate for μ can be extracted from a fit of Eq. 7.4 to the data on Fig. 7.8. Using a value of $T_K = 2.3$ K and the electronic coefficient $\gamma(0) = 2460 \text{ mJ/K}^2 \text{ Ce mol}$, extrapolated from the zero-field NRG solution, the best fit

gives $\mu = 0.46 \pm 0.02 \mu_B$, a smaller, but comparable value to that obtained from the NRG solutions. The discrepancy between the expected moment and the value obtained from the fit might be due to two factors. First, the uncertainty in the measurement of $\gamma = \Delta C(0.4\text{K})/T$. Second, the smaller value of μ indicates a weaker field dependence of γ , especially at high fields, which may be due to the neglect of the contribution to the specific heat from the lowest Zeeman-split level of the excited Γ_8 crystal-field state.

The present study confirmed that the specific heat of $\text{Ce}_{0.6}\text{La}_{0.4}\text{Pb}_3$ follows the field dependence predicted by the $S = \frac{1}{2}$ Kondo model [26, 30], with its maximum shifting toward higher temperatures and its magnitude approaching that of a free-spin Schottky anomaly at high fields. This is the first direct evidence of Kondo behavior in the specific heat of a concentrated system in magnetic fields. Similar studies have been conducted in dilute systems, like $\text{Ce}_x\text{La}_{1-x}\text{Al}_2$ [163] ($S = \frac{1}{2}$) and $\text{Ce}_x\text{La}_{1-x}\text{B}_6$ [162] ($S = \frac{3}{2}$). The agreement of the present data with the theory is comparable to that of previous studies.

This study also revealed that the weak maxima observed in $\Delta C/T$ for $H \geq 5\text{T}$ may be due to single impurity effects rather than to some exotic cooperative phenomena. The maxima can also be observed in the low-temperature C/T data of CePb_3 at 10 and 14 T (see Fig. 7.1), and in previous measurements at 16 and 20 T [94]. These features are also evident in C/T data of $\text{Ce}_{0.3}\text{La}_{0.7}\text{Al}_3$ at 10 and 14 T (Fig. 6.37, Chapter 6). The appearance of a maximum in $\Delta C/T$ at large fields suggests a careful reevaluation of field-induced transitions reported in other heavy-fermion systems, in particular the so-called B -phase of CeCu_2Si_2 [164, 165, 166]. This compound exhibits a line of transitions above 7 T between the paramagnetic region and the unidentified B -phase [165]. The transitions are characterized by weak maxima in C/T [164, 166] that shift toward higher temperatures with increasing magnetic field.

CHAPTER 8 CONCLUSION

This chapter summarizes the results of thermodynamic measurements on CeAl₃-based and CePb₃-based alloys as a function of doping concentration, temperature, and magnetic field, and discusses possible interpretations of the data. New ideas for experiments on each compound are then addressed in order to stimulate further the ongoing interest in both CeAl₃ and CePb₃.

8.1 Summary

The determination of the lattice parameters a , c , V , and c/a from x-ray diffraction studies of Ce_{1-x}M_xAl₃ alloys (M=La, Y) helped establish the nature of the chemical pressure effect induced by Y doping ($x \leq 0.5$) and La doping ($0 \leq x \leq 1$), in agreement with previous studies [71, 89]. Substitution of La on the Ce sites expands, while Y contracts the hexagonal lattice. For both Y and La substitutions, the c parameter is less affected than a , especially with La, so that most of the volume change occurs in the a - b plane.

A temperature-concentration phase diagram, depicting T_K and T_m , was constructed for Ce_{1-x}La_xAl₃. Specific heat and magnetic susceptibility measurements as a function of La doping are consistent with a Kondo necklace picture [42, 43], assuming that the maxima in the specific heat and in C/T are associated with a magnetic phase transition. The temperature location of the transition, whose precursor exists in the pure compound, has a nonmonotonic concentration dependence. A maximum in the concentration dependence of the temperature T_m is observed at $x \approx 0.3$. This maximum is not only suppressed by changes in the cou-

pling J , but also by a reduction in the overall concentration of magnetic impurities (dilution effect). The Kondo temperature, extracted from the magnetic entropy above T_m , decreases with La concentration. These changes are consistent with a continuous decrease of the coupling J between the $4f$ moment and the conduction electrons. A decrease in J is in turn related to an expansion of the unit-cell volume and therefore of the average distance between Ce and Al atoms.

The specific heat and lattice parameters of $\text{Ce}_{1-x}\text{Y}_x\text{Al}_3$ were compared to those of CeAl_3 as a function of pressure. Substitution of Y led to more anisotropic changes in a and c , while hydrostatic pressure caused a stronger reduction in both c and the size of the anomaly in C/T . These results imply that the characteristic energy of magnetic interactions T_{RKKY} is more sensitive to the hybridization between hexagonal planes than that in the a - b plane. A similar interpretation was also suggested by alloying and pressure studies on hexagonal Kondo lattices CePd_2Al_3 and CeCu_5 . In addition, the lack of a reduction of T_m with Y doping up to $x = 0.2$ is consistent with a previous study [61] attributing the development of the anomaly at this temperature to an angular dependence of the f -ligand hybridization, related to the absolute-value change in c/a .

The lattice parameters of the alloy $\text{Ce}_{0.8}(\text{La}_{0.6}\text{Y}_{0.4})_{0.2}\text{Al}_3$ are identical to those of CeAl_3 within uncertainty. This similarity allowed for a study of thermodynamic properties on a CeAl_3 -like system with a net reduction in the overall number of Ce moments (increase in $R_{\text{Ce-Ce}}$), yet assuming an average hybridization equivalent to that of the undoped compound. Specific heat measurements on the above alloy did not show an anomaly in C/T down to 0.4 K. Alloying on the Ce sites using both Y and La dopants was found to drive the transition temperature to below 0.4 K by increasing the distance between Ce atoms, therefore reducing T_{RKKY} . This result is an indication that the concentration of impurities and their intersite interactions are also important for the development of this maximum.

Both C/T (between at least 0.38 and 1.7 K) and χ vs T for $\text{Ce}_{0.8}(\text{La}_{0.6}\text{Y}_{0.4})_{0.2}\text{Al}_3$ follow a power law at low temperatures, with an exponent that can be related to a model based on a Griffiths phase [58, 59]. This model provides a common physical description for the non-Fermi-liquid effects seen in many heavy-fermion systems, like UCu_4Pd [144] and $\text{Th}_{1-x}\text{U}_x\text{Pd}_2\text{Al}_3$ [145]. In this respect, the alloying procedure described above represents a novel method of tuning antiferromagnetic Kondo lattices through their quantum critical point. Measurements of χ vs T and C/T vs T in $\text{Ce}_{0.8}(\text{La}_{0.6}\text{Y}_{0.4})_{0.2}\text{Al}_3$ and similar alloys at lower temperatures are needed in order to verify the above temperature dependence over more than one decade.

Results for the specific heat of La-doped alloys in magnetic fields revealed considerable discrepancies between trends of the data and the predictions of the anisotropic Kondo model [36, 37]. The temperature T_m of the anomaly in the alloy $\text{Ce}_{0.8}\text{La}_{0.2}\text{Al}_3$ decreased slowly, and the electronic coefficient γ increased slightly with applied field, while the model predicts a large decrease in γ and a shift of T_m toward higher temperatures [37, 149]. The increase in γ with field in this alloy is consistent with the suppression of magnetic order. Thus, a single-impurity anisotropic Kondo description cannot be applied to $\text{Ce}_{1-x}\text{La}_x\text{Al}_3$ alloys.

The specific heat measurements on polycrystalline CePb_3 in magnetic fields up to 14 T were motivated by the unusual behavior of the field dependence of the A coefficient in the resistivity found for a single crystal [100]. The electronic coefficient γ has a maximum around 6 T, and its field dependence is similar to that of A . The ratio A/γ^2 , postulated as a universal value for heavy-fermion systems, is approximately constant in the paramagnetic state ($H > 6$ T), while it is enhanced and field-dependent in the magnetic regime ($H < 6$ T). This is the first comprehensive study of this ratio on a heavy-fermion system as a function of a wide range of magnetic fields. The behavior of A/γ^2 in the paramagnetic and magnetic

regions seem to be in agreement with previous data on magnetic Ce-based heavy fermions.

Specific heat data of the heavy-fermion alloy $\text{Ce}_{0.6}\text{La}_{0.4}\text{Pb}_3$ in magnetic fields up to 14 T showed that the electronic specific heat can be described in terms of the $S = \frac{1}{2}$ Kondo model in magnetic fields [30], with a Kondo temperature $T_K = 2.3$ K. This result complements previous zero-field studies [96] which support a single-ion description for $\text{Ce}_{1-x}\text{La}_x\text{Pb}_3$ alloys. In fact, the current specific heat study in magnetic fields provides further evidence that the mechanism responsible for heavy-fermion behavior is particularly of a single-impurity Kondo nature.

This study also led to the discovery of previously unknown magnetic-field induced anomalies in C/T below 2 K for $\text{Ce}_{0.6}\text{La}_{0.4}\text{Pb}_3$. A direct comparison of $\Delta C/T$ results with NRG solutions indicate that the anomalies appear to be an intrinsic feature of the theoretical solutions for the $S = \frac{1}{2}$ Kondo model. Moreover, a comparison of the data to C/T data for CePb_3 and $\text{Ce}_{0.3}\text{La}_{0.7}\text{Al}_3$ (Figs. 7.1 and 6.37, respectively) at $H = 10$ T and 14 T revealed that the anomalies are also present in other Ce heavy-fermion compounds.

8.1.1 Ideas for Future Work

Without a doubt, there is still a great deal of experimental work to be done on CeAl_3 and its related alloys. Although the nature of the anomaly in CeAl_3 could be attributed to magnetic correlations, the physical circumstances that lead to its formation are still elusive. In order to investigate further the magnetic character of the anomaly in CeAl_3 , an extensive μSR study of $\text{Ce}_{1-x}\text{La}_x\text{Al}_3$ alloys would be desirable. Muon spin relaxation measurements probe the local magnetic structure and are able to detect local magnetic fields at different interstitial sites, which would better help determine the effective moment of Ce atoms in these alloys. Future measurements in the millikelvin range would aid in the determination of Ce local moments at low temperatures.

It is of utmost importance to develop proper techniques to synthesize high-quality single crystals of CeAl₃ that are large enough for measurements to be performed with reasonable accuracy. The orientational dependence of thermodynamic and transport properties is currently a topic of interest in the study of Ce-based Kondo lattices (e.g., CeCu₅ [141] and CePd₂Al₃ [139]). In addition, uniaxial pressure studies on single crystals of CeAl₃ are essential to understand its magnetic behavior. At the present time, the synthesis of single crystals of CeAl₃ is an arduous task, but a necessary one for a compound that appears to have a strong anisotropy in its physical properties.

Single crystals are also essential to understand the directional dependence of physical properties in CePb₃. A field-induced spin flop transition along (110) has been inferred in CePb₃ from features in the magnetoresistance, magnetic susceptibility, and the elastic constants, but its nature has not yet been determined. Neutron diffraction measurements on single crystals in magnetic field could help determine the magnetic structure and the effective moment of this field-induced phase. Specific heat measurements along (100) and (110) at millikelvin temperatures and magnetic fields up to 15 T would be useful in understanding the orientational and temperature dependences of this phase. These experiments would also help search for signatures of field-induced non-Fermi-liquid behavior, suggested by magnetoresistance measurements along (110). Finally, an analysis of the field dependence of the magnetization in Ce_{0.6}La_{0.4}Pb₃ may be used to verify the agreement of the data with the predictions of the $S = \frac{1}{2}$ Kondo model.

REFERENCES

- [1] A. J. Schofield. *Contemporary Physics*, 40:95, 1999.
- [2] D. K. K. Lee and A. J. Schofield. *Phil. Trans. R. Soc. Lond. A*, 358:111, 2000.
- [3] G. R. Stewart. *Rev. Mod. Phys.*, 73, 2001.
- [4] Z. Fisk, H. R. Ott, T. M. Rice, and J. L. Smith. *Nature*, 320:124, 1986.
- [5] G. R. Stewart. *Rev. Mod. Phys.*, 56:755, 1984.
- [6] N. Grewe and F. Steglich. Heavy fermions. In *Handbook on the Physics and Chemistry of Rare Earths*, volume 14, page 343, Amsterdam, 1991. Elsevier Science. Edited by K. A. Gschneidner Jr. and L. Eyring.
- [7] H. R. Ott. *Progress in Low Temperature Physics*, volume 11, page 215. Elsevier, Amsterdam, 1987.
- [8] P. A. Lee, T. M. Rice, J. W. Serene, L. J. Sham, and J. W. Wilkins. *Comments Condens. Matter Phys.*, 12:99, 1986.
- [9] C. Kittel. *Introduction to Solid State Physics*. John Wiley & Sons, Inc., New York, 1986.
- [10] N. W. Ashcroft and N. D. Mermin. *Solid State Physics*. W. B. Saunders Co., Philadelphia, 1976.
- [11] B. Andraka, R. Pietri, S. G. Thomas, G. R. Stewart, E.-W. Scheidt, and T. Schreiner. *Eur. Phys. J. B*, 12:55, 1999. See also references therein.
- [12] *J. Phys.: Condens. Matter*, 8, 1996. Proceedings of the Conference of Non-Fermi-liquid Behavior in Metals, Santa Barbara, CA, June 17-21, 1996.
- [13] P. Gegenwart, F. Kromer, M. Lang, G. Sparn, C. Geibel, and F. Steglich. *Phys. Rev. Lett.*, 82:1293, 1999.
- [14] J. S. Kim, J. Alwood, S. A. Getty, F. Sharifi, and G. R. Stewart. *Phys. Rev. B*, 62:6986, 2000.
- [15] E. A. Goremychkin, R. Osborn, B. D. Rainford, and A. P. Murani. *Phys. Rev. Lett.*, 84:2211, 2000.
- [16] L. D. Landau. *Sov. Phys.-JETP*, 3:920, 1957.

- [17] A. Ron. Theory of fermi liquids. In *The Helium Liquids: Proceedings of the 15th Scottish Universities Summer School in Physics, 1974*, page 211.
- [18] L. D. Landau and E. M. Lifshitz. *Statistical Physics*, volume 2. Pergamon Press, Oxford, New York, 1980.
- [19] G. Baym and C. Pethick. *Landau Fermi-Liquid Theory: Concepts and Applications*. John Wiley & Sons, Inc., New York, 1991.
- [20] K. Andres, J. E. Graebner, and H. R. Ott. *Phys. Rev. Lett.*, 35:1779, 1975.
- [21] Kei Yosida. *Theory of Magnetism*. Springer-Verlag, Berlin, Heidelberg, Germany, 1996.
- [22] P. W. Anderson. *Phys. Rev.*, 124:41, 1961.
- [23] J. A. Mydosh. *Spin Glasses: An Experimental Introduction*. Taylor & Francis, Bristol, PA, 1993.
- [24] J. R. Schrieffer and P. A. Wolff. *Phys. Rev.*, 149:491, 1966.
- [25] Jun Kondo. *Prog. Theor. Phys.*, 32:37, 1964.
- [26] N. Andrei, K. Furuya, and J. H. Lowenstein. *Rev. Mod. Phys.*, 55:331, 1983.
- [27] N. Andrei. *Phys. Rev. Lett.*, 45:379, 1980.
- [28] P. B. Wiegmann. *JETP Lett.*, 31:364, 1980.
- [29] P. Schlottmann. *Phys. Rep.*, 181:1, 1989.
- [30] P. D. Sacramento and P. Schlottmann. *Phys. Rev. B*, 40:431, 1989.
- [31] P. W. Anderson and G. Yuval. *Phys. Rev. Lett.*, 23:89, 1969.
- [32] A. M. Tsvelick and P. B. Wiegmann. *Adv. Phys.*, 32:453, 1983.
- [33] H. Shiba. *Prog. Theor. Phys.*, 43:601, 1970.
- [34] A. J. Leggett, S. Chakravarty, A. T. Dorsey, M. P. A. Fisher, A. Garg, and W. Zwerger. *Rev. Mod. Phys.*, 59:1, 1987.
- [35] T. A. Costi and C. Kieffer. *Phys. Rev. Lett.*, 76:1683, 1996.
- [36] T. A. Costi. *Phys. Rev. Lett.*, 80:1038, 1998.
- [37] T. A. Costi and G. Zaránd. *Phys. Rev. B*, 59:12398, 1999.
- [38] F. Guinea, V. Hakim, and A. Muramatsu. *Phys. Rev. B*, 32:4410, 1985.
- [39] N. B. Brandt and V. V. Moshchalkov. *Adv. Phys.*, 33:373, 1984.

- [40] F. G. Aliev, N. B. Brandt, V. V. Moshchalkov, and S. M. Chudinov. *J. Low Temp. Phys.*, 57:61, 1984.
- [41] N. B. Brandt and V. V. Moschalkov. *Sov. Phys. Uspekhi*, 29:725, 1986.
- [42] S. Doniach. *Valence Fluctuations and Related Narrow Band Phenomena*, page 169. Plenum Press, New York, New York, 1977.
- [43] S. Doniach. *Physica B*, 91:231, 1977.
- [44] J. R. Iglesias, C. Lacroix, and B. Coqblin. *Phys. Rev. B*, 56:11820, 1997.
- [45] S. Süllow, M. C. Aronson, B. D. Rainford, and P. Haen. *Phys. Rev. Lett.*, 82:2963, 1999.
- [46] D. L. Cox. *Phys. Rev. Lett.*, 59:1240, 1987.
- [47] P. Schlottmann and P. D. Sacramento. *Adv. Phys.*, 42:641, 1993.
- [48] F. G. Aliev, S. Vieira, R. Villar, and V. V. Moshchalkov. *J. Phys.: Condens. Matter*, 8:9807, 1996.
- [49] O. O. Bernal, D. E. MacLaughlin, H. G. Lukefahr, and B. Andraka. *Phys. Rev. Lett.*, 75:2023, 1995.
- [50] V. Dobrosavljević, T. R. Kirkpatrick, and G. Kotliar. *Phys. Rev. Lett.*, 69:1113, 1992.
- [51] E. Miranda, V. Dobrosavljević, and G. Kotliar. *J. Phys.: Condens. Matter*, 8:9871, 1996.
- [52] J. A. Hertz. *Phys. Rev. B*, 14:1165, 1976.
- [53] A. J. Millis. *Phys. Rev. B*, 48:7183, 1993.
- [54] A. M. Tsvelik and M. Reizer. *Phys. Rev. B*, 48:9887, 1993.
- [55] T. Moriya and T. Takimoto. *J. Phys. Soc. Jpn.*, 64:960, 1995.
- [56] S. L. Sondhi, S. M. Girvin, J. P. Carini, and D. Shahar. *Rev. Mod. Phys.*, 69:315, 1997.
- [57] F. Steglich, B. Buschinger, P. Gegenwart, M. Lohmann, R. Helfrich, C. Langhammer, P. Hellmann, L. Donnevert, S. Thomas, A. Link, C. Geibel, M. Lang, G. Sparn, and W. Assmus. *J. Phys.: Condens. Matter*, 8:9909, 1996.
- [58] A. H. Castro Neto, G. Castilla, and B. A. Jones. *Phys. Rev. Lett.*, 81:3531, 1998.

- [59] M. C. de Andrade, R. Chau, R. P. Dickey, N. R. Dilley, E. J. Freeman, D. A. Gajewski, M. B. Maple, R. Movshovich, A. H. Castro Neto, G. Castilla, and B. A. Jones. *Phys. Rev. Lett.*, 81:5620, 1998.
- [60] R. B. Griffiths. *Phys. Rev. Lett.*, 23:17, 1969.
- [61] S. Corsépius, M. Lenkowitz, and G. R. Stewart. *J. Alloys Comp.*, 259:29, 1997.
- [62] J. H. N. Van Vucht and K. H. J. Buschow. *J. Less-Comm. Met.*, 10:98, 1965.
- [63] K. H. Mader and W. M. Swift. *J. Phys. Chem. Solids*, 29:1759, 1968.
- [64] J. L. C. Daams, P. Villars, and J. H. N. Van Vucht. *Atlas of Crystal Structure Types for Intermetallic Phases*. ASM International, Materials Park, OH, 1991.
- [65] J. V. Mahoney, V. U. S. Rao, W. E. Wallace, R. S. Craig, and N. G. Nereson. *Phys. Rev. B*, 9:154, 1974.
- [66] M. H. van Maaren, K. H. J. Buschow, and H. J. van Daal. *Solid State Commun.*, 9:1981, 1971.
- [67] G. E. Brodale, R. A. Fisher, N. E. Phillips, and J. Flouquet. *Phys. Rev. Lett.*, 56:390, 1986.
- [68] C. D. Bredl, S. Horn, F. Steglich, B. Lüthi, and R. M. Martin. *Phys. Rev. Lett.*, 52:1982, 1984.
- [69] S. Barth, H. R. Ott, F. N. Gygax, B. Hitti, E. Lippelt, A. Schenck, C. Baines, B. van den Brandt, T. Konter, and S. Mango. *Phys. Rev. Lett.*, 59:2991, 1987.
- [70] J. L. Gavilano, J. Hunziker, and H. R. Ott. *Phys. Rev. B*, 52:R 13106, 1995.
- [71] B. Andraka, C. S. Jee, and G. R. Stewart. *Phys. Rev. B*, 52:9462, 1995.
- [72] B. Andraka, G. Fraunberger, J. S. Kim, C. Quitmann, and G. R. Stewart. *Phys. Rev. B*, 39:6420, 1989.
- [73] G. E. Brodale, R. A. Fisher, N. E. Phillips, J. Flouquet, and C. Marcenat. *J. Magn. Magn. Mater.*, 54-57:419, 1986.
- [74] G. Lapertot, R. Calemczuk, C. Marcenat, J. Y. Henry, J. X. Boucherle, J. Flouquet, J. Hammann, R. Cibin, J. Cors, D. Jaccard, and J. Sierro. *Physica B*, 186-188:454, 1993.
- [75] O. Avenel, J. S. Xia, B. Andraka, C. S. Jee, M-F. Xu, Y. J. Qian, T. Lang, P. L. Moyland, W. Ni, P. J. C. Signore, E. D. Adams, G. G. Ihas, M. W. Meisel, G. R. Stewart, N. S. Sullivan, and Y. Takano. *Phys. Rev. B*, 45:5695, 1992.

- [76] D. Jaccard, R. Cibin, A. Bezinge, J. Sierro, K. Matho, and J. Flouquet. *J. Magn. Magn. Mater.*, 76-77:255, 1988.
- [77] G. Oomi and T. Kagayama. *J. Phys. Soc. Jpn.*, 65:2732, 1996.
- [78] H. R. Ott, O. Marti, and F. Hulliger. *Solid State Commun.*, 49:1129, 1984.
- [79] U. Rauchschwalbe, F. Steglich, A. de Visser, and J. J. M. Franse. *J. Magn. Magn. Mater.*, 63-64:347, 1987.
- [80] G. Remenyi, A. Briggs, J. Flouquet, O. Laborde, and F. Lapierre. *J. Magn. Magn. Mater.*, 31-34:407, 1983.
- [81] D. Jaccard, R. Cibin, and J. Sierro. *Helv. Phys. Acta*, 61:530, 1988.
- [82] H. Nakamura, Y. Kitaoka, K. Asayama, and J. Flouquet. *J. Phys. Soc. Jpn.*, 57:2644, 1988.
- [83] W. H. Wong and W. G. Clark. *J. Magn. Magn. Mater.*, 108:175, 1992.
- [84] S. Barth, H. R. Ott, F. N. Gygax, B. Hitti, E. Lippelt, A. Schenck, and C. Baines. *Phys. Rev. B*, 39:11695, 1989.
- [85] A. Schenck and F. N. Gygax. *Handbook of Magnetic Materials*, volume 9, page 151. Elsevier, North Holland, Amsterdam, 1995.
- [86] B. R. Coles, S. Oseroff, and Z. Fisk. *J. Phys. F*, 17:L169, 1987.
- [87] E. A. Goremychkin, R. Osborn, and I. L. Sashin. *J. Appl. Phys.*, 85:6046, 1999.
- [88] P. M. Levy and S. Zhang. *Phys. Rev. Lett.*, 62:78, 1989.
- [89] R. Pietri and B. Andraka. *Physica B*, 230-232:535, 1997.
- [90] R. Osborn, E. A. Goremychkin, B. D. Rainford, I. L. Sashin, and A. P. Murani. *J. Appl. Phys.*, 87:5131, 2000.
- [91] K. A. Gschneidner, Jr., and F. W. Calderwood. *Binary Alloy Phase Diagrams*, volume 1, p. 134, Second Edition. ASM International, Materials Park, OH, 1990.
- [92] F. Canepa, G. A. Costa, and G. L. Olcese. *Solid State Commun.*, 45:725, 1983.
- [93] C. L. Lin, J. Teter, J. E. Crow, T. Mihalisin, J. Brooks, A. I. Abou-Aly, and G. R. Stewart. *Phys. Rev. Lett.*, 54:2541, 1985.
- [94] N. A. Fortune, G. M. Schmiedeshoff, J. S. Brooks, C. L. Lin, J. E. Crow, T. W. Mihalisin, and G. R. Stewart. *Jpn. J. Appl. Phys. (Suppl.)*, 26-3:541, 1987.

- [95] T. Kirsch, A. Eichler, P. Morin, and U. Welp. *Z. Phys. B*, 86:83, 1992.
- [96] C. L. Lin, A. Wallash, J. E. Crow, T. Mihalisin, and P. Schlottmann. *Phys. Rev. Lett.*, 58:1232, 1987.
- [97] H. von Löhneysen. *J. Phys.: Condens. Matter*, 8:9689, 1996.
- [98] D. Nikl, I. Kouroudis, W. Assmus, B. Lüthi, G. Bruls, and U. Welp. *Phys. Rev. B*, 35:6864, 1987.
- [99] H. Suzuki, H. Kitazawa, T. Naka, J. Tang, and G. Kido. *Solid State Commun.*, 107:447, 1998.
- [100] J. McDonough and S. R. Julian. *Phys. Rev. B*, 53:14411, 1996.
- [101] K. Kadowaki and S. B. Woods. *Solid State Commun.*, 58:507, 1986.
- [102] D. Dürkop, E. Braun, B. Politt, H. Schmidt, B. Roden, and D. Wohlleben. *Z. Phys. B*, 63:55, 1986.
- [103] T. Ebihara, K. Koizumi, S. Uji, C. Terakura, T. Terashima, H. Suzuki, H. Kitazawa, and G. Kido. *Phys. Rev. B*, 61:2513, 2000.
- [104] S. Lipiński. *J. Magn. Magn. Mater.*, 192:553, 1999.
- [105] B. Renker, E. Gering, F. Gompf, H. Schmidt, and H. Rietschel. *J. Magn. Magn. Mater.*, 63-64:31, 1987.
- [106] C. Vettier, P. Morin, and J. Flouquet. *Phys. Rev. Lett.*, 56:1980, 1986.
- [107] A. Schenck, D. Andreica, P. Pinkpank, F. N. Gygax, H. R. Ott, A. Amato, R. H. Heffner, D. E. MacLaughlin, and G. J. Nieuwenhuys. *Physica B*, 259-261:14, 1999.
- [108] V. T. Rajan. *Phys. Rev. Lett.*, 51:308, 1983.
- [109] J. C. Arcas Soberino, J. J. Rieger, E.-W. Scheidt, and G. R. Stewart. *Phys. Rev. B*, 51:11469, 1995.
- [110] S. Rahman, J. Timlin, J. E. Crow, T. Mihalisin, and P. Schlottmann. *J. Appl. Phys.*, 67:5209, 1990.
- [111] S. Rahman, T. Mihalisin, J. E. Crow, and P. Schlottmann. *Solid State Commun.*, 75:279, 1990.
- [112] J. Teter, R. Freitag, A. Maury, J. E. Crow, and T. Mihalisin. *J. Appl. Phys.*, 53:7910, 1982.
- [113] C. L. Lin, J. E. Crow, P. Schlottmann, and T. Mihalisin. *J. Appl. Phys.*, 61:4376, 1987.

- [114] H. von Löhneysen, T. Pietrus, G. Portisch, H. G. Schlager, A. Schröder, M. Sieck, and T. Trappmann. *Phys. Rev. Lett.*, 72:3262, 1994.
- [115] James F. Shackelford. *Introduction to Materials Science for Engineers*. MacMillan Publishing Co., New York, NY, p. 180, 1985.
- [116] G. E. Brodale, R. A. Fisher, C. M. Lisse, N. E. Phillips, and A. S. Edelstein. *J. Magn. Magn. Mater.*, 54-57:416, 1986. See also references therein.
- [117] B. D. Cullity. *Elements of X-Ray Diffraction, Second Edition*. Addison-Wesley, Reading, MA, 1978.
- [118] R. Bachmann, Jr. F. J. DiSalvo, T. H. Geballe, R. L. Greene, R. E. Howard, C. N. King, H. C. Kirsch, K. N. Lee, R. E. Schwall, H.-U. Thomas, and R. B. Zubeck. *Rev. Sci. Instrum.*, 43:205, 1972.
- [119] R. E. Schwall, R. E. Howard, and G. R. Stewart. *Rev. Sci. Instrum.*, 46:1054, 1975.
- [120] G. R. Stewart. *Rev. Sci. Instrum.*, 54:1, 1983.
- [121] J. S. Kim. PhD thesis, University of Florida, 1992.
- [122] M. J. Naughton, S. Dickinson, R. C. Samaratunga, J. S. Brooks, and K. P. Martin. *Rev. Sci. Instrum.*, 54:1529, 1983.
- [123] T. Kagayama and G. Oomi. *Physica B*, 186-188:624, 1993.
- [124] T. Kagayama and G. Oomi. *J. Magn. Magn. Mater.*, 140-144:1227, 1995.
- [125] D. M. Bailey. *Acta Cryst.*, 23:729, 1967.
- [126] R. L. Snyder. PhD thesis, Iowa State University, 1960.
- [127] J. Callaway. *Quantum Theory of the Solid State*. Academic Press, Inc., San Diego, CA, 1991. 2nd Editon, p. 448.
- [128] A. S. Edelstein, R. L. Holtz, D. J. Gillespie, R. A. Fisher, and N. E. Phillips. *J. Magn. Magn. Mater.*, 63-64:335, 1987.
- [129] C. S. Jee, B. Andraka, J. S. Kim, H. Li, M. W. Meisel, and G. R. Stewart. *Phys. Rev. B*, 42:8630, 1990.
- [130] C. S. Jee, B. Andraka, J. S. Kim, and G. R. Stewart. *Phys. Rev. B*, 43:2656, 1991.
- [131] A. J. Millis. *Physica B*, 259-261:1169, 1999.
- [132] J. S. Kim, B. Andraka, C. S. Jee, S. B. Roy, and G. R. Stewart. *Phys. Rev. B*, 41:11073, 1990.

- [133] C. M. Varma. *Phys. Rev. Lett.*, 55:2723, 1985.
- [134] C. M. Varma. *Comments Solid State Phys.*, 11:221, 1985.
- [135] F. Steglich, P. Gegenwart, R. Helfrich, C. Langhammer, P. Hellmann, L. Donnevert, C. Geibel, M. Lang, G. Sparn, W. Assmus, G. R. Stewart, and A. Ochiai. *Z. Phys. B*, 103:235, 1997.
- [136] F. Steglich, C. Geibel, R. Helfrich, F. Kromer, M. Lang, G. Sparn, P. Gegenwart, L. Donnevert, C. Langhammer, A. Link, J. S. Kim, and G. R. Stewart. *J. Phys. Chem. Solids*, 59:2190, 1998.
- [137] F. Steglich, P. Gegenwart, C. Geibel, P. Hinze, M. Lang, C. Langhammer, G. Sparn, and O. Trovarelli. *Physica B*, 280:349, 2000.
- [138] A. Schröder, G. Aeppli, R. Coldea, M. Adams, O. Stockert, H. von Löhneysen, E. Bucher, R. Ramazashvili, and P. Coleman. *Nature*, 407:351, 2000.
- [139] S. A. M. Mentink, G. J. Nieuwenhuys, A. A. Menovsky, J. A. Mydosh, H. Tou, and Y. Kitaoka. *Phys. Rev. B*, 49:15759, 1994.
- [140] A. N. Medina, D. P. Rojas, F. G. Gandra, W. R. Azanha, and L. P. Cardoso. *Phys. Rev. B*, 59:8738, 1999.
- [141] M. Lorenzen, M. Hanfland, E. Bauer, F.-W. Schaper, and A. Eichler. *Physica B*, 259-261:20, 1999.
- [142] E. Bauer, G. Amoretti, L. C. Andreani, B. Delley, M. Ellerby, K. McEwen, R. Monnier, E. Pavarini, and P. Santini. *J. Phys.: Condens. Matter*, 10:4465, 1998.
- [143] G. R. Stewart, A. L. Giorgi, J. O. Willis, and J. O'Rourke. *Phys. Rev. B*, 34:4629, 1986.
- [144] B. Andraka and G. R. Stewart. *Phys. Rev. B*, 47:3208, 1993.
- [145] M. B. Maple, M. C. de Andrade, J. Herrmann, Y. Dalichaouch, D. A. Gajewski, C. L. Seaman, R. Chau, R. Movshovich, M. C. Aronson, and R. Osborn. *J. Low Temp. Phys.*, 99:223, 1995.
- [146] C. Broholm, J. K. Kjems, W. J. L. Buyers, P. Matthews, T. T. M. Palstra, A. A. Menovsky, and J. A. Mydosh. *Phys. Rev. Lett.*, 58:1467, 1987.
- [147] B. Andraka and Y. Takano. *Rev. Sci. Inst.*, 67:4256, 1996.
- [148] S. Chakravarty. *Phys. Rev. Lett.*, 49:681, 1982.
- [149] R. Pietri, K. Ingersent, and B. Andraka. *Phys. Rev. Lett.*, 86:1090, 2001.

- [150] K. Heuser, J. S. Kim, E-W. Scheidt, T. Schreiner, and G. R. Stewart. *Physica B*, 259-261:392, 1999.
- [151] G. Oomi, K. Izuki, J. Suzuki, and N. Mori. *J. Magn. Magn. Mater.*, 76-77:647, 1988.
- [152] T. Takimoto and T. Moriya. *Solid State Commun.*, 99:457, 1996.
- [153] F. Lapierre, P. Haen, A. Briggs, and M. Sera. *J. Magn. Magn. Mater.*, 63-64:76, 1987.
- [154] S. Paschen, E. Felder, and H. R. Ott. *Eur. Phys. J. B*, 2:169, 1998.
- [155] J. L. Gavilano, P. Vonlanthen, B. Ambrosini, J. Hunziker, F. Hulliger, and H. R. Ott. *Europhys. Lett.*, 32:361, 1995.
- [156] D. Kaczorowski, A. Leithe-Jasper, P. Rogl, H. Flandorfer, T. Cichorek, R. Pietri, and B. Andraka. *Phys. Rev. B*, 60:422, 1999.
- [157] K. Heuser, E.-W. Scheidt, T. Schreiner, and G. R. Stewart. *Phys. Rev. B*, 57:R 4198, 1998.
- [158] E. S. R. Gopal. *Specific Heats at Low Temperatures*. Plenum Press, New York, 1966.
- [159] B. Andraka, J. S. Kim, G. R. Stewart, and Z. Fisk. *Phys. Rev. B*, 44:4371, 1991. See also references therein.
- [160] K. D. Schotte and U. Schotte. *Phys. Lett.*, 55A:38, 1975.
- [161] H.-U. Desgranges and K. D. Schotte. *Phys. Lett.*, 91A:240, 1982.
- [162] P. Schlottmann. *Jour. Magn. Magn. Mater.*, 63-64:205, 1987.
- [163] V. T. Rajan, J. H Lowenstein, and N. Andrei. *Phys. Rev. Lett.*, 49:497, 1982.
- [164] B. Andraka, G. R. Stewart, and F. Steglich. *Phys. Rev. B*, 48:3939, 1993.
- [165] G. Bruls, B. Wolf, D. Finsterbusch, P. Thalmeier, I. Kouroudis, W. Sun, W. Assmus, B. Lüthi, M. Lang, K. Gloos, F. Steglich, and R. Modler. *Phys. Rev. Lett.*, 72:1754, 1994.
- [166] T. C. Kobayashi, A. Koda, H. Honda, K. Amaya, Y. Kitaoka, K. Asayama, C. Geibel, and F. Steglich. *Physica B*, 206-207:600, 1995.

BIOGRAPHICAL SKETCH

Richard Pietri Santiago was born August 7, 1971 in Hato Rey, Puerto Rico to Gilberto Pietri and Palmira Santiago. Raised in Río Piedras, Puerto Rico he attended Colegio Calasanz, where he graduated from high school in May 1989. Motivated by a strong interest in the physical sciences, he then decided to cross the Atlantic Ocean in search of new challenges. He attended Massachusetts Institute of Technology, where he graduated with a Bachelor of Science degree in Physics in May 1993. While at MIT, he worked as an undergraduate assistant at the Center for Space Research CCD Laboratory, where his research interests developed toward condensed matter physics. There is a saying that an MIT education is like attempting to drink water from a firehose. Therefore, after spending 4 years in front of a firehose, he attended graduate school at the University of Florida, where he pursued a Ph. D. degree in experimental condensed matter physics. His area of study was on uranium, cerium, and ytterbium-based heavy-fermion systems. While at UF, he worked in Prof. Greg Stewart's lab under the supervision of Dr. Bohdan Andraka. He also worked as a Physics I and II laboratory instructor, presented results at conferences and condensed matter seminars (Johns Hopkins U., William & Mary), and co-authored many publications in journals such as Physical Review B and Physical Review Letters.

I certify that I have read this study and that in my opinion it conforms to acceptable standards of scholarly presentation and is fully adequate, in scope and quality, as a dissertation for the degree of Doctor of Philosophy.

Bohdan Andraka, Chairman
Associate Scientist, Physics

I certify that I have read this study and that in my opinion it conforms to acceptable standards of scholarly presentation and is fully adequate, in scope and quality, as a dissertation for the degree of Doctor of Philosophy.

Gregory R. Stewart
Professor of Physics

I certify that I have read this study and that in my opinion it conforms to acceptable standards of scholarly presentation and is fully adequate, in scope and quality, as a dissertation for the degree of Doctor of Philosophy.

Mark W. Meisel
Professor of Physics

I certify that I have read this study and that in my opinion it conforms to acceptable standards of scholarly presentation and is fully adequate, in scope and quality, as a dissertation for the degree of Doctor of Philosophy.

Pradeep Kumar
Professor of Physics

I certify that I have read this study and that in my opinion it conforms to acceptable standards of scholarly presentation and is fully adequate, in scope and quality, as a dissertation for the degree of Doctor of Philosophy.

Cammy R. Abernathy
Professor of Materials Science and
Engineering

This dissertation was submitted to the Graduate Faculty of the Department of Physics in the College of Liberal Arts and Sciences and to the Graduate School and was accepted as partial fulfillment of the requirements for the degree of Doctor of Philosophy.

August 2001

Dean, Graduate School

LD
1780
2001

P629

UNIVERSITY OF FLORIDA



3 1262 08554 4350